Effect of Feedstock Powder, Processing Parameters, and Post-Heat Treatment on Cold-Sprayed Cu Alloys: Development of Heterogeneous Material

by

Niloofar Eftekhari

A thesis

presented to the University of Waterloo

in fulfillment of the

thesis requirement for the degree of

Doctor of Philosophy

in

Mechanical and Mechatronics Engineering

Waterloo, Ontario, Canada, 2025

© Niloofar Eftekhari 2025

Examining Committee Membership

The following served on the Examining Committee for this thesis. The decision of the Examining Committee is by majority vote.

External Examiner	TANVIR HUSSAIN, Ph.D. Professor, University of Nottingham
Supervisor	HAMID JAHED, Ph.D. Professor, University of Waterloo
Internal Member	EHSAN TOYSERKANI, Ph.D. Professor, University of Waterloo
Internal Member	HJ KWON, Ph.D. Professor, University of Waterloo
Internal-External Member	BILL ANDERSON, Ph.D. Professor, University of Waterloo

Author's Declaration

This thesis consists of material all of which I authored or co-authored: see Statement of Contributions included in this thesis. This is a true copy of the thesis, including any required final revisions, as accepted by my examiners.

I understand that my thesis may be made electronically available to the public.

Statement of Contributions

The research presented in this thesis was supported by Natural Sciences and Engineering Research Council of Canada (NSERC). The candidate is the primary author of all manuscripts, and was directly responsible for data collection, result analysis, and writing of the manuscripts. The contributions of co-authors to the research presented in this thesis are gratefully acknowledged:

- Prof. Hamid Jahed: Supervision of the research, providing the original idea for the current thesis, editing and reviewing papers, providing experimental facilities, providing funding.

- Dr. Dulal Saha: Providing technical training in cold spray system and editorial feedback in the preparation of the individual manuscript in Chapter 4.

Abstract

Cold spray (CS) is a solid-state powder deposition technique that utilizes high-velocity impact to bond particles onto a substrate or previously deposited layers in a layer-by-layer approach. This technology is extensively used for repairing high-performance components, protective and functional coatings, and 3D printing applications. However, a major challenge in cold spray additive manufacturing (CSAM) is understanding the relationship between feedstock powder characteristics and the final deposit properties. This thesis focuses on characterizing feedstock powders and analyzing the microstructure, physical properties, and mechanical behavior of cold-sprayed deposits. A key limitation in CS-deposited materials is their low ductility. To address this, various strategies, including process optimization and post-deposition heat treatment, are explored to enhance their mechanical properties. Furthermore, a novel approach has been introduced to improve ductility through the fabrication of heterogeneous laminated structures, where alternating layers of hard and soft alloys create a microstructure with fine-grained and coarse-grained regions, ultimately enhancing the mechanical performance of CS deposits.

To explore this, the cold-sprayability of various Cu powders produced by electrolysis, gas atomization, and grinding was examined and compared using scanning electron microscopy (SEM), electron backscatter diffraction (EBSD), particle analysis (CAMSIZER, FT4 powder flow tester), and nano-hardness testing. The results indicated that the spherical morphology of gas-atomized powders had a lower surface area compared to the irregular-shaped electrolytic and ground powders, reducing surface interactions and improving powder flowability. Additionally, gas-atomized Cu powders with equiaxed grains exhibited an average nano-hardness value, balancing flowability and deformability. Therefore, these powders were identified as promising feedstock materials for CS applications. Furthermore, the impact of these powders on coating microstructure and mechanical properties was investigated. A comprehensive statistical model was developed to optimize process gas temperature and pressure for deposition. It was found that operating near the upper temperature and pressure limits of the low-pressure cold spray (LPCS) system resulted in coatings with minimal porosity, high flattening ratio, increased microhardness, and enhanced bonding strength. Surface and microstructural evolution analysis revealed that lower oxide content near the surface of more spherical, satellite-free powders significantly enhanced plastic deformation and grain refinement during deposition.

Improving the mechanical properties of CS depositions for optimal strength and ductility under uniaxial tensile testing leads to the next step, which involves investigating the effects of different processing gases (Nitrogen and Helium) and post-heat treatment on pure Cu. The findings suggest that while Cu 3D-printed parts processed with He exhibit higher deposition efficiency, N_2-processed samples show greater plastic deformation and lower porosity due to the higher number of deposition passes and the peening effect required to achieve the same thickness as He-processed samples. Heat treatment, when applied at an appropriate temperature and duration, enhances interfacial bonding, promotes recrystallization, and facilitates grain growth, leading to strength and ductility improvements of up to 2.7 times and 28 times, respectively. Heat treatment also plays a critical role in defining the microstructure and mechanical performance of CSAM CuCrZr alloys, an area that remains less explored. The as-sprayed CuCrZr alloy exhibited weakly bonded particle interfaces and porosity, which were significantly reduced by solution annealing and age hardening (SA+AH). This process led to grain reorganization, interfacial healing, solid-state diffusion bonding and precipitation of ultra fine particles resulting in strength and ductility enhancements of up to 2.4 times and 9 times, respectively.

Engineering heterogeneous microstructures has emerged as an effective strategy to enhance the mechanical behavior of materials processed through various thermomechanical and manufacturing techniques. However, this approach remains largely unexplored in 3D-printed cold-sprayed components. In this study, a dual heterogeneous laminated Cu/CuCrZr composite structure with varying interface spacing was developed using LPCS followed by post-heat treatment. This tailored microstructure consists of alternating coarse- and fine-grained regions, generating microstructural contrast that induces hetero-deformation-induced (HDI) strengthening. The mechanical incompatibility between the soft Cu and hard Cu-Cr-Zr layers enhances strength and ductility, with decreasing interface spacing improving strength and ductility by up to 10% and 28%, respectively. To further understand the strain hardening mechanisms, loading-unloading-reloading (LUR) experiments and microstructural analyses were conducted. The findings attribute the enhanced mechanical performance to well-bonded particles and HDI strengthening, driven by geometrically necessary dislocations (GNDs) at heterogeneous interfaces. This effect improves work-hardening capacity, leading to simultaneous increases in both strength and tensile ductility of the laminated alloy. While this innovative heterogeneous design strategy for cold-sprayed materials requires further exploration across various topologies, heat treatment methods, and alloy systems, it presents a promising approach to enhancing strength and ductility in low-pressure cold spray materials.

Acknowledgements

This research would not have been possible without the support and assistance of several individuals, to whom I am deeply grateful.

First and foremost, I would like to extend my heartfelt gratitude to my supervisor, Prof. Hamid Jahed, for his continuous support, guidance, and patience throughout this research. I am especially thankful for his encouragement, mentorship, and assistance during my graduate studies at the University of Waterloo.

I hereby acknowledge my thesis examining committee members, Prof. Tanvir Hussain from University of Nottingham, Prof. Ehsan Toyserkani, Prof. Hyock Ju Kwon, and Prof. Bill Anderson from the University of Waterloo for taking time to review my thesis and provide their valuable and constructive insights.

I am also deeply thankful to all my colleagues at FATSLAB laboratory, Dr. Dulal Saha, Dr. Behzad Behravesh, and Dr. Bahareh Marzbanrad, for their friendship and support. I am especially grateful to Alan Woo, whose guidance and assistance were essential to the completion of this work.

I would like to thank Henry Ma, Francis Dibia, Nadia Azizi and Dr. Ehsan Marzbanrad from MSAM laboratory for facilitating access to the characterization and heat treatment equipment at this lab.

I would like to acknowledge Neil Griffett, Jason Benninger, and Douglas Hirst for their help with troubleshooting and assisting in the cold spray and materials laboratories works.

I thank Dr. Bipasha Bose and Dr. Mohammad Chowdhury from the McMaster Manufacturing Research Institute (MMRI), Zhi (George) Zhang from Thompson Engineering, Western University, and Chris Butcher from the Canadian Centre for Electron Microscopy (CCEM), McMaster University, for facilitating the experimental work.

I would also like to acknowledge the support provided by the Natural Sciences and Engineering Research Council of Canada (NSERC), the Ontario Graduate Scholarship (OGS) Program, and CenterLine (Windsor) Limited, with special thanks to Jianfeng Wang and Harvey Ye.

Lastly, and most importantly, I extend my heartfelt thanks to my parents, Maryam and Aliakbar, as well as my dear siblings, for their endless love and support. I am profoundly grateful to my husband, Milad, for his continuous encouragement, collaboration, and help throughout this journey, this accomplishment would not have been possible without him.

Dedication

Dedicated to my beloved family

my parents, Maryam and Aliakbar, and love of my life, Milad

Table of Contents

List of Figures xv

List of Tables xxv

Chapter 1 Introduction 1

1.1 Motivation 1

1.2 Research objectives 3

1.3 Thesis overview 6

Chapter 2 Literature review 8

2.1 Background on cold spray technology 8

2.1.1 Principle and setup 8

2.1.2 Deposition mechanism 9

2.1.3 Cold spray parameters 11

2.1.4 Materials and applications 12

2.1.5 Feedstock powder 12

2.2 Metallic powder manufacturing methods 13

2.2.1 Gas atomization 13

2.2.2 Plasma atomization 14

2.2.3 Electrolysis 15

2.2.4 Grinding 16

2.2.5 Hydrometallurgy 17

2.3 Characteristics of feedstock powders 18

2.3.1 Particle size distribution 18

2.3.2 Particle Morphology 20

2.3.3 Flowability 22

2.3.4 Microstructure of powders 24
2.4 Powder cold sprayability 25
2.4.1 The effect of surface oxidation on cold sprayability 26
2.4.2 The effect of ceramic particles and metal-alloy powder blends on enhancing the sprayability 26
2.4.3 The effect of powder mixtures with nano and micron grain sizes on cold sprayability 28
2.5 Heterogeneous materials 29
2.5.1 Deformation behavior, strengthening and work hardening mechanisms 29
2.5.2 Creation of heterogeneous materials through cold spray additive manufacturing 32
2.5.3 Effect of feedstock powders on creation of heterogeneous materials 38
2.5.4 Dual heterogeneous laminated composites 40
2.6 Critical gaps in the literature 45
Chapter 3 Methodology 46
3.1 Characterization of as-received powders 46
3.1.1 Morphology and microstructure 46
3.1.2 Particle size and shape analysis 47
3.1.3 Powder flowability 47
3.1.4 Nanoindentation 48
3.2 Cold spray process 48
3.3 Post-deposition heat treatment 52
3.4 Characterization of cold sprayed depositions 53
3.4.1 Thickness and weight 53
3.4.2 Microstructure 53
3.4.3 Microhardness 54

3.4.4 Adhesion/Cohesion strength 55
3.4.5 Tensile test and Fractography 55
3.4.6 Loading unloading reloading (LUR) experiment 57
3.4.7 Hetero deformation induced (HDI) strength measurement 57
Chapter 4 A comparative study on the powder manufacturing effect on flowability and deformability of pure Cu powders for cold spray application 60
4.1 Abstract 60
4.2 Introduction 60
4.3 Experimental Methods 62
4.4 Results and discussion 63
4.4.1 Morphology and microstructure of pure Cu powders 63
4.4.2 Particle size distribution of pure Cu powders 69
4.4.3 Flowability of pure Cu powders 71
4.4.4 Nano-indentation analysis of pure Cu powders 73
4.5 Conclusion 76
Chapter 5 Comparative Analysis of Microstructural and Mechanical Attributes in Low-Pressure Cold-Spray Coatings: Impact of Varied Cu Feedstock Powders 77
5.1 Abstract 77
5.2 Introduction 78
5.3 Materials and Methods 82
5.3.1 Feedstock powders characterization and cold spray process 82
5.3.2 Characterization of cold spray depositions 85
5.4 Results and discussion 86
5.4.1 Feedstock powder characterization 86

5.4.2 Design of experiment (DOE) to obtain optimum deposition parameters 88
5.4.3 Microstructure of deposited samples 97
5.4.4 Microstructure of substrate 105
5.4.5 Microhardness of coatings 108
5.4.6 Adhesion or cohesion strength of coatings 109
5.4.7 Deposition behavior 110
5.5 Conclusion 112
Chapter 6 Evolution of Microstructure, Strength, and Ductility in 3D-Printed Low-Pressure Cold Spray Copper: Effects of Process Gas and Heat Treatment 114
6.1 Abstract 114
6.2 Introduction 115
6.3 Experimental Methods 118
6.3.1 Feedstock powder and CS manufacturing procedure 118
6.3.2 Heat treatment 122
6.3.3 Microstructural characterization 122
6.3.4 Physical and mechanical properties 122
6.4 Results and discussion 123
6.4.1 Effect of process gas species on particle velocity and deposition efficiency 123
6.4.2 Microstructures of CSAM Cu materials made by using different process gasses before and after heat treatment 125
6.4.3 Microhardness 134
6.4.4 Tensile properties 135
6.4.5 Fracture surface analysis 142
6.5 Conclusion 143

Chapter 7 Microstructural Evolution and Mechanical Behavior of Low-Pressure Cold-Sprayed 3D-Printed CuCrZr Alloy through Solution Annealing and Age Hardening 145
7.1 Abstract 145
7.2 Introduction 146
7.3 Experiment and characterization 150
7.3.1 Materials and equipment 150
7.3.2 Experimental method and characterization 151
7.4 Results and discussion 154
7.4.1 Microstructure and texture of CSAM CuCrZr alloy in different states 154
7.4.2 XRD analysis 165
7.4.3 Microhardness 168
7.4.4 Tensile properties 170
7.5 Conclusion 176
Chapter 8 Engineering Dual Heterogeneous Laminated Microstructure to Unlock Strength and Ductility in Cold Sprayed Copper Alloys 178
8.1 Abstract 178
8.2 Introduction 178
8.3 Experimental procedures 182
8.4 Results and discussion 186
8.4.1 Microstructure 186
8.4.2 Microhardness 195
8.4.3 Tensile Behavior 196
8.4.4 Discussion on the improvement of strength-ductility 200
8.5 Conclusion 206

Chapter 9 Summary, Conclusions, and Future Work/Outlook 208
9.1 Summary 208
9.2 Conclusions 209
9.3 Thesis contributions 211
9.4 Recommendations and future work 212
References 215

List of Figures

Figure 1: Thesis graphical abstract 6
Figure 2: Schematic illustration of the cold spray process [10] 8
Figure 3: Schematic drawings of (A) plastic deformation in interface leading to cold welding and (B) deformation localization because of shear instability as a result of particle impact in cold spraying [9]. 10
Figure 4: Schematic illustration of (a) gas atomization process and (b) plasma atomization process [51,53] 15
Figure 5: An electrolytic cell for the deposition of metal powder. 16
Figure 6: (a) volume fraction (%), volume-based particle size distribution showing D10 = 10 µm, D50 = 30 µm, and D90 = 50 µm, indicating the fine, median, and coarse fractions and (b) accumulative volume fraction (%) graphs showing the percentage of particles below a given size, reaching ~100% below 32 µm [61]. 19
Figure 7: Different types of powder particles morphologies [27,63] 21
Figure 8: Graphical illustration of different parameters attainable from Powder Yield Locus [65] 23
Figure 9: SEM images of the (a) Al-Mg-7wt% Al_2O_3 and (b) Al-Mg-10wt% Al_2O_3 coatings. Red marks show the deformed Al–Mg particles and the dotted white circle displays the alumina particles which are un-deformed and trapped in the matrix [73]. 27
Figure 10: Porosity illustration of (a) 95% Ti_6Al_4V + 5% Ti, (b) 90% Ti_6Al_4V + 10% Ti, and (c) 80% Ti_6Al_4V + 20% Ti [42] 28
Figure 11: (a) Inverse Pole Figure (IPF) maps from the coatings with 10%, 20%, and 30% micron grain size powders and (b) deposition efficiency, porosity percent, and hardness of coatings vs. the content of micron grain size powder [76]. 29
Figure 12: (A) Dislocation pile-ups shown by green lines in a heterogeneous lamella Ti. (B) Schematic representation of GNDs pilling up, strain gradient and plastic strain as a function of distance from the domain interface, the effective stress that is obtained [78,80]. 31
Figure 13: Schematic illustration of a lamellar structure featuring soft coarse-grained regions dispersed within an ultrafine-grained matrix. 32
Figure 14: (a) Stress-strain curves and (b) EBSD IPF maps of cold sprayed Cu at high and low process parameters [86]. "Fine" in the image refers to the fine powder characterized by D10 = 6.2 µm,

D50 = 11.8 μm, and D90 = 17.8 μm, while "coarse" corresponds to the coarse powder with D10 = 18.9 μm, D50 = 26.1 μm, and D90 = 40 μm. 34
Figure 15: EBSD IPF maps for the grain structures of the deformed single particle at the (a) bottom and (b) peripheral regions, and (c) OM of the etched sample showing the severely deformed particles [87]. 35
Figure 16: CSAM deposit with harmonic gradient nano-structure: (a) as-received particle with micron size grains, (b) the deformed particle with gradient nano-structure, (c) bonding of many deformed particles and (d) the final microstructure [87]....35
Figure 17: Cross-sectional EBSD grain orientation maps of cold sprayed Cu: (a) process gas N2 and (b) process gas He and (c) measured work hardening rate ($d\sigma/d\varepsilon$, Θ) obtained from the stress-strain curves [88]....37
Figure 18: (a) OM image, (b) grain size distribution map, and (c–d) BSE images of AZ91 substrate near the bonding surface [89]....38
Figure 19: a) Stress-strain curves of as-sprayed samples; b) The elongations to failure vs. volume fraction of MC powders [77]....39
Figure 20: Schematic illustration of different strengthening mechanisms happening at different conditions for wide particle size distribution of feedstock powder [91]....40
Figure 21: (a) Cross-sectional micro-hardness distributions profile, (b) layer interface of Cu/Cu-Cr-Zr laminates sample [99]. 41
Figure 22: Tensile curves of pure Cu, CuCrZr180, the experimentally measured CuCrZr/Cu180 composite, and the corresponding curve predicted using the rule of mixtures [98]. "180" denotes the CuCrZr powder that underwent ball milling for a duration of 180 minutes. 42
Figure 23: (a) engineering stress–strain curves are presented for the layered CuCrZr alloy, CuCrZr, and pure Cu following thermomechanical processing. The labels 200, 400, and 600 correspond to cold-pressed billets of layered CuCrZr–Cu composites, each featuring equal layer thicknesses (ELT) of 200 μm, 400 μm, and 600 μm, respectively. "60" indicates that the layered CuCrZr alloys underwent secondary aging for a duration of 60 minutes. (b) Corresponding plots show the strain hardening rate as a function of logarithmic strain, with the inset illustrating the relationship between the strain hardening index and logarithmic strain [100]. 43
Figure 24: The correlation between the average GND density and the equivalent distance from the CuCrZr/Cu interface in the 400-ELT60 layered alloy subjected to 3% tensile strain [100]....43

Figure 25: (a) Unloading-reloading tensile curves of N2, N3, N5 samples that have 4, 8 and 32 layers, respectively. (b) The calculated back stress at corresponding strain levels [101]. 44
Figure 26: Averaged GND density in copper layer versus the equivalent distance from the interfaces at different strain levels of (a) N2 sample, (b) N3 sample, (c) N5 sample [101].....44
Figure 27: The commercial Cold Spray System (Series P) by Supersonic Spray Technologies (SST), manufactured by Centerline in Windsor, Canada, installed and operated in the Cold Spray lab at the University of Waterloo, located in room 2116A, E3 building.....49
Figure 28: Top and side views of the cold spray coatings produced using powders (a) and (b) A, (c) and (d) B, (e) and (f) C, and (g) and (h) D. The numbers marked on the plates correspond to various experimental trials and their repetitions. The substrates have a thickness of 3.16 mm, while the coatings are in the micron range. 50
Figure 29: Macroscopic images of cold-sprayed copper materials using different process gases: (a) nitrogen (N_2) as the process gas, and (b) helium (He) as the process gas.....50
Figure 30: Image of the cold-sprayed CuCrZr material deposited using nitrogen (N_2) as the process gas. 51
Figure 31: Macroscopic images of laminated Cu/CuCrZr structures with varying layer configurations: (a) 7-layer laminate and (b) 14-layer laminate.....52
Figure 32: Photographs showing coupon samples in (a) as-sprayed and before grinding, (b) post-grinding to smooth the coating surface, (c) alignment fixture clamped the parts together, (d) schematic of coupon geometry with threaded hole, and (e) test setup.....56
Figure 33: (a) dimensions of the tensile specimen; and (b) the extracted tensile specimen from the deposit. 56
Figure 34: Schematic illustration of the unloading–reloading loop used to define the unloading yield stress (σ_u), reloading yield stress (σ_r), back stress (σ_b), and frictional stress (σ_f), along with the effective Young's moduli during unloading (E_u) and reloading (E_r) [109]. 59
Figure 35: Low and high magnification SEM images depicting the morphology of the as-received pure Cu powders (a) and (b) A, (c) and (d) B, (e) and (f) C, (g) and (h) D and (i) and (j) E, respectively. Red arrows in (h) represents fine and coarse cells structures. 66
Figure 36: SEM cross-sectional micrographs of pure Cu powder particles of (a) and (b) A, (c) and (d) B, (e) and (f) C, (g) and (h) D, and (i) and (j) E in as-received condition. 69

Figure 37: (a) volume fraction (%) and (b) accumulative volume fraction (%) of different pure Cu powders. Powder C data measured by Camsizer X2 has been obtained from the vender. 70
Figure 38: Rheological properties of as-received powders obtained from shear cell test showing (a) cohesion value, (b) flow function (ffc) and (c) angle of internal friction. 72
Figure 39: Particle sphericity distributions of pure Cu powders of (a) A, (b) B, (c) C, (d) D, and (E). 73
Figure 40: Nano-indentation impressions on the investigated pure Cu powders: (a) A, (b) B, (c) C, (d) D, and (E). 75
Figure 41: (a) Load- displacement curves, and (b) nano-hardness and elastic modulus of pure Cu powders obtained from nano-indentation..... 75
Figure 42: Scanning electron microscopy (SEM) morphologies of copper powders prepared through (a) electrolysis, (b), (c) and (d) gas atomization. 83
Figure 43: Top and side view of the cold sprayed coatings obtained from powders (a) and (b) A, (c) and (d) B, (e) and (f) C and (g) and (h) D. Numbers on the plates refer to different trials and their repetitions. Thickness of substrates is 3.16 mm and thickness of coatings are micron scale. 84
Figure 44: EBSD grain orientation map for cross-sectional powders of (a) A, (b) B, (c) C and (d) D. 87
Figure 45: Weight change of substrates and thickness of coatings at different pressures and temperatures for Cu powders of (a) A, (b) B, (c) C, and (d) D. 92
Figure 46: Pareto charts of the standardized effects (α = 0.05) of Cu powders for the responses of (a) weight change and (b) thickness, respectively. 93
Figure 47: Contour plots of weight change for Cu powders of (a) A, (c) B, and (e) C, respectively and Contour plots of thickness for Cu powders of (b) A, (d) B, (f) C, and (g) D, respectively. 97
Figure 48: Optical microscopy of cold-sprayed coatings after metallographic etching of polished cross section samples from the interface to the top of coatings obtained from (a), (b) and (c) powder A, (d), (e) and (f) powder B and (g), (h) and (i) powder C..... 99
Figure 49: XPS survey spectra..... 100
Figure 50: high-resolution Cu 2p XPS spectra displaying the dominant Cu 2p3/2 emission line at 932-933 eV, with shake-up peaks of varying intensities at 940-945 eV for different feedstock powders. 101
Figure 51: High magnification and low magnification SEM cross-sectional images of cold sprayed coatings using powders (a) A, (b) B, and (c) C, red arrows show large visible pores and blue arrows show the tiny pores..... 102

Figure 52: (a and b) Inverse pole figure (IPF) and (c and d) Kernel Average Mis orientation (KAM, orientation legend at the bottom of figures in degrees) maps of cold sprayed coatings obtained from (a) and (c) powder B and (b) and (d) powder C. Yellow box indicates the interface area between coating and substrate. 104
Figure 53: Grain size distribution for coatings from (a) powder B and (b) powder C, corresponding to the coating sections illustrated in Figure 52, points to heterogeneous deformation of Cu splats and a non-uniform distribution of grain sizes. 105
Figure 54: low and high magnification OM images of the (a) and (b) as received sample, (c) and (d) coating using powder A, (e) and (f) coating using powder B and (g) and (h) coating using powder C, respectively. Red curves indicate the interface between the coating and substrate. 106
Figure 55: Changes in grain size of substrate adjacent to the interface before and after deposition: as received, coated using powder A, coated using powder B and coated using powder C. 107
Figure 56: Vickers microhardness distribution from the substrate to the top of cold sprayed Cu coatings obtained from different Cu powders. 108
Figure 57: The adhesion or cohesion bonding strength and failure surface images of cold spray coatings evaluated through a tensile pull-off test, according to the ASTM C633 standards. [a] CCF-Cohesive Coating Failure, ACF-Adhesive Coating Failure. 110
Figure 58: (a) Morphologies of copper powder observed by SEM, (b) EBSD grain orientation map for cross-sectional powder particles, (c) volume fraction (%) and (d) accumulative volume fraction (%) of pure Cu powder. 119
Figure 59: Macro images of cold sprayed Cu materials with different process gasses: (a) process gas N_2, (b) process gas He. 121
Figure 60: (a) dimensions of the tensile specimen; and (b) the extracted tensile specimen from the 3D-printed part. 121
Figure 61: Particle velocities vs. particle size of pure Cu with different process gases of He and N_2 at optimum gas temperature and pressure of 400°C and 1.99 MPa, respectively. 124
Figure 62: XRD spectra of the as-sprayed and heat treated Cu deposits produced using N_2 and He process gases, the XRD reference for pure copper is PDF card number 04-0836 from the ICDD PDF-4+ database. 125

Figure 63: (a) Williamson-Hall plots for XRD diffraction patterns, (b) calculated dislocation density, and crystallite size for as sprayed and heat treated Cu deposits produced by N_2 and He process gases. 128
Figure 64: Optical micrographs of (a, b) as-sprayed, (c, d) 500 °C HT, (e, f) 700 °C HT. (a, c, e) show the cold spray deposits produced using N_2 process gas and (b, d, f) show the cold spray deposits produced using He process gas. The red arrows, green dashed and blue dotted lines in (a) and (b) shows well-bonded interfaces, grains with minimal deformation and recrystallized grains, respectively. The yellow and green arrows in (c) and (d) highlight the non-bonded particle–particle interface and spheroidized voids, respectively. Purple arrows in (e) and (f) indicate recrystallization twins. 131
Figure 65: Inverse pole figure (IPF) and image quality (IQ) maps of (a, b) as-sprayed, (c, d) 500 °C HT, (e, f) 700 °C HT. (a, c, e) show the cold spray deposits produced using N_2 process gas and (b, d, f) show the cold spray deposits produced using He process gas.....133
Figure 66: Grain size distribution of (a, b) as-sprayed, (c, d) 500 °C HT, (e, f) 700 °C HT. (a, c, e) show the cold spray deposits produced using N_2 process gas and (b, d, f) show the cold spray deposits produced using He process gas. 134
Figure 67: Comparison of microhardness of Cu cold spray deposits produced using N_2 and He process gases in the as-deposited and different heat-treated conditions. 135
Figure 68: Stress-strain curves showing limited strength and elongation of as sprayed deposits, and higher strength and ductility of heat-treated deposits. 136
Figure 69: Comparison of tensile properties of Cu deposits produced using N_2 and He process gas in the as-deposited and different heat treated conditions showing: (a) yield strength; (b) ultimate tensile strength; and (c) elongation.....137
Figure 70: (a) Elongation to failure and (b) ultimate tensile strength of Cu deposits in the as-sprayed state and under various annealing conditions at different temperatures are presented for this study alongside other research findings in the literature. For comparison, the graph also includes data for severely cold-rolled and annealed bulk Cu [182,183,197,202,203]. 141
Figure 71: Fracture surface of different deposits: (a, b) as-sprayed by N_2, (c, d) as-sprayed by He, (e, f) 500 °C HT for N_2 samples, (g, h) 500 °C HT for He samples, (i, j) 700 °C HT for N_2 samples and (k, l) 700 °C HT for He samples. (b, d, f, h, j, l) are high magnification of (a, c, e, g, i, l), respectively. The fracture surfaces' distinctive traits are illustrated as follows: Blue arrows denote splat detachment,

red arrows signify brittle inter-particle fractures, green arrows indicate micro-cracks along inter-splat boundaries, the yellow arrow points out a river-like pattern, brown arrows mark fine dimples, and purple arrows depict enlarged dimples. 143
Figure 72: SEM morphology of CuCrZr powder in (a) low and (b) high magnification, and (c) cross section showing grain microstructure. 150
Figure 73: (a) Cold spray 3D printed CuCrZr, before machining samples, (b) the tensile specimen dimensions; and (c) the tensile specimen sectioned from the deposited material....152
Figure 74: (a) and (b) Schematic of post heat treatment of cold sprayed printed CuCrZr (DAH: Direct Age Hardening, SA: Solution Annealing, SA+AH: Solution Annealing + Age Hardening). 153
Figure 75: (a) SEM micrograph of as-printed CuCrZr, with corresponding EDS maps showing the elemental distribution maps of (b) Cu, (c) Cr and (d) Zr, showing uniform Cr and Zr distribution in copper matrix. 156
Figure 76: Microstructures of CuCrZr samples at low and high magnifications following the etching process in (a) and (b) as-sprayed (CS), (c) and (d) solution annealed (SA), (e) and (f) solution annealed +age hardened (SA+AH), and (g) and (h) direct age hardened state at 480 °C/1 h (DAH). Yellow ellipses indicate heavily deformed splats, while green arrows point to visible pores caused by the less effective deposition of smaller particles and poorly bonded interfaces. Pink arrows highlight sherardized voids, and blue ellipses reveal the internal grain structure within the powder splats.....157
Figure 77: SEM images of CuCrZr alloy specimens. (a) CS, (b) SA, (c) SA+AH, (d) DAH. The white arrows, yellow circles and red ellipses highlight the porosity, micro-pores and non-bonded particle–particle interface, respectively. 158
Figure 78: Cross-sectional EBSD images, PF maps, and IPF maps of (a) and (b) as-sprayed sample and different heat-treated samples: (c) and (d) SA sample; (e) and (f) SA+AH sample, and (g) and (h) DAH sample.....160
Figure 79: Grain boundary distribution map (superimposed on band contrast map), recrystallized fraction (RF) map and kernel average misorientation (KAM) map of samples before and after heat treatments: (a1)-(a3) as-sprayed sample, (b1)-(b3) SA sample, (c1)-(c3) SA+AH sample and (d1)-(d3) DAH sample. 165
Figure 80: (a) XRD patterns of CuCrZr powder (P) and cold-sprayed (CS) samples subjected to different heat treatments, (b) a magnified view of the XRD peaks highlighted by yellow rectangles in (a) and (c) the enlarged spectra of 42–45◦ shown by black rectangle in (a). 167

Figure 81: (a) Williamson-Hall plots for XRD diffraction patterns, (b) calculated dislocation density, and crystallite size for the powder, as sprayed and heat-treated CuCrZr deposits. 168
Figure 82: (a) Microhardness of CS CuCrZr specimens with and without heat treatment. (b) Variation in microhardness under different aging times. (c) Variation in microhardness under different aging temperatures. 169
Figure 83: Comparison of stress–strain curves in different states of as sprayed, and after different heat-treatments. 170
Figure 84: Comparison of tensile properties of CuCrZr deposits in the as-sprayed and different heat-treated conditions showing: (a) yield strength; (b) ultimate tensile strength; and (c) elongation. 171
Figure 85: SEM images of the fracture surface of (a) CS, showing cleavage-like brittle fracture along splat boundaries, (b) SA, showing dimple-like morphology, indicating plastic deformation, (c) SA+AH, also showing plasticity and void formation and coalescence, (d) DAH specimens, showing failure along splat boundaries with no indication of plasticity. 172
Figure 86: Comparison of the tensile properties of CuCrZr alloys in their as-built and heat-treated states, manufactured using SLM [220,225,228], LPBF [223,224,227], WAAM [226] and cold spray [229] additive manufacturing techniques, depicting: (a) ultimate tensile strength and yield strength and (b) percentage elongation. 175
Figure 87: SEM micrographs of pure Cu (a, c) and CuCrZr (b, d) alloy powders: (a) and (b) display the morphology, while (c) and (d) show the equiaxed grain microstructure; and (e) Particle size distributions for pure Cu and CuCrZr. 183
Figure 88: Macro images of laminated Cu/CuCrZr materials with different layer configurations: (a) 7-layer laminate and (b) 14-layer laminate. 184
Figure 89: (a) Dimensions of the tensile specimen; and (b) the extracted tensile specimen from the 3D-printed part. 185
Figure 90: Optical micrographs of as-sprayed heterostructured laminated samples consisting of different Cu–CuCrZr layer counts: (a) 7 layers (7L) and (b) 14 layers (14L). Yellow arrows indicate the presence of porosity, micro-pores, and unbonded interfaces between the particles. 187
Figure 91: Optical micrographs of solution annealed+ age hardened heterostructured laminated Cu–CuCrZr samples with (a) 7L and (b) 14L. At this magnification, (a) displays portions of one Cu layer and one CuCrZr layer, while (b) reveals two Cu layers, one complete and two incomplete CuCrZr layers. The inset in (a) presents a higher magnification view of the interface between the Cu and

CuCrZr layers. Images (c) and (d) show the microstructures of the heat-treated Cu and CuCrZr layers individually at higher magnifications. Blue arrows highlight annealing twins, red arrows indicate porosity and unbonded particle interfaces, and green ellipses highlight individual splats that have retained their morphology after heat treatment. 189
Figure 92: Inverse pole figure (IPF) maps of laminated Cu–CuCrZr samples with varying layer counts: (a) 7 layers (7L) and (b) 14 layers (14L), both in the as-sprayed condition. Yellow rectangles show larger grains in particle interiors. 190
Figure 93: Inverse pole figure (IPF) maps, band contrast images, grain boundary distribution maps (overlaid on band contrast), recrystallized fraction (RF) maps, and kernel average misorientation (KAM) maps of heat-treated laminated samples: (a), (c), (e), (g), and (i) correspond to the 7-layer (7L) sample, while (b), (d), (f), (h), and (j) correspond to the 14-layer (14L) sample. IPF maps (a, b) show recrystallized structures in both Cu and CuCrZr, with CuCrZr exhibiting finer, more fragmented grains. Yellow rectangles highlight the coarser grains located within splat interiors, which, together with finer grains along splat boundaries, form a bimodal grain structure in the CuCrZr layer. An orange mark in (b) highlights a splat boundary along the build-up direction, and yellow ellipses indicate finer grains near Cu–CuCrZr interfaces. Band contrast images (c, d) show Σ3 twin boundaries (green lines), more prevalent in CuCrZr. Blue arrows indicate porosity more noticeable in Cu. Grain boundary maps (e, f) reveal a high fraction of HAGBs, while LAGBs (green lines) appear more in Cu. RF maps (g, h) confirm high recrystallization, and KAM maps (i, j) indicate low internal misorientation post-treatment, with some localized strain accommodation remaining in Cu. 194
Figure 94: (a) Microhardness of Cu and CuCrZr layers before and after heat treatment, showing better thermal stability, likely due to Cr and Zr presence; (b) Micro-hardness in both the heat-treated Cu and CuCrZr layers for the first 7 layers in 7L and 14L samples. This sharp mechanical contrast between layers suggests a significant degree of mechanical incompatibility. 196
Figure 95: (a) Engineering stress–strain curves of heat-treated Cu–CuCrZr laminated alloys with 7 layers (7L) and 14 layers (14L), alongside pure CuCrZr and pure Cu for comparison. Also shown are the predicted curves based on ROM for 7L and 14L, a; (b) corresponding strain hardening rate versus true strain curves, derived from the experimental data in (a), for pure Cu, pure CuCrZr, 7L, and 14L samples. 199
Figure 96: Comparison of experimentally measured tensile properties of yield strength, ultimate tensile strength, and uniform elongation (%) for heat-treated pure Cu, pure CuCrZr, and laminated 7L

and 14L samples. Also included are the corresponding values for pure Cu after optimum heat treatment from previous work, as well as predictions based on the rule of mixtures (ROM) for the 7L and 14L laminates. 200
Figure 97: (a) LUR curves obtained from samples of pure Cu, pure CuCrZr, 7L, 14L, (b) Enlarged LUR curves showing the hysteresis loops, (c) and (d) The individual hysteresis loops observed in the 7L and 14L laminates indicate early yielding and considerable anelastic recovery strain (ε_{ae}) during unloading. Here, ε_e represents the elastic portion of the recovery strain, and (e) Calculated HDI stress of different samples. 202
Figure 98: (a) and (c) Band contrast maps depicting the interfaces between fine-grained CuCrZr and coarse-grained Cu regions in the laminated 7L and 14L sample subjected to a true strain of 7.5% and 9%, respectively. (b) and (d) Corresponding GND (geometrically necessary dislocation) density maps of the same regions, illustrating the dislocation distribution within both fine and coarse grain domains. 203
Figure 99: Schematic representation of deformation behavior in laminated Cu/CuCrZr structures with increasing strain and interface density. The buildup of GNDs near interfaces arises from mechanical incompatibility between neighboring layers. As interface density increases, so does the accumulation of GNDs, leading to the development of long-range internal stress fields that contribute to HDI hardening. 205
Figure 100: Representative fracture surface at the interface between coarse-grained Cu and fine-grained CuCrZr in the 14L laminate. The interface location is indicated by white dotted arrows. Dimple features are visible in the fine-grained CuCrZr region, adjacent to brittle fracture zones observed in the coarse-grained Cu layer. 205

List of Tables

Table 1: The effect of cold spray process parameters on the deposition conditions [9] 11
Table 2: Summary of powder particle morphologies 21
Table 3: Supplier, production method and copper content (wt.%) of each powder 46
Table 4: Specification of SST cold spray system 49
Table 5: Supplier, production method and copper content (wt.%) of each powder 62
Table 6: Particle size of pure Cu powders particles 71
Table 7: Summary of the detailed processing parameters and the measured/calculated resultant properties of the deposits fabricated via different Cu feedstock powders 80
Table 8: Specification of SST cold spray system 84
Table 9: Feedstock powder characterization [146] 87
Table 10: Cold spray deposition parameters for different Cu powders 89
Table 11: Calculated particle velocity (m/s) for different feedstock powders under different conditions 89
Table 12: P value for temperature and pressure obtained from ANOVA tables 93
Table 13: Porosity of cold sprayed coatings obtained from different Cu powders 102
Table 14: Cold spray deposition parameters for N_2 and He processed samples 119
Table 15: Specification of SST cold spray nozzle 120
Table 16: Variation in porosity of pure Cu cold spray deposits in the as sprayed (AS) and heat-treated (HT) conditions produced using N_2 and He process gases 138
Table 17: Chemical composition of the CuCrZr alloy powder 150
Table 18: Specification of SST cold spray nozzle 151
Table 19: Cold spray deposition parameters 151
Table 20: Heat treatment types and process parameters of the experiment 153
Table 21: Chemical composition of the CuCrZr alloy powder 183
Table 22: Specification of SST cold spray nozzle 184
Table 23: Cold spray deposition parameters [Chapter 6, Chapter 7] 184

Chapter 1
Introduction

1.1 Motivation

Solid-state additive manufacturing (AM) has emerged as a transformative approach for fabricating and repairing high-value components across a wide range of industrial sectors [1,2]. Fusion-based AM methods, including selective laser melting (SLM), directed energy deposition (DED), and electron beam melting (EBM), have proven effective for complex geometries, but their reliance on material-specific thermal and optical properties limits their applicability to metals such as copper, aluminum, and magnesium, which exhibit high thermal conductivity and low absorptivity [3–5]. This technological gap highlights the need for AM processes that operate below melting. Operating below the melting point of materials, solid-state AM eliminates many challenges associated with fusion-based techniques, such as residual stress, thermal distortion, and compositional changes. These advantages make it particularly suitable for applications requiring dimensional precision and material integrity at both small and large scales, ranging from localized micro-repairs to the additive refurbishment of large aerospace structures. Cold spray addresses this limitation by enabling the additive manufacturing and repair of a broad class of materials at various length scales [6]. Its scalability, material flexibility, and ability to retain feedstock properties position cold spray as a critical enabler in expanding the capabilities and industrial relevance of additive manufacturing.

Cold Spray (CS) is a solid-state powder deposition technique that relies on high-velocity particle impact to achieve bonding, enabling layer-by-layer buildup on a substrate. In this process, a gas, such as air, nitrogen, or helium, is typically preheated to a temperature ranging from room temperature to elevated levels depending on the system configuration. This gas is then accelerated through a converging-diverging De Laval nozzle [7–10]. Powder feedstock, introduced separately into or upstream of the nozzle, is entrained in the gas flow and propelled to supersonic speeds before impacting the substrate. While the impact velocity is influenced by spray parameters and gas type, the particle temperature remains significantly below the melting point, determined by factors like nozzle geometry, gas temperature, and particle heat capacity. Unlike conventional thermal spray methods, CS avoids melting, grain growth, phase transformations, and oxidation, making it particularly advantageous for

preserving material integrity [11,12]. Owing to these benefits, CS has gained significant industrial interest in recent years for its use in repairing high-performance components [6], applying functional and protective coatings [13,14], and enabling 3D printing [15].

Although research on CS processing has gained momentum in recent years [16–18], a well-established correlation between feedstock powder characteristics and the resulting deposition properties remains sparse. In CS, the quality of the feedstock powder plays a crucial role in determining the final performance of the deposited coatings. Key powder attributes, such as particle size and grain structure, morphology, flowability, density, and plastic deformability, significantly influence deposition behavior and coating quality. However, there is still a lack of in-depth studies linking specific powder characteristics, based on their production methods, to the mechanical or microstructural properties of CS-fabricated materials. Furthermore, most commercially available powders are not specifically designed or optimized for CS, making it difficult to achieve targeted properties. Compared to other CS process variables, limited experimental data is available to guide researchers and manufacturers in selecting suitable powders or defining optimal combinations of powder properties for enhanced performance.

A major limitation of CS deposition is the inherently low ductility of the as-deposited materials. To overcome this, early efforts have focused on optimizing processing parameters and applying post-deposition heat treatments [19–21]. More recently, the design of engineered microstructures has emerged as a promising approach to achieve enhanced strength–ductility synergy in metals and alloys produced by various processing techniques. Among these, heterogeneous architectures, such as bimodal, laminated, lamellar, and harmonic structures, are characterized by the coexistence of hard and soft domains with pronounced strength contrast; the hard regions contribute to mechanical strength, while the soft regions facilitate ductility [22,23]. Despite the proven benefits of such architectures in other processing methods, the potential of cold spray 3D printing to intentionally design heterogeneous microstructures remains largely untapped and requires exploration.

This research aims to achieve two main goals. The first is to establish a correlation between the characteristics of feedstock powders and the final properties of CS deposits. To this end, different types of copper powders, as one of the most favorable elements in CS, produced via gas atomization, electrolysis, and mechanical grinding, will be evaluated using advanced characterization techniques.

By analyzing the microstructure and mechanical properties of samples deposited under optimized conditions (based on statistical modeling) in low-pressure CS system, a direct relationship between powder properties and CS performance will be identified. The second objective focuses on improving the ductility of CS 3D-printed components. This will begin with examining the influence of process gases (helium vs. nitrogen) on microstructural development and mechanical performance. The study will then identify optimal post-deposition heat treatment conditions based on tensile results for pure Cu and CuCrZr alloy. Finally, a novel approach will be pursued by fabricating a laminated heterogeneous structure with alternating layers of coarse-grained Cu (soft domain) and fine-grained CuCrZr (hard domain), combining sequential cold spray deposition and post-deposition heat treatment to enhance both strength and ductility.

1.2 Research objectives

To accomplish the research goals, this study will pursue the following four objectives as visually summarized in the graphical abstract presented in Figure 1.

O1. comprehensive characterization of various Cu powders and evaluation of their CS deposition behavior;

O2. fabrication of 3D-printed pure Cu using different process gases (nitrogen and helium), followed by post-deposition heat treatments to assess microstructural and mechanical evolution;

O3. 3D printing of CuCrZr alloy followed by standard heat treatments specific to this material to evaluate its precipitation behavior, microstructural evolution, and mechanical properties; and

O4. development of a laminated heterogeneous Cu/CuCrZr structure using CS 3D printing, aimed at strength–ductility improvement through architectural design.

O1- Characterization of various feedstock powders and evaluation of their CS deposition behavior

In this study, the cold-sprayability of five distinct Cu feedstock powders, produced via gas atomization, electrolysis, and grinding techniques, is systematically investigated and compared. Key powder characteristics, including microstructure (equiaxed grains or dendritic cells and grain size),

morphology, porosity, particle size distribution, flowability, surface oxygen content, and hardness, are identified as critical factors influencing the quality and performance of CS-deposited materials. These properties are analyzed using a range of techniques such as optical microscopy (OM), scanning electron microscopy (SEM), electron backscatter diffraction (EBSD), particle size and shape analysis (CAMSIZER X2), powder flowability testing (FT4), X-ray photoelectron spectroscopy (XPS), and nanoindentation hardness testing. Optimal coating conditions are then determined using a statistical model based on CS processing parameters. Following this, an extensive evaluation is conducted, including physical assessments (coating thickness and weight gain), microstructural analysis (porosity, dynamic recrystallization, and grain size), and mechanical characterization (bonding strength measurement and microhardness) of the coatings, interfaces, and substrates. These findings highlights the critical role of feedstock powder characteristics in shaping the final properties and microstructure of Cu coatings, ultimately establishing a clear correlation between powder attributes and the performance of CS-deposited materials.

O2- 3D printing of pure Cu using different process gases followed by post-deposition heat treatments

Building on previous findings, the feedstock powder exhibiting the best flowability and deformability will be chosen for cold spray 3D printing. This study will examine the influence of nitrogen and the more expensive helium as process gases on particle velocity, deposition efficiency, and dislocation density (by XRD analysis) in the as-sprayed materials. Post-deposition heat treatment, recognized as a key method for improving interfacial bonding and reducing defects, will be applied to enhance the structural integrity of the printed parts. Comprehensive evaluations, including microstructural characterization (OM, SEM, EBSD), mechanical testing (microhardness and tensile testing), and fracture surface analysis, will be conducted to identify the optimal gas and heat treatment combination for maximizing strength and ductility in parts fabricated by low-pressure CS.

O3- 3D printing of CuCrZr alloy followed by standard post-deposition heat treatments

CuCrZr, a precipitation-hardened alloy known for its strength improvement through the formation of strengthening precipitates, will be fabricated by CS additive manufacturing. In this study, three primary heat treatment strategies, Solution Annealing (SA), Age Hardening (AH), and Direct Age Hardening (DAH), will be applied as post-deposition treatments to optimize the alloy's properties. A

comprehensive evaluation of the microstructure, texture, precipitation behavior, and mechanical performance of the CS-deposited CuCrZr, both before and after heat treatment, will be carried out using OM, SEM-EDX, EBSD, XRD, microhardness testing, tensile testing, and fracture surface analysis. The goal is to identify the most effective post-processing approach that maximizes tensile strength and ductility in low-pressure cold sprayed CuCrZr components.

O4- Development of a laminated heterogeneous Cu/CuCrZr structure using CS 3D printing

A novel heterogeneous material will be fabricated using a low-pressure CS system through a sequential 3D printing approach. This involves alternating deposition of CuCrZr and Cu layers to form laminated structures with varying layer counts. The printed samples will then undergo a heat treatment process previously optimized for CuCrZr alloy to enhance mechanical performance. The resulting microstructure will consist of alternating coarse- and fine-grained layers, exhibiting clear contrasts in composition and hardness, thus creating soft and hard domains essential for heterostructured materials. Comprehensive microstructural analysis and quasi-static tensile testing will be conducted to assess improvements in strength and ductility. Additionally, loading–unloading–reloading (LUR) experiments will be performed to evaluate interface behavior and confirm the role of hetero-deformation-induced (HDI) strengthening mechanism.

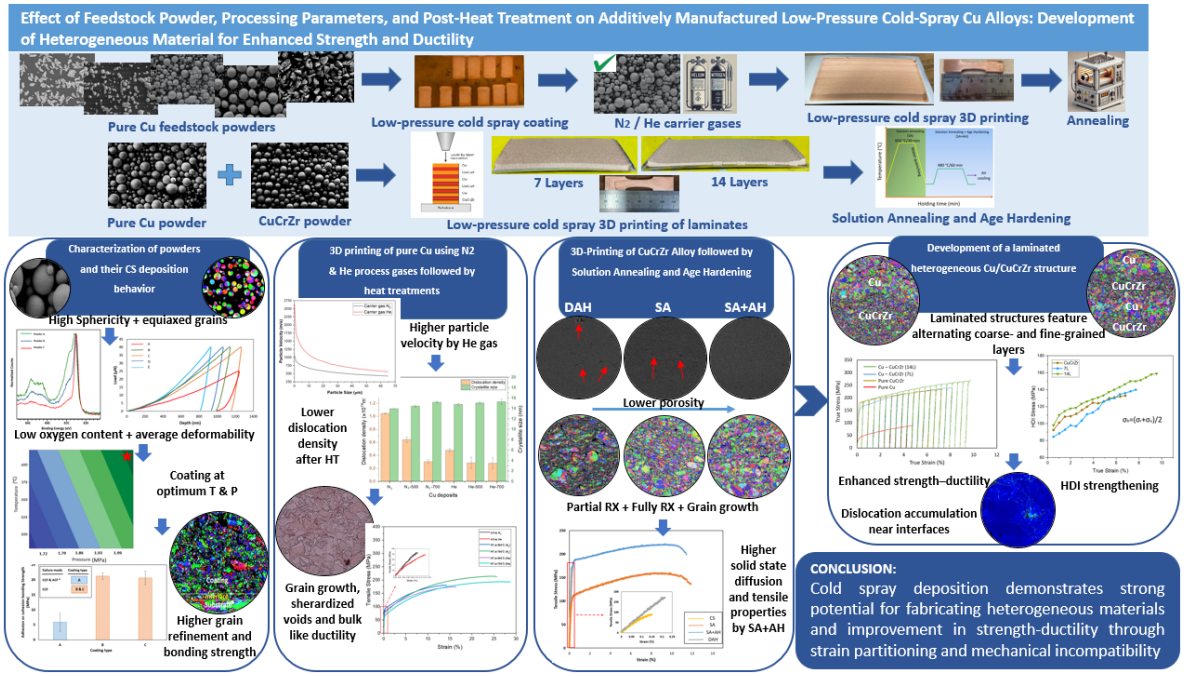


Figure 1: Thesis graphical abstract

1.3 Thesis overview

This thesis is structured in a manuscript-based format and comprises 9 chapters. Chapter 1 presents the research motivation, problem statement, and objectives. Chapter 2 reviews key topics and literature relevant to the study. Chapter 3 details the materials, experimental procedures, and methodologies applied. Chapters 4 through 8 consist of individual manuscripts that have been published, or are being prepared for submission. A minor revision was made to Chapter 4 by including additional feedstock powder analysis for a fifth Cu powder, produced by grinding, which was acquired post-publication for comparison with the other four powders. Minor formatting adjustments, including consistent references and standardized table and figure numbering, were made across the manuscripts to ensure cohesion within the thesis.

Chapter 4 examines how different powder manufacturing techniques influence the cold sprayability of pure copper powders. The study concludes that gas-atomized powders with spherical morphology and equiaxed grain structures offer the most favorable combination of flowability and deformability, making them strong candidates for optimized CS feedstock. Building on these findings, Chapter 5

presents a comparative investigation into how each powder type affects the microstructural development and mechanical performance of coatings deposited using a low-pressure cold spray system. Optimal spray conditions, specifically gas temperature and pressure, were determined through a statistical modeling approach, and the corresponding particle velocities were calculated. The resulting coatings were assessed based on porosity, particle flattening ratio, grain size distribution, microhardness, and bonding strength. Furthermore, the study evaluated grain size evolution and hardness gradients near the substrate surface and interface, highlighting the influence of dynamic recrystallization. A key outcome of this research is the demonstrated ability of satellite-free gas-atomized powders, due to their lower surface area and oxide content, to undergo substantial plastic deformation and grain refinement, leading to high-quality coating formation.

Following the results from the last chapter, the most suitable feedstock powder for 3D printing was identified. Chapter 6 delves into the CS 3D printing of pure copper, examining how different process gases (nitrogen and helium) and post-spray heat treatments affect its microstructure and mechanical properties. Analysis of dislocation density in the as-sprayed state, along with observations of recrystallization and grain growth during annealing, indicated that nitrogen, when paired with an optimized heat treatment, can be a cost-efficient substitute for helium, achieving mechanical strength and ductility comparable to bulk copper. Chapter 7 shifts focus to the CS 3D printing of CuCrZr, a precipitation-hardened alloy with enhanced mechanical performance. As one of the few studies on this topic, it evaluates the effects of conventional heat treatment routes, solution annealing (SA), solution annealing followed by age hardening (SA+AH), and direct age hardening (DAH). The results show that the SA+AH process most effectively promotes recrystallization, improves solid-state diffusion, enhances densification, and facilitates the formation of ultrafine precipitates leading to superior tensile strength and ductility. Building on the outcomes of the heat treatment studies, Chapter 8 investigates the capabilities of cold spray additive manufacturing (CSAM) combined with post-processing heat treatments for producing heterogeneous laminated structures, aiming to assess how the interface between Cu and CuCrZr layers can contribute to simultaneous enhancement of strength and ductility. Furthermore, the chapter analyzes strain-hardening behavior and results from LUR experiments to investigate hetero-deformation-induced (HDI) strengthening, driven by the presence of geometrically necessary dislocations (GNDs). Finally, chapter 9 presents the concluding remarks and outlines directions for future research.

Chapter 2
Literature review

2.1 Background on cold spray technology

Cold Spray (CS) is a material consolidation process. A spray gun fitted with a De Laval rocket nozzle accelerates micron-sized particles of a metal, ceramic, and/or polymer to form a near-net shaped part or a coating, by means of ballistic impingement [10,24–26]. A heated high-pressure gas (i.e., helium or nitrogen) carries the feedstock powder particles such that they exit at supersonic velocities and consolidate when impacts an appropriate surface [10,27] as shown in Figure 2. Depending on the CS system, feedstock particles can be suspended within a pressurized powder feeder either in the same line as the main gas stream or in a separate line. In addition, the feedstock particles, may be injected into the nozzle down-or up-stream.

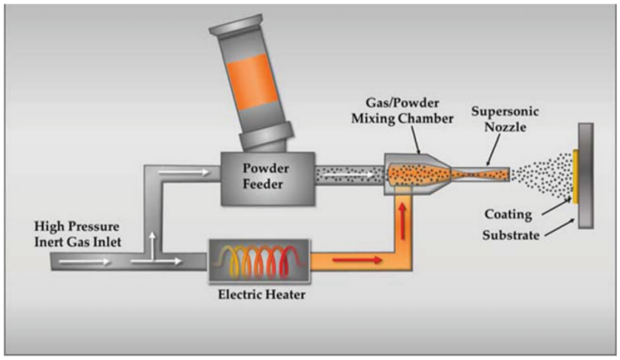


Figure 2: Schematic illustration of the cold spray process [10]

2.1.1 Principle and setup

Several different CS systems are commercially available. Different parameters such as the type of nozzle and the powder injection method define the system [10,28]. These systems can be categorized as upstream system (or high-pressure CS system) and downstream system (or low-pressure cold spray system). Both systems can be classified as sonic and supersonic. A supersonic system expands the gas to supersonic conditions and has a converging–diverging or de Laval nozzle. A sonic nozzle with a converging section followed by a section maintains the flow at sonic conditions. Expanding the gas to

higher velocities by controlling the cross-sectional area of the nozzle is the main principle of both versions of the CS systems. In an upstream powder injection system, the powder is going into the nozzle before the throat of the nozzle. Gas pressure is higher than the atmospheric pressure at the particle injection point. Therefore, a high-pressure and robust powder feeding system is essential to deliver a positive flow into the nozzle. The nozzle configuration may contain a pre-chamber that is used to heat the particles they enter to the nozzle. In a system based on downstream powder injection, the powder is entered after the nozzle throat. The gas pressure is lower than the atmospheric pressure at the injection point; thus less complicated feeding system is used as the process gas flow is derived by the atmospheric pressure [10].

2.1.2 Deposition mechanism

There are two different types of bonding in cold spray deposition that should be studied [9]. Particle-to-substrate bonding and particle-to-particle bonding. The first one is necessary for the creation of the first layer of particles, therefore related to the adhesion strength of the coating to the substrate, and later concerns the build-up of the cold-sprayed deposit. In general, bonding happens when atomically-flat and clean surfaces of two components are in contact. Principally, this can take place without fusion, heating or mechanical interlocking. Practically, metallic components rarely have flat surfaces and generally are covered by an oxide layer. In order to build a solid-state bonding and reach the tight contact of clean metallic surfaces, the surface oxide layers should be broken up or removed. The way to attain this goal is to stretch and compress the interfacial region through plastic deformation, as displayed in a schematic in Figure 3A. Bonding in CS is considered to be based on this kind of interfacial deformation, which causes the oxide layers' breakup and atomic contact of metallic surfaces. Therefore, the oxide layer should be considered as a geometrical restriction and it is not an energy barrier to metallurgical bonding [9,29]. In CS, the bonding mechanism could be compared to bonding in magnetic pulse welding and explosive welding [9]. In these procedures, bonding happens as a consequence of two solid objects impact at high-velocity. In both processes, the formation and ejection of a material jet, under the effect of adiabatic shear instability (ASI), at the interface of the interacting bodies is a common feature as shown in Figure 3B.

Recent investigation using in situ micro particle impact experiments combined with site-specific micromechanical testing have revealed a pronounced gradient in bond strength across the impact-

induced interface [30]. Specifically, bond strength was observed to be weakest near the impact center, followed by a sharp increase, approximately twofold, reaching values that exceed the bulk material's yield strength, and eventually stabilizing into a plateau region extending toward the periphery of the interface. The interfacial strength gradient, with a magnitude of ~50 MPa/μm, was linked to early-stage localized surface openings occurring between the impact center and periphery. High-resolution transmission electron microscopy studies have further shown that the morphology of the native oxide at the interface, whether as continuous layers, discrete particles, or fragmented debris, strongly influences the bond strength. Strong bonding was attributed to two primary factors: extensive surface exposure that enables the fragmentation of native oxide films into nanoscale debris, thereby exposing clean metal surfaces; and the generation of high local contact pressures in the range of several gigapascals, facilitating atomic-scale contact between particle and substrate. Based on these insights, a predictive framework for impact-induced bond strength has been developed, offering guidance for the optimization of material systems and processes involving supersonic particle deposition.

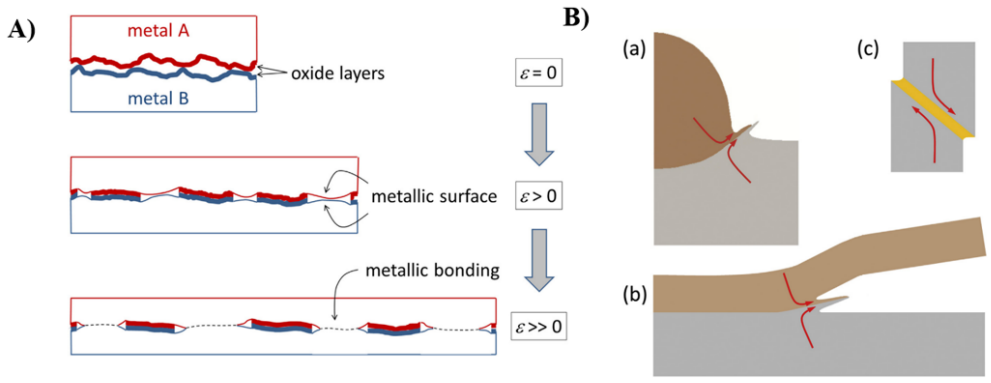


Figure 3: Schematic drawings of (A) plastic deformation in interface leading to cold welding and (B) deformation localization because of shear instability as a result of particle impact in cold spraying [9].

There is extensive literature and ongoing debate surrounding the bonding mechanisms in cold spray processes. While numerous studies have explored factors such as particle velocity, temperature, and surface conditions, the exact nature of metallurgical bonding, particularly the role of oxide fracture, adiabatic shear, and localized plastic deformation, remains an active area of research and discussion.

2.1.3 Cold spray parameters

Cold spray parameters may be divided into three groups of process parameters, substrate properties and powder properties. There are several process parameters such as gas conditions, nozzle design and spraying kinematics that play crucial roles in CS [31]. Several CS research in recent years aimed to study the effect of the process parameters on the final properties of the deposits and deposition efficiency. In addition, deposition properties mainly depend on the particle impact conditions such as particle impact temperature, T_p, particle impact velocity, v_p and surface temperature of the substrate T_{sub}. In this regard, the goal of most studies has been to investigate the relationship between the cold spray process parameters and v_p, T_p and T_{sub}. Table 1 presents a qualitative summary of the influence of several process parameters on the impact parameters. In addition, mechanical properties of the substrate influence the adhesion strength [9,32]. In CS, the impact power, which is the kinetic energy dissipation rate during a single particle impact, is usually around 50 W. For harder substrates, the value of impact power increases and the heat generation is constrained to smaller volumes that causes more noticeable rise of temperature and assisted ASI on the particle. Similarly, a softer substrate is impacted more deeply by the particles, easing ASI on the substrate, while the impact power may be lower. Combination of energy dissipation distribution in particle and substrate and impact power influences the adhesion strength. Thus, substrate hardness is a significant factor for the adhesion strength. In addition, the flattening ratio of the particles as an intrinsic property of the coating depends on substrate hardness. Deformation of first layer of deposited particles can be constrained by a hard substrate. Therefore, influences the first layer and subsequent layers' cohesion. Moreover, the surface temperature is another substrate property that has effect on the particle bonding. Surface temperature is influenced by many factors such as the spraying condition and the thermal properties and substrates dimensions. Finally, substrate roughness can cause higher deposition efficiency and play a crucial role. Powder properties as an important CS parameter is the focus of this research, which will be reviewed thoroughly later.

Table 1: The effect of cold spray process parameters on the deposition conditions [9]

Factor	Parameter	Effect on V_p	Effect on T_p	Effect on T_{sub}
Gas	Type	V_p (He) > V_p (N_2)	T_p (He) < T_p (N_2)	
	T_{gas}	$T_{gas}\uparrow \rightarrow V_p\uparrow$	$T_{gas}\uparrow \rightarrow T_p\uparrow$	$T_{gas}\uparrow \rightarrow T_{sub}\uparrow$
	P_{gas}	$P_{gas}\uparrow \rightarrow V_p\uparrow$	$P_{gas}\uparrow \rightarrow T_p\uparrow\downarrow$	

Nozzle	Length, l	l↑→ V_p ↑	l↑ → T_p↓	l↑ → T_{sub}↓
	Exp. Ratio, r	r↑ → V_p↑	r ↑ → T_p ↓	r ↑ → T_{sub} ↓
	Diameter, d	d↑ → V_p ↑		
Pre-chamber Procedure	Length, l_{pre}		l_{pre}↑→ T_p ↑	
	Standoff distance, s	s↑→ V_p ↑↓	s↑ → T_p↓	s↑→ T_{sub} ↓
	Spraying angle, ω	ω↑ → V_p↓		
	Traverse speed, V_{gun}			V_{gun}↑ → T_{sub}↓
	Powder feed rate, f	f↑ → V_p↓	f↑ → T_p ↑	f↑ → T_{sub} ↑

2.1.4 Materials and applications

Repair, coating and 3D printing additive manufacturing (AM) are the fields that can use cold spraying process [7,33,34]. All metal-ceramic composites and metallic materials could be deposited to thicknesses above 50 mm. These applications can be classified based on the high purity of deposits, superior properties obtained through well bonding and low input of heat to the substrate. Well bonded and high purity coats lead in high thermal and electrical conductivity. In addition, they result in high oxidation and corrosion resistance along with high mechanical strength. Applications in chemical, biomedical and electronics industries needs CS deposits with high chemical purity and homogeneity. In addition, CS is appropriate for applications where the substrate cannot tolerate the thermal shock. In this regard, metals coatings on ceramic or glass are functional. CS coating also can be considered as a way to enhance the fatigue strength of substrate [35,36].

2.1.5 Feedstock powder

The selection and engineering of powder feedstocks are critical for the performance and industrial scalability of CS additive manufacturing. Traditionally, powders optimized for other processes such as conventional powder metallurgy and thermal spraying were repurposed for CS. However, the increasing availability of high-purity, spherical powders produced via gas or plasma atomization, initially developed for laser and electron beam powder bed fusion, has created new opportunities for improving CS performance. Key powder characteristics influencing cold sprayability include particle size distribution, morphology, and chemical composition. Beyond these, the microstructure and surface state of powders are increasingly recognized as decisive factors in ensuring high deposition efficiency,

strong bonding, and consistent mechanical properties. Powder flowability, influenced by surface roughness, size, and storage conditions, directly affects feed stability and process reliability [37–39]. Likewise, deposition ability is governed by the particle's capacity to reach and exceed its critical velocity, which is modulated by microstructure, surface oxides, and density [40,41].

Recent studies have highlighted the potential of powder engineering strategies such as alloy blending [42], ceramic additives [43,44], surface cladding [45], and tailored porosity [46] to enhance deposition. Heat treatments, including homogenization and solutionizing [47,48], have been effective in softening powders and improving interparticle bonding. These developments underscore the need for CS-specific powder design to optimize sprayability, deposit properties, and manufacturing repeatability.

2.2 Metallic powder manufacturing methods

Mechanical or chemical methods are used for metal powders production [49–51]. Water and gas atomization, mechanical alloying, milling, electrolysis and chemical methods such as oxide reductions are commonly used methods. Selection of appropriate methods for production of powders depend on required powder properties, production rates and physical and chemical properties of materials. For producing high purity powders, chemical and electrolytic methods are suitable. Mechanical and milling methods are the most commonly used ones for production of hard metals powders and oxides. Atomization methods are the most adaptable ones that can produce metal powders in a large production rate and wide range of particle sizes. Gas atomization and electrolysis are the widely and economical used methods.

2.2.1 Gas atomization

Gas atomization (GA) is the process in that a high velocity jet of argon, nitrogen, helium or air disperses the liquid metal. This is used for commercial production of different elements and alloys such as copper and copper alloys, aluminum and its alloys, titanium and titanium alloys, etc. [51]. The basic nozzle design of gas atomization process is shown in Figure 4a. An annular orifice delivers the atomizing gas around the nozzle at the converging angle. The suction (aspiration) effect created by the gas flow at the nozzle tip draws the molten metal into the nozzle. The size of the air gap and pressure and temperature of the gas controls the amount of gas delivered by the nozzle. The resultant powder particle size and

rate of metal flow are under the effect of the nozzle metal orifice diameter, aspiration force and the vertical distance between the molten metal level and the nozzle.

Many gas atomizer designs are classified as free fall or closed (confined) nozzles [51]. The closed nozzles designs are also called as close-coupled nozzle designs. In the free gas atomizer, the liquid metal falls in the form of a stream from a tundish. Then it is atomized by means of an annular or discrete directed at the point of metal stream meeting. This is an easy method to operate however not very efficient and not appropriate for production of fine powders. On the other hand, the confined nozzle design by maximizing the density at the meeting with the metal stream and the gas velocity makes it easier to obtain the particle size powders in the range of 40-60 μm. However, freezing of the molten metal at the end of the tundish nozzle is the disadvantage of these units, which quickly leads to atomizing stop. Moreover, the interaction of nozzle tip with the gas stream can form a pressure, which may significantly increase the melt flow rate, stop it, and blow the gas into tundish. Therefore, setting up the closed nozzles and its control during atomization need a great care. The atomization pressure in conventional gas atomization processes are typically in the range of 0.5 to 4 MPa and also the gas velocities range from Mach 1 to 3 in the nozzles [51,52]. However, gas velocities in free fall atomizers in the impingement zone usually falls to 50-150 m/s (for air or nitrogen). Gas atomized powders typically have log normal size distribution and are spherical. The average particle sizes are generally in the range of 10 to 300 μm and the oxygen content is in the range of 100 to 1000 ppm. Typical gas flow rate range in conventional atomizers are from 1 to 50 m^3/min when the pressure range is from 350 KPa to 4 MPa. The differential between the melting point temperature and the temperature that the atomization of molten metal happens- which is called the superheat of molten metal- is usually between 75-150 °C. The cost of gas consumption in gas atomization is significant and a way to circulate and promote the gas reuse especially in large-scale services are important.

2.2.2 Plasma atomization

Plasma atomization technology is using for the process of metal powders making. This technology has been developed widely which have caused a high purity titanium in various range of grain sizes in powder microstructure. Plasma atomization is able to produce titanium powders with very fine (-25 μm) to coarse (+125 μm) particle size distribution [53]. Metal powders with round-shaped morphology have a good flowability and they are able to produce high density product. Figure 4b shows a schematic

of plasma atomization process, which uses three plasma arcs and a titanium wire as a material feed. This plasma arc works as heat source with high enthalpy, which will melt and sprays the molten titanium wire resulting in a high purity titanium powder with very spherical shape morphology.

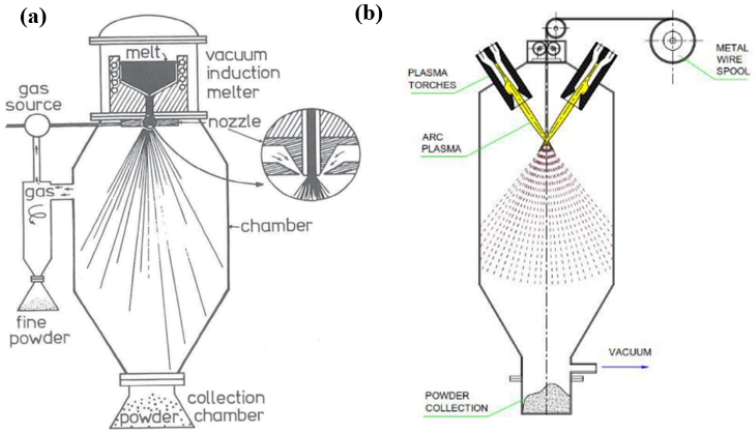


Figure 4: Schematic illustration of (a) gas atomization process and (b) plasma atomization process [51,53]

2.2.3 Electrolysis

Electrolysis is the process of decomposing ionic compounds into their elements [54] as shown in Figure 5. The cations are reduced at cathode and oxidation of anions occurs at the anode. The main components of this process are an electrolyte, electrodes and external power source. Electrolysis is usually done in a vessel under the name of electrolytic cell containing cathode and anode. In this process, cations take electrons from cathode and is discharged into neutral atom. On the other hand, anions give up their extra electrons and is oxidized to neutral atoms at the anode. The minimum potential needed for the electrolysis process depends on their ability of the individual ions to absorb or release electrons, which is the minimum voltage (difference in electrode potential) between anode and cathode of an electrolytic cell that enables electrolysis to occur. Powder properties could be defined through the appropriate process parameters such as current density, cathode potential, size and type of cathode and anode and their distance from each other. A variety of metal powders such as copper, zinc, nickel could be manufactured by electrodeposition of metals. Deposition of metal is controlled through material transfer toward the phase boundary. The maximum rate of this reaction could be defined by limit current density (i_{lim} , A/m^2) [51]:

$$i_{\lim} = \frac{zFDC_0}{(1-t_k)\delta} \quad (1)$$

z is the number of electrons in the process of cathode; F is the Faraday constant (96 500 Kl/mol or 26.8 A.h/mol); D is defined as the diffusion coefficient, m^2 /s (≈ 10^{-9}); C_0 is the concentration of discharging metal ions in the solution, mol/m^3; t_k is the number of cations transfer (0.4–0.6); δ is the thickness of the diffusion layer, m (≈ 10^{-4}) [51]. The crystallized deposit due to the shaking could falls off or it could be brushed off from the cathode. This stage depends on the metal precipitated. To avoid the passivation, usually the anode current density across the soluble anodes is not higher than the cathode one. Removing and dehydration stages follow the powder deposition. The powder is washed and stabilized to avoid from oxidation, then milled and screened, and finally it will be blended, mixed and packed. Another technology for powder treatment includes washing the powders, dry it, sinter it in a reducing atmosphere, mill it and finally screening. In this way, powder has higher apparent density and flowability, however, it has a lower corrosion resistance due to the destruction of stabilizing layers in the sintering stage [55].

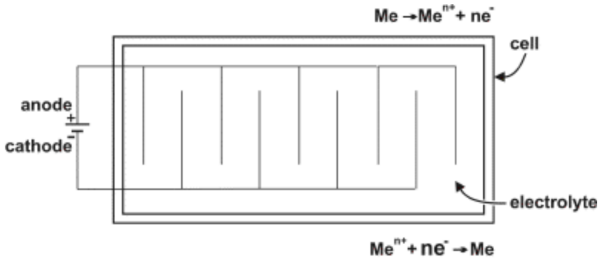


Figure 5: An electrolytic cell for the deposition of metal powder.

2.2.4 Grinding

Grinding-based powder production is an emerging technique for generating metallic powders, particularly from difficult-to-process or non-spherical materials [7,56]. Unlike conventional atomization methods, such as gas or water atomization, grinding offers a mechanical route for producing powders, often from bulk materials or machining by-products. In this approach, metallic swarf generated during controlled surface grinding is collected, processed, and repurposed as feedstock

for additive manufacturing and other applications. Studies have shown that parameters such as grinding wheel composition, velocity, depth of cut, and work piece clamping influence the thermal and mechanical conditions under which particles are formed [57]. For instance, the use of alumina grinding wheels under specific velocities can promote high localized temperatures at the chip formation zone, enhancing material fragmentation and enabling the formation of fine particulates suitable for powder applications. Proper work holding, such as using physical clamps instead of magnetic chucks, is critical to avoid residual magnetism in ferrous powders, which could adversely affect their flowability and feed behavior. Post-processing steps, including sieving, drying, and moisture removal, play a pivotal role in ensuring the quality and flowability of ground powders. The presence of ambient moisture has been found to promote agglomeration, reducing the effectiveness of powder delivery systems. Comparative studies with gas-atomized powders suggest that, under optimized conditions, ground powders can perform competitively, particularly when enhanced by post-treatment or integrated with laser-based deposition systems. Overall, grinding-based powder production represents a promising low-cost and sustainable alternative for generating metallic feedstock, especially in contexts where recycling, custom alloy formation, or small-batch processing are of interest.

2.2.5 Hydrometallurgy

Hydrometallurgical processing has emerged as a versatile and environmentally favorable route for producing high-purity metallic powders, particularly for non-ferrous and refractory metals [58–60]. This approach involves aqueous chemistry-based extraction, purification, and subsequent metal recovery, typically via chemical or electrochemical reduction. Key advantages of hydrometallurgical methods include precise compositional control, scalability, lower energy consumption compared to pyrometallurgy, and the ability to process low-grade ores or industrial wastes. Hydrogen reduction of metal salts or oxides is a widely adopted step in this route, especially for the production of nickel, copper, cobalt, and other transition metal powders. Factors such as solution concentration, pH, temperature, and reducing gas flow play significant roles in dictating particle size, morphology, and purity of the final powders. Studies have shown that hydrogen-reduced powders often exhibit high surface area and controlled particle characteristics, making them suitable for applications in batteries, catalysts, and additive manufacturing. The hydrometallurgical route has also enabled the synthesis of complex alloy powders and offers potential for recovering valuable metals from electronic waste and

mining residues. However, process optimization and waste management remain critical for industrial-scale deployment. Overall, the hydrometallurgical pathway represents a promising and sustainable strategy for the tailored production of metallic powders across a wide range of materials.

2.3 Characteristics of feedstock powders

There are various powders characteristics, which have direct effect on their feeding behavior and cold spraying. The feedstock powder characteristics significantly influence the cold sprayed coatings quality. The basic requirement of the powder feeder in cold spray system is the transportation of the powder to the downstream and upstream of the convergent-divergent nozzle that the powder particles accelerated towards the substrates. Powder feeding problem in industry which is known as powder flowability, is the first aspect to be considered for choosing the feedstock material for cold spray [27]. Feedstock powder characteristics can be usually divided into two classifications: chemical and physical characteristics. Particle size and grain size of microstructure, external morphology of the powder (spherical, globular, angular or presence of satellites) along the internal morphology (porosity), flowability and apparent density which are under the effect of other properties, thermal and electrical conductivity or resistance are the physical properties of powder particles. The typical chemical properties of the powder particles could be divided as chemical composition (levels of oxygen and nitrogen, purity), precipitation distribution and crystallographic information (solid solutions). Powders with good flowability and satellite free are the most desired ones for cold spray process. In fact, satellite particles are fine particles causes the agglomeration the feeding problems due to the sticking to larger particles [61]. This section reviews the powder characteristics and measurement techniques.

2.3.1 Particle size distribution

The particle size distribution of powder particles as shown in Figure 6 is illustrated by three values of D_{10}, D_{50} and D_{90}. D_{10} shows that 10% of particles are smaller than the mentioned size. It can also be shown by a statistical symbol as DV (0.1). D_{90} means that 90% of powder particles are smaller size of this value and finally for D_{50}, one can say that 50% of powder particles are smaller/larger than this size. Obviously, D_{50} could be called as median particle size distribution [61]. These three values usually calculate the degree of consistency of particles in size. A laser particle size analyzer uses laser in various angles and the diffraction pattern could be retrieve from the image sensors.

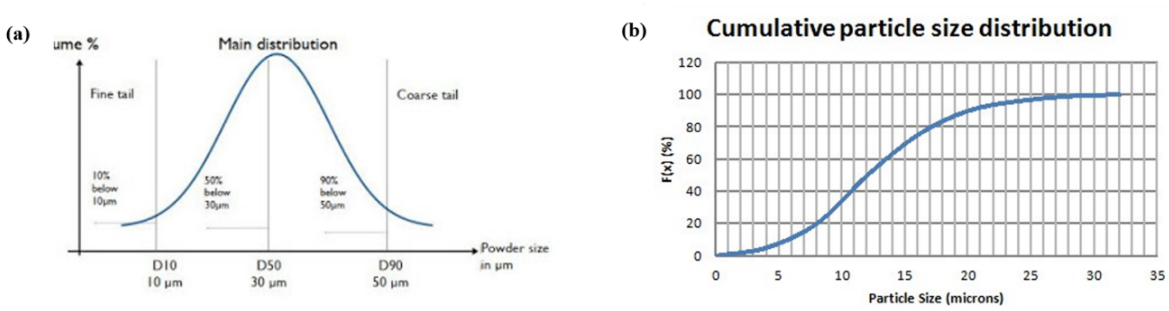


Figure 6: (a) volume fraction (%), volume-based particle size distribution showing D10 = 10 µm, D50 = 30 µm, and D90 = 50 µm, indicating the fine, median, and coarse fractions and (b) accumulative volume fraction (%) graphs showing the percentage of particles below a given size, reaching ~100% below 32 µm [61].

By preforming cross analysis, addition or subtraction, the statistical proportion of the particle size will be determined. By comparing the literature on different metal powders especially gas-atomized ones and based on a relationship expanded by Wigg, an empirical equation has been derived for the average particle size (δ) measurement [51]. This relation is:

$$\frac{\delta_m}{d_0} = K\left[\frac{v_m}{v_g}\frac{1}{We}\left(1+\frac{M}{A}\right)\right]^{1/2} \tag{2}$$

where W_e is defined as the Weber number, δ_m is defined as the mass median particle diameter, d_0 is called the diameter of the metal stream, V_m is defined as the kinematic viscosity of liquid metal, V_g is defined as the kinematic viscosity of the atomizing medium, the mass flow rate to gas is M/A and K is a constant. For electrolytic powders, different nucleation and growth mechanisms can define the powder particle sizes. This means that the dendritic deposit is under the effect of the dynamic of the dendrite growth [55]. The character and the degree of the cathode over-voltage affect the particle structure. If the over voltage diffusion concurred, sharply dendrites with different degree of twining are formed. Increasing the transition over-voltage (for copper up to 70%) causes the smooth spheroidal crystallization. Dendrite particles with subsieve size (up to 1-10 µm) are produced in a two-layer cell electrolysis and the chemical reduction from the solution. In addition, large size dendrites (50-100 mm) are crystallized from the metal melts. Particles with 5-200 µm are crystallized from electrolysis of aqueous solutions [51].

2.3.2 Particle Morphology

Shape or morphology of powder particles is a function of the powder manufacturing process. Morphology of powder affects flowability, cold sprayability, apparent density and finally the coating porosity and deposition efficiency (DE). Usually, spherical shape particles feed more easier than irregular shaped ones because the irregular particles pack together closely [62]. Plasma atomized and gas atomized particles have spherical morphology and subsequently better flowability. External morphology of powder particles can be directly investigated through scanning electron microscope, and internal structure and porosity can be determined by metallographic preparation of cross section of powders. In this regard, powders compressed in the resin, grinded and polished for further characterization. Figure 7 presents various morphologies commonly observed in metal powders used for additive manufacturing and coating processes. Spherical particles offer optimal flowability and packing uniformity due to their smooth, round shape. Splat Cap particles exhibit partial flattening or cap-like features, often formed during rapid solidification or collisions in atomization. Open Porosity particles contain large surface openings or internal voids, which can compromise powder density and mechanical performance. Elongated particles deviate from the ideal spherical shape, potentially disrupting powder flow and layer uniformity. Broken particles are the result of mechanical fragmentation and may lead to inconsistencies in deposition. Agglomerated particles are clusters of finer particles loosely bonded, typically reducing flowability and homogeneity. Irregular particles have non-uniform, rough surfaces that affect flow dynamics. Lastly, Satellited particles consist of small particles adhered to larger ones, commonly seen in gas-atomized powders, which can influence both flow and packing behavior. In addition, Table 2 has been created to summarize the particle morphologies along with their key characteristics.

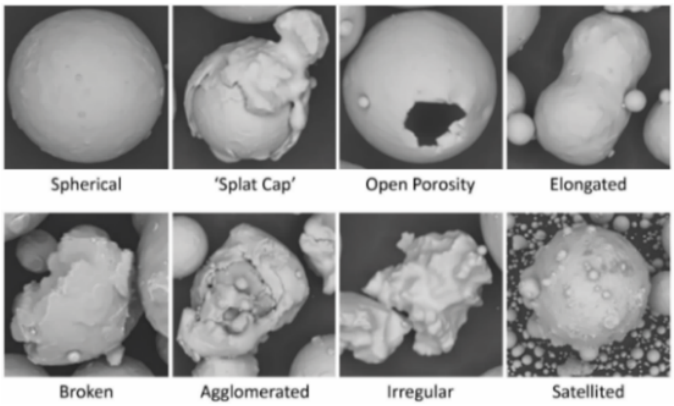


Figure 7: Different types of powder particles morphologies [27,63]

Table 2: Summary of powder particle morphologies

Morphology type	Description	Key characteristics and implications
Spherical	Smooth, round particles typically formed through gas or plasma atomization	Excellent flowability and packing density; preferred for additive manufacturing
Spheroidal	Nearly spherical but slightly irregular or flattened in shape	Good flowability, but slightly less than fully spherical powders
Elongated	Rod-like or oval-shaped particles with significant aspect ratio	Poor flowability and orientation-dependent packing; undesirable for uniform layers
Irregular	Asymmetrical particles with jagged or rough surfaces	Inconsistent flow, increased interlocking, and variable deposition behavior
Agglomerated	Clusters of fine particles bonded by van der Waals forces or partial sintering	Poor flowability and feeding consistency; often leads to nozzle clogging
Broken	Fractured particles from mechanical processing or brittle solidification	Sharp edges, inconsistent sizes; may reduce deposit integrity

Porous	Particles containing internal or surface pores	Lower density, higher surface area
Hollow	Thin-walled particles with empty cores	Very low density; useful in specialized applications (e.g., thermal insulation)
Satellited	Large particles with smaller particles attached to their surface	Common in gas atomized powders; may reduce flowability and increase oxidation risk
Splat Cap	Particles partially flattened during atomization or impact	Indicates irregular solidification; may impair packing and bonding

2.3.3 Flowability

Among the most important methods for determining the properties of powder flow, the shear cell method can be applied under a wide range of stress conditions and parameters that are useful to predict the powder behavior such as unconfined yield strength and flow factor. The principle of this method could be explained based on the shear stresses that are applied from the outside [64]. In fact, a powder in a hopper cannot easily flow due to the adhesion or agglomeration of particles. When a sufficient large shear stress is applied, the powder will start to flow. The shear cell method determines the flow behavior of a powder in the static state when is going to be transited to non-static state. This transition occurs when a powder is sheared by a normal stress. A maximum shear stress just before failure and the dynamic friction force of steady state are measured. The testing procedure consists of conditioning, consolidation, pre-shearing and shearing. First, the powder is filled into a glass cylinder, and then a helical blade moves downwards during conditioning and moves upward. The initial consolidation stress to the powder is applied during consolidation by a vented piston. Then the powder is sheared to achieve a steady state. The normal stress and the shear stress is considered as a pre shear point. After this stage, the normal stress is lowered and the powder sample is sheared more to achieve a yield point. This procedure is repeated 5 different times to attain a yield locus [64]. The plot of shear stress-normal stress known as τ–σ diagram is obtained. A common approach to develop a linearized yield locus is Mohr-Coulomb model. A schematic plot of Mohr circle analysis is shown in Figure 8. A linear regression is fitted by the yield points to achieve an expression for the yield locus. Cohesion (τ_1) is defined as the intercept of yield locus on the shear stress axis, which means the required shear stress to deform the

powder when normal stress is not applied. The slope of the linearized yield locus (tan (φ)), which is called the angle of internal friction, is a measure on how easily the powder particles will slide past on each other [65]. For extraction of other flow indices, a Mohr circle is plotted tangent to the yield locus and passing through the origin. The intercept of this circle with the normal stress axis is called the unconfined yield strength (σ_c). The intercept of second Mohr circle on the normal stress axis is called the major principal stress (σ_1). The flow function coefficient (ff_c) is defined as the ratio of major principal stress and the unconfined yield stress that is used as a quantitative classification for powder flowability indication. Lower ff_c indicates the powder with less flowability and higher ones shows easy and free flowing materials [65]. For high-performance cold spray applications, powders must exhibit favorable flowability characteristics, including low cohesion, a moderate internal friction angle, and a sufficiently high flow function. These traits collectively ensure stable and uninterrupted powder feeding, minimize the risk of nozzle clogging, and support uniform and consistent layer deposition. Powders that do not meet these flowability standards often require additional conditioning steps such as drying, sieving, or surface modification to address issues related to moisture absorption, particle agglomeration, or excessive fine content. Achieving optimal flow behavior is essential for maintaining process reliability and coating quality in cold spray systems.

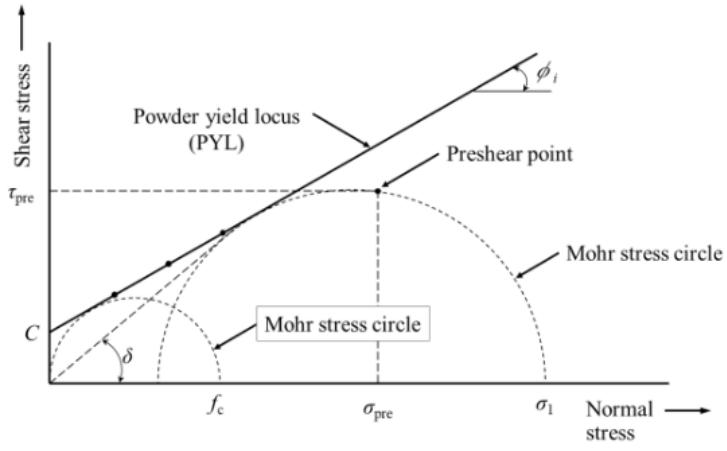


Figure 8: Graphical illustration of different parameters attainable from Powder Yield Locus [65].

In addition, the Hall-Carney method is another technique widely used for flowability measurement due to its simplicity and cost-effectiveness. This method measures the time taken for a fixed mass of powder to flow through a standardized funnel (Hall or Carney funnel), offering a comparative index of flow behavior [39,66,67]. For cold spray applications, powders exhibiting rapid and uninterrupted flow through the funnel are generally considered suitable. While exact flow time thresholds vary, powders that do not flow under gravity are typically classified with poor flowability and require further conditioning or rejection. Additionally, angle of repose and bulk/tapped density (Hausner ratio) measurements are used to assess flow indirectly, though they are less predictive for process performance compared to hall- carney and shear testing [61,66,68]. The angle of repose reflects the powder's flowability, where a larger angle signifies higher cohesion and reduced flowability. The Hausner ratio is determined using the results of auto-tapper testing, which measures both freely settled and tapped densities. A higher Hausner ratio typically indicates greater powder cohesion. Overall, for critical CS processes, combining methods like Hall–Carney with shear cells ensures robust powder selection and quality control.

2.3.4 Microstructure of powders

The microstructure of feedstock powders is a critical factor influencing deposition efficiency, bonding mechanisms, and the mechanical properties of coatings produced by cold spray (CS). As a solid-state process, cold spray relies on high-velocity particle impacts that induce severe plastic deformation without melting. Therefore, the deformation behavior of individual powder particles, strongly governed by their internal microstructure, directly affects the bonding quality and coating integrity. Powders produced by gas atomization are commonly used in CS due to their fine, equiaxed grains, high sphericity, and relatively clean surfaces. These features enable better flowability and greater particle deformability upon impact. For instance, Champagne et al. emphasized the importance of using thermally softened powders to improve deposition of high-strength alloys like Al and Ti [69]. Similarly, Assadi et al. demonstrated through numerical simulations that particle deformation and bonding in CS are highly sensitive to the initial yield strength and strain-hardening behavior, both of which are determined by the microstructure [40]. On the other hand, mechanically produced powders (e.g., through grinding or milling) often exhibit work-hardened microstructures with elongated grains, residual stresses, or surface contamination, which can impede plastic deformation during spraying. As

a result, such powders frequently show lower deposition efficiencies and inferior coating properties unless thermally treated prior to spraying [57]. Several studies have explored the role of powder heat treatment in tailoring microstructure for improved CS performance. For example, Champagne et al. [70] reviewed the cold spray of heat-treated aluminum alloy powders and reported that annealing significantly enhanced deposition efficiency and coating uniformity by reducing particle hardness and promoting greater plastic deformation upon impact. Similarly, studies by Villafuerte et al. [27] reviewed that solution heat treatment of Cu and Al alloy powders enhances sprayability by promoting grain refinement and eliminating brittle phases or oxide inclusions.

Recent advancements include engineered powders with core-shell structures [71], controlled porosity [46], or microalloyed compositions [72] that enhance deformability and reduce critical velocities. The concept of powder microstructure engineering, involving controlled processing routes and targeted post-treatment, is becoming increasingly central to the development of CS-specific feedstock. In summary, optimizing the microstructure of feedstock powders, through atomization techniques, alloy selection, and post-processing, has a direct and substantial impact on cold spray performance. Continued research into powder design and microstructural tailoring is essential for expanding the range of materials suitable for cold spray and improving the performance of CS-based coatings and additive structures.

2.4 Powder cold sprayability

Powder cold sprayability consider the powder flowability and powder ability to deposit. As mentioned before, good flowability is an essential requirement for an appropriate powder feeding in the cold spray technology and homogenous-deposited thickness per layer/pass. Less flowability of specific materials is a big disadvantage for full industrialization of the cold spray technology especially as precise additive manufacturing process. On the other hand, the powder ability for deposition is directly depends on its acceleration through gas jet and its deformability and adhesion after impact to the substrate or the previously deposited powder particles. It is generally reported that during deposition, the ratio of impact velocity to the critical velocity, the minimum velocity needed for particle deposition needs to be maximized to obtain a high deposition efficiency and also strong bonding in order to cause an optimal deposition properties [45]. For maximizing the particle velocity for a set of cold spray process parameters and a specific material, different characteristics of powder particles such as shape, size and

surface roughness could be optimized. In addition, microstructure of powder and surface chemistry significantly affect the final cold sprayed product characteristics. In this section, different aspects of cold sprayability enhancement through optimization of feedstock powder properties will be investigated.

2.4.1 The effect of surface oxidation on cold sprayability

Formation of superficial oxide scale on powder surface causes an increase in the critical velocity and subsequently reduction in sprayability and deposition efficiency. One of the studies on this topic reported the effect of different oxygen content levels in copper powder on the critical velocity. It was clearly shown that particle oxidation condition significantly affect the critical velocity in cold spray [29]. The increase of oxygen content from 0.02 to 0.14 wt. %, changed the critical velocity of Cu particle from 310 to 550 m/s. It is also worth noting that the critical velocity range of different materials places in a narrow range by increasing the oxygen content in powder compared with materials with low oxygen content. This fact makes it clear that the differences in the critical velocity due to the materials type when oxidation happens in the metal alloy are less significant. It is more related to the fact that powder particles during the cold spray impact need to break and extrude the oxide surface to make a bond formation with the previously deposited particles. When the oxygen content makes a thick oxide layer, a high impact energy should be assumed to break the oxide surface of material. Therefore, it is important to monitor the oxygen level of metal powder for cold spraying.

2.4.2 The effect of ceramic particles and metal-alloy powder blends on enhancing the sprayability

Addition of ceramic particles have a strong effect on increasing the deposition efficiency of metallic powders, for low-pressure cold spray. Adding and blending of hard particles with a metal powder can improve the deposition efficiency of cold spray coating. It was shown that the deposition efficiency could be increased more than 300% as compared to the metal cold spray coating. In addition, ceramic-metal mixture can improve the coating quality by reduction of the coating porosity and enhancement of bond strength of coatings to the substrate [43,44]. It was reported that the large Al powders made a coating with a porous microstructure [43]. A weak adhesion strength was also observed by its delamination from the substrate during metallographic sample preparation. However, adding only 7

wt.% Al_2O_3 to the Al feedstock powder causes a dense deposition with strong adhesion strength to the substrate. In fact, the deformability of Al particles was so remarkable. Ceramic particles cannot build-up a coating lonely and they play a crucial role on peening and roughening of the layers during cold spray deposition. The micro-asperities that are created by hard ceramic particles enhance the Al particles bonding and increase the surface area of substrate and coating. This was more evaluated by addition of the reinforcement phase to the ductile Al-Mg alloy [73]. In this study, a highly dense aluminum based-metal matrix composite (AMMC) was obtained with low-pressure cold spray. In fact, the hard phase produces the tamping and shot peening effect, which causes the compressive stress on the ductile matrix and improves the denseness of metal matrix composites. On the other hand, the compaction and shot peening effect of hard phase results the severe plastic deformation of ductile matrix and subsequent mechanical interlocking of powder particles and substrate bonding, as shown in Figure 9. Al_2O_3 particles with large size and velocity less than the critical velocity do not contribute to the coating build-up and their main effect is in compaction and shot-peening effect. The interaction of ceramic particles with previously deposited Al_2O_3 particles results in rebounding of them. Simultaneously, the ceramic particle that are retained within the composite coatings are due to the deformed ductile particles embedding and trapping the hard phase. In addition, the brittle nature of the Al_2O_3 particles causes the ceramic particles fracture during high velocity impact on the Al-Mg particles and previously deposited Al_2O_3, which are shown in Figure 9.

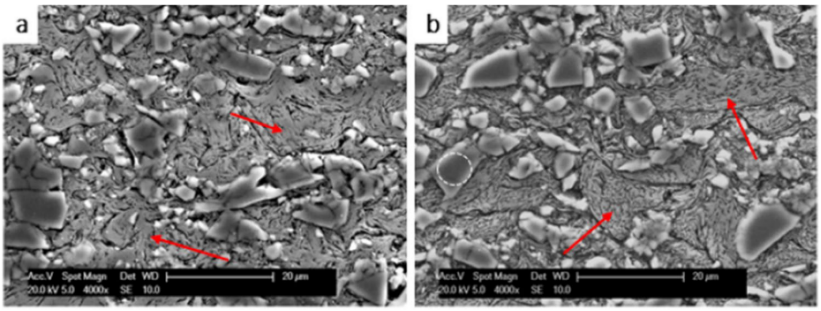


Figure 9: SEM images of the (a) Al-Mg-7wt% Al_2O_3 and (b) Al-Mg-10wt% Al_2O_3 coatings. Red marks show the deformed Al–Mg particles and the dotted white circle displays the alumina particles which are un-deformed and trapped in the matrix [73].

Blending of metal-alloy powders like ceramic-alloy have shown a remarkable improvement for both cold sprayability and coating properties. Improved deformation of softer matrix, tampering effect of

hard phase and their retention forming a continuous matrix are the critical factor for this achievement. For example, addition of 316L stainless steel to Fe powder improved the deposition efficiency [74]. In the other study addition of small amount of Al improved the deposition efficiency of NdFeB material for the cold spray deposition of permanent magnets with complex-shape [75]. Also, adding a low amount of Ti to Ti_6Al_4V led to the porosity reduction of deposited coatings [42]. As shown in Figure 10, the optimum amount of 10% leads to porosity reduction in the product, however less than or more than this value did not change the result significantly.

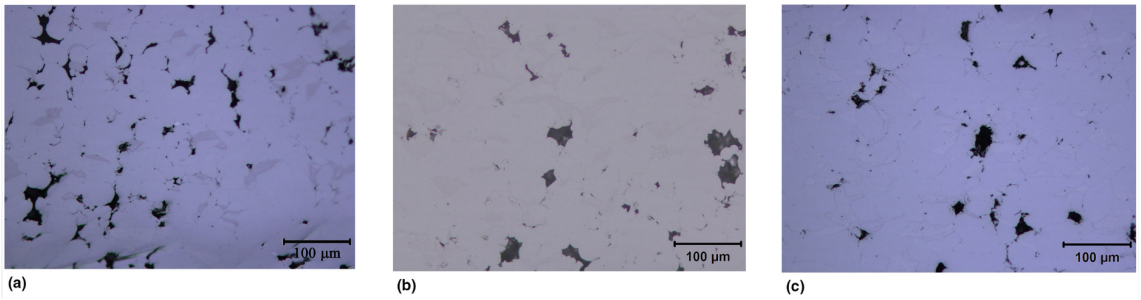


Figure 10: Porosity illustration of (a) 95% Ti_6Al_4V + 5% Ti, (b) 90% Ti_6Al_4V + 10% Ti, and (c) 80% Ti_6Al_4V + 20% Ti [42]

2.4.3 The effect of powder mixtures with nano and micron grain sizes on cold sprayability

Metallic materials with nanocrystalline microstructures and grain sizes of less than 100 nm shows unique characteristics, such as high strength, high corrosion resistance and high level of ductility [76]. It has been shown that a nanocrystalline metallic coating has a hardness of over 300 HV, however, the deposition efficiency is decreased significantly [76]. In this regard, in order to improve the deposition efficiency, powder mixtures comprising powders with nano and micron grain sizes are being used. As shown in Figure 11a, some regions with coarse grain sizes have been originated from micron grain size powders. This result illustrates that different amount of 10%, 20% and 30% of powders with micron grain sizes in the mixed powder can be widely distributed throughout the coating microstructure. Both coarse grains and nano size grains could be observed in the microstructure. The amount of coarse grain size microstructure was controlled by the different volume of them in the mixed feedstock powder. Referring to the recent works on bimodal microstructure of cold sprayed products [76,77], they are

anticipated to show excellent mechanical properties. The relationship between the amount of powder with micron grain size and the deposition efficiency, hardness and porosity of cold spray coatings in Figure 11b shows these properties could be controlled by changing different amount of powders with nano size and micron size grains.

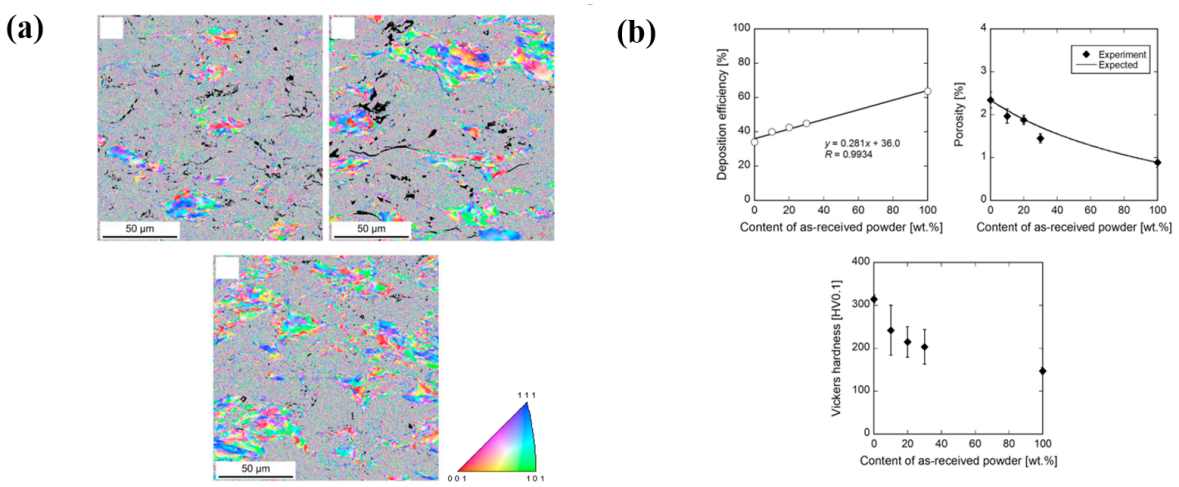


Figure 11: (a) Inverse Pole Figure (IPF) maps from the coatings with 10%, 20%, and 30% micron grain size powders and (b) deposition efficiency, porosity percent, and hardness of coatings vs. the content of micron grain size powder [76].

2.5 Heterogeneous materials

Heterogeneous materials with bimodal, harmonic, gradient, laminates, dual phase and lamellar structures are a new group of materials that possess superior combination of ductility and strength, which is not easy to get in homogeneous counterparts [23,78]. These materials have domains with significant strength differences. During deformation, near the interfaces of these domains, large strain gradients are produced which produces a large back stress to strengthen the material and increase the work hardening to achieve a good ductility. To maximize the back-stress and improving mechanical properties of material, high interface density is required.

2.5.1 Deformation behavior, strengthening and work hardening mechanisms

The deformation process of the heterogeneous materials with increasing the applied strain can be categorized into three stages. In the first stage, soft and hard domains deform elastically like a

conventional homogeneous material. In the next stage, dislocation slip will be activated in soft domains to produce plastic strain, while the hard domains will stay elastic, and a deformation incompatibility is created. As the soft domains must deform with the neighboring hard domains, they cannot plastically deform freely. The softer domain typically accommodates more strain, forming a plastic strain gradient near the domain interfaces, where it must deform compatibly with its neighboring hard domain. Geometrically necessary dislocations (GND) accommodate the strain gradients and make the softer phase stronger. This leads to increase the global measured yield strength of the material. In an ideal case, hard domains are completely surrounding the soft domains and prevent their shape change until the hard ones start to deform plastically. GND pile-up at domain boundaries in the soft domain section but cannot transmit, resulting in high back-stress as shown in Figure 12A. In this regard, soft domain will be as strong as hard domains and the global strength increases even more than the one is estimated by the rule of mixture [79]. In the last stage (stage three), the soft domains tolerate higher strain than the harder ones, thus strain partitioning will be produced. With increasing the strain partitioning, strain gradients near the domain boundaries become larger and produce back-stress work hardening. This back-stress work hardening helps to prevent the necking during tensile testing and improve the ductility. As shown in Figure 12B, A, a dislocation source at point X emits GNDs toward the domain boundary and help the system to reach an equilibrium state when a shear stress is applied. In fact, a long-range stress is produced by these dislocations, which counterbalances the applied stress. Therefore, back-stress is a long-range stress, which is produced by GNDs. Plastic strain and back-stress are connected to each other. Increase of strain and decrease of strain gradient with increasing the distance from the interface could be observed. This is because the plastic strain is created by dislocation slip and leaving a displacement of one Burgers vector. Therefore, the strain is zero at domain interface and increased at the dislocation source. In addition, stress gradient due to the pile-up of GNDs is produced in domain interfaces.

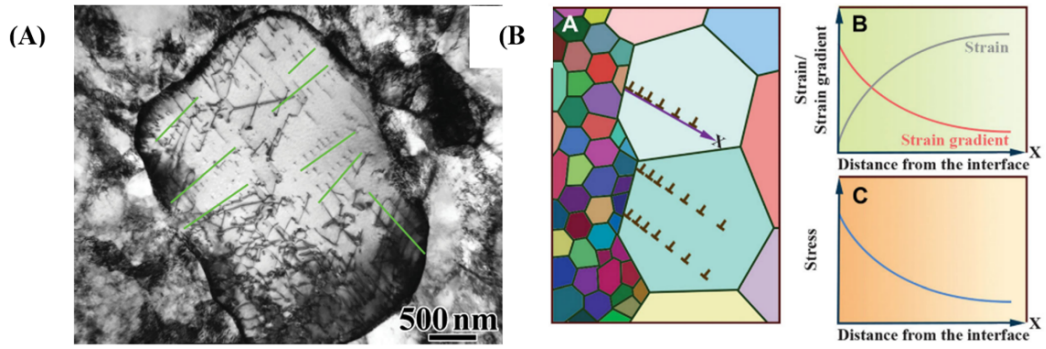


Figure 12: (A) Dislocation pile-ups shown by green lines in a heterogeneous lamella Ti. (B) Schematic representation of GNDs pilling up, strain gradient and plastic strain as a function of distance from the domain interface, the effective stress that is obtained [78,80].

To maximize the back-stress for achieving the best mechanical properties, heterogeneous structures could be designed. The first design factor should be the high density of interfaces because the back-stresses are produced by dislocation pile-up at interfaces. In addition, the spacing between domain interfaces is important, as it should be large enough to allow the dislocation pile-ups in soft domains. Maximizing the strain partitioning among the soft and hard domains is another design factor, which will increase the back-stress work hardening. Therefore, a large strength difference between the hard and soft domains are desirable to produce a significant strain partitioning [78]. Considering these two factors, heterogeneous structures such as bimodal, harmonic, gradient, laminates, dual phase and lamellar structures could be evaluated for achieving the ideal case. For a gradient structure, although dislocation density accumulate over the microstructure of whole sample, the interface density is low and has a low potential for back-stress work hardening [81]. In addition, in a bimodal structure, the interface density is not maximized and back-stress hardening is not at a high level [82]. For a laminate structure, soft and hard domains are under the same applied strain and a large strain partitioning cannot be developed in the microstructure [83]. In dual phase microstructures such as dual phase steel, the hard domains (martensitic) are about 5-30% by volume [84]. Although it produces a significant strain partitioning and increase the back-stress work hardening, the material yield at low stress because of the continuous soft matrix. Dual-phase materials have a very high ductility but limited improvement in strength. In a harmonic structure, the soft domains are surrounded by hard domains and can enhance the ductility, but the strength enhancement is not significant. This could be improved by decreasing the

spaces between the domain interfaces and increasing the hard domain volume fraction to constrain the soft ones, more. In a heterogeneous lamella structure as shown in Figure 13, the soft lamella domains are surrounded in a hard matrix [80]. The hard matrix makes a rigid constraint for the soft ones during deformation stage of two and make them as strong as the hard domains. In addition, the large strain partitioning during the last stage of deformation produces a high strain hardening and increases the ductility significantly. Therefore, high density of interlamellar interfaces and mutual constraints between the hard and soft domain make the heterogeneous lamella microstructure as an ideal case among the aforementioned topologies. On the other hand, it has been reported that the elongated inclusions can create higher work hardening especially when the long axis is aligned in the loading direction [80,85].

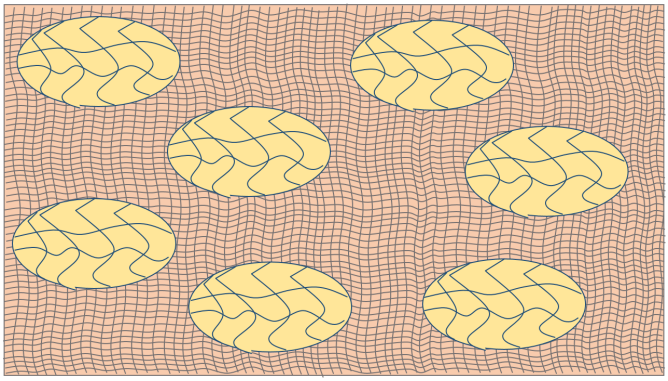


Figure 13: Schematic illustration of a lamellar structure featuring soft coarse-grained regions dispersed within an ultrafine-grained matrix.

2.5.2 Creation of heterogeneous materials through cold spray additive manufacturing

Different researchers in recent years have focused on improving the ductility of cold sprayed products through creation of a heterogeneous microstructure. Singh et al. [86] studied the influence of process parameters and powder particle sizes on microstructural and mechanical properties of cold spray additive manufactured Cu. The Cu deposits exhibited high ductility without any heat treatment in the as-sprayed state. The cheaper process gas (N_2) was used and no significant trade-off regarding to their mechanical properties was seen. The stress-strain curves (Figure 14a) shows that the curves obtained from cold spray deposition of powder particles at high processing parameters (T= 750 °C and P= 5 MPa) possess high tensile strength and high ductility which are fully comparable to the bulk (i.e., non-

AM) counterpart. This result for a cold sprayed Cu has not been reported previously. In addition, depositions obtained from finer powder show higher strength when comparing with coarser ones, although its effect is not as significant as the effect of the process parameters. These results suggest that at high processing parameters, Cu deposits could have a heterogeneous microstructure with high strength and ductility. To evaluate this hypothesis, EBSD analysis have been performed. The IPF maps shown in Figure 14b reveal bimodal microstructures which coarse grain areas are surrounded by a continuous network of ultra-fine grains along the particles' rims. The IPF maps of depositions obtained from fine powders shows bimodal microstructure at both high and low processing parameters. However, at low processing parameters, the topological distribution of fine and coarse grains is not homogenous. Contrary to this, the microstructure obtained from fine powders at high processing parameters shows a homogenous distribution of bimodality. Similar microstructures were obtained from depositions obtained from coarse Cu powders at high and low processing parameters. Again, high processing parameters led to homogeneous distribution of coarse grain and ultra fine grain areas. The presented results suggest that at low processing parameters, the time of elevated temperature condition is not sufficient, and recrystallization cannot fully change the microstructure. Therefore, heterogeneous bimodal microstructure consists of highly strained areas is formed. This results in high strength product with low ductility. Contrary to low processing condition, higher parameters induce higher particle velocity and subsequently higher temperatures, which facilitate dynamic recrystallization and can develop a homogenous and relaxed bimodal microstructure. Coarse grain areas, which surrounded by network of ultrafine grains have a synergetic effect on high strength and high ductility of cold sprayed product. Therefore, this study shows the processes parameters can influence more on the mechanical properties of product when compared with average particle size. The ultimate tensile strength of 286 MPa and 24% ductility was achieved in this effort [86]. However, similar results on other materials have not been reported yet.

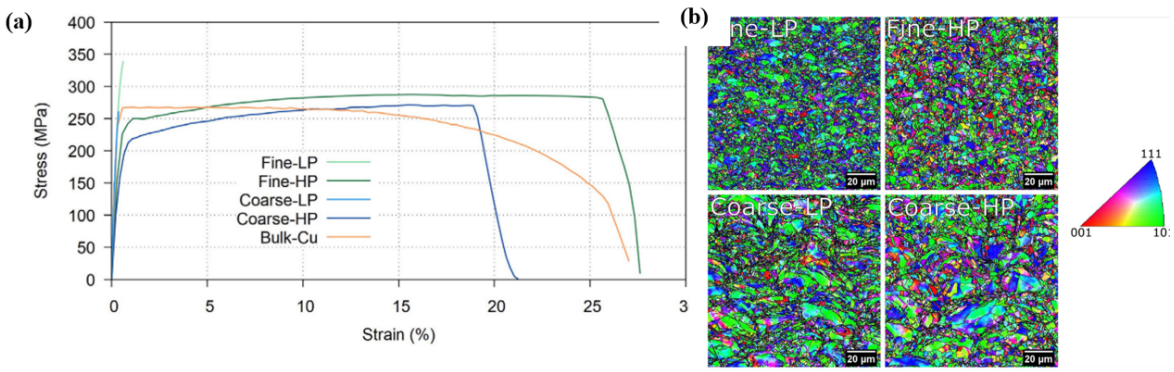


Figure 14: (a) Stress-strain curves and (b) EBSD IPF maps of cold sprayed Cu at high and low process parameters [86]. "Fine" in the image refers to the fine powder characterized by D10 = 6.2 µm, D50 = 11.8 µm, and D90 = 17.8 µm, while "coarse" corresponds to the coarse powder with D10 = 18.9 µm, D50 = 26.1 µm, and D90 = 40 µm.

Chen et al. [87] reported excellent strength and ductility of 271 MPa and 43.5%, respectively for a pure Cu prepared by cold spray additive manufacturing without additional post-treatments. The particle deposition was preformed using helium (2 MPa and 800 °C) as the process gas. Based on the observation, the Cu particles formed a gradient nano-grained (GNG) structure after deposition. The deformed particle (Figure 15a and b) shows a typical GNG structure which the elongated ultrafine grains present at the particle/ substrate interface and the micro-grain remaining at the top area of particle. These grain structures are retained in the full deposit in the as sprayed state, therefore the particle boundaries as shown in Figure 15c are blurred as a result of the extremely sever plastic deformation and interfacial particle melting during the successive impacts. The bulk structure does not show the characteristics of traditional cold sprayed microstructure. Therefore, the localized melting can improve the metallurgical bonding at the particle interfaces and help to reach a material with high strength and good ductility. The schematic diagram shown in Figure 16 summarize the deposition behavior of Cu to form a GNG structure. The Young's modulus is an important parameter to investigate the quality of cold spray additive manufacture deposits. Pores and inter-particle cracks can deteriorate the Young's modulus of deposits. Thus, the fully densified structure and significant inter-particle bonding lead to the high value of modulus in the bulk material. The authors in this research discuss that bimodal structure consists of ultrafine grains can improve the strength based on the Hall-Petch relation and ensure the ductility by the presence of coarse grains. In addition, nano twins in this sample could

provide an ability to increase the work hardening and stable deformation. In fact, twin boundaries have a blocking effect on dislocation motion, help the strengthening, and improve the ductility during plastic deformation.

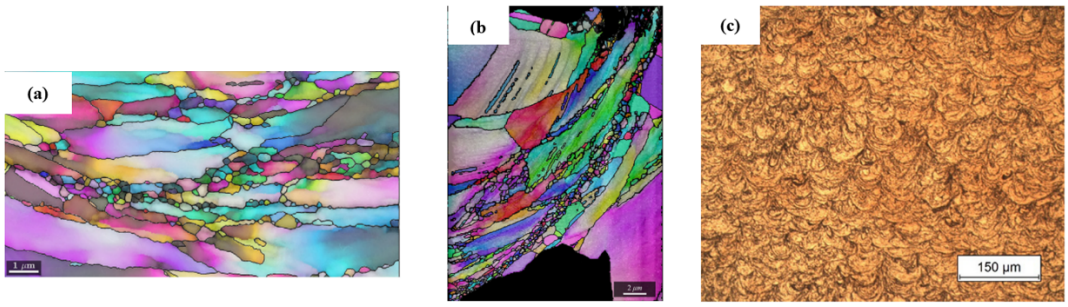


Figure 15: EBSD IPF maps for the grain structures of the deformed single particle at the (a) bottom and (b) peripheral regions, and (c) OM of the etched sample showing the severely deformed particles [87].

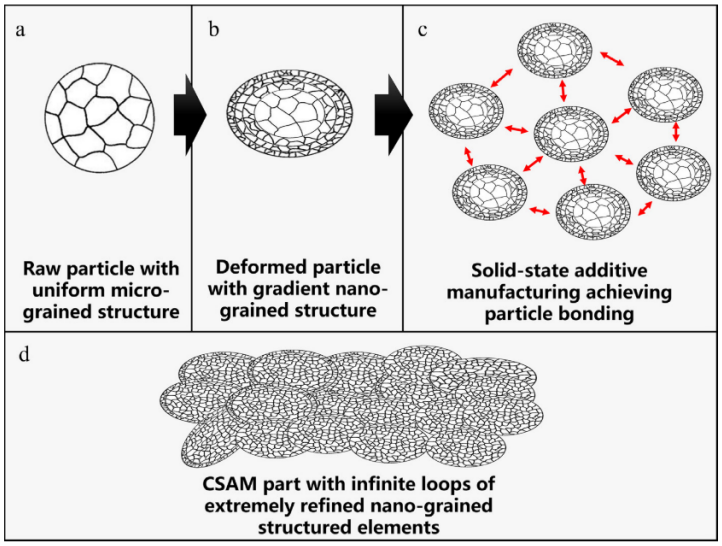


Figure 16: CSAM deposit with harmonic gradient nano-structure: (a) as-received particle with micron size grains, (b) the deformed particle with gradient nano-structure, (c) bonding of many deformed particles and (d) the final microstructure [87].

Kim et al. [88] also reported the fabrication of heterogeneous microstructures in cold sprayed materials. They have shown that Cu manufactured with process gas of N_2 (3 MPa and 600 °C) and He (2.6 MPa and 437 °C) reveal a bimodal microstructure consisting of ultra fine grains at the particle interface and coarser grains in inner particles. However, deposition with He gas led to the ultra fine grains in most areas (see Figure 17a and b). Compressive test was performed and the outstanding yield strength level of 340 MPa and 415 MPa for the N_2 gas material and He gas material were achieved respectively. In addition, strain-softening phenomenon that does not typically occur at room temperature happened for both samples. It has been shown that dynamic recovery and recrystallization were developed, although it was deformed at room temperature. To describe the work softening behavior according to the gas species, the work hardening curves (Figure 17c) have been investigated. The N_2 gas material has a larger area of coarse grains that is capable of plastic deformation accommodation and easier dislocation multiplication, which result in greater work hardening in stage one. Subsequently by activation of dynamic recovery and recrystallization, the work hardening rate will be decreased in stage two. Finally, dynamic recovery and sub grain rotation recrystallization dominate the plastic deformation and only work softening happen in stage three. On the other hand, the He gas material does not show the stage one of work hardening. By initiation of plastic deformation, the deformation mode of stage two was observed. This is because of limited dislocation multiplication and wide area of dynamic recrystallization. Additionally, because of less coarse grain area in this microstructure, domination of work softening starts from lower amount of deformation compared to the material obtained from N_2 gas. Based on the findings, higher ultra fine grain fraction causes the work-softening phenomenon.

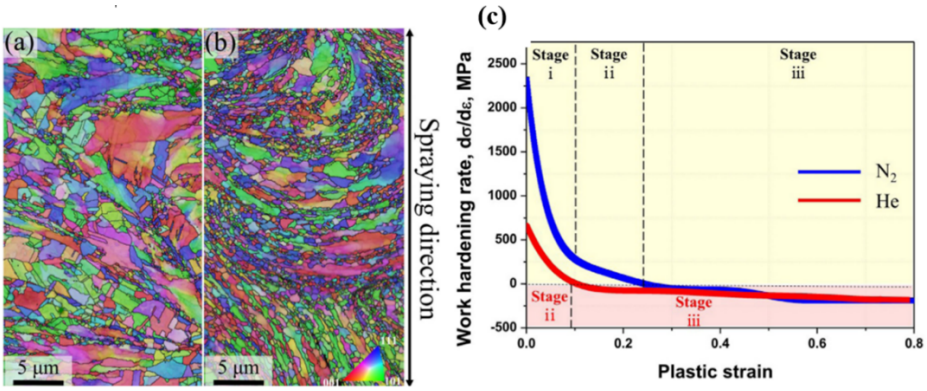


Figure 17: Cross-sectional EBSD grain orientation maps of cold sprayed Cu: (a) process gas N2 and (b) process gas He and (c) measured work hardening rate (dσ/dε, Θ) obtained from the stress-strain curves [88].

In addition, a novel study on creation of heterogeneous materials, outside Cu, using cold spray has been done recently, which involves the use of high entropy alloys (HEAs), multi-principal element alloys known for their excellent mechanical strength, corrosion resistance, and structural stability, combined with ceramic phases to create gradient or composite structures [89]. In this work, the development of CoCrFeNi/Al_2O_3 composite coatings on AZ91 magnesium alloy substrates by solid-state cold spray has been investigated. The incorporation of 30 vol% Al_2O_3 into the CoCrFeNi HEA matrix not only reduced material cost and density but also introduced a gradient-like structure at the interface as shown in Figure 18a-d. The OM image, grain size distribution map, and BSE images of AZ91 substrate near the bonding surface, presents the microstructure details that enhanced the bond strength and enabled dynamic recrystallization (DRX) in the underlying substrate. This led to grain refinement and a significant increase in hardness across the interface, transitioning smoothly from the soft AZ91 base (~73 HV) to the harder coating region (~363 HV). The resulting coating was dense, crack-free, and exhibited low porosity, with a notably smooth surface finish. It showed excellent wear resistance, with wear depth reduced to one-tenth of the substrate's, and a higher friction coefficient due to the presence of hard ceramic reinforcements. Electrochemical testing further revealed a dramatic improvement in corrosion resistance, with a five-order magnitude drop in corrosion current and an efficiency of 99.92%, attributed to the formation of a stable, oxide-rich passive film dominated by Al_2O_3. This study exemplifies the capability of cold spray to produce functionally graded and

mechanically interlocked heterogeneous structures. It demonstrates how the combination of HEAs and ceramics, tailored through cold spray, can yield lightweight coatings with superior surface properties.

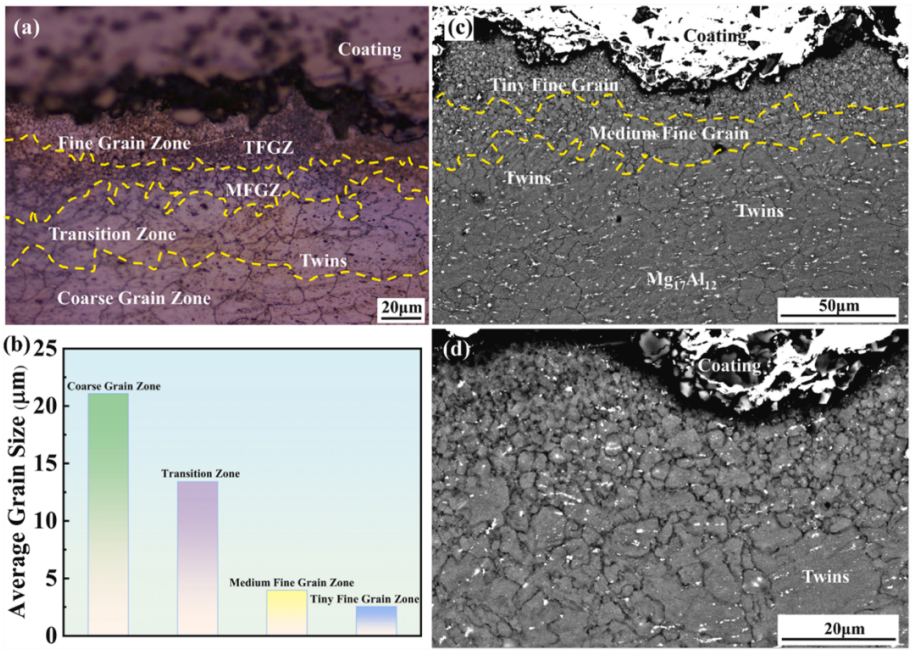


Figure 18: (a) OM image, (b) grain size distribution map, and (c–d) BSE images of AZ91 substrate near the bonding surface [89].

2.5.3 Effect of feedstock powders on creation of heterogeneous materials

Different cold spray process parameters could be adopted for fabrication of bulk heterogeneous materials with various forms and distribution of heterogeneities. The effect of feedstock powder as one of the important parameters have been investigated in recent years. Blending of nano crystalline and microcrystalline powders in different ratios as a feedstock has been a new strategy for fabrication of heterogeneous materials with bimodal grain size microstructures. Rodela et al. [90] blended non-cryogenically (NCM) milled and cryomilled (CM) AA5083 with 50 wt% and 30 wt% gas-atomized (GA) AA5083 before cold spraying. However, the bimodal distribution of grain sizes was not retained, as was expected, in the cold sprayed microstructure and a wide grain size distribution in the ultra fine grain regime has been obtained. Recrystallization of larger micron scale grains resulted in the average grain size of 241 ± 123 nm, 196 ± 124 nm and 141 ± 73 nm for the samples sprayed using CM and 50%

GA powder, NCM and 50% GA and NCM and 30 GA powder, respectively. UTS in the range of 306-337 MPa and elongation of 6.7-8.7% were obtained for the samples. No correlation was found between the percentage of conventional powder in the feedstock and the obtained strength and ductility. The fracture surface revealed a brittle failure and the particle bonds were the weak links in the materials. Optimization of the spray parameters has been suggested for obtaining fully dense samples with high strength particle bonds. Bagherifard et al. [77] successfully fabricated bimodal structures composed of nano grain size and micro grain size. A direct relationship between the volume fraction of microcrystalline phase (MC), the elongation to failure and tensile strength have been seen. By increasing the amount of MC phase volume fraction, yield strength and ultimate tensile strength decreased (Figure 19). These samples showed a highly brittle failure and no necking or notable deformation was observed. It is worth noting that a trade-off between strength and elongation to failure has been found in the results. This trend was because of significant difference in deformability and strength of the two phases.

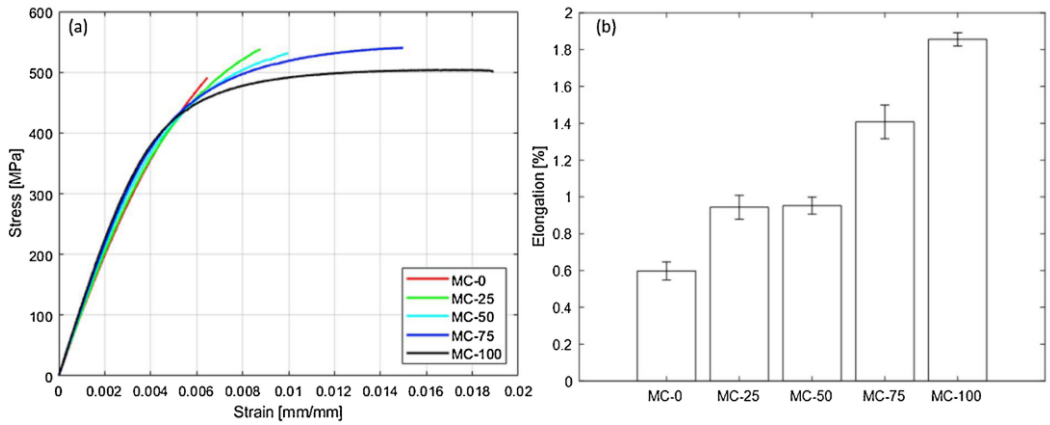


Figure 19: a) Stress-strain curves of as-sprayed samples; b) The elongations to failure vs. volume fraction of MC powders [77].

The other novel strategy to fabricate high performance cold spray depositions with the help of feedstock parameter has been proposed based on the synergetic effect of a wide particle size distribution of feedstock powder and very low processing parameters [91]. It has been shown that the product fabricated by considering wide particle size distribution and low temperature is 12% stronger than the products fabricated by the same particle size distribution along with high temperature or He gas. Although ductility in the product was only about 3.15% (1-2% more than the other two products), the

porosity decreased and stronger inter particle bonding formed. In fact, under the proposed condition (N_2, 3.0 MPa, 300 ◦C) which lead to lower impact velocity, the deposition window and subsequently a successful deposition are narrow. As illustrated in Figure 20, a large proportion of feedstock powders specifically the larger ones are outside of the required deposition window (Figure 20a), thus, the bigger particles after deposition rebound from the substrate. These particles continuously compacted the already formed deposits and will create a densified microstructure by inducing more plastic deformation. In contrast, Figure 20b shows that at higher temperatures, the rebounding effect is less and some non-closed pores left in the structure. However, microstructure obtained from He gas is densified and high deposition efficiency has been reached (Figure 20c).

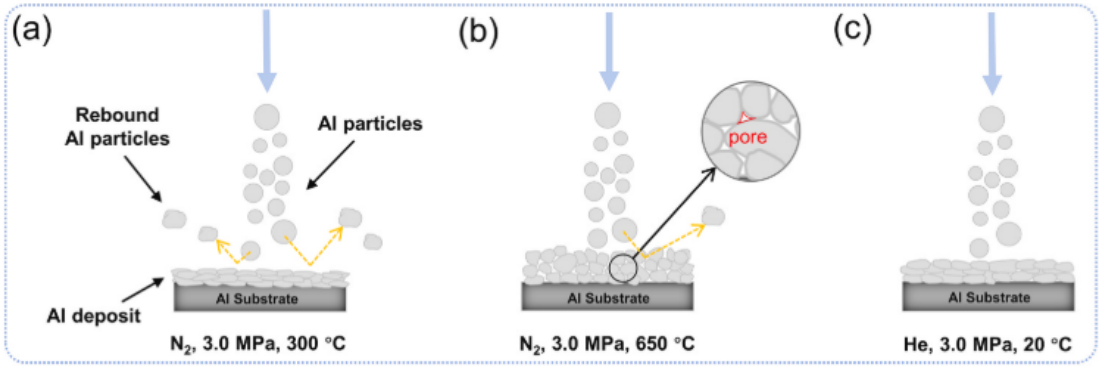


Figure 20: Schematic illustration of different strengthening mechanisms happening at different conditions for wide particle size distribution of feedstock powder [91].

2.5.4 Dual heterogeneous laminated composites

The mechanical properties of materials are largely influenced by their internal interfaces, such as grain boundaries, phase boundaries, twin boundaries, and lamella boundaries [92]. Recently, significant research has focused on metals with a high density of interfaces [93–95], including laminated metals with enhanced mechanical properties [96,97]. These studies suggest that designing internal interfaces can yield superior mechanical properties. Numerous researchers [98–100] have concentrated on fabricating dual heterogeneous laminated Cu/Cu-Cr-Zr composites using a combination of accumulative roll bonding (ARB) and appropriate annealing processes, and cold pressing followed by sintering. The cross-sectional micro-hardness distributions across the layer interfaces, as shown in Figure 21a, display a sharp transition from the soft pure Cu layer to the hard Cu-Cr-Zr alloy layer, while

the hardness values within each layer remain relatively uniform. This indicates a clear mechanical incompatibility between the pure Cu and Cu-Cr-Zr alloy layers, which is expected to generate significant back-stress hardening, thereby simultaneously improving strength and ductility.

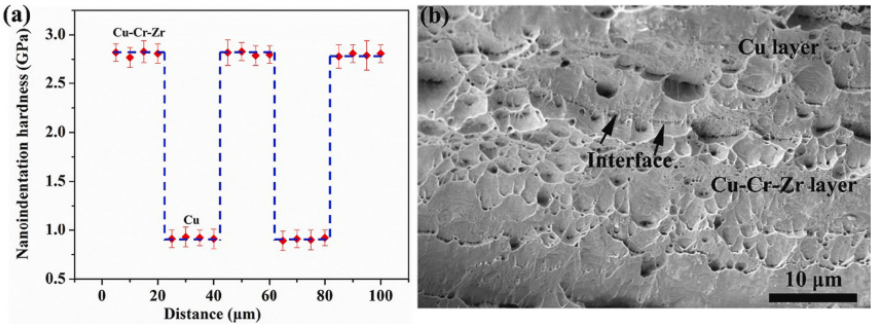


Figure 21: (a) Cross-sectional micro-hardness distributions profile, (b) layer interface of Cu/Cu-Cr-Zr laminates sample [99].

One notable approach involves the development of heterostructured Cu–Cr–Zr alloys by powder metallurgy, where micrometer-scale pure copper grains are embedded in a matrix of ultrafine CuCrZr grains with nanoscale precipitates [98]. This architecture enables a synergistic combination of mechanical and electrical performance: enhanced strength from the refined CuCrZr matrix, high conductivity through pure Cu channels, and retained ductility due to strain hardening induced by GNDs at domain interfaces. The result is a remarkable property set with an ultimate tensile strength exceeding predictions based on the rule of mixtures, along with high conductivity (~83% IACS) and 11% uniform elongation as shown in Figure 22. In the other work, by analyzing the strain hardening rate (θ) and strain hardening index (n) as functions of logarithmic strain, researchers demonstrated that layered CuCrZr alloys, exhibit improved work-hardening behavior and maintain stable deformation over a longer strain range compared to monolithic counterparts [100]. Unlike pure Cu and conventional CuCrZr alloys, which show early plastic instability and necking, the layered structures sustain work hardening at larger strains as shown by tensile stress-strain and work hardening curves in Figure 23a and b, respectively. This is evidenced by a linear increase in the instantaneous hardening index at higher strain levels, reaching values as high as 0.28. The findings suggest that the enhanced ductility of layered CuCrZr alloys is primarily due to their superior work-hardening capacity and the activation of additional deformation mechanisms during plastic flow. In particular, investigations under 3% tensile strain

revealed a clear gradient in GND density near the CuCrZr/Cu interface as shown in Figure 24. This gradient arises from the inhomogeneous yet continuous strain distribution across the layered structure, which necessitates the accumulation of GNDs to accommodate local strain mismatches. The resulting dislocation structures contribute to hetero-deformation induced (HDI) hardening, enhancing the alloy's ability to retain ductility under load. Notably, GNDs tend to concentrate near the CuCrZr/Cu interface, forming an interface-affected zone approximately 10 μm wide, while their density progressively decreases with distance into the Cu layers, highlighting the localized influence of interface-induced strengthening.

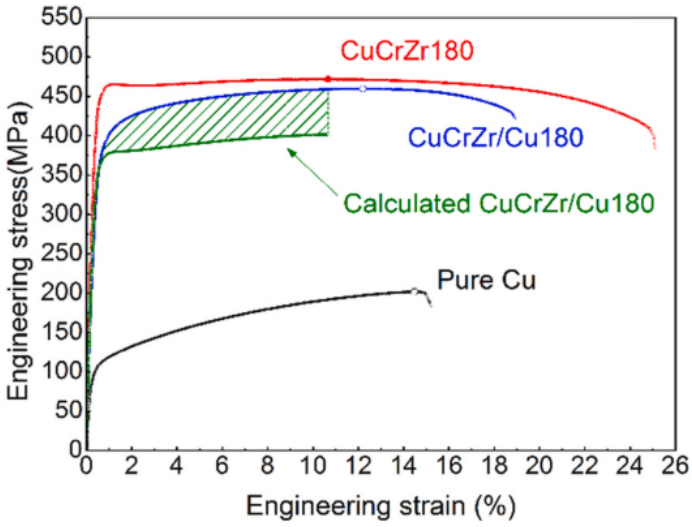


Figure 22: Tensile curves of pure Cu, CuCrZr180, the experimentally measured CuCrZr/Cu180 composite, and the corresponding curve predicted using the rule of mixtures [98]. "180" denotes the CuCrZr powder that underwent ball milling for a duration of 180 minutes.

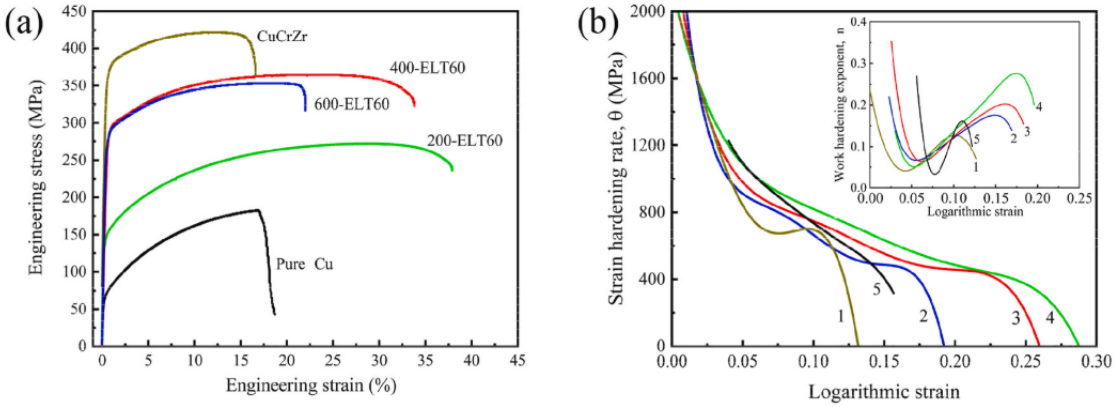


Figure 23: (a) engineering stress–strain curves are presented for the layered CuCrZr alloy, CuCrZr, and pure Cu following thermomechanical processing. The labels 200, 400, and 600 correspond to cold-pressed billets of layered CuCrZr–Cu composites, each featuring equal layer thicknesses (ELT) of 200 μm, 400 μm, and 600 μm, respectively. "60" indicates that the layered CuCrZr alloys underwent secondary aging for a duration of 60 minutes. (b) Corresponding plots show the strain hardening rate as a function of logarithmic strain, with the inset illustrating the relationship between the strain hardening index and logarithmic strain [100].

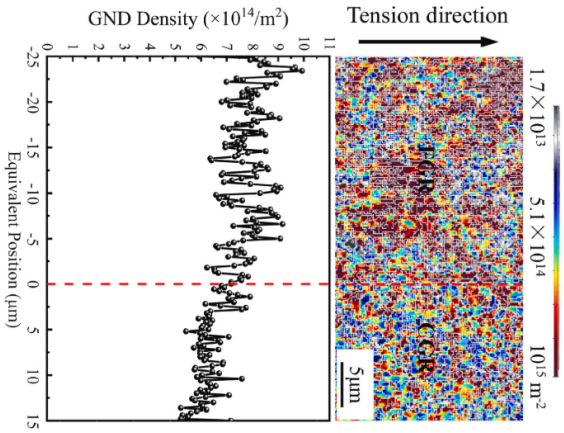


Figure 24: The correlation between the average GND density and the equivalent distance from the CuCrZr/Cu interface in the 400-ELT60 layered alloy subjected to 3% tensile strain [100]**.**

Additionally, Ma et al. [101] produced copper/bronze laminates with varying interface spacing through ARB and subsequent annealing to systematically study the interface effect on mechanical properties. The back-stress from unloading-reloading test curves at different tensile strains (see Figure 25a) was calculated. As shown in Figure 25b, the resulting back-stress is higher in samples with smaller interface spacing (higher interface density).

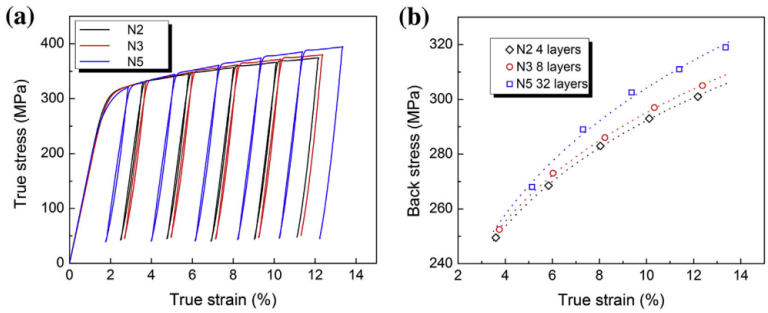


Figure 25: (a) Unloading-reloading tensile curves of N2, N3, N5 samples that have 4, 8 and 32 layers, respectively. (b) The calculated back stress at corresponding strain levels [101].

This can be explained with the help of Figure 26, which shows that each interface creates an interface-affected zone due to considerable GND pile-ups. Consequently, higher interface density results in more GND pile-ups within a given sample volume, leading to a higher observed back-stress at the current spacing scale.

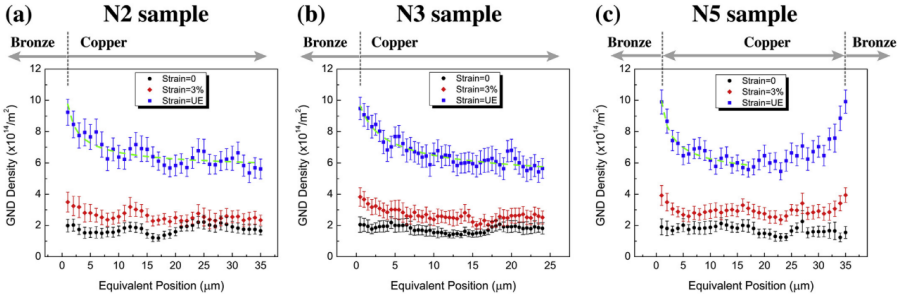


Figure 26: Averaged GND density in copper layer versus the equivalent distance from the interfaces at different strain levels of (a) N2 sample, (b) N3 sample, (c) N5 sample [101].

2.6 Critical gaps in the literature

Despite the growing interest in CSAM, significant knowledge gaps persist in understanding how feedstock powder characteristics influence the final properties of cold-sprayed components. While previous studies have explored various aspects of cold spray processing, a systematic and comprehensive correlation between powder attributes, particularly those arising from different manufacturing methods, and the resulting coating quality remains underdeveloped. Most existing works lack the depth needed to identify which specific powder traits most critically affect targeted mechanical or microstructural outcomes in the deposited materials. Moreover, compared to other processing parameters, limited experimental data are available to guide researchers and industry practitioners in selecting appropriate feedstock powders or optimizing their properties.

Although it has been shown that annealing improves ductility, a rigorous evaluation of the intrinsic properties of low-pressure cold-sprayed Cu, particularly when processed with different process gases such as nitrogen and helium, is still lacking. These gases induce varying degrees of work hardening, which in turn affect the material's response to post-deposition heat treatments. Additionally, while solution annealing (SA), solution annealing plus aging (SA+AH), and direct aging (DAH) are widely used in heat treatment regimes, their comparative effects on the microstructural evolution and mechanical performance of cold-sprayed CuCrZr alloys remain unexplored.

Furthermore, although heterostructures have been extensively studied in conventionally processed materials, their design and development within CSAM systems remains an emerging area with limited research. The unique non-melting characteristic of CSAM, which enables the use of diverse powder materials with tailored microstructures to optimize performance, is significantly underexplored and, in many cases, entirely untested. Advancing research in this area could unlock the fabrication of performance-driven materials/structures that are currently impractical or impossible to produce using traditional manufacturing methods.

Addressing these gaps forms the core motivation of this study and provides the foundation for the objectives outlined in the introduction chapter.

Chapter 3
Methodology

This chapter outlines the methodologies used for characterizing the as-received powders, conducting cold spray (CS) deposition, applying post-deposition heat treatments, and analyzing the resulting CS-deposited samples.

3.1 Characterization of as-received powders

Five types of pure copper powders, designated as A, B, C, D, and E, were examined and used for deposition in this study. Table 3 provides the supplier, manufacturing method, and copper content (wt.%) for each powder.

Table 3: Supplier, production method and copper content (wt.%) of each powder

Powder type	**A**	**B**	**C**	**D**	**E**
Supplier	Centerline Ltd., Windsor, Canada	ECKART TLS GmbH., Bitterfeld, Germany	5N Plus Inc., Quebec, Canada	Solvus Global., Worcester, USA	Metal Powder Works, Pennsylvania, USA
Production method	Electrolysis	Gas atomization (contain microsatellite particles)	Gas atomization (Satellite free)	Gas atomization (satellite free)	Grinding
Cu (Wt. %)	>99.7	>99.9	>99.9	100	>99.5

3.1.1 Morphology and microstructure

Morphological and microstructural analyses were carried out on five types of copper powders. For morphological examination, the powders were placed on conductive carbon adhesive tapes and observed using a scanning electron microscope (SEM, Zeiss Leo UltraPlus FESEM model). For microstructural characterization, a small quantity of each powder was hot-mounted in resin, then ground using 240, 400, and 600-grit SiC papers, followed by polishing with MD-Largo and MD-Mol 3 μm cloths. The initial polishing step used DiaPro Allegro/Largo 9 μm suspension, while the second

step used DiaPro Mol R3 µm suspension. Between each step, the samples were cleaned in an ultrasonic ethanol bath. Etching was performed using either a nitric acid solution (50 ml nitric acid + 50 ml distilled water) or a ferric chloride solution (100–120 ml distilled water or ethanol + 25–50 ml hydrochloric acid + 5–10 g ferric chloride). The resulting microstructures were examined with SEM equipped with energy-dispersive X-ray spectroscopy (EDS). To analyze surface chemistry, X-ray Photoelectron Spectroscopy (XPS) was employed. The analysis was conducted on free powders using a ThermoFisher Scientific K-alpha spectrometer, which utilized a monochromated Al Kα X-ray source with a 400 µm beam size. Charge compensation was applied during measurement. Two spectra were recorded for each powder type, yielding consistent results. To ensure accuracy, spectra were charge-corrected by aligning the adventitious carbon (C 1s) peak to 284.8 eV, and a standard Shirley background was used throughout the analysis.

3.1.2 Particle size and shape analysis

The particle size distributions and sphericity of the powders were assessed using a particle size and shape analyzer (Camsizer X2, RETSCH, Germany). The analyzer generated a particle flow that was examined using a high-resolution optical system capable of capturing over 300 images per second. These images were processed in real time by advanced software to evaluate particle characteristics.

3.1.3 Powder flowability

The flowability and shear characteristics of the powders were determined using a rotational shear cell integrated into the FT4 Powder Rheometer (Freeman Technology Inc., Worcestershire, UK). The powders were loaded into a borosilicate glass vessel, and a 316 stainless steel blade first moved downward and then upward to ensure uniform powder conditioning. Following this, a piston applied a consolidation stress, and the powder was sheared until reaching a steady-state flow, generating the initial normal and shear stress values known as the preshear point. Subsequently, the normal stress was gradually reduced in five steps, and the corresponding shear stress was recorded at each level to define yield points. This process was used to construct a yield locus. Shear stress values were then plotted against normal stress, and the rheological behavior of each powder sample was interpreted using the Mohr–Coulomb model [61,64]. During testing, applied normal stresses ranged from 1 to 3 kPa, and the

final flowability and shear properties were calculated based on the average of at least three repeated measurements.

3.1.4 Nanoindentation

Nanohardness measurements were carried out on the as-received copper powders, which were mounted in resin, then ground and polished to expose flat cross-sections (as described in the above microstructural analysis section). The tests were performed using an Anton Paar NHT3 nanoindenter equipped with a diamond Berkovich tip. Indentation was conducted under load control, applying a maximum load of 50 mN over a loading time of 60 seconds. For each type of Cu powder, 20 measurements were taken on different particles of varying sizes. The nanohardness values were determined from load–displacement curves following the method proposed by Oliver and Pharr [102]. Nanoindentation was specifically chosen to minimize any influence from the underlying mounting material.

3.2 Cold spray process

A commercial Cold Spray System (Series P) from Supersonic Spray Technologies (SST), manufactured by Centerline in Windsor, Canada, as shown in Figure 27, was utilized for coating and 3D printing the as-received pure Cu and CuCrZr alloy powders. In this process, the powders were propelled to supersonic speeds using a converging–diverging de Laval UltiLife™ nozzle within a low-pressure system. The specifications of the cold spray equipment used are provided in Table 4. Multiple rectangular substrate samples measuring 8 cm × 20 cm and 3.16 mm in thickness, made from Cu, Al 6061, and Al 5052 alloy sheets, were used for coating and 3D printing purposes. Before the cold spray deposition, all substrates were cleaned using alcohol to ensure surface cleanliness. The optimal CS coating parameters, including process gas temperature and pressure, step-over distance, nozzle travel speed, and standoff distance, for each type of Cu powder were determined using the Design of Experiments (DOE) approach. A full factorial design was employed to plan 9 coating trials for each powder type. To ensure accuracy and reproducibility, each trial was repeated three times. The optimized parameters are further discussed in Chapter 5. Coatings produced using the different copper feedstock powders are illustrated in Figure 28. Powder C, identified as the most suitable feedstock, was utilized for CS 3D printing under optimized processing conditions. Additionally, another gas-atomized pure

copper powder with 99.9% purity, provided by Metalpine GmbH (Austria), and considered more favorable for 3D printing, was also employed in this study. Using these powders, bulk copper components were fabricated via Cold Spray Additive Manufacturing (CSAM) with nitrogen (N_2) and helium (He) as process gases, as illustrated in Figure 29. The resulting CS Cu parts produced with both process gases measured 125 mm in length, 60 mm in width, and 3.5 mm in thickness. Deposition efficiency was evaluated using Cu parts printed onto aluminum substrates. Each substrate was weighed on a precision digital balance (accurate to 0.0001 g) before and after the spraying process to measure weight gain. Deposition efficiency was then calculated by dividing the weight gain by the total mass of powder delivered to the substrate, determined from the mass feed rate and spraying duration.

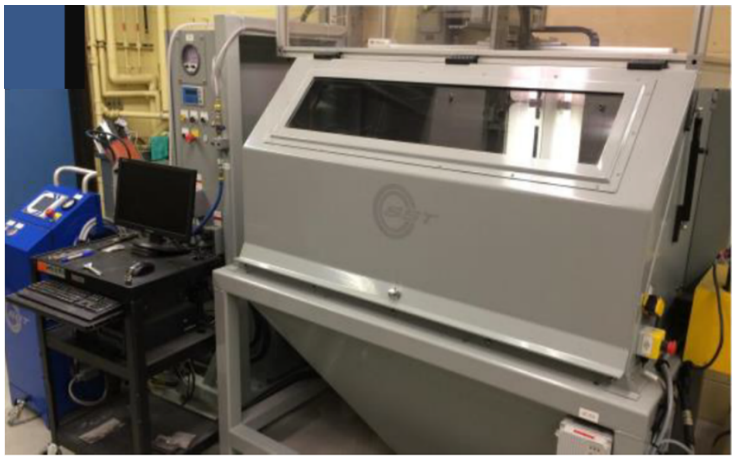


Figure 27: The commercial Cold Spray System (Series P) by Supersonic Spray Technologies (SST), manufactured by Centerline in Windsor, Canada, installed and operated in the Cold Spray lab at the University of Waterloo, located in room 2116A, E3 building.

Table 4: Specification of SST cold spray system

Process Gas	Nozzle type	Nozzle Length	Nozzle Orifice Diameter	Nozzle Exit Diameter
N_2 & He	De Laval UltiLife™	120mm	2 mm	6.3 mm

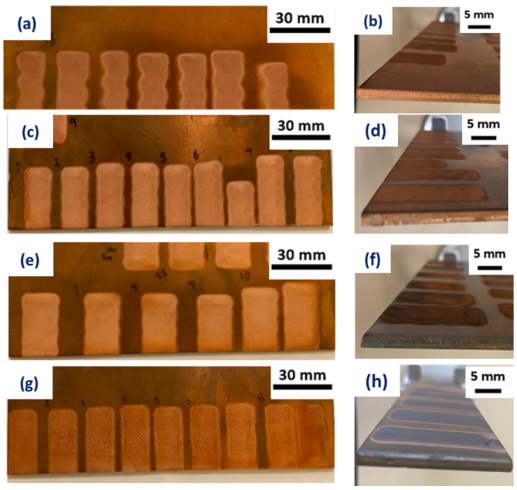


Figure 28: Top and side views of the cold spray coatings produced using powders (a) and (b) A, (c) and (d) B, (e) and (f) C, and (g) and (h) D. The numbers marked on the plates correspond to various experimental trials and their repetitions. The substrates have a thickness of 3.16 mm, while the coatings are in the micron range.

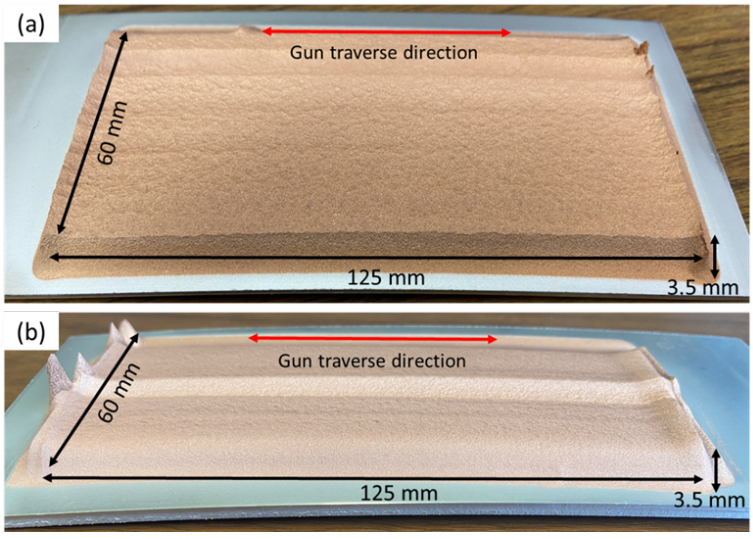


Figure 29: Macroscopic images of cold-sprayed copper materials using different process gases: (a) nitrogen (N_2) as the process gas, and (b) helium (He) as the process gas.

Additionally, a Cu–0.45 wt% Cr–0.05 wt% Zr alloy powder, supplied by EOS North America Inc. and produced via gas atomization, was used as another feedstock material in this study. Using nitrogen as the process gas, this CuCrZr powder was 3D printed onto Al 5052 substrates under the following conditions: a standoff distance of 25 mm, gas pressure of 1.99 MPa, gas temperature of 400 °C, and nozzle travel speed of 80 mm/s. The resulting deposition is presented in Figure 30.

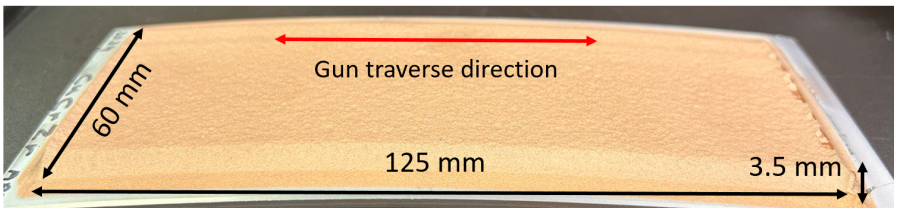


Figure 30: Image of the cold-sprayed CuCrZr material deposited using nitrogen (N_2) as the process gas.

CSAM laminated samples comprising 7 and 14 alternating layers of CuCrZr and pure Cu powders were produced by low-pressure CS system (Figure 31). The fabrication process involved sequentially depositing CuCrZr as the first layer, followed by pure Cu as the second, repeating this sequence to achieve the target number of layers. The 7-layer (7L) sample, created using nitrogen as the process gas, had dimensions of 125 mm in length, 60 mm in width, and 4.2 mm in thickness. The 14-layer (14L) sample, also deposited with nitrogen, measured 125 mm × 60 mm × 3.8 mm. For the 7L sample, processing parameters included a nozzle pressure of 1.99 MPa, a gas temperature of 400 °C, and a nozzle travel speed of 80 mm/s. In contrast, the 14L sample was fabricated at a higher gun speed of 120 mm/s. During deposition, Cu and CuCrZr powders were sprayed onto aluminum substrates from standoff distances of 20 mm and 25 mm, respectively.

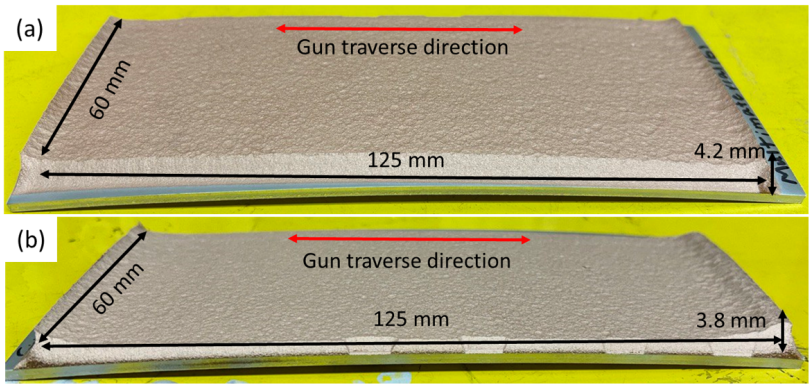


Figure 31: Macroscopic images of laminated Cu/CuCrZr structures with varying layer configurations: (a) 7-layer laminate and (b) 14-layer laminate.

3.3 Post-deposition heat treatment

Post-deposition heat treatments were conducted to evaluate their effects on the microstructural evolution and mechanical performance of cold-sprayed samples, including pure Cu, CuCrZr alloy, and Cu/CuCrZr laminated structures.

For the pure copper Cu samples, heat treatments were performed in a vacuum tube furnace (models GSL-1500X-50-UL and GSL-1600X-50-UL, manufactured by MTI Corporation). Specimens were heated to 500 °C and 700 °C, held for 4 hours at each temperature under an argon atmosphere, using a heating rate of 10 °C/min. After the hold period, samples were allowed to cool naturally to room temperature inside the furnace.

For the CuCrZr samples, a range of heat treatment protocols was employed to optimize mechanical properties. Two primary methods were used:

- Solution Annealing (SA): Samples were heated to 950 °C for 30 minutes in a tube furnace and then quenched in water.
- Age Hardening: SA-treated samples were further aged at 480 °C for 30 minutes to enhance precipitation strengthening.

In addition, Direct Age Hardening (DAH) was explored by subjecting as-deposited CuCrZr samples to five different aging temperatures: 400 °C, 450 °C, 480 °C, 520 °C, and 560 °C, with hold times of 30, 60, 120, and 170 minutes. All samples were subsequently air-cooled to room temperature.

For the laminated Cu/CuCrZr materials, a combined thermal treatment approach was used to strengthen the composite structure. The process involved solution annealing at 950 °C for 30 minutes, followed by water quenching, and then age hardening at 480 °C for 30 minutes. This dual-step treatment was selected based on prior studies demonstrating its efficacy in improving the mechanical properties of cold-sprayed CuCrZr materials fabricated via CSAM.

3.4 Characterization of cold sprayed depositions

Cold-sprayed depositions were analyzed through physical, microstructural, mechanical, and postmortem characterization techniques.

3.4.1 Thickness and weight

The thickness of the deposited coatings was measured using a digital caliper with 0.01 mm accuracy, along with SEM imaging. To ensure accuracy, an average thickness was determined from at least 20 measurements taken at various points along the cross-section over the entire length of the coatings. The coating weight was calculated using a high-precision digital scale (accuracy of 0.0001 g) by measuring the difference in sample weight before and after deposition.

3.4.2 Microstructure

Pure Cu, CuCrZr and laminated cold sprayed depositions were sectioned perpendicular to the nozzle travel direction, then hot-mounted, polished, and etched with nitric acid solution and a solution containing 2 mL HCl, 1 g $FeCl_3$, and 20 mL H_2O, respectively. These samples were examined using a digital microscope (Keyence VHX-7000) and an optical microscope (Olympus BX41). EBSD analysis of cold-sprayed coatings and 3D-printed pure Cu was carried out using a TESCAN VEGA3 SEM equipped with a BRUKER e−FlashFS EBSD detector. Prior to EBSD, samples underwent vibratory polishing for approximately 6 hours on a Buehler VibroMet2 using 50 nm colloidal silica to remove surface deformation. EBSD scans were performed at 25 kV accelerating voltage with a step size of 500 nm. To investigate the microstructural evolution of CuCrZr and laminated samples before and after

heat treatment, EBSD analysis was conducted using a Thermo Fisher Scientific Apreo 2 S LoVac SEM, equipped with a Symmetry S3 EBSD detector and an Ultim Max 170 mm² EDS detector (both from Oxford Instruments Ltd.). A standard scan used a step size of 200 nm over a 550 × 550 μm² area, while detailed interface characterization employed a finer step size of 50 nm over a 40 × 40 μm² area. Data collection and analysis were performed using Aztec version 6.1 SP1 and ATEX© software.

The flattening ratio of splats was determined using image analysis software (ImageJ). The center of each oval-shaped splat was defined as the point where its major and minor axes intersect, and the flattening ratio was calculated by dividing the length of the major axis by the minor axis, as described in reference [103]. To ensure statistical reliability, measurements were taken from at least 200 splats across 10 micrographs per sample. Splats with diameters smaller than 10 μm and those positioned at the edges of the images were excluded to improve measurement accuracy. Porosity in the cold-sprayed coatings and 3D printed parts was evaluated in accordance with ASTM E2109, using SEM images captured at both lower (x2000) and higher (x8000) magnifications [104]. A total of 25 SEM images were analyzed across the cross-section of each coating, employing binary segmentation via ImageJ for quantification.

The average grain size of the substrates near the surface was determined using the ASTM E112 standard test method of lineal intercept procedure [105]. In addition, Phase identifications for the 3D printed components were conducted using a Bruker D8-Discover X-ray diffraction (XRD) system, which is equipped with a VÅNTEC-500 area detector and utilizes Cu-Kα radiation (λ = 1.5406 Å) under operating conditions of 40 kV and 40 mA.

3.4.3 Microhardness

Vickers microhardness measurements were performed on all deposited samples using a Manual Vickers Hardness Tester (Wilson). For cold-sprayed coatings, 5 to 8 indents were made at each position along the longitudinal cross-section, while twenty measurements were taken for the 3D-printed bulk samples. According to ASTM E384, a 10 g load with a 10-second dwell time was applied for coating measurements, and a 200 g load with a 15-second dwell time was used for bulk material testing [106].

3.4.4 Adhesion/Cohesion strength

The adhesion and cohesion strength of the cold-sprayed coatings were assessed using a tensile pull-off test, following the ASTM C633 standard [107]. The test setup, including coupon geometry and alignment fixture, is illustrated in Figure 32. Copper cylindrical coupons were used, with the cold spray coating applied to the top circular face. Both the coupons and their mating counterparts had a radius of 12 mm. Prior to testing, the coating surfaces were ground for improved smoothness, resulting in a post-processed thickness of approximately 380 μm. All mating surfaces were cleaned and degreased, then bonded using Master Bond EP15ND-2 epoxy adhesive, with a bond line thickness between 50 and 127 μm. During assembly, the components were aligned and clamped using a specialized fixture to ensure uniform adhesive thickness and avoid misalignment or bending stress. The adhesive was then cured in a Thermo Scientific Lindberg/Blue M oven at 150–177 °C for 60–90 minutes, while still held in the alignment fixture. Tensile tests were performed on an Instron 8874 testing machine (25 kN capacity) at a constant displacement rate of 0.015 mm/s, in accordance with ASTM C633–13. For each Cu coating type, five replicate tests were conducted. After failure, the mode of fracture was examined, and the maximum load at rupture was recorded. Bonding strength was calculated by dividing this load by the cross-sectional area of the bonded circular surface.

3.4.5 Tensile test and Fractography

After deposition, the cold-sprayed components were separated from their substrates and machined into tensile specimens using Electrical Discharge Machining (EDM). The detailed specimen dimensions are shown in Figure 33a, with the final geometry illustrated in Figure 33b. All tensile specimens were oriented parallel (0°) to the gun traverse direction. Quasi-static tensile tests were conducted in accordance with ASTM E8/E8M-15a using an Instron 8874 servo-hydraulic testing machine, featuring a ±25 kN load capacity and 100 Nm torque capacity. Testing was performed under displacement control at a rate of 0.05 mm/min. For strain measurement, a GOM ARAMIS 3D Digital Image Correlation (DIC) system was employed, offering 5-megapixel resolution and a maximum frame rate of 15 fps. Between three and six specimens were tested for each condition, including both as-sprayed and heat-treated 3D-printed samples. Post-fracture, the fractured surfaces were examined using Scanning Electron Microscopy (SEM) to investigate failure modes and microstructural features.

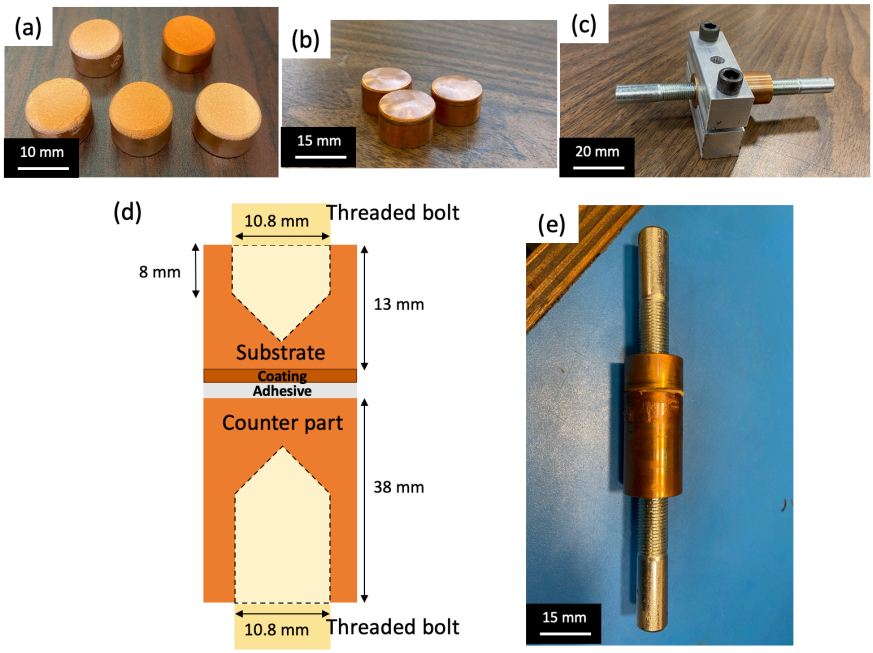


Figure 32: Photographs showing coupon samples in (a) as-sprayed and before grinding, (b) post-grinding to smooth the coating surface, (c) alignment fixture clamped the parts together, (d) schematic of coupon geometry with threaded hole, and (e) test setup.

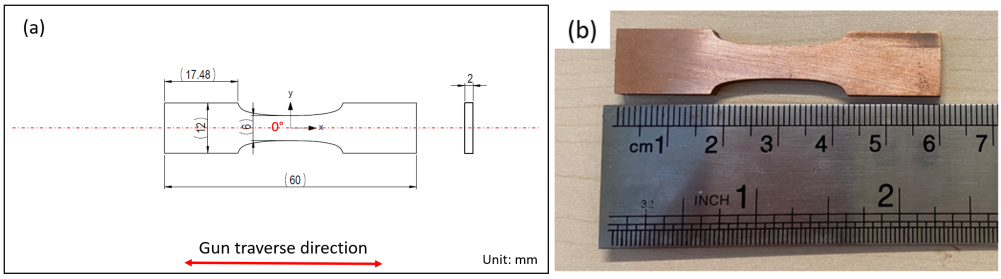


Figure 33: (a) dimensions of the tensile specimen; and (b) the extracted tensile specimen from the deposit.

3.4.6 Loading unloading reloading (LUR) experiment

To assess back-stress during tensile deformation, loading–unloading–reloading (LUR) tests were conducted. At predetermined true strain levels, specimens were unloaded under load-control mode at a rate of 200 N/min until the load dropped to 20 N. They were then reloaded to the same load level before proceeding to the next unloading strain. The specimens used in these tests had the same geometry as those used in the monotonic tensile experiments.

3.4.7 Hetero deformation induced (HDI) strength measurement

The back-stress (σ_b) [108], a long-range internal stress mainly due to the pile-up of geometrically necessary dislocations (GNDs), was quantified using a physics-based approach developed from the tensile unloading–reloading hysteresis loop. This method is particularly suitable for heterogeneous structures where strain incompatibility across regions leads to internal stress gradients. When a material is loaded in tension and partially unloaded before being reloaded again (forming a hysteresis loop), two key features emerge: The unloading yield stress (σ_u) marks the point where mobile dislocations begin to reverse direction and the reloading yield stress (σ_r) marks the point where forward dislocation motion resumes. These two yield points bracket the internal resistance and stored long-range stress within the material. The key assumption is that the back stress remains approximately constant during the unloading segment before plastic flow begins in the reverse direction. The schematic description of this test method measurement is shown in Figure 34. The unloading–reloading hysteresis loop consists of Segment AB: initial stress relaxation, Segment BC: linear elastic unloading (slope ≈ Eu). Point C, unloading yield stress (σ_u), Segment EF, linear elastic reloading (slope ≈ Er), Point F: reloading yield stress (σ_r). Assuming Eu = Er, the stress difference between these two points reflects internal back stress and frictional resistance (σ_f). The following equations are used for back stress and frictional stress measurement:

$$\boldsymbol{\sigma_b = (\sigma_r + \sigma_u)/2} \tag{3}$$

$$\boldsymbol{\sigma_f = (\sigma_r - \sigma_u)/2} \tag{4}$$

These are derived from the idea that during unloading and reloading:

$$\boldsymbol{\sigma_b = (\sigma_u + \sigma_f)} \tag{5}$$

$$\boldsymbol{\sigma_r = (\sigma_b + \sigma_f)} \tag{6}$$

These equations assume dislocation configuration is reversible and frictional resistance remains constant throughout the loop.

The inelastic behavior observed at the onset of unloading (Segment AB) is due to internal stress relaxation mechanisms that occur once the external load is reduced. Although macroscopically unloading may appear elastic, at the microscopic level, residual dislocation structures, internal back stresses, and frictional resistance between dislocation walls result in a nonlinear or delayed elastic response. This gives rise to a hysteresis loop between unloading and reloading paths, even when the slopes of the elastic regions (segments BC and EF) are nearly equal. The frictional resistance stress reflects the difference between the reloading and unloading yield points results from internal frictional resistance to reverse dislocation motion. It quantifies the irreversible energy loss and internal opposition to deformation, distinct from recoverable elastic effects. Physically, taking the half of the stress difference centers σ_f between the unloading and reloading points, assuming symmetric hysteresis behavior.

This method introduces a slope deviation criterion for identifying yield points on the unloading and reloading curves. The process begins by determining the linear elastic region of the curves, characterized by the effective Young's modulus (Eu). The yield points, unloading yield stress (σ_u) and reloading yield stress (σ_r), are then defined as the points where the local slope decreases by a fixed percentage (commonly 5%, 10%, or 15%) from Eu. To ensure consistency and reliability, the same slope deviation percentage should be applied when identifying both σ_u and σ_r. In practice, this involves performing a tensile test that includes at least one unloading–reloading cycle at a specific true strain. The stress–strain data surrounding the hysteresis loop is extracted, and the linear segments of the unloading and reloading curves are fitted to determine Eu. Using the predefined slope deviation criterion, the points where the slope reduces, indicating σ_u and σ_r, are identified. Once these yield stresses are determined, the back stress (σ_b) is calculated using the appropriate equations derived from the hysteresis loop analysis.

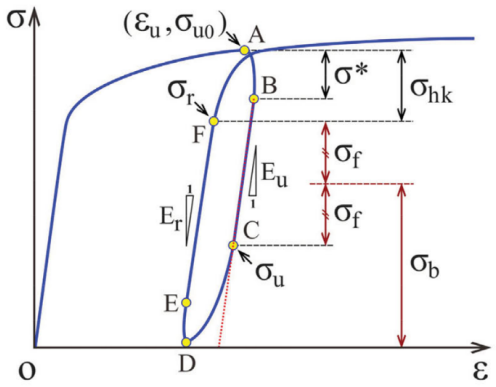


Figure 34: Schematic illustration of the unloading–reloading loop used to define the unloading yield stress (σ_u), reloading yield stress (σ_r), back stress (σ_b), and frictional stress (σ_f), along with the effective Young's moduli during unloading (E_u) and reloading (E_r) [109].

Chapter 4

A comparative study on the powder manufacturing effect on flowability and deformability of pure Cu powders for cold spray application

(Published manuscript, International Thermal Spray Conference, ITSC 2023, 560-566)

4.1 Abstract

The quality of feedstock powder is a critical factor in determining the properties of coatings deposited using cold spray (CS). However, most commercially available powders are not designed or optimized for CS applications, making it challenging to tailor powders to desired quality. In this research, we investigated and compared the cold-sprayability of five different Cu powders produced by electrolysis, gas atomization and mechanical grinding methods. We assessed the powders' microstructure, particle morphology and size distribution to understand the effect of manufacturing methods on Cu powder characteristics. We also studied the flowability of the powders using the shear cell method and evaluated their mechanical properties and deformability for CS using nano-indentation. Our results showed that gas-atomized powders with equiaxed grains exhibited promising flowability and deformability for CS applications, outperforming the other powders tested. Specifically, the spherical morphology of gas-atomized powders provided less surface area than the irregular-shaped electrolytic powder, reducing the interaction of surface forces and contributing to smooth powder flow. Additionally, the mechanically ground powder with ultra-fine grain sizes and gas atomized powder with small dendrites in the microstructure exhibited the higher nano-hardness values (HIT= 2.1±0.15 GPa and 1.6±0.1 GPa, respectively), while the porous electrolytic Cu powder had the lowest value (HIT= 0.7±0.2 GPa). In conclusion, we found that gas-atomized Cu powders with equiaxed grains may hold promise as the optimized feedstock for CS application, considering both effective metrics of flowability and deformability.

4.2 Introduction

Cold spray (CS) is a solid-state powder deposition technology that uses kinetic energy to adhere particles on substrates or upon one another in a layer-by-layer manner. In CS method, a process gas

(air, nitrogen, or helium) is preheated between room temperature (RT) and a high temperature depending on the CS system before propelling through a converging-diverging De-Laval type nozzle [10,28]. A fluidized powder feedstock, through a separate line, is fed into or upstream/downstream of the nozzle. The gas stream accelerates the powder particles to supersonic velocities before impacting the substrate. The particle temperature before impact remains well below the melting temperature of powders. The process has received increased popularity in industry in recent years because of its important differences from conventional thermal spray procedures [27,110]. The key differences between CS and thermal spray methods are that, contrary to thermal spray process, powder melting, grain growth, phase changes and oxidation do not exist in CS. CS has found many applications in repairing high-end components [8], coating for protection and/or activation of surfaces [111], and additive manufacturing [112].

The primary feedstock powder is an important parameter in CS processing which has a strong effect on the performance of deposited product. Currently, the metal powders are produced by electrolysis, mechanical, chemical, and atomization methods. Metal powders manufactured by each of these methods have different characteristics, including particle size distribution, morphology, chemistry, microstructure and oxide content. These properties play a crucial role in improving the flowability and deformability of powders and subsequently maximising the cold-sprayability for obtaining the best deposition properties [37,113].

Previous studies have shown the effect of various powders fabricated through different techniques on the resultant flowability [66,114,115]. Brika, et al. [115] preformed a comprehensive study on three gas and plasma atomized Ti-6Al-4V powders; they discovered that more spherical powders flow smoother due to the lower inter-particles mechanical interlocking and surface friction. In addition, powder containing the finer particles has higher inter particle friction and negatively affects the particle packing and density of printed parts. In other study, Zegzulka, et al. [61] reported poor flowability of elongated shape and sharp-edged Cu, Mn and bronze powder particles due to the mutual blocking of particles. In addition, extensive work characterizing the deformability of powder particles have been conducted previously [42,46]. Powder density is an important factor, which influences the plastic deformation behaviour. The presence of porosities changes the deformability of powder particles [116]. Furthermore, microstructure of particles, which is influenced by the manufacturing methods makes

differences in deformability and deposition behaviour. Recently, lots of studies on Al alloys have indicated that solute elements and grain sizes had significant impact on particles deposition behavior during CS [117,118].

Therefore, understanding the powders characteristics resulted from different production methods is a key to engineer the CS-deposited properties. Despite the increased popularity of research focusing on CS, comprehensive experimental study on feedstock characteristics and their relation to the coating quality are not available. In this regard, four types of Cu feedstock powders, produced through electrolysis and different gas atomization processes, are studied here through advanced characterization and particle analysing methods.

4.3 Experimental Methods

Five types of pure Cu powders labeled as A, B, C, D and E were investigated in this research. Table 5 lists the supplier, production method and Cu Wt.% of each powder, respectively.

Table 5: Supplier, production method and copper content (wt.%) of each powder

Powder type	**A**	**B**	**C**	**D**	**E**
Supplier	Centerline Ltd., Windsor, Canada	ECKART TLS GmbH., Bitterfeld, Germany	5N Plus Inc., Quebec, Canada	Solvus Global., Worcester, USA	Metal Powder Works, Pennsylvania, USA
Production method	Electrolysis	Gas atomization (contain microsatellite particles)	Gas atomization (Satellite free)	Gas atomization (satellite free)	Grinding
Cu (Wt. %)	>99.7	>99.9	>99.9	100	>99.5

The morphological and microstructural studies were conducted on 5 types of Cu powders. For morphological analysis, powders were put on the conductive carbon adhesive tapes and were studied via a scanning electron microscope (SEM, model: Zeiss Leo and UltraPlus FESEM). For microstructural analysis, powders particles were hot mounted, and were grinded using 240, 400 and

600-grit SiC papers, and polished by MD-Largo and MD-Mol 3 Micron. The first polishing was performed using a DiaPro Allegro/Largo 9 μm solution and the second one was preformed using DiaPro Mol R3 μm solution. After each polishing step, samples were cleaned in an ultrasonic ethanol bath. Etching was performed using nitric acid etchant and ferric chloride etchant. The microstructures were studied via SEM equipped with energy-dispersive X-ray spectroscopy (EDS).

The size distributions and sphericity of the powders were evaluated using a particle size and shape analyzer (Camsizer X2, RETSCH, Germany). A particle flow was produced by the Camsizer X2 and was characterized by a high-resolution optical system.

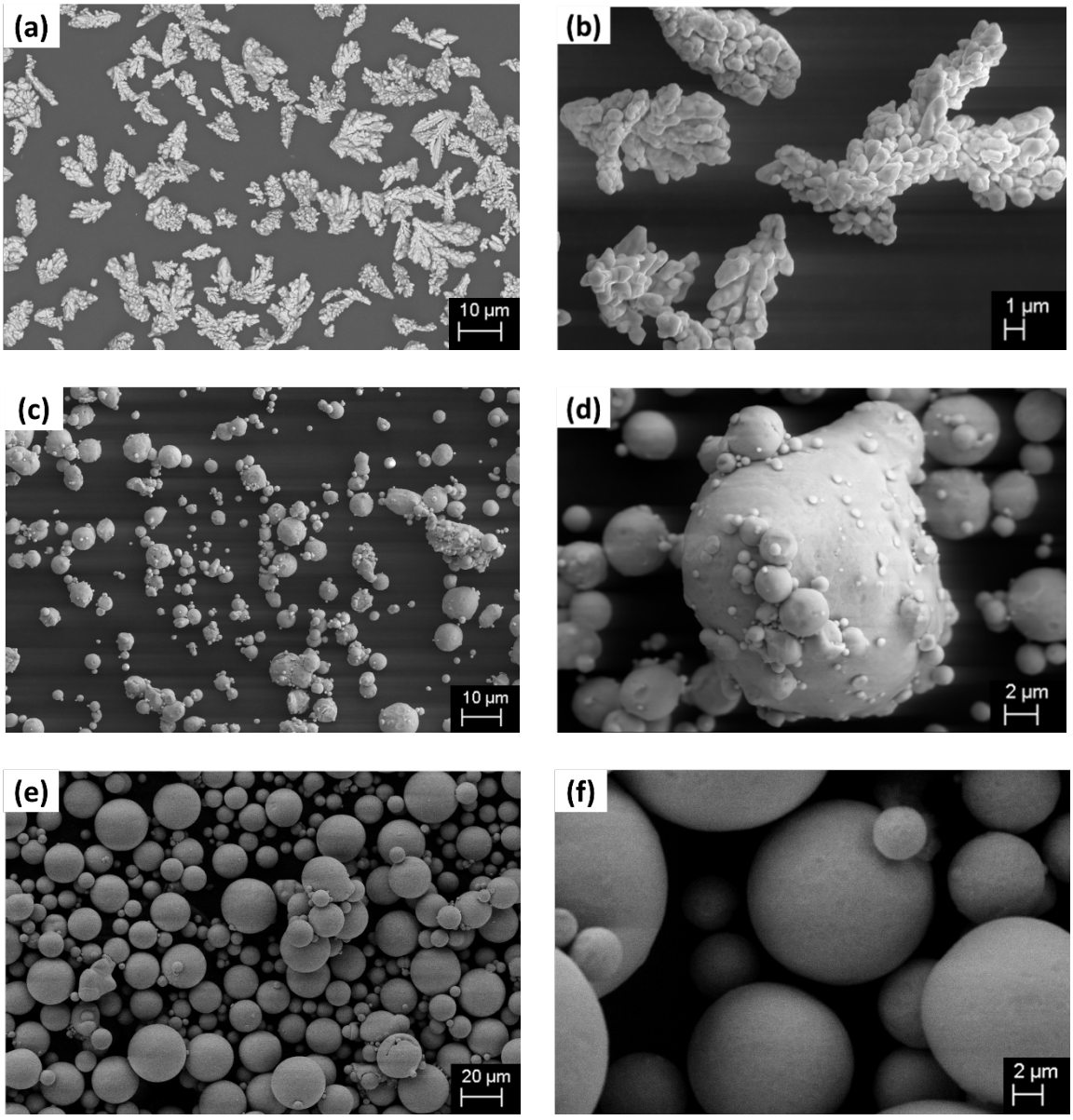
The flowability and shear properties of the powders were measured using a rotational shear cell supplied as a component of the FT4 Powder Rheometer (Freeman Technology Inc., Worcestershire, UK). Nano-hardness evaluation was performed on as-received Cu powders, which were mounted in resin, then ground and polished to obtain the flat surface of powders, using a nanoindenter (Anton Paar Nanoindenter NHT^3) with a diamond Berkovich tip. Nanoindentation was conducted on the cross sections of powders under load control at a maximum load of 25 mN for powder A and 50 mN for powders B, C and D with dwell time of 60 s. 20 nano-hardness measurements were made on different powder particles of various sizes for each Cu powder type. Load-displacement curves were used to calculate the nano-hardness as explained by Oliver and Pharr [102].

4.4 Results and discussion

4.4.1 Morphology and microstructure of pure Cu powders

Low and high magnification SEM micrographs of each powder type are shown in Figure 35, revealing the powder morphology. The shape of Cu powder particles is related to their production method. It can be seen from Figure 35a and b that powder A particles obtained from electrolysis method are sponge-like. These particles have a cauliflower-like structure. The structure of the powder particulates is dependent upon the electrolysis parameters such as concentration of electrolyte, current density, rotation speed of the cylindrical cathode and the electrolyte temperature [119]. The effects of these parameters were determined by the limiting current density phenomenon. Limiting current density is the minimum current density for the formation of powder [120]. At lower current densities, higher concentration of Cu ions, higher rotation speed of the cathode and higher electrolyte temperature, the

hydrodynamic conditions changes and the limiting diffusion current density increases [121,122]. In fact, at lower current densities the deposition time is lower than the induction time for dendritic growth and the cauliflower- like shape of the powder particles similar to one obtained in Figure 35a and b forms. The gas atomized powders particles, on the other hand, are characterized by a spherical morphology. Solidification of liquid droplets during atomization will lead to these morphologies (Figure 35c, d, e, f, g, and h). Figure 35c and d show that the particle size distribution of the gas atomized powder B is bimodal which consists of smaller and larger particles. During solidification, the smaller particles which are known as microsatellite particles (sizes < 5 μm) tend to agglomerate around larger ones to create irregular shapes of the powder agglomerates [123]. This satellite effect, generally seen among powders produced by gas-atomization, can be explained by the in-flight contact of small size partially solidified droplets with larger solidified particles [124]. Powder C is likely to be more spherical (Figure 35e and f), because, prior to the solidification, the droplets spend more time at high temperature than in the case of powders B and D shown in Figure 35c, d, g, and h. By inspection of Figure 35d, f, and h, the smooth surface texture of the powder particles is detected. The featureless surface of powder B and C (Figure 35d and f) shows that the powder particle experiences rapid solidification accompanying with high under-cooling [123]. This can be probable in a process like atomization since the atomizing gas is used at a low temperature (compared to the molten metal) and at high pressure which leads to a high cooling rate. In this way, nucleation appears on the surface of the atomized droplet, where undercooling is maximized. After the nucleation, the solid-liquid interface advances quickly, causing in a featureless surface [125]. Finally, a cellular structure on the powder surface of D (Figure 35h) represents as a recessed grooves showing fine and coarse cells. Figure 35i and j display the morphology of powder produced through mechanical grinding, a top-down fabrication method that reduces bulk materials into fine particles using mechanical force. This process involves repeated collisions that fragment the material while introducing significant work hardening and a high density of dislocations. The resulting particles exhibit irregular, angular, and flaky shapes, characteristics typical of fracture and shear-driven breakage. Additionally, the surfaces show striations and cracks, reflecting the intense plastic deformation and impact experienced during grinding [7,27].


(a)
10 µm
(b)
1 µm
(c)
10 µm
(d)
2 µm
(e)
20 µm
(f)
2 µm

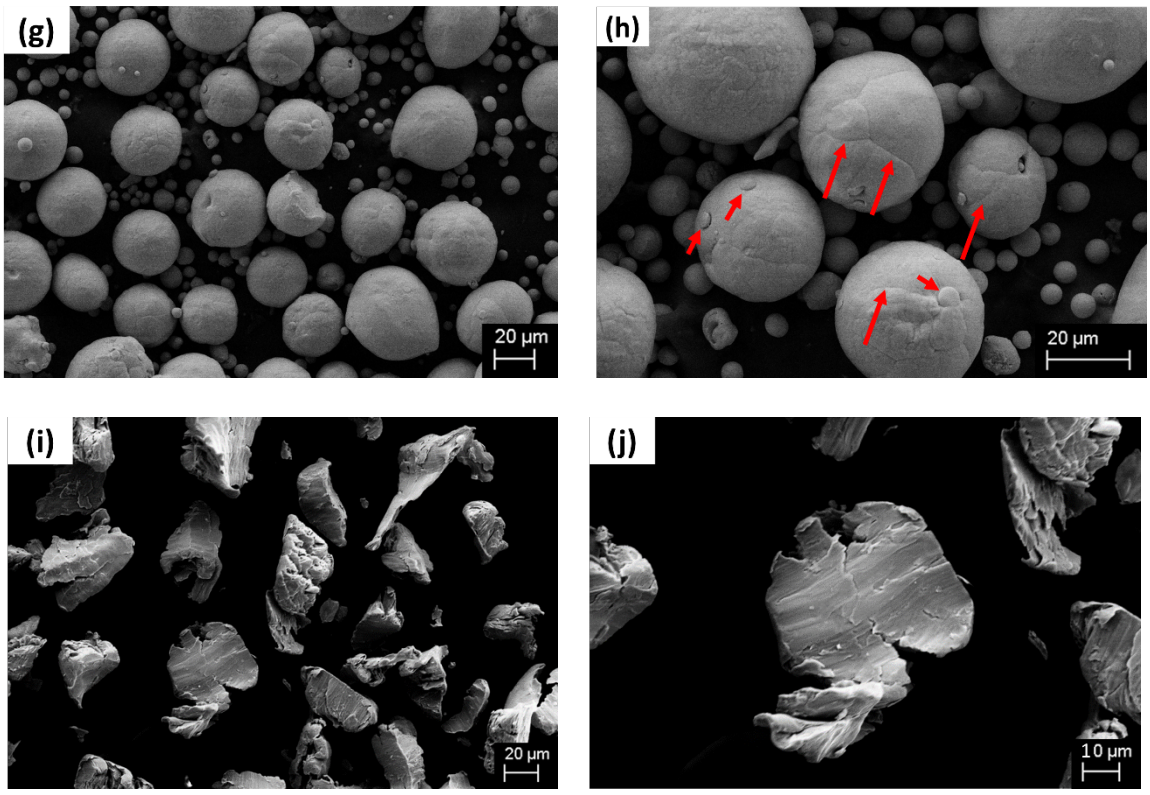


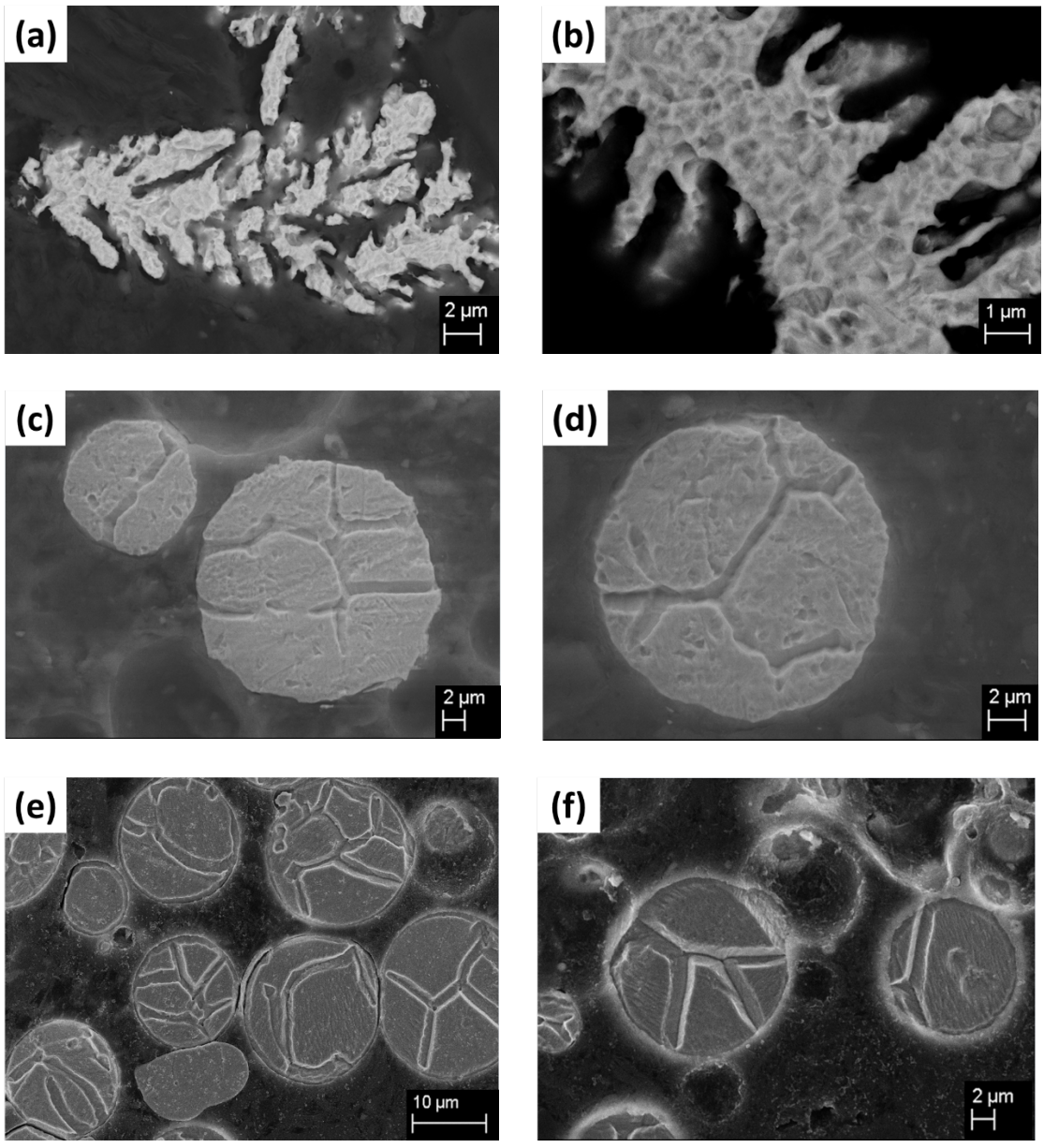
Figure 35: Low and high magnification SEM images depicting the morphology of the as-received pure Cu powders (a) and (b) A, (c) and (d) B, (e) and (f) C, (g) and (h) D and (i) and (j) E, respectively. Red arrows in (h) represents fine and coarse cells structures.

Figure 36 shows SEM cross-sectional micrographs of the as-received powders in etched condition. Powder A particles obtained from electrolysis process are characterized by a porous microstructure (Figure 36a and b). The gas atomized powder B and C particles shown in Figure 36c, d, e, and f, respectively, are characterized by equiaxed grains. The gas atomized powder D particles shown in Figure 36g and h exhibit dendritic cells besides elongated and fine equiaxed grains. The microstructure of gas atomized powders has been related to several causes, including rapid solidification and high cooling rate [124,126], pre-solidified microdroplets and dendrite fragments, and thermal equilibration and partial remelting of solid particles [124]. In fact, solidification structure of materials is extremely under the effect of the degree of undercooling at nucleation. Once nucleation happens in the undercooled melt, coarse dendrites from a nucleation center grow at high-speed. The fragmentation of

the first-formed dendrites is expected to arise at an early stage of temperature increasing during the latent heat release of solidification (referred to as recalescence) when the dendrites are thin and fragile. At the next stage, secondary and tertiary dendrite arms, which grow after the recalescence, become misoriented by extra increase of under cooling. This misorientation is under the effect of coarsening and remelting processes to form sub-grains [127]. In addition, it is possible that due to the solidification shrinkage, a stream of liquid in a direction opposite to the dendrite growth direction flows. When undercooling is sufficient, it can lead to the fracture of the growing side arms and rotate them to give randomly oriented fine grains. It is worth noting at higher undercooling the dendrite trunks cannot be remelted due to a zero-remelting effect, and thus can be preserved in the solidification microstructure, leading to the presence of the elongated grained structure. In addition, for rapid solidifications happening at a quite high undercooling, the advance of the solid/liquid interface occurs at high velocity. Therefore, a large volume contraction due to the rapid solidification will cause a high shrinkage stress developing in the system. The strain energy stored in the fragmented dendrite parts will drive recrystallization, leading to a grain refined recrystallization microstructure [127–129].

In the case of powders B and C, the equiaxed grains with rather straight grain boundaries in microstructures (see Figure 36c, d, e, and f) strongly suggest that the undercooling is larger than a critical value and the formation of the solidification microstructure is due to recrystallization. The dendrite cells of powder D shown in Figure 36g that originate at metal interface surround the elongated grain microstructure that is normally present in the central section of solidified materials. In addition, Figure 36h demonstrates the presence of elongated and equiaxed grains in the microstructure of powder D. The appearance of elongated grained structure is attributed to the vanished remelting effect in the post-recalescence period [128].

The microstructural analysis of ground powder (Figure 36i and j) indicate that the mechanically ground powder has experienced intense plastic deformation, leading to a highly strained and defect-rich structure. Although grain boundaries are not visible, the microstructure is likely ultrafine or nanocrystalline due to the severe fragmentation and strain introduced during grinding. This non-equilibrium state with high dislocation density and stored energy, suggests that post-grinding annealing may be beneficial to relieve internal stresses, stabilize the microstructure, and enhance the material's suitability for further processing.


(a)
2 µm
(b)
1 µm
(c)
2 µm
(d)
2 µm
(e)
10 µm
(f)
2 µm

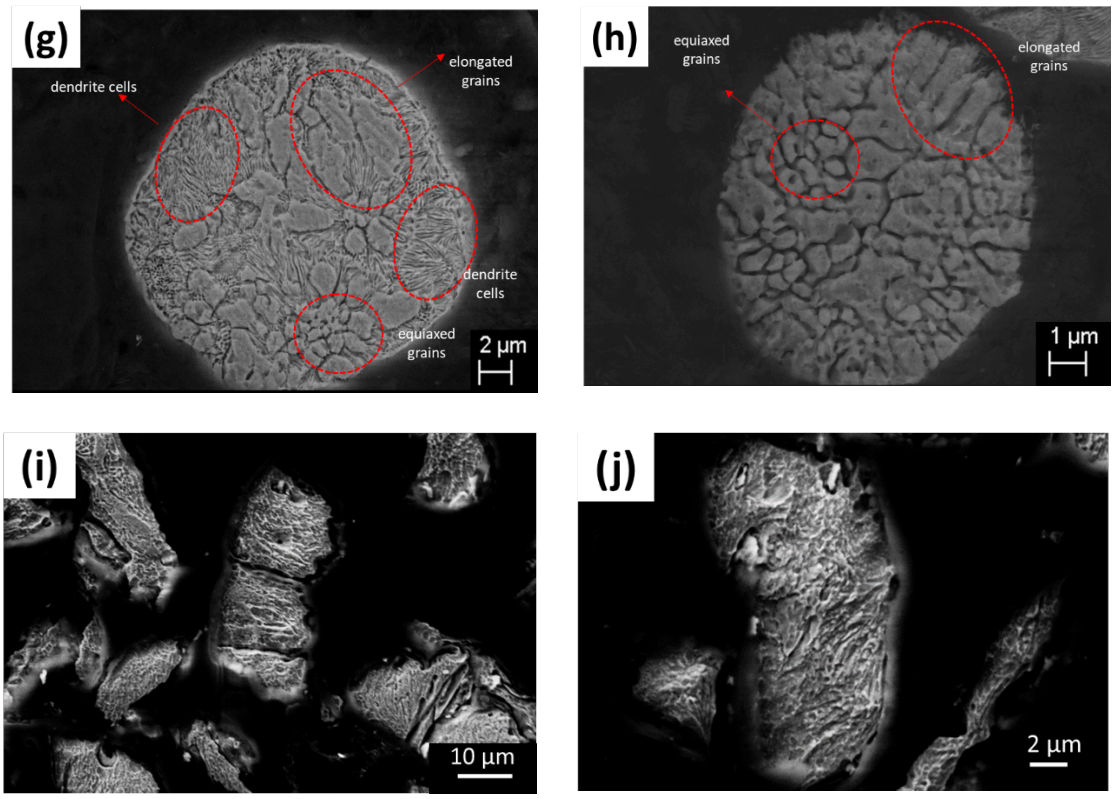


Figure 36: SEM cross-sectional micrographs of pure Cu powder particles of (a) and (b) A, (c) and (d) B, (e) and (f) C, (g) and (h) D, and (i) and (j) E in as-received condition.

4.4.2 Particle size distribution of pure Cu powders

The particle size distributions of the four types of Cu powder particles are shown in Figure 37. The values are shown in Table 6. According to the parameters given in Table 6 and Figure 37, powder D, with D_{90} equal to 138 µm, has the largest particle size. Other Cu powders reach a maximum of 64 µm for parameter D_{90}. The smallest particles are contained in powder B. Span shows the breadth of the particle size distribution. Highest span is also for powder B. A symmetrical particle size distribution is more obvious for powder A and powder C (Table 6 and Figure 37). For the powder obtained by the electrolysis process the limiting current density can affect the average particle size of powders [119]. In addition, the size distribution of the atomized droplets depends on the processing parameters, thermodynamic properties of material, and thermodynamic properties of the gas used [128]. It is well-established that as the pressure of the atomizing gas increases when all the other variables being kept

constant, the mass median diameter decreases [128,130]. This is ascribed to the effects of an increase in the mass flow rate, and an increase in kinetic energy of the gas. However, gas pressure has a complex influence on the atomization process and can increase the average powder particle size because of the length change of the supersonic core in the gas jets [130]. It is worth noting that the particle size distribution in mechanical grinding is influenced by factors such as the material's hardness and brittleness, grinding time and speed, and grinding media characteristics. Harder, more brittle materials tend to break into finer, more uniform particles, while ductile materials may lead to agglomeration. Longer grinding times and higher energy input generally reduce particle size but can also broaden the distribution. Other factors, like cryogenic conditions or inert atmospheres, can further affect fragmentation behavior and final powder particle sizes [7,27].

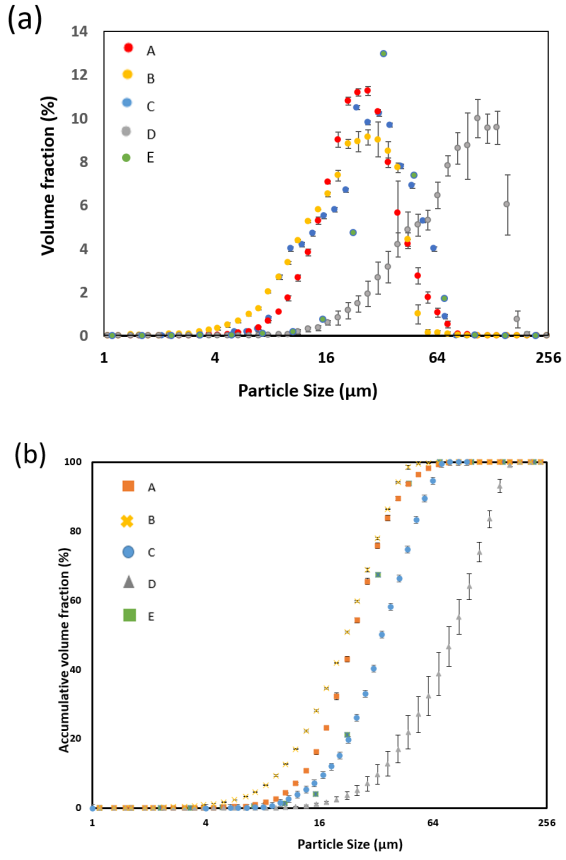


Figure 37: (a) volume fraction (%) and (b) accumulative volume fraction (%) of different pure Cu powders. Powder C data measured by Camsizer X2 has been obtained from the vender.

Table 6: Particle size of pure Cu powders particles

Powder type	Particle size [μm]			Span
	D_{10}	D_{50}	D_{90}	$(D_{90}-D_{10})/D_{50}$
A	13	24	42	1.19
B	10	22	39	1.31
C	17	34	58	1.18
D	33	81	138	1.29
E	28	42	64	0.85

4.4.3 Flowability of pure Cu powders

The rheological properties of five types of powders evaluated using FT4 powder rheometer are reported in Figure 38. The cohesion value (C) which is an indication of the internal forces that bond the particles together [115,131] is shown in Figure 38a. The cohesion value varied from 0.144 KPa to 0.403 KPa. The cohesive powder has high cohesion value. In this regard, powder A has good flowability, powder B, C and E have fair flowability and powder D has poor flowability. Angle of internal friction (ϕ) (Figure 38b) is a measure of internal friction between the powder particles under the consolidation conditions [64]. A total of three rank classifications [61,131] could be defined as 'good powder flowability' (ϕ <20°) – powder C, 'fair powder flowability' (20° < ϕ <30°) – powders B and D, and 'poor powder flowability' (ϕ > 30°) – powder A and E. Flow function (ffc) shown in Figure 38c is used as a quantitative classification of powder flowability. The relationship between ffc and powder flowability have been defined by Jenike and has been used in several researchers [61,64], a powder can be classified as 'free-flowing' (ffc > 10), 'easy-flowing' (4 < ffc <10), 'cohesive' (2 < ffc <4), 'very cohesive' (1 < ffc < 2) and 'not flow' (ffc < 1). In this work, three ranks are classified as 'free-flowing' -powder A, 'easy-flowing'- powders B, C and E and 'cohesive'- powder D. This conflict between the result of cohesion value and angle of internal friction ranking for powder A and E needs to be investigated. As can be seen according to the cohesion value (C) and ffc, powder D belong to the cohesive group, i.e., to a breadth that is having a flowability that is worse than the four other Cu powders. This could be attributed to the microstructure and mechanical properties of powder D that

will be investigated by nano-indentation. In fact, cohesion is the failure shear stress at zero normal stress for an unconfined powder, obtained by extrapolation of the powder yield locus [64]. In this regard, increasing the strength of powder particles can lead to the resistance to initiation of flow. The ranking of flowability obtained using the angle of internal friction (ϕ) correlates with the results of the sphericity assessment shown in Figure 39. It can be seen that powder A and E (Figure 39a and e), produced from electrolysis and grinding processes contain the smaller number of spherical particles and they have more irregular-shaped particles. In this regard, more spherical powders (powder B, C, and D produced from the gas atomization methods), flow easier due to a lower surface friction [115]. The lowest angle of internal friction (Figure 38c) obtained for powder C, pointing to a superior flowability of more spherical powders. According to the three measured parameters of C, ffc and ϕ (Figure 38), powders B and C shows better flowability properties due to their particle size distribution and morphology.

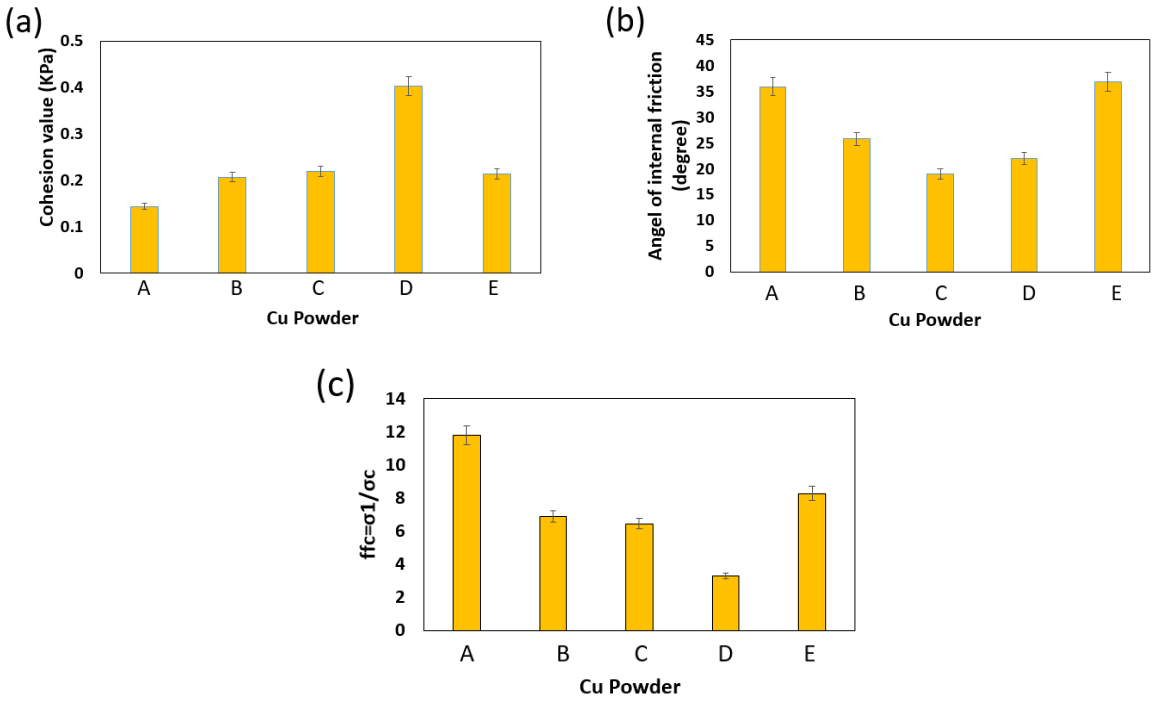


Figure 38: Rheological properties of as-received powders obtained from shear cell test showing (a) cohesion value, (b) flow function (ffc) and (c) angle of internal friction.

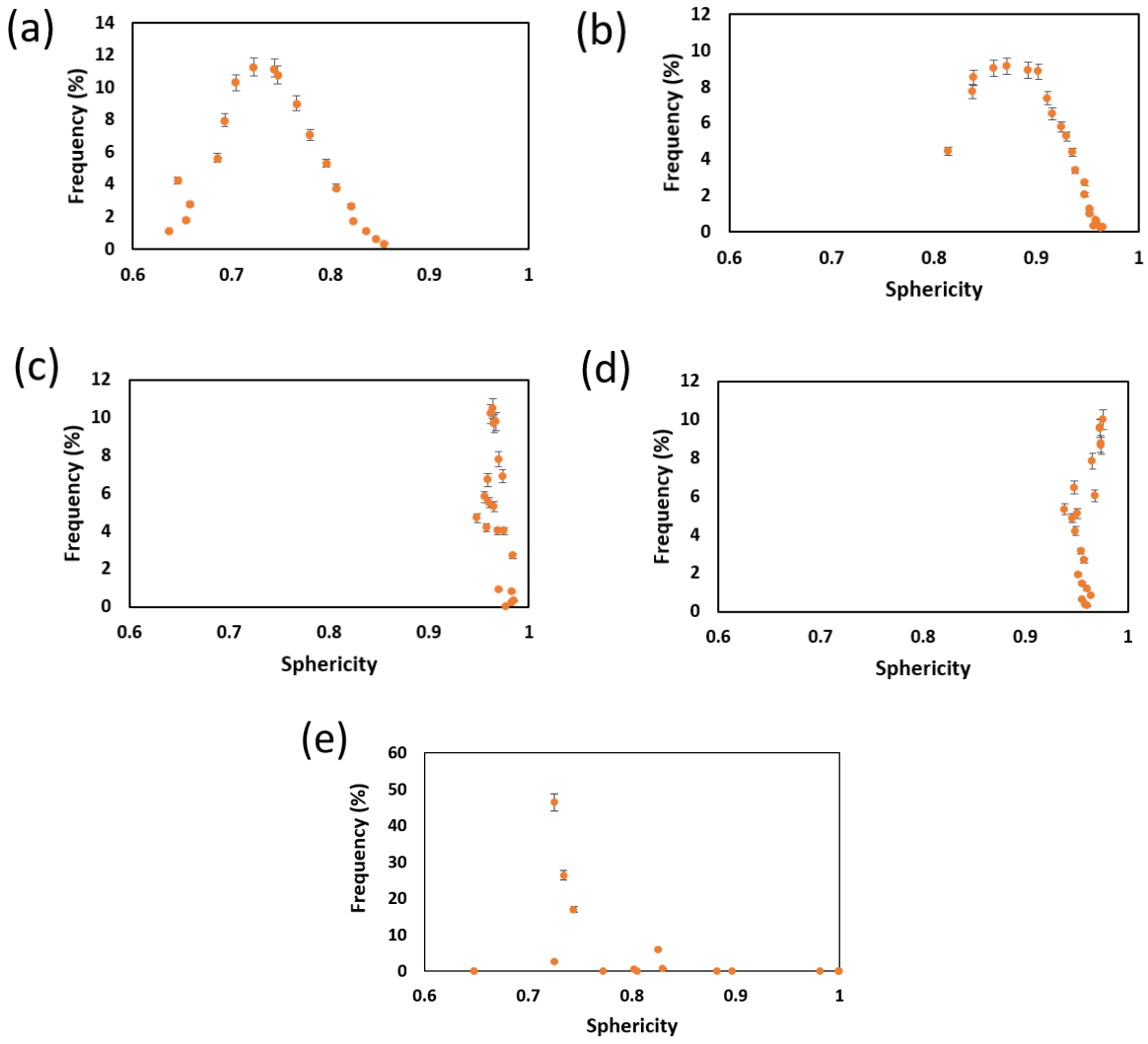
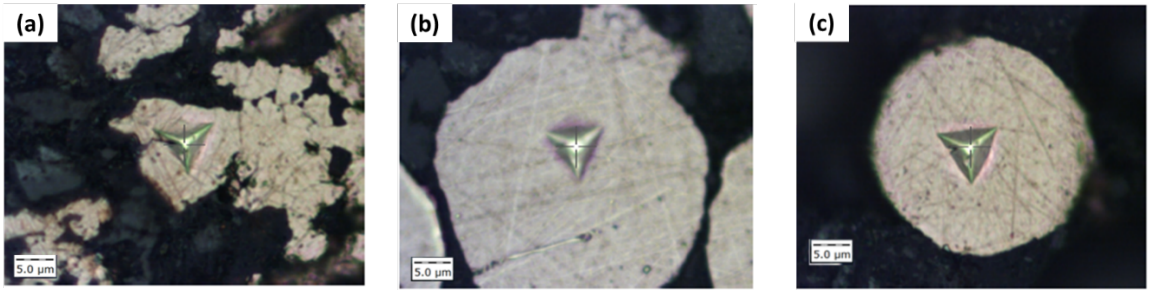


Figure 39: Particle sphericity distributions of pure Cu powders of (a) A, (b) B, (c) C, (d) D, and (E).

4.4.4 Nano-indentation analysis of pure Cu powders

The representative optical images of different Cu powder particles after nano indentations are shown in Figure 40. The typical nano-indentation load-displacement (P-d) curves obtained from different powders in Figure 41a indicates that the Cu powders follow an elastic-plastic behavior. It is observed that indenter displacement vs. indenter load was in the order of powder E < powder D < powder B < powder C < powder A. Smaller depths of penetration in powder D and E compared to the other powders,

representing its higher hardness. The unusual shape of the unloading curve for powder A in Fig. 41 is likely due to the irregular morphology and porous microstructure of the particles. These characteristics can cause the indentation to partially occur on the mounting resin rather than entirely within the powder particle, particularly if the particle is loosely bonded or has voids beneath the surface. Although nearly 20 measurements were conducted to ensure reproducibility, all consistently exhibited a similar unloading behavior for powder A, distinguishing it from the other powders. Despite this deviation, the data was retained in the analysis as it accurately reflects the mechanical response of powder A under the given test conditions and highlights the influence of its inherent structural characteristics. The hardness (HIT) and elastic modulus (EIT) values of the indentation test were determined from the P–d curve according to the Oliver–Pharr (O-P) method [102] and the results are shown in Figure 41b. As seen in Figure 41b, powder D and E obtained elastic modulus and nano- hardness values of 69.6±8.1 GPa and 62±15, and 1.6±0.1 GPa and 2.1±0.15 GPa, respectively. These values are higher than those of powder A (EIT= 31.6±5.9 GPa, HIT= 0.7±0.2 GPa), powder B (EIT= 55.7±8 GPa, HIT= 1.3±0.2 GPa) and powder C (EIT= 54.9±7.1 GPa, HIT= 1.1±0.1 GPa). The difference in nano-hardness and elastic modulus observed between these powders is associated with the manufacturing technology and microstructure of powders that subsequently influences their plastic deformation behavior. Higher elastic modulus and hardness of ground powder E and gas atomized powder D could be attributed to the smaller grain size of microstructure (Figure 36g, h, I and j) which well follows the Hall-Petch relation [132]. Besides, for powder A prepared by electrolysis process, the obtained values are far lower than those of gas atomized and ground powders, which could be attributed to the porous powder microstructure producing better compressibility during CS.



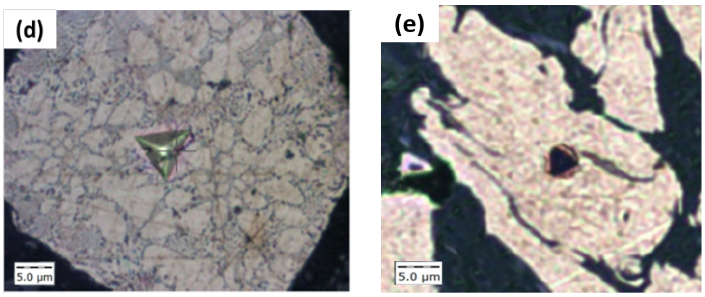


Figure 40: Nano-indentation impressions on the investigated pure Cu powders: (a) A, (b) B, (c) C, (d) D, and (E).

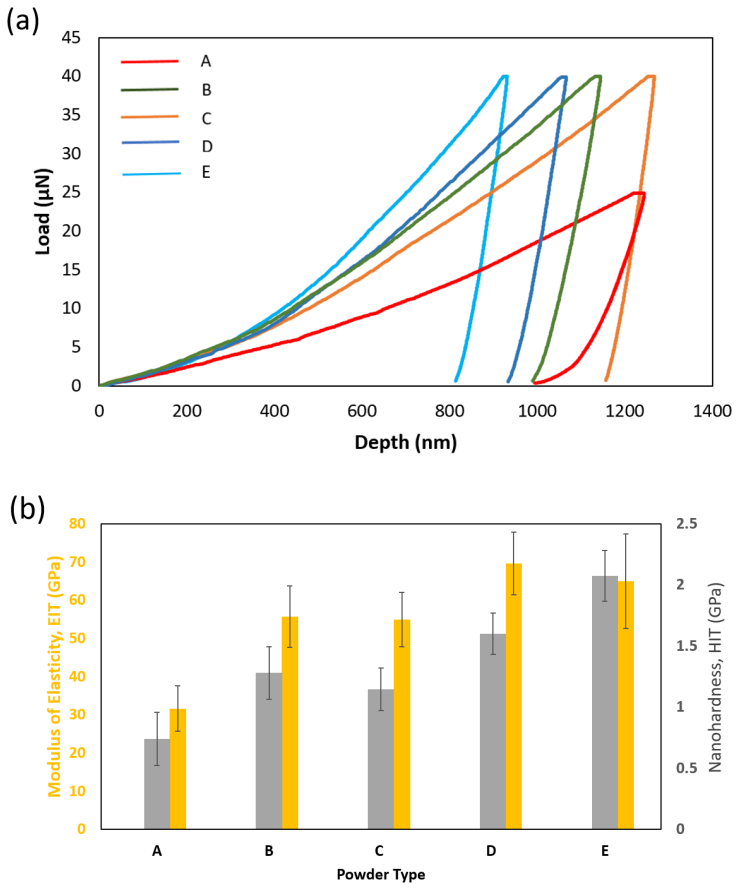


Figure 41: (a) Load- displacement curves, and (b) nano-hardness and elastic modulus of pure Cu powders obtained from nano-indentation

4.5 Conclusion

This paper evaluates five Cu feedstock powders characteristics produced by electrolysis, different gas-atomization and mechanical grinding processes in terms of cold-sprayability. A detailed examination was preformed to understand the effect of manufacturing methods on flowability and deformability of Cu powders. Electrolytic and mechanically ground powders exhibited irregular particle shapes, whereas gas-atomized powders displayed a predominantly spherical morphology. Electrolytic powder was characterized by a porous microstructure, whereas gas atomized powders with high and low undercooling comprised a dense equiaxed grains and dendrite cells in the microstructure, respectively. The ground powder also exhibited an ultrafine-grained microstructure. Gas-atomized powder containing micro-satellite particles showed the smallest particle size among the five feedstock powders. Based on the flow parameters calculated from the measurements of shear cell method, the spherical gas atomized powders can lead to a better flowability as the surface area of the particles decreases, the surface area for the interaction of surface forces decreases, leading to a smoother flow. The results indicated that the minimum values of hardness were obtained for the porous electrolytic Cu powder, which is more conducive to produce better deformability, followed by gas-atomized ones with equiaxed grains. Ground powder with ultrafine grains and gas-atomized powder with small dendrites in the microstructure exhibited the highest nano-hardness. As a result, considering both metrics of flowability and plastic deformation, the better cold sprayability may be obtained using gas atomized Cu powder with equiaxed grains in the microstructure.

It is worth noting that a comparative study regarding Cu feedstock powders fabricated using different methods on the microstructure and mechanical properties of coatings produced through low-pressure cold spray process has been conducted and will appear in our future paper.

Chapter 5

Comparative Analysis of Microstructural and Mechanical Attributes in Low-Pressure Cold-Spray Coatings: Impact of Varied Cu Feedstock Powders

(Published manuscript, Journal of Thermal Spray Technology 33 (2), 629-651, 2024)

5.1 Abstract

In this study, the role of feedstock powder in influencing the characteristics of cold spray deposition is explored. Four distinct types of Cu feedstock powders, derived through electrolysis and employing varied gas atomization methods, are applied to a Cu substrate via low-pressure cold spray coating. We investigated the impact of feedstock powder on the resultant coatings' microstructure and mechanical properties. A comprehensive statistical model is developed, considering the cold spray parameters, weight change, coating thickness, and discerning their significance and interactions. Optimal conditions for process gas temperature and pressure are identified at approximately 400 °C and 1.99 MPa, respectively, consistent across all Cu powders. Velocity analysis reveals particle velocities ranging from 373 m/s to 564 m/s under these optimal conditions. Coatings deposited using satellite-free gas atomized powder, characterized by enhanced sphericity, exhibit superior characteristics, including minimal porosity (0.66 ± 0.35%), high flattening ratio (3.57 ± 1.51), elevated microhardness (107±3 HV) and high bonding strength (20.7±2.3 MPa). In contrast, coatings deposited with gas atomized powder featuring microsatellite particles and electrolytic powder with irregular shapes display distinct properties. The observed trends are attributed to lower oxygen content and reduced oxide levels near the surface of the more spherical, satellite-free powder. This powder also demonstrates heightened plastic deformation during deposition. The increased peening effect of satellite-free gas-atomized powder during cold spray results in elevated dynamic recrystallization near the substrate surface, leading to smaller grains at the interface. Microstructural evolution analysis, utilizing electron backscatter diffraction, further elucidates the heterogeneous deformation and grain refinement occurring in Cu splats during cold spray coating.

5.2 Introduction

Cold spray (CS) is a powder deposition technology that operates at the solid-state level, using kinetic energy to adhere particles on a substrate and together in a layer-by-layer process. CS is a method of deposition/consolidation, where a process gas - air, nitrogen, or helium - is generally pre-heated between room temperature and a higher temperature based on the specifics of the CS system, before being pushed through a De-Laval type nozzle [10,27,28] . The powder material is introduced into this gas stream via a separate line, either at or prior to the nozzle. The gas flow then propels the powder particles at supersonic velocities towards the substrate. The velocity of impact depends on the spray parameters and the selected process gas. Various factors like the nozzle's design, gas temperature, and heat capacity of particles influence the pre-impact temperature of the particles, which is kept significantly lower than their melting point. CS has become increasingly popular in industry due to its unique characteristics compared to traditional thermal spray methods [27,110]. The main distinctions are that powder melting, grain growth, phase changes, and oxidation do not occur in CS. The technique has been employed in a variety of applications such as repairing of high-end parts [8], surface coatings for protection or activation [133] , and 3D printing [112].

The feedstock powder is an important parameter in CS processing. The excellent performance of the deposited product strongly depend on the optimized characteristics of the feedstock. However, cold spray users have typically relied on using powder feedstocks that were originally designed or optimized for other processes such as conventional powder metallurgy or thermal spray techniques. Using non-optimized powders for cold spray can result in limitations on the range of materials that can be successfully sprayed, hinder the attainment of optimal deposit properties, and lead to issues such as low deposition efficiencies, powder losses, and increased processing costs. To expedite the commercialization and industrialization of cold spray technology, it is essential to develop powder feedstocks specifically tailored for this process. The characteristics of powder feedstocks must be carefully manipulated to optimize cold sprayability, deposit properties, and manufacturing reproducibility while also keeping costs under control [45]. At present, spherical powders generated through gas or plasma atomization, alongside irregular powders produced using electrolysis, are readily accessible for cold spray applications.

Previous studies have shown that feedstock powder characteristics that might affect the CS-deposited properties and the final performance of product are microstructure (equiaxed grains and dendritic cells, grain size, plastic strain boundary types and texture), morphology, porosity, particle size distribution, flowability and hardness [37,123,134,135]. Tang, et al. [116] explored the impact of three types of Ta feedstock powders produced by hydrogenation de-hydrogenation and mechanical pulverization methods when cold sprayed onto a Ti6Al4V substrate, particularly how they affected the resulting coating's microstructure and mechanical traits. The study determined that the morphology of the powder, especially the porous characteristics of Ta powder, contributed to excellent compressibility and compaction behavior during deposition, leading to a high-quality coating with minimal porosity, superior deposition efficiency, increased micro-hardness, and robust adhesion strength. Munagala, et al. [67] reported coatings deposited with spherical Ti6Al4V powders demonstrated a significant decrease in hardness due to particle de-bonding and considerable porosity. Poor inter-splat bonding were evident from residual indents, as adjacent particles seemed to slide over these indents, further contributing to the substantial hardness loss. In this regard, the CS deposition behaviour of various feedstock powders are not similar to each other, therefore for obtaining a coating with excellent final performance, the understanding of these differences is important. It has been indicated that the main factor in deposition behaviour of powders is macrostructure/microstructure evolution of the feedstock powder and its mechanical or metallurgical bonding characteristics on the substrate [136,137].

A comparison of different research on cold-sprayed Cu coatings, as shown in Table 7, reveals that despite the increased popularity of research focusing on the CS processing it lacks an established link between feedstock powder characteristics and final properties. In most cases, there is no profound study that could relate a specific characteristic of powder based on their manufacturing process to a selected property of CS-deposited product. Also, compared to the other CS processing parameters, there are still not enough experimental results that guide researchers and manufacturers in selecting proper feedstock powders and finding the optimum combination of powder properties.

This study investigates the low pressure cold spray (LPCS) coating of four types of Cu feedstock powders, as one of the most favorable elements in CS, produced through different gas atomization and electrolysis processes. Analysis of the feedstock powder evolution with respect to morphology, particle size distribution, grain structure and the work-hardening ability is preformed. CS coatings are designed

via a statistical model to obtain the optimum coating conditions based on the CS processing parameters. A complete physical, microstructural and mechanical characterization of these coated samples will be done. Finally, a link between feedstock powder characteristics and final product will be established. This provides important information on the role of feedstock powders on the CS coating quality and bonding features. The goal is to identify a copper powder that demonstrates efficiency and suitability for low-pressure cold spray applications. This entails the search for a copper powder that meets the specific requirements and performance criteria of LPCS.

Table 7: Summary of the detailed processing parameters and the measured/calculated resultant properties of the deposits fabricated via different Cu feedstock powders

Cu powder		**Processing Parameters**			**Particle velocity, (m/s)**	**Porosity (%)**	**Mechanical properties**		**Refs.**
Morphology	**Particle size distribution (µm)**	**Pressure, P, (MPa), Temperature, T, (°C)**	**Working Gas**	**Substrate**			**Hardness (HV)**	**Adhesion strength (MPa)**	
Spherical	D50: 24.8	P= 5 T= 800	N_2	Al 6061	-	-	-	77.4	[138]
Dendritic	D50: 64.6	P= 5 T= 800	N_2	Al 6061	-	-	-	39.45	[138]
Dendritic	D50: 30	P= 5 T= 600	N_2	Al 6061	~1000	< 0.3	154 ± 5	-	[139]
Spherical	D50: 11	P= 5 T= 600	N_2	Al 6061	~1000	< 0.3	156 ± 1	-	[139]
Spherical	D50: 40	P= 5 T= 600	N_2	Al 6061	~1000	< 0.3	136 ± 5	-	[139]
Spherical	D50: 33	P= 5 T= 800	N_2	carbon steel	699	-	-	>72	[140]

Spherical	D50: 39	P= 5 T= 800	N_2	carbon steel	675	-	-	>73	[140]
Spherical	D50: 39	P= 5 T= 800	He	carbon steel	1110	-	-	-	[140]
Spherical	D50: 55	P= 5 T= 800	N_2	carbon steel	675	-	-	47 ± 9	[140]
Spherical	D50: 66	P= 5 T= 800	N_2	carbon steel	n/a	-	-	26 ± 5	[140]
Dendritic	<63	P= 0.6 T= 540	air	Fe52 steel	-	corrosion spots (%): ~95	83	~8	[141]
Spherical	-25 + 5	P= 0.6 T= 540	air	Fe52 steel	-	corrosion spots (%): ~40	106	~13	[141]
Spherical	-25 + 5	P= 3 T= 400	N_2	Fe52 steel	570-585	-	145 ± 3.4	36 ± 4.8	[135]
Spherical	-25 + 5	P= 0.6 T= 540	air	Fe52 steel	350	-	106 ± 6.0	13 ± 2.5	[135]
Spherical	D50: 28	P= 3.2 T= 400 ± 20		1100Al	-	1.1	163	-	[142]
Dendritic	D50: 23	P= 3.2 T= 400 ± 20		1100Al	-	1.9	101	-	[142]
Spherical	-25+5	P= 3 T= 305	N_2	Cu	600	-	150	38	[143]
Spherical	-25+5	P= 2.5 T= 305	He	low carbon steel	900	-	150	55	[143]

Dendritic	-45+10	P= 1.4 T= 300	air	Al	455	0.78	100	-	[144]
Dendritic	-45+10	P= 1.8 T= 300	air	Al	481	0.5	105	-	[144]
Dendritic	-45+10	P= 2.2 T= 300	air	Al	501	0.35	118	-	[144]
Spherical	-20+10	P= 3 T= 520	N_2	Al	-	-	160	58	[145]
Spherical	-30+10	P= 3 T= 520	N_2	Al	-	-	130	30	[145]

5.3 Materials and Methods

5.3.1 Feedstock powders characterization and cold spray process

Four types of pure Cu powders labeled as A (Electrolytic, Centerline Ltd., Canada), B (Gas atomized, ECKART TLS GmbH., Germany), C (Gas atomized, 5N Plus Inc., Canada) and D (Gas atomized, Solvus Global., USA) as shown in Figure 42 were the materials deposited in the experiments. For morphological analysis, powders were put on the conductive carbon adhesive tapes and were studied via a scanning electron microscope (SEM, model: Zeiss Leo UltraPlus FESEM). X-ray Photoelectron Spectroscopy (XPS) was employed for the assessment of the copper powder's surface chemistry. The free powder was examined in a ThermoFisher Scientific K-alpha spectrometer, which utilized a monochromated Al Ka x-ray source. The x-ray beam had a size of 400 μm, and charge compensation was applied during the analysis. Two spectra were analyzed for each type of powder, and the results were found to be in agreement with each other. To ensure accuracy, all spectra underwent charge correction to align the adventitious C 1s spectral component to a binding energy of 284.8 eV. Furthermore, a standard Shirley background was employed during the analysis.

A commercial Supersonic Spray Technologies (SST) Series P Cold Spray System, manufactured by Centerline, Windsor, Canada, was used to coat the as-received Cu powders. In this process, pure Cu

powders were accelerated through a converging–diverging de Laval UltiLife TM nozzle to supersonic velocities in a low-pressure system. Table 8 lists the specification of cold spray machine used in this study. Several 8 cm × 20 cm rectangular specimens of 3.16-mm-thick Cu sheets were used as the substrate samples for coating. Prior to cold spray deposition, the substrates were cleaned with alcohol. The optimum processing parameters including process gas temperature and pressure, step over, nozzle speed and standoff distance for each Cu powder were determined using Design of Experiment (DOE) method, which will be discussed later. Based on the full factorial design, 9 trials were planned for cold spray coating of each Cu powder. To obtain the accurate results, each trial repeated for 3 times. The cold sprayed coatings per each powder for different trials in 15 mm x 36 mm are shown in Figure 43.

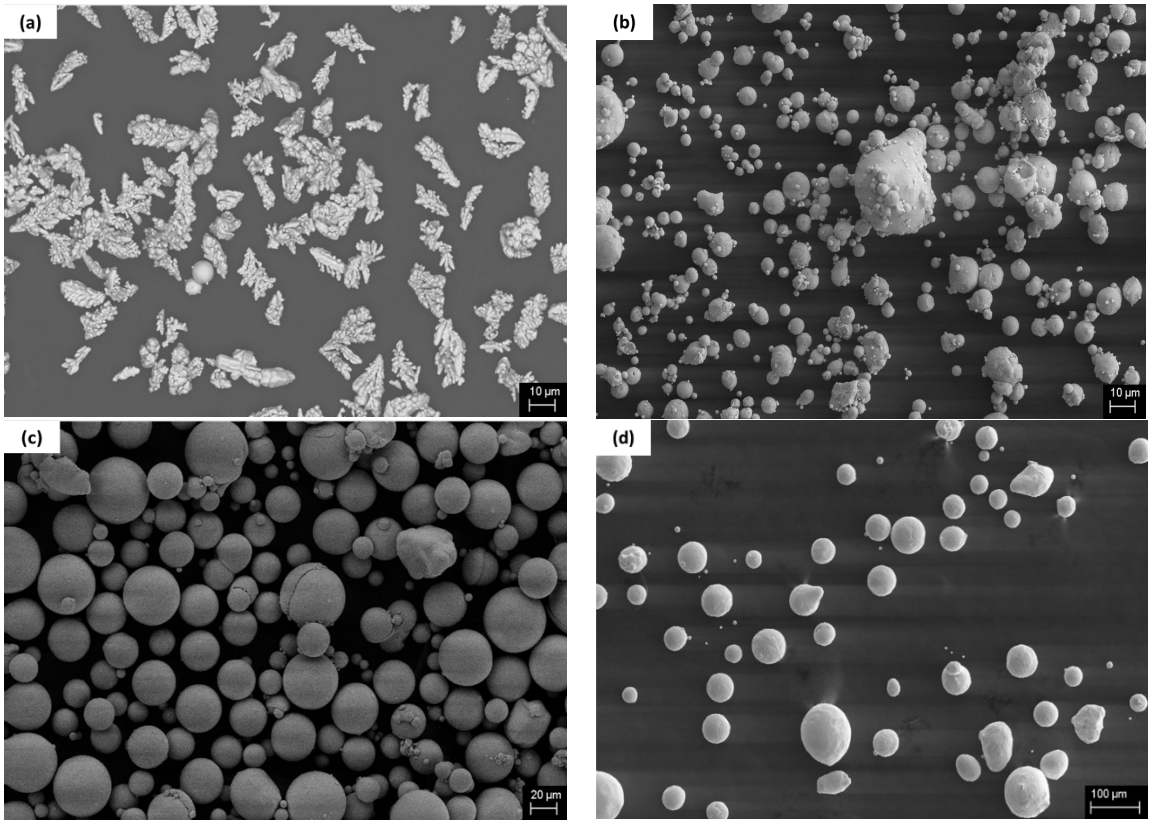


Figure 42: Scanning electron microscopy (SEM) morphologies of copper powders prepared through (a) electrolysis, (b), (c) and (d) gas atomization.

Table 8: Specification of SST cold spray system

Process Gas	Nozzle type	Nozzle Length	Nozzle Orifice Diameter	Nozzle Exit Diameter
N_2	De Laval UltiLife™	120mm	2 mm	6.3 mm

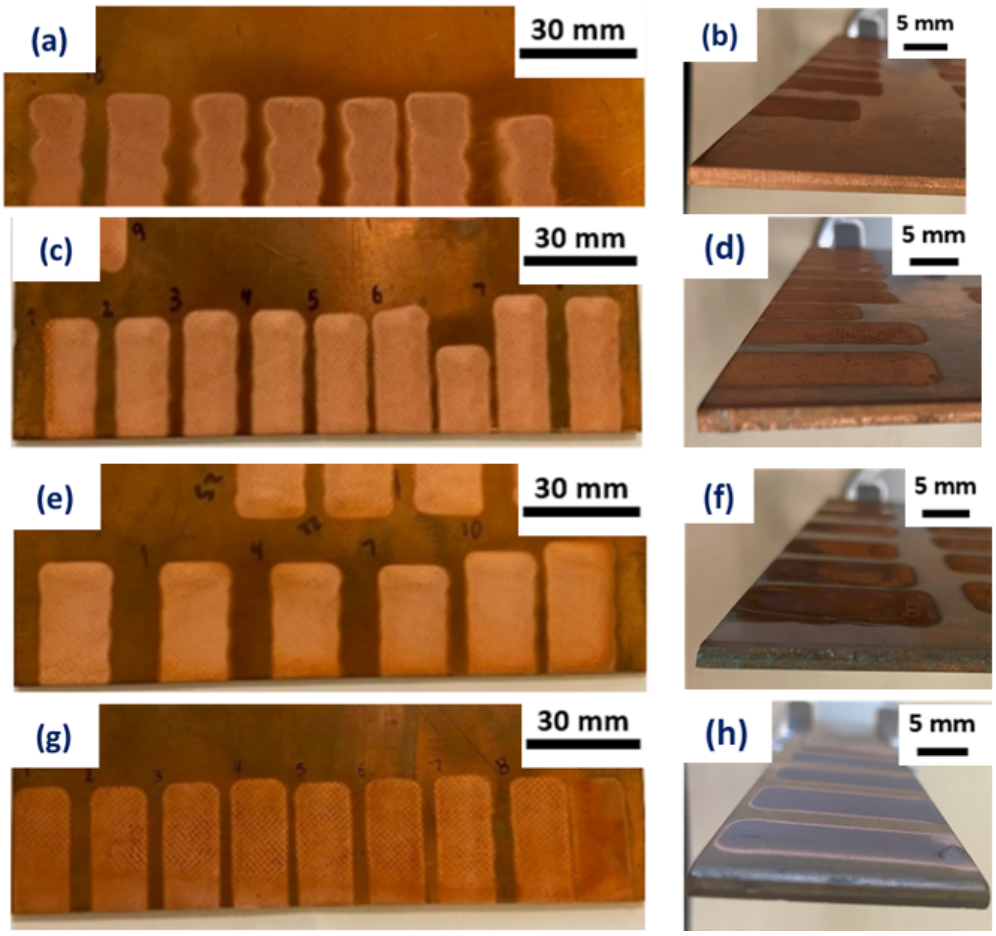


Figure 43: Top and side view of the cold sprayed coatings obtained from powders (a) and (b) A, (c) and (d) B, (e) and (f) C and (g) and (h) D. Numbers on the plates refer to different trials and their repetitions. Thickness of substrates is 3.16 mm and thickness of coatings are micron scale.

5.3.2 Characterization of cold spray depositions

Cold sprayed depositions were characterized using the physical, microstructural and mechanical analysis. A digital caliper with 0.01 mm precision was used to calculate the thickness of the deposited coatings. An average of at least 20 measurements at different positions of cross section throughout the whole length of coatings was taken to determine the thickness. The weight of the coatings was calculated using a digital weight scale with precision of 0.0001 g by taking the differences between the weight of the sample before and after coating deposition. Coatings were cut perpendicular to the gun traverse direction, hot mounted, polished and etched using nitric acid etchant (50 ml nitric acid + 50 ml distilled water). These samples were observed under a digital microscope (VHX-7000, Keyence). As sprayed coatings were also vibratory polished for 6 hours using 50-nm colloidal silica to remove the deformed surface layer for electron backscatter diffraction (EBSD) characterization. The accelerating voltage was 25 kV, and the step size was 500 nm. The flattening ratio of the splat was obtained by image analysis software (ImageJ). The center of oval splats were defined as the intersection of its minor and major axis, and the flattening ratio was calculated based on the ratio of major axis to the minor axis of the oval splat [103]. At least 200 splats from 10 micrographs of each sample were measured. To improve the accuracy of the average flattening ratio, small splats less than 10 μm in diameter and those located at the edge of the micrographs were excluded. Porosity was investigated according to the ASTM E2109 standard with the use of micrographs at lower magnifications of X2000 and higher magnifications of X8000 [104]. A total of 25 SEM images were recorded across the cross section of each coating. This measurement were performed using binary segmentation method by image processing software (ImageJ). The average grain size of the substrates near the surface was determined using the ASTM E112 standard test method of lineal intercept procedure [105]. For all deposits, Vickers microhardness was obtained using the Manual Vickers Hardness Tester (Wilson) by preforming 5-8 indents at each position across the longitudinal direction for a dwell time of 10 s under a load of 10 g as described in ASTM E384 [106]. The adhesion strength of cold spray coatings was evaluated through a tensile pull-off test, according to the ASTM C633 standards [107]. The test utilized copper coupon samples, shaped like short cylinders and Cu coating deposited on the top circular face. The coupons and counterpart pieces both had a radius of 12 mm. The coating surfaces were ground to produce a smoother surface and post-processed coatings were ~380 μm thick. the mating surfaces were cleaned and degreased. They were then bonded using Master Bond EP15ND-2 adhesive, with a bond line

thickness ranging from 50 to 127 μm. The setup in the Instron machine involved aligning and securing the coupon samples and counterparts, followed by adhesive application and grip adjustment for bond line thickness. An alignment fixture clamped the parts together to maintain even adhesive thickness and prevent eccentric loading or bending stress during the test. The adhesive was cured in a Thermo Scientific Lindberg/Blue M oven at 150–177 °C for 60 to 90 minutes, using the alignment fixture. The testing adhered to ASTM C633–13 displacement rates, employing a rate of 0.015 mm/s. Each type of Cu specimen underwent five tests using the 25 kN capacity 8874 Instron frame. After examining the failure mode, the peak load at rupture was used, and the adhesion strength was calculated by dividing this load by the circular cross-sectional area of the sample.

5.4 Results and discussion

5.4.1 Feedstock powder characterization

The particles for different feedstock powders are shown in Figure 42. The EBSD grain orientation maps for cross-sectional as-received powders has been shown in Figure 44. The average grain size of the initial powders of A, B, C and D measured approximately 3.5 μm, 16.9 μm, 22.6 μm and 17 μm, respectively. Eftekhari. et al. [146] have performed a detailed examination to understand the effect of manufacturing methods on the characteristics of these Cu powders. The summary of the powder characterization results is shown in Table 9. The measurements from the shear cell method showed that spherical gas atomized powders can enhance flowability. As the surface area of the particles diminishes, the interacting surface forces decrease, resulting in a smoother flow. The findings showed that the porous electrolytic Cu powder has the lowest hardness values, suggesting potentially a better deformability. This was followed by gas-atomized powders featuring equiaxed grains, while the gas-atomized powder, characterized by small dendrites within the microstructure, displayed the highest value of nano-hardness [146].

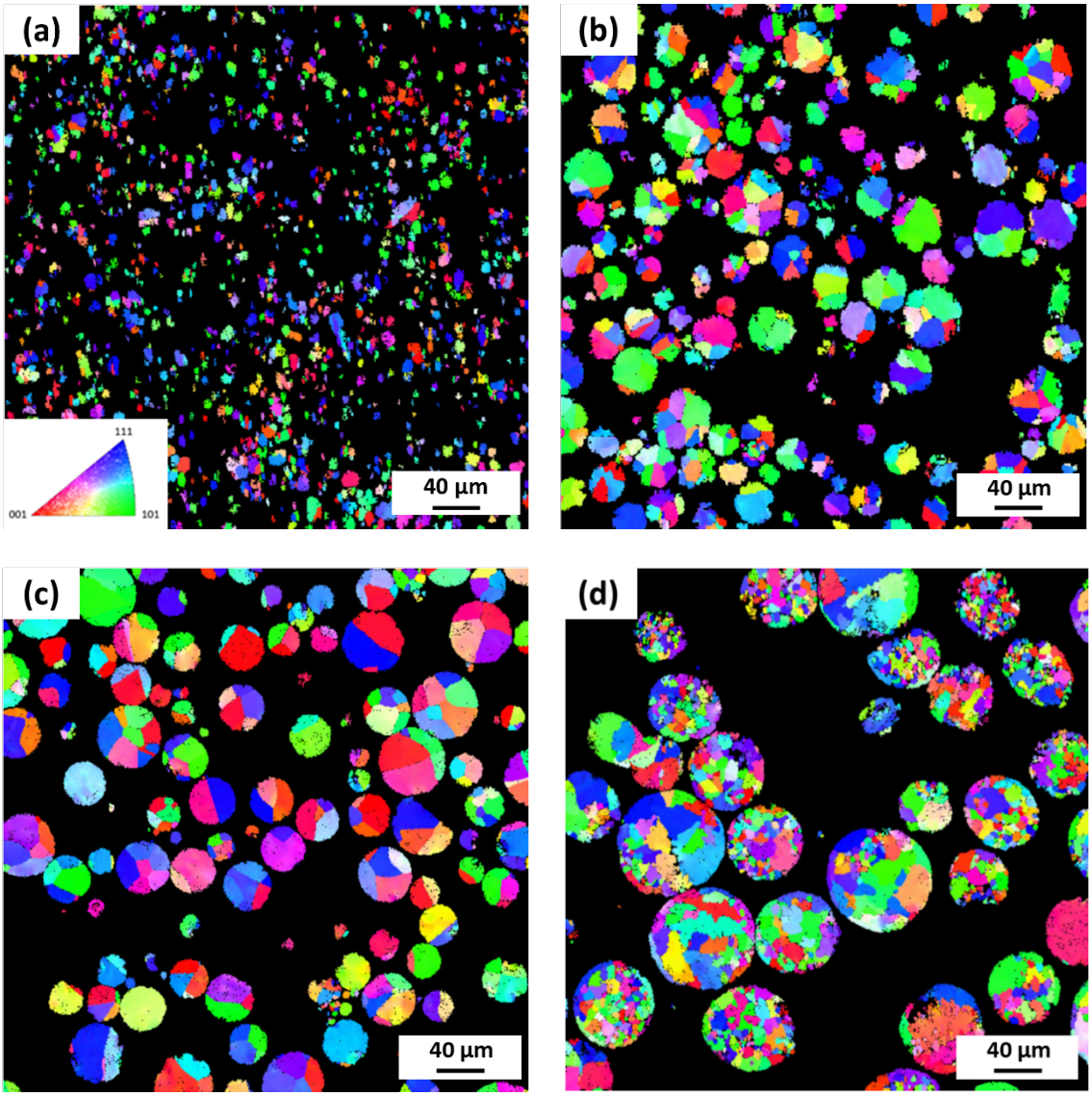


Figure 44: EBSD grain orientation map for cross-sectional powders of (a) A, (b) B, (c) C and (d) D.

Table 9: Feedstock powder characterization [146]

Feedstock powder	A	B	C	D
Production method	Electrolysis	Gas atomization	Gas atomization	Gas atomization

Cu (Wt.%)	>99.7	>99.9	>99.9	100
Morphology	Irregular	Less spherical	More spherical	Medium spherical
Microstructure	Porous	Equiaxed	Equiaxed	Dendrite cells, Equiaxed
D_{50} (µm)	24	22	34	81
Angel of internal friction (degree)	35 ± 1.2	25.75 ± 0.1	19.7 ± 1	22.3 ± 0.4
Nano hardness (GPa)	0.74 ± 0.2	1.3 ± 0.2	1.14 ± 0.2	1.6 ± 0.2

5.4.2 Design of experiment (DOE) to obtain optimum deposition parameters

The DOE was developed to evaluate the contribution of significant cold spray processing factors on the deposition efficiency as measured by weight change and thickness of coated samples for the four different Cu powders. This design has 2 factors: temperature and pressure of process gas. Within the successful coating range for Cu, three levels of temperature, T: 300 °C, 350 °C and 400 °C, and three levels of pressure, P: 1.72 MPa, 1.86 MPa and 1.99 MPa, were considered for each of these factors. These selections are based on the range of SST low-pressure cold spray machine, encompassing low, moderate, and peak levels that can be attained. Based on the full factorial design, 3^2 trials were planned for each Cu powder. The other processing parameters for the respected Cu powders are listed in Table 10. The rationale behind the adoption of these processing parameters for each feedstock is elaborated as follows: The choice of stand-off distance is based on the consideration of the bow shock effect, a concept thoroughly detailed in Reference [147]. In the case of nozzle speed and X-offset, these parameters have been determined through empirical experimentation to achieve optimal coatings without substrate delamination at varying temperatures and pressures. The decision to maintain a constant number of layers (1) for all Cu powder depositions was made to ensure consistency across the study. Similarly, the selection of the number of cycles was driven by the aim of depositing a uniform area (15mm x 16mm) for each feedstock. The feed rates, indicating the quantity of powder (in grams) exiting the nozzle per minute, were established through experimental assessments using the SST cold spray machine for each respective feedstock. Table 11 outlines velocity estimates for particles based on the model and parametric equations [31,148,149] used for nine varied experimental settings in this

study. The model assesses particle velocity by considering variables such as the average size of the particles, material properties, and gas properties. The drag coefficient, which depends on the Mach number and the size of the particle [31,149], were estimated for particles with average sizes of 25 μm, 27 μm, 31 μm, and 81 μm, corresponding to powders A, B, C, and D, respectively; this coefficient assumed to be constant across different temperatures. The difference in velocities noted in Table 11 were predominantly from the variance in average particle size of the powders. It is important to mention that these calculations do not account for the differences in the morphology of the powder particles (assuming them to be spherical) [123]. When gas temperature and pressure remain constant, irregularly shaped particles may be more readily accelerated by the process gas due to increased drag force, thus, irregular particles of the same size usually achieve higher velocities [67,123]. However, It is generally accepted, for high-quality deposition to be achieved, the ratio of particle velocity to critical velocity needs to be maximized [40,41].

Table 10: Cold spray deposition parameters for different Cu powders

Powder Type	standoff distance (mm)	nozzle speed (mm/s)	X-offset (mm)	No. of layers	No. of cycles	feed rate (g/min)
A	20	120	-1	1	8	0.6
B	20	40	-0.5	1	15	12.5
C	20	40	-0.5	1	15	20.8
D	20	40	-0.25	1	24	21.5

Table 11: Calculated particle velocity (m/s) for different feedstock powders under different conditions

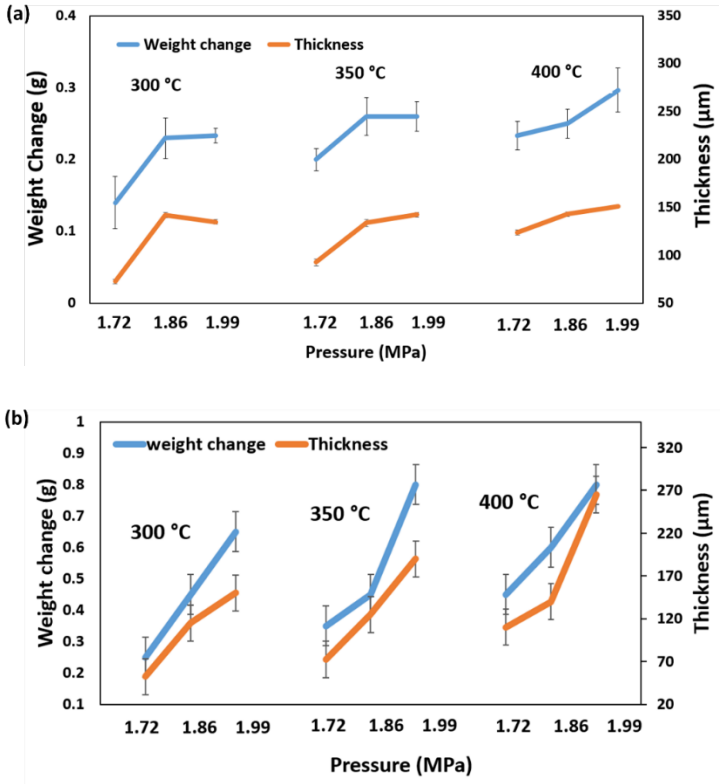
Powder Type / **Temperature, Pressure**	**A**	**B**	**C**	**D**
T= 300 C, P= 1.72 MPa	522	508	486	345
T= 300 C, P= 1.86 MPa	531	517	496	354
T= 300 C, P= 1.99MPa	540	526	504	362

T= 350 C, P= 1.72 MPa	533	519	497	351
T= 350 C, P= 1.86 MPa	543	529	506	359
T= 350 C, P= 1.99 MPa	552	538	515	368
T= 400 C, P= 1.72 MPa	545	529	505	355
T= 400 C, P= 1.86 MPa	555	540	516	365
T= 400 C, P= 1.99 MPa	564	548	525	373

The responses for each trial included thickness of coatings and weight change of substrate samples as an indication of deposition efficiency. Minitab statistical software version 20.1 was employed to analyze the results with a confidence level of 95%. Figure 45 shows the weight change of substrates and thickness of coatings versus pressure and temperature for all types of Cu powders. Weight change and thickness increased with increasing process gas temperature and pressure. The results reveal that the maximum values of weight change and thickness were obtained for powder C under all test conditions, followed by powder B and A, and powder D exhibits thinnest coating. In addition, weight change of the sample using powder D remained constant (0.05 g) under all test conditions, so it is not shown in graph (Figure 45d) and not investigated by Minitab software.

In cold spraying, bonding happens when the impact velocities of particles (v_{impact}) exceed a certain value, known as critical velocity (v_{crit}) [150]. According to the size dependence of critical velocity, there will be an optimum size range where v_{impact} is considerably higher than v_{crit}. When particle sizes are higher than the optimum range, which is about -45+10 μm, v_{crit}, and v_{impact} are nearly parallel and coatings show decreased deposition efficiency with larger particle sizes. Powder D has the largest particle size distribution (D_{90} is 138.29 μm) which is not in the optimum size range of Cu powder particles [150]. In this regard, it has the lowest values of responses among all four types of Cu powders. On the other hand, the microstructure of powder particles plays a crucial role in the deposition behavior of feedstock powders. In fact, deposition behavior of feedstock powders depends on the extent of plastic deformation experiences by the powder particles. Microstructural features such as different phases, precipitation and grain size alter the level of deformation as were reported for Ti, Al and Cu alloys, respectively [123,124,132]. Based on the Hall-Petch relation powder D with the small grain size

distribution has the highest hardness resulting in poor plastic deformation and low deposition efficiency [132]. Through powder particles morphology analysis, it was found that powder A has irregular shape particles with a porous microstructure and the other Cu powders are spherical with a dense microstructure. Irregular particles have a larger drag coefficient [116], which can achieve higher particle velocity during deposition and can form better mechanical interlocking. In addition, the porous microstructure leaves the particles more disposed to adiabatic shear instability and results in stronger particle/particle and particle/substrate bonding [151,152]. However, the experimental results show the opposite phenomenon, that is, the weight change and thickness of powders B and C with the spherical morphology is higher than powder A. This can be attributed to the higher flowability and subsequent feed rate of powders B and C, which deposit higher number of powder particles in a constant time.



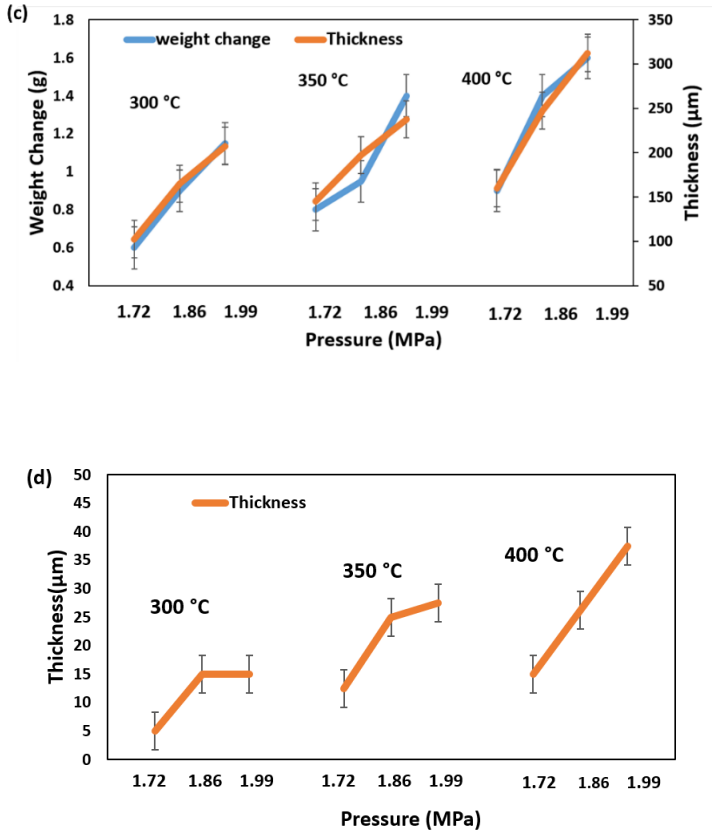


Figure 45: Weight change of substrates and thickness of coatings at different pressures and temperatures for Cu powders of (a) A, (b) B, (c) C, and (d) D.

To define which parameters contribute the most to the variability in the response, a Pareto chart of the effects is used to associate the relative magnitude and the statistical significance of factors (Figure 46). The effects are plotted by Minitab in the decreasing order of their absolute values. The reference line on the chart shows which effects are significant. A significance level of 0.05 was used to draw the reference line. In these results, pressure (blue column) is statistically significant factor on the weight change and thickness of coatings obtained from all Cu powders (Figure 46a and b). On the other hand, temperature (orange column) is also the significant factor on the weight change of powder B and C (Figure 46a), and thickness of powders B and D (Figure 46b). However, pressure extends more than temperature in all the Pareto charts. In addition, P values obtained from ANOVA tables (Table 12) are used to confirm the relation between the responses and parameters. According to Table 12, the P values

of pressure for weight change and thickness of all four types of Cu powders are less than significant level (0.05). It could be concluded that there is a statistically significant association between the weight change and thickness and the pressure term. However, the P values of temperature for the weight change of powder A and thickness of powders A and C are higher than 0.05, which means that there is not a statistically significant association between the considered responses and temperature term. Therefore, the effect of pressure appears to be more significant than temperature on the weight change and thickness of all four types of Cu powders.

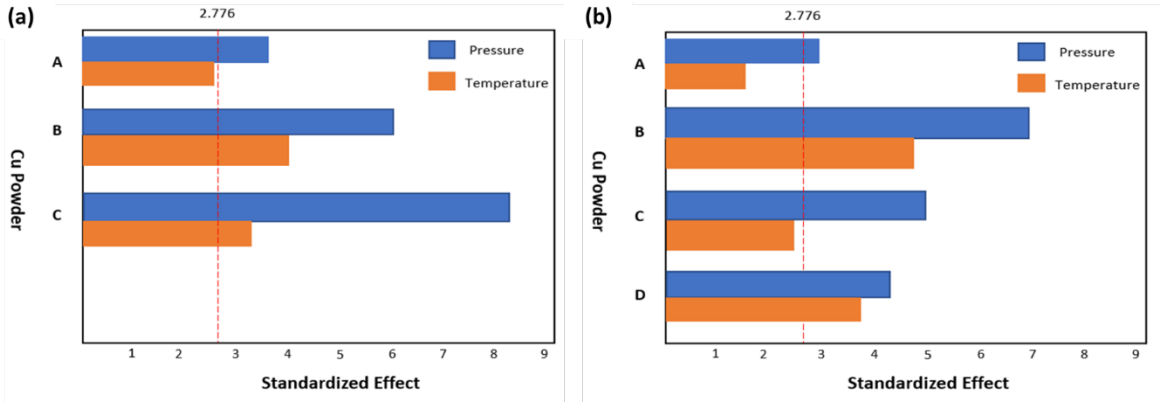


Figure 46: Pareto charts of the standardized effects (α = 0.05) of Cu powders for the responses of (a) weight change and (b) thickness, respectively.

Table 12: P value for temperature and pressure obtained from ANOVA tables

Powder type	P Value (α=0.05)			
	Weight change		Thickness	
	Pressure	**Temperature**	**Pressure**	**Temperature**
A	0.024	0.052	0.039	0.140
B	0.004	0. 014	0.002	0.008

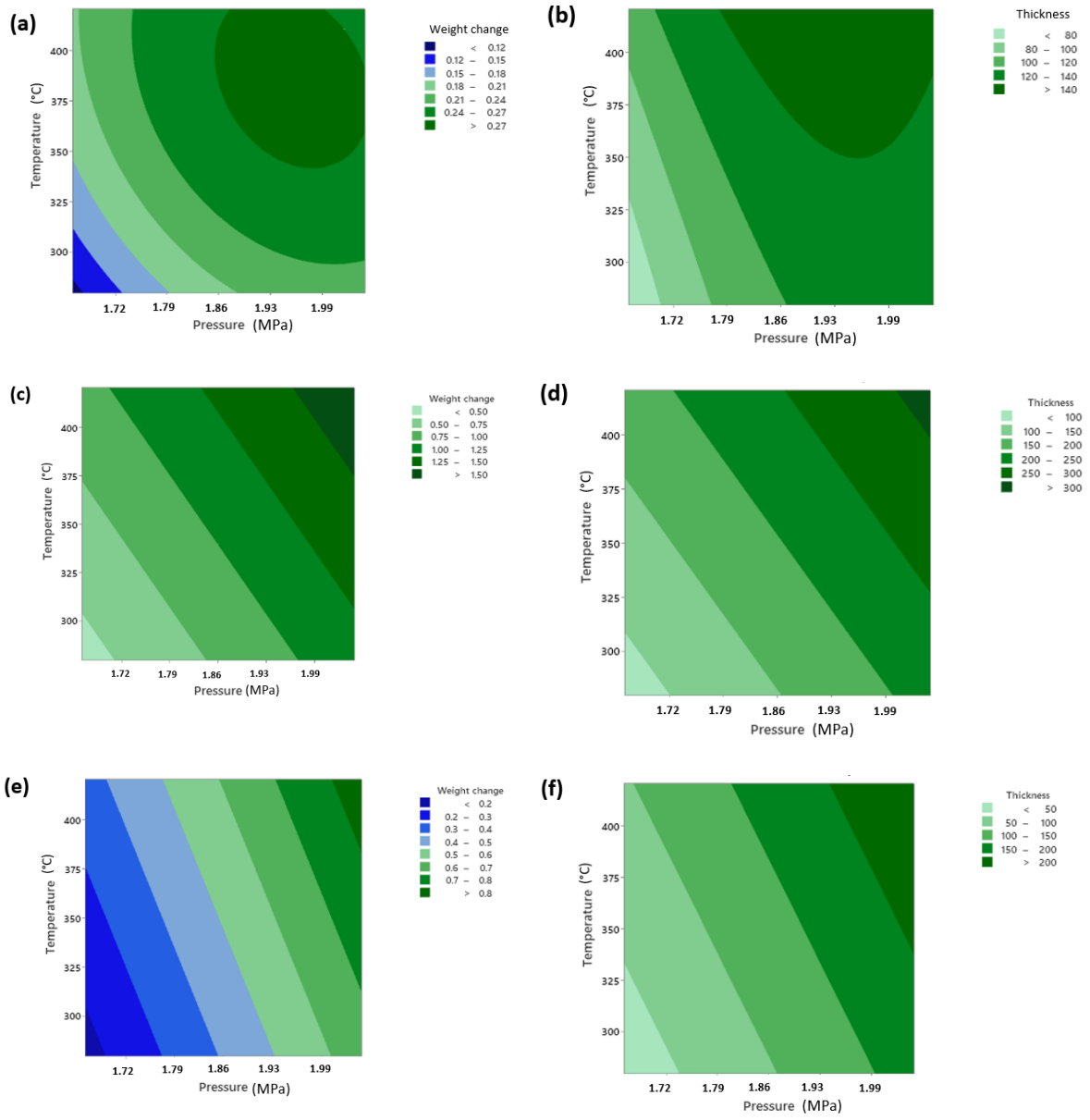
C	0.001	0.028	0.007	0.059
D	NA	NA	0.013	0.017

Finally, contour plots were obtained to show the relationship between the optimum fitted weight change and thickness and two continuous variables of pressure and temperature in Figure 47. In these graphs, darker regions indicate the optimum condition of coatings with higher weight change and thickness values. It could be seen for powder A that higher values of weight change form an oval shape from upper left of the graph to the lower right part. The region in the lower left of the graph shows the least values of weight change of substrate after CS coating (Figure 47a). In addition, higher values of thickness were obtained from upper right of the graph. The other regions have the least average thickness obtained after CS coating (Figure 47b). However, the other powders show a linear relation between the fitted data and continuous variables. It could be concluded that higher values of weight change and thickness were obtained by increasing the temperature and pressure (Figure 47c, d, e, f, and g). Therefore, the optimum cold sprayed coatings will be obtained at temperature of 400 °C and pressure of 285 psi (1.96 MPa) for powder A and temperature of 420 °C and pressure of 290 psi (1.99 MPa) for the other Cu powders. As evident, the most favorable processing parameters have been achieved using nearly the uppermost capabilities of the SST cold spray machine. In fact, higher temperatures can soften the substrate surface, necessitating a lower critical velocity for successful bonding. On the other hand, increased pressure can lead to denser gas and improved particle acceleration, allowing effective bonding to occur at lower critical velocities. In addition, when temperature is raised, particles tend to possess higher kinetic energy, resulting in elevated particle velocities. Similarly, higher gas pressures can accelerate particles more effectively, increasing their velocities [31].

For more clarification, it is worth mentioning that a full factorial design of experiments (DOE) was employed to assess the influence of process gas temperature and pressure, which are the primary process variables affecting particle velocity and deposition efficiency in low-pressure cold spray. These parameters were selected based on the operational range of the SST system, while other factors like stand-off distance were held constant to minimize experimental complexity and isolate the effects of temperature and pressure. The analysis focused on deposition efficiency (DE), measured through

coating thickness and substrate weight gain, as the primary response due to its direct relevance to process performance. Although properties like strength and porosity are important, they were excluded from the initial optimization due to the time-intensive nature of their measurement and their dependence on multiple variables beyond the scope of this DOE.

Optimization was carried out using Minitab software, leveraging ANOVA and Pareto charts to identify significant effects and optimal parameter combinations. While pressure was found to be statistically significant across all powders, temperature showed significance only for certain powders. Nonetheless, temperature levels were still selected based on their interaction with pressure and observed trends, acknowledging the presence of synergistic effects captured through interaction terms in contour plots. Validation of optimal parameters was performed via replicate trials and comparison with predicted values, confirming the consistency and reliability of the selected processing conditions.


(a)
Temperature (°C)
400
375
350
325
300
1.72
1.79
1.86
1.93
1.99
Pressure (MPa)
Weight change
< 0.12
0.12 – 0.15
0.15 – 0.18
0.18 – 0.21
0.21 – 0.24
0.24 – 0.27
> 0.27
(b)
Temperature (°C)
Pressure (MPa)
Thickness
< 80
80 – 100
100 – 120
120 – 140
> 140
(c)
Temperature (°C)
Pressure (MPa)
Weight change
< 0.50
0.50 – 0.75
0.75 – 1.00
1.00 – 1.25
1.25 – 1.50
> 1.50
(d)
Temperature (°C)
Pressure (MPa)
Thickness
< 100
100 – 150
150 – 200
200 – 250
250 – 300
> 300
(e)
Temperature (°C)
Pressure (MPa)
Weight change
< 0.2
0.2 – 0.3
0.3 – 0.4
0.4 – 0.5
0.5 – 0.6
0.6 – 0.7
0.7 – 0.8
> 0.8
(f)
Temperature (°C)
Pressure (MPa)
Thickness
< 50
50 – 100
100 – 150
150 – 200
> 200

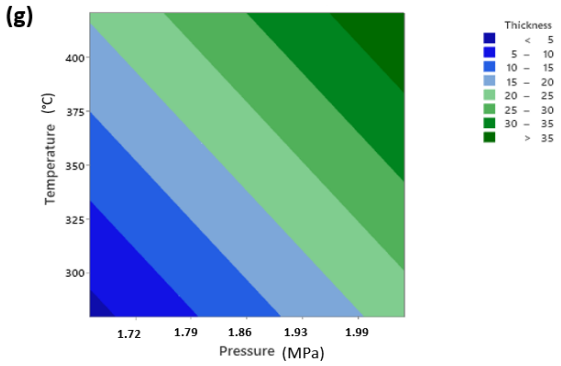


Figure 47: Contour plots of weight change for Cu powders of (a) A, (c) B, and (e) C, respectively and Contour plots of thickness for Cu powders of (b) A, (d) B, (f) C, and (g) D, respectively.

5.4.3 Microstructure of deposited samples

Considering the poor cold spray ability of powder D, only coatings obtained from optimum conditions of powders A, B and C are further investigated. Figure 48 shows cross sectional optical images of cold sprayed Cu depositions from substrate/coating interface to top of coatings performed using powders A, B and C. Irregular shaped particles of powder A were deformed upon impact, as shown in Figure 48a-c. Extensive number of darker areas between primary particles could be observed as oxidized boundaries in the microstructure. Oxidized areas were produced by oxidized layers on the particle surfaces in the starting powder. This could be attributed to the considerable amount of oxygen (< 0.2 wt. %) containing chemical composition of as-received powder and large surface areas of irregular shaped particles compared with spherical particles which leads to high number of naturally oxidized primary particle boundaries during exposure to atmospheric condition [141]. It has been shown that a little variation in oxygen content of feedstock powders (e.g. from 0.01 to 0.06%) or a minor gain of oxygen during oxidization in air (e.g. only about 0.007%) result in an increase in powder critical velocity of about 150 m/s and a decrease in powder deposition efficiency of 15%, respectively [29,140]. This indicates that higher plastic deformation would be needed for breakage of the initial oxide layers of particles of powder A. After the elimination of oxide layers, the metallic bonding could be achieved between the surfaces of primary Cu particles [141]. In addition, this coating shows a weak adhesion to the substrate as appeared by its delamination from the substrate during metallographic preparation (Figure 48a). It is well established that deposition with the powder of higher oxygen content remarkably

degrades the adhesive strength of the coating due to the more oxide inclusions at the interfaces that reduce the particle bonding areas and prevent the effective metallurgical bonding of fresh metals [153,154]. Furthermore, the mechanical interlocking phenomenon, which has been reported as an additional process for bonding between irregular shaped particles and the substrate, is dependent on extent of plastic deformation and subsequent adiabatic shear instability. Thus mechanical interlocking is not a dominant bonding mechanism in the case of powder A due to the higher required plastic deformation for elimination of oxide layers [116,155]. This coating contains also a porous layer near to the coating surface due to the lack of tamping effect in this area [156] (Figure 48c). In addition to the coating obtained from irregular shaped Cu feedstock, the structure of coatings prepared from spherical Cu powders of B and C are presented in Figure 48d-i. These coatings appear to be dense, and the porous microstructure appeared from powder A, was not present here. Spherical particles have lower amount of primary particle surfaces, which indicates the probability to have lower amount of primary oxide layers and higher potential for plastic deformation [141]. However, evaluation of the interfaces between coatings obtained from spherical Cu powders of B and C and the substrate (Figure 48d and g); illustrate the possibility of more oxide inclusions presented at the interface of coating/substrate obtained from powder B. Because this interface shows some porosities (Figure 48d) which could be an indication of less adhesion, while that of powder C is faultless and tightly adhered (Figure 48g). Besides, lower flattening ratio of splats for powder B (FR: 2.87 ± 1.59) comparing with powder C (FR: 3.57 ± 1.51) shows less plastic deformation of this powder. Considering the resemblance in chemical composition of powder B and C which are 99.9 % pure copper powders with less than 0.015% oxygen contents, the lower sphericity of powder B comparing with powder C plays a crucial role in the higher amount of primary oxide layers and less plastic deformation of powder particles B. Moreover, the satellite free specification of powder C is another factor for its higher plastic deformation during cold spray deposition. In other words, micro-satellite particles with less than 5 μm sizes in powder B imply large ratio of surface area to volume (surface area / volume has an inverse relationship with the size [157]), thereby significantly increase the number of oxide layers in powder particles B. Furthermore, it should be noted that except the different oxidation behavior of powders B and C, powder B with smaller particle size than powder C has lower particle temperature and subsequently higher critical velocity which restrict the plastic deformation upon impact. This is attributed to the fact that the critical velocity of a powder significantly depends on its temperature and Schmidt et al.

reported that large Cu powders of 50 µm shows considerably higher powder temperatures (330 ◦C) than do smaller Cu powders of 5 µm (190 ◦C) [41].

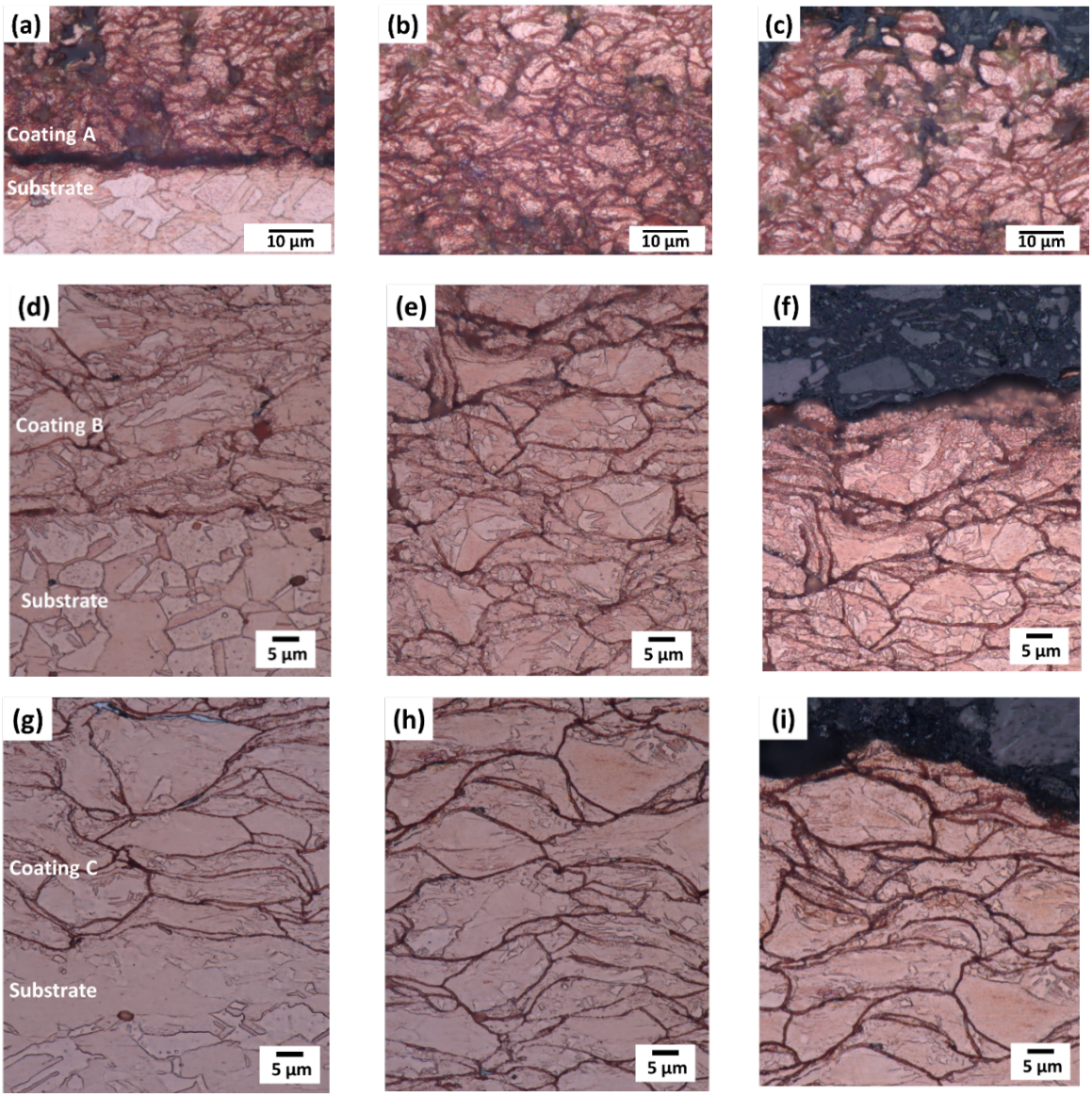


Figure 48: Optical microscopy of cold-sprayed coatings after metallographic etching of polished cross section samples from the interface to the top of coatings obtained from (a), (b) and (c) powder A, (d), (e) and (f) powder B and (g), (h) and (i) powder C.

The powder's surface chemistry was explored through XPS. The examined layers had a thickness of roughly 10-20 nm. The results of the XPS analyses are depicted in Figure 49, highlighting the existence of Cu, O, and C exclusively. It is worth noting that C is attributed to contamination on the surface. These findings corroborate that the oxygen content near the surface of powders A and B is greater than that in powder C. To better understand the chemical state of copper present on the powder surface - whether as Cu(0) (metal Cu), Cu(I) (Cu2O), or Cu(II) (CuO) - high-resolution Cu 2p XPS spectra were gathered (Figure 50). These spectra displayed the dominant Cu 2p3/2 emission line at 932-933 eV, with shake-up peaks of varying intensities at 940-945 eV. As a result, the primary Cu 2p3/2 emission line is made up of contributions from Cu(0), Cu(I), and Cu(II), while the intensity of the shake-up satellite is entirely due to the Cu(II) state. In this study, powder type A shows a strong shake-up peak, whereas types B and C exhibit medium and weak shake-up peaks, respectively. Therefore, in qualitative terms, both type A and B powders contain more CuO than type C powder.

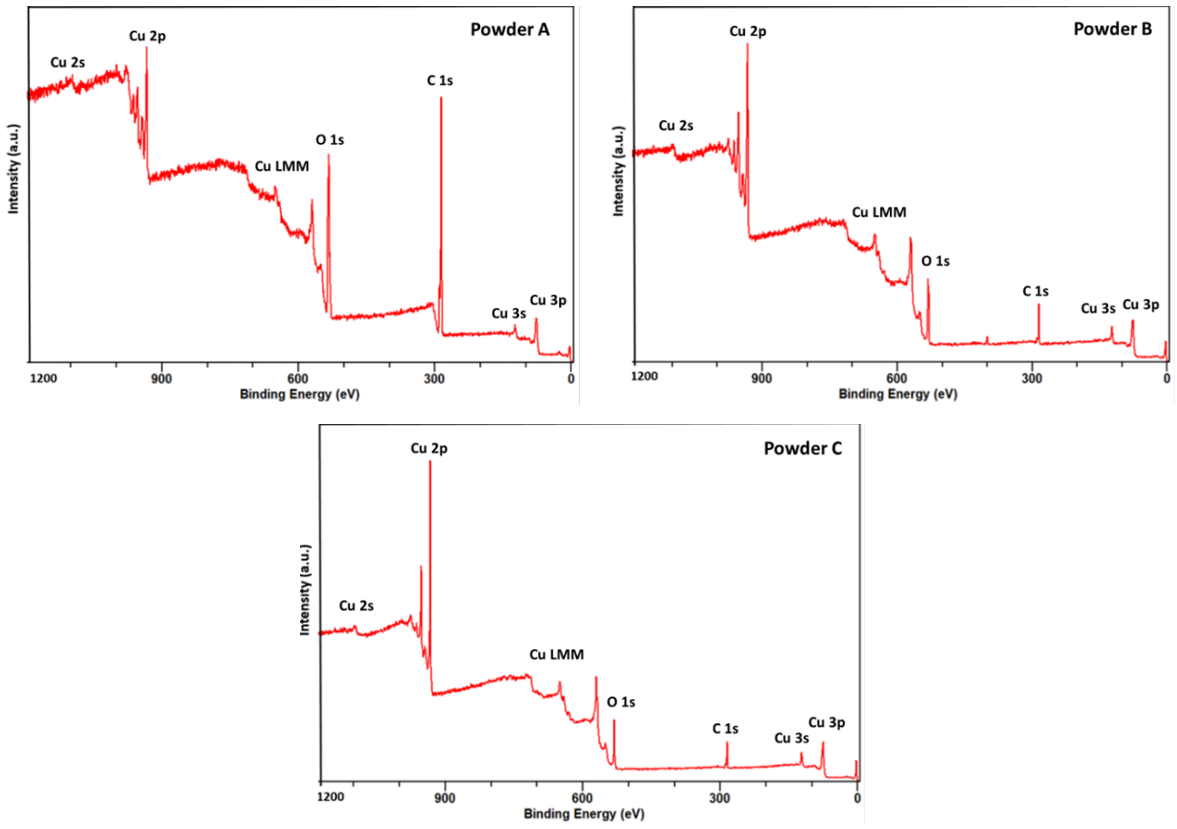


Figure 49: XPS survey spectra

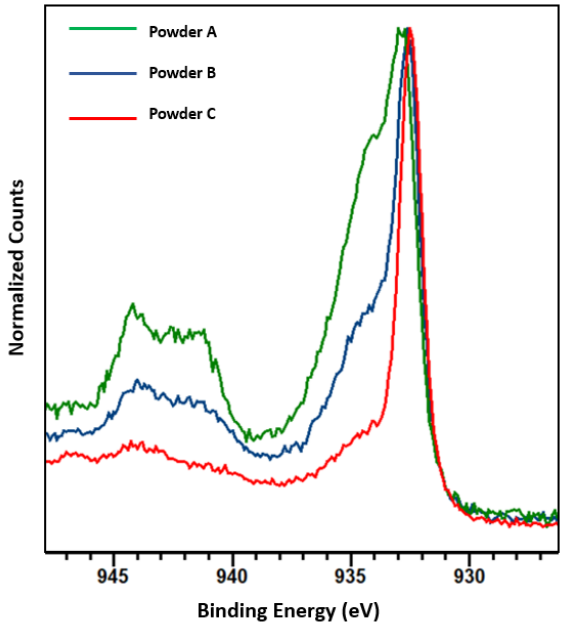


Figure 50: high-resolution Cu 2p XPS spectra displaying the dominant Cu 2p3/2 emission line at 932-933 eV, with shake-up peaks of varying intensities at 940-945 eV for different feedstock powders.

According to the results presented in Figure 51 and Table 13, cold sprayed coatings deposited from feedstock of B and C have denser structure compared with the coating prepared from feedstock of A. This result indicates particle bonds were tighter in the coatings prepared from spherical particles with higher deformation level compared with dendritic particles. In fact, for spherical powder particles of B and C, formation of the interfacial jets during adiabatic shear localization can be expected to clean the contacting surfaces and promote the tight metal-metal bonding [158]. However, in the coatings prepared from spherical particles, some pores with polygonal shapes, located at triple-junctions of the splats could be detected in the high magnification. Visible pores are little in as-polished coating of powder C (Figure 51c), while numerous pores are observable in the coating of powder B (Figure 51b). On the other hand, irregular shaped particles of powder A, have higher amount of particle boundaries arising from larger surface areas which act as the weak points in the structure. In this regard, unbounded particle's boundaries could be clearly observed in the coating of powder A (Figure 51a).

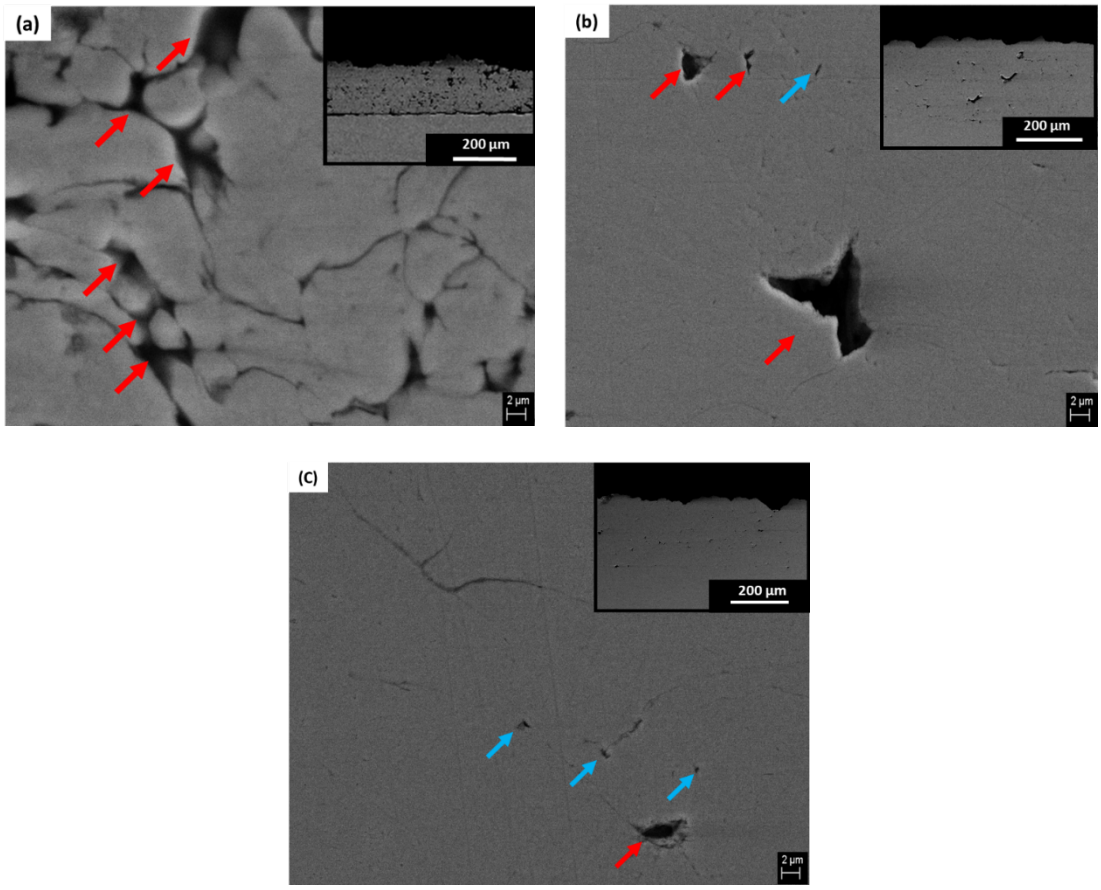


Figure 51: High magnification and low magnification SEM cross-sectional images of cold sprayed coatings using powders (a) A, (b) B, and (c) C, red arrows show large visible pores and blue arrows show the tiny pores.

Table 13: Porosity of cold sprayed coatings obtained from different Cu powders

Powder type	**A**	**B**	**C**
Porosity (%)	5.73 ± 0.5	1.70 ± 0.37	0.66 ± 0.35

In the following microstructural evolution of spherical powder particles of B and C during cold spray are examined through EBSD maps in Figure 52. Figure 52a and b display the inverse pole figure (IPF) maps for coatings derived from powders B and C. Microstructures of coatings consist predominantly

of particles that are heterogeneously deformed, displaying random grain orientations. The microstructural characteristics of these coatings are largely influenced by the degree of plastic deformation each powder particle undergoes. In both types of coatings, there's notable refinement of grains, resulting in average grain sizes of 7.7 μm for coating B and 7.8 μm for coating C. Notably, as shown in Figure 44, the initial grain size of powder B (16.9 μm) is smaller than that of powder C (22.6 μm). Additionally, certain regions that did not index (appearing as black contrasts) were noticed, which could be attributed to ultrafine crystallites size, lattice strain, a high concentration of defects, porosity, or incomplete bonding among particles [159]. Figure 53 illustrates the grain size distribution across the coatings depicted in Figure 52. This variation underscores the uneven deformation and refinement of grains within the coatings and Cu splats, a consequence of the high strain rate compressive forces applied. For coatings B and C, it was noted that 70% and 75% of the grains are smaller than 8μm, respectively, while 30% and 25% of the grains exceed this size, leading to a diverse grain size distribution. It is well documented that grain sizes tend to be smaller closer to the interface than near the center. This suggests that the interface zone of cold spray depositions is more significantly affected by a peening effect, which leads to greater plastic deformation that, in turn, decreases the average grain size and distribution to finer dimensions [160] evident in the sections marked with yellow, illustrating the interfaces in Figure 52a and b. Consequently, the highly deformed areas at the coating and substrate interface is conducive to the formation of new ultrafine grains, mainly due to dynamic recrystallization [161]. In addition, it has been established that at the splat boundaries, where deformation is most intense, recrystallized grains emerge due to the ongoing dynamic recrystallization process; however, the grains in the center of the particles which are only partially deformed, are larger [162,163]. Since the splat boundaries had become indistinguishable in the microstructure this phenomenon is not easily seen in Figure 521a and b. Nonetheless, to accurately assess the extents of the fully recrystallized, sub-structured, and deformed regions within both microstructures, a more detailed analysis is required. Furthermore, Figure 52c and d exhibit the Kernel Average Misorientation (KAM) maps for coatings made from powders B and C. A larger proportion of higher KAM values is noticeable in the microstructure derived from powder C. In fact, regions with elevated KAM values, indicative of significant strain and defect density, pointing to a greater degree of local plastic deformation endured by particles of powder C.

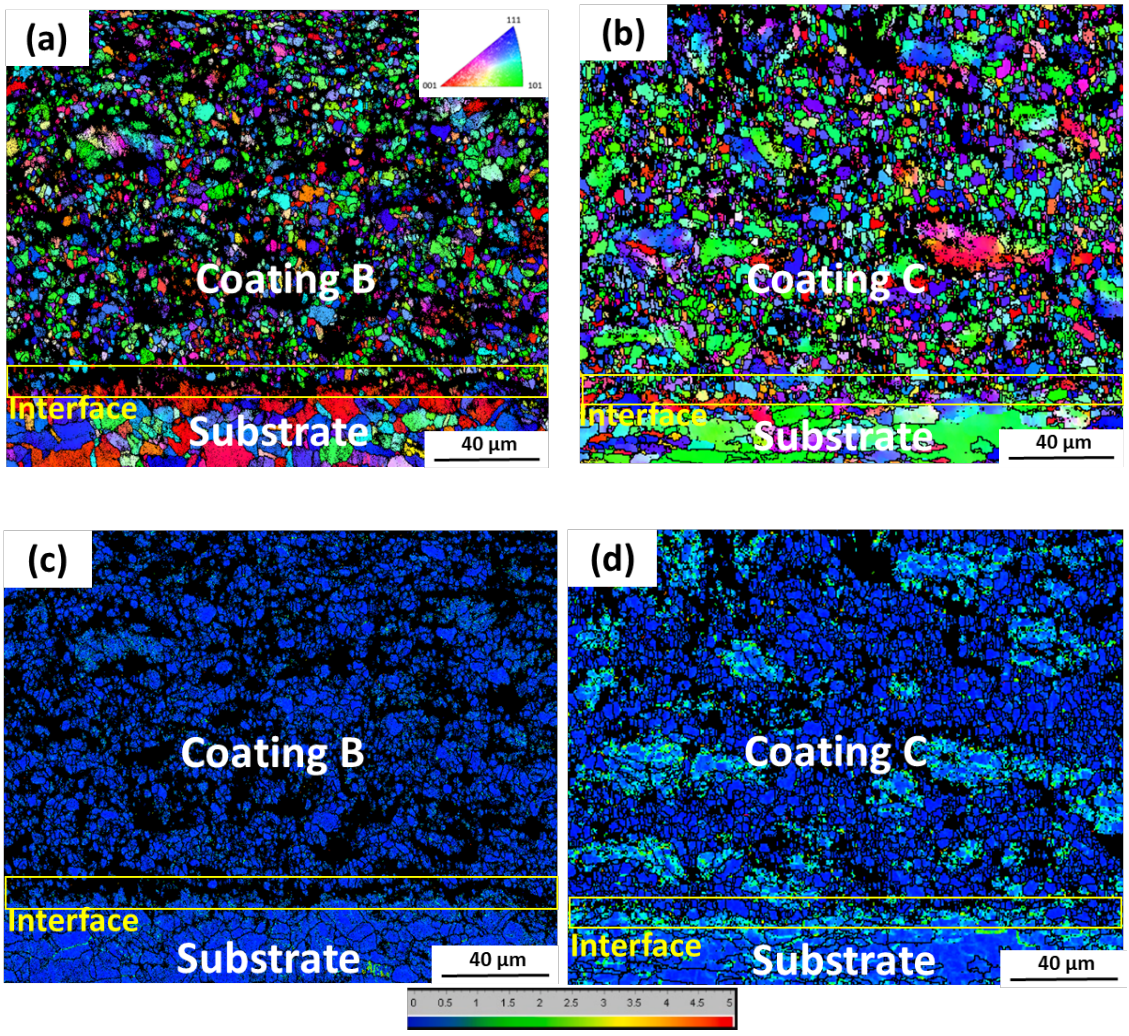


Figure 52: (a and b) Inverse pole figure (IPF) and (c and d) Kernel Average Mis orientation (KAM, orientation legend at the bottom of figures in degrees) maps of cold sprayed coatings obtained from (a) and (c) powder B and (b) and (d) powder C. Yellow box indicates the interface area between coating and substrate.

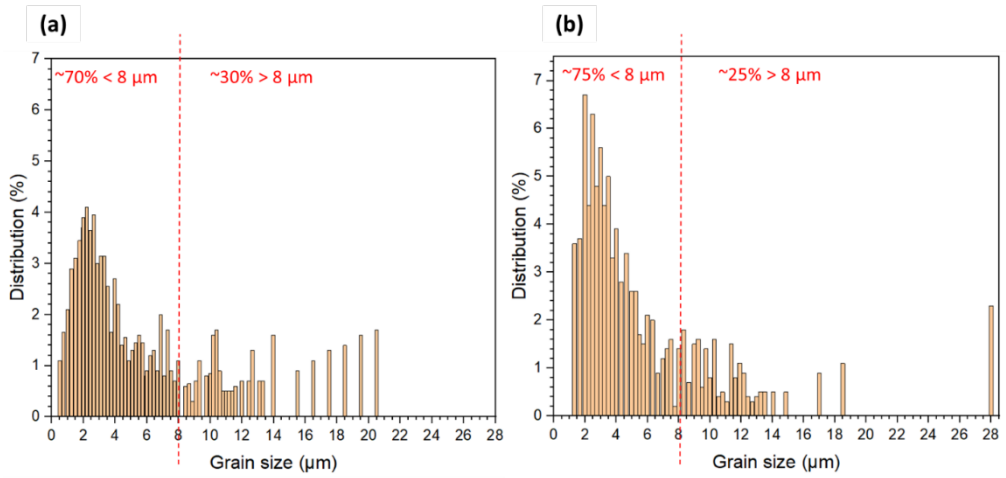


Figure 53: Grain size distribution for coatings from (a) powder B and (b) powder C, corresponding to the coating sections illustrated in Figure 52, points to heterogeneous deformation of Cu splats and a non-uniform distribution of grain sizes.

5.4.4 Microstructure of substrate

To study the effect of cold spray coating of different Cu feedstock powders on the microstructure of Cu substrate samples, grain structure evaluations of different sample cross sections are conducted before and after deposition. Low and high magnification optical microstructural images of the as-received substrate are shown in Figure 54a and b. These images reveal that the microstructure of the as-received substrate close to the surface is uniform, and significant differences on the surface or in the bulk close to the surface are not observable. After cold spray coating with different Cu powders of A, B and C the grain size of the Cu substrates near the interfaces were decreased as shown in low and high magnification optical images of the cross sections (Figure 54c and d, Figure 54e and f and Figure 54g and h, respectively). It is well known that the densities of crystal lattice defects are increased by plastic deformation of a crystalline material [163]. An accumulation of the increased dislocations in the deformed grains resulting in local misorientation in the grains that increases the crystal's energy; thus, the dislocations align inside of the grain and make sub-grain boundaries to reduce the excess energy. Further deformation of these grains would produce more rotation in the sub-grains, forming high angle grain boundaries and dividing the grains into smaller individual grains [163]. Based on this explanation, greater deformation should result in smaller grains.

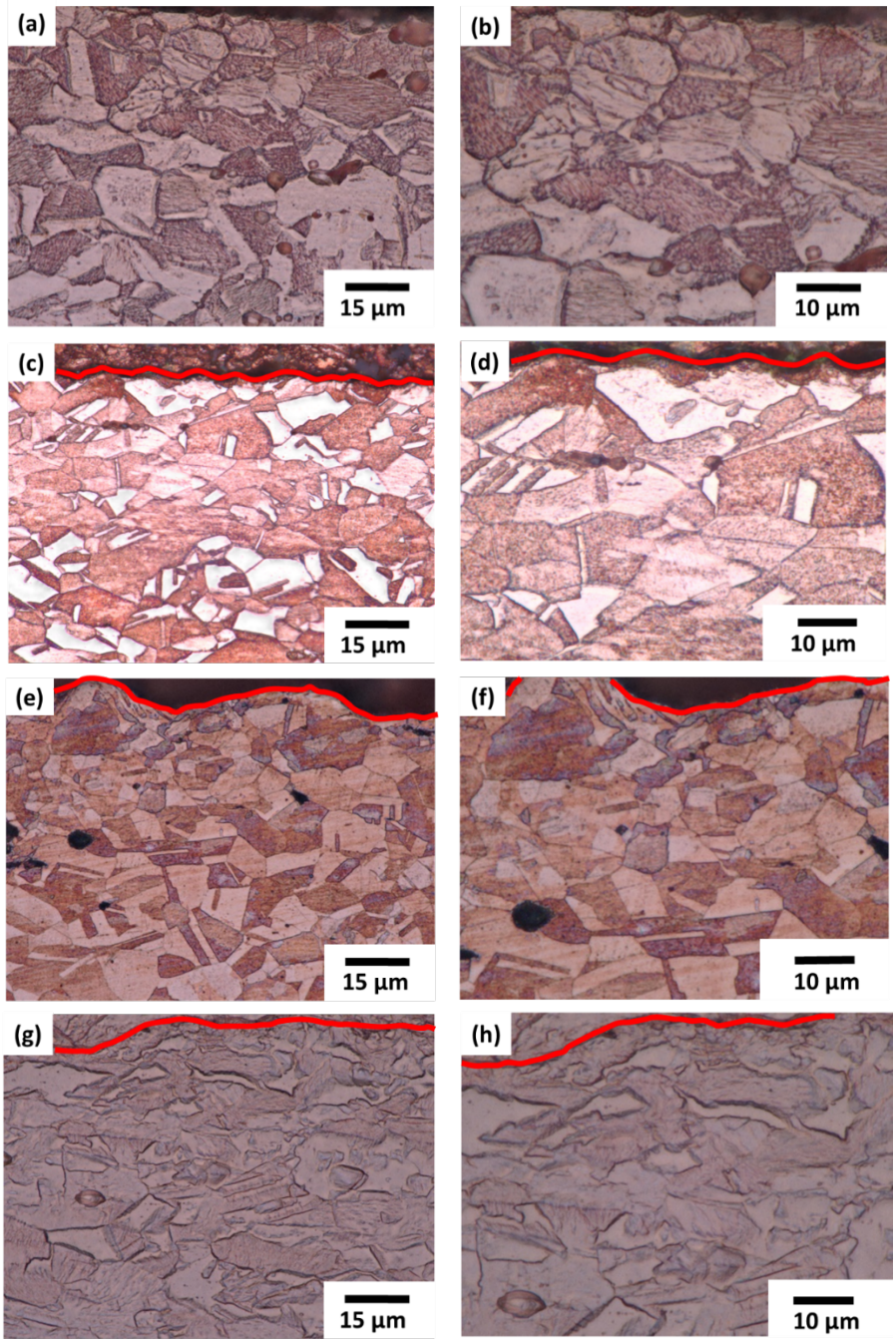


Figure 54: low and high magnification OM images of the (a) and (b) as received sample, (c) and (d) coating using powder A, (e) and (f) coating using powder B and (g) and (h) coating using powder C, respectively. Red curves indicate the interface between the coating and substrate.

To compare the microstructure evolution in the samples, the grain size of each sample was measured at the interface to 30 µm below the surface as shown in Figure 55. Based on this measurement, the average grain size of the as-received substrate is 4.95 µm. For the cold spray coating with powder C the minimum grain size (1.23 µm) is smaller than that seen after cold spray coatings with powder B (2.14 µm) and powder A (2.85 µm). In fact, cold spray with powder C leads to higher plastic deformation in the substrate. This is attributed to the extreme peening effect of particles because of more flattening and plastic deformation during coating. In addition, the effect of peening is observable in deeper areas. In the same manner, cold spray of the other spherical powder of B resulting in higher peening effect on the substrate comparing with that obtained after cold spray of irregular shaped powder. However, grain refinement in the substrate coated by powder A still observable when is compared to the as-received substrate. In this regard, higher amount of peening effect is the determining factor for the higher plastic deformation created in the substrate after cold sprayed deposition.

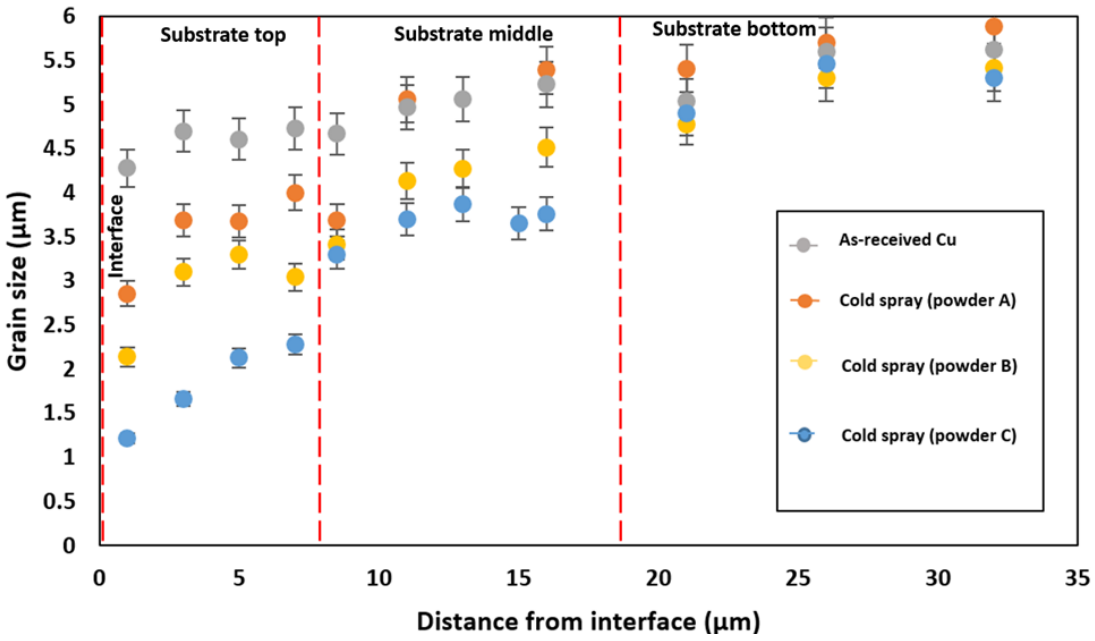


Figure 55: Changes in grain size of substrate adjacent to the interface before and after deposition: as received, coated using powder A, coated using powder B and coated using powder C.

5.4.5 Microhardness of coatings

The microhardness profiles across the coating/substrate interface are plotted in Figure 56 in order to investigate the differences in the mechanical properties of cold sprayed coatings obtained from different-type powder characteristics. In fact, the microhardness comparison of as-sprayed coatings is a competition between coating's porosity and work hardening caused by particle bombarding in cold spray process. Strain hardening and related compressive residual stresses during deposition enhance the hardness of cold sprayed coatings [164], while porosity decreases the hardness of coatings.Cu coating prepared with irregular shaped feedstock powder of A have lower hardness than coatings sprayed with spherical particles of B and C. Furthermore, hardness increases for the coating sprayed with powder particles of C, indicating the high deformation and thus, the higher hardening effect. The observed trend in hardness values of different coatings is comparable to the microstructural evaluations, showing the strong effect of powder type on the deformation, particle bonding, denseness and work hardening. The microhardness result again indicates that powder C has better deposition performance than the other two powders. The increased hardness at the surface of the substrate is attributable to the work hardening effect resulted from particles impact on the substrate, which is identical to the shot peening process [36]. The higher microhardness within the coating near the interface is the consequence of subsequent impact effect of the inflight particles on the previously formed coating, which dominates the work hardening.

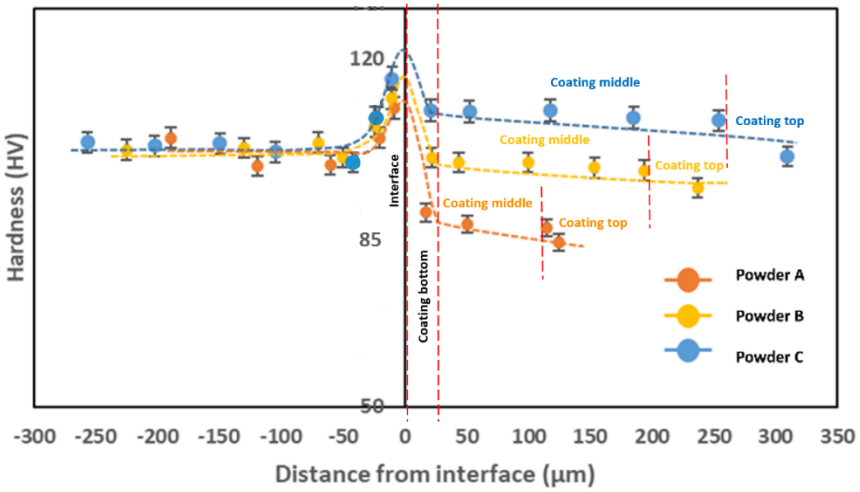


Figure 56: Vickers microhardness distribution from the substrate to the top of cold sprayed Cu coatings obtained from different Cu powders.

5.4.6 Adhesion or cohesion strength of coatings

In this experimental setup, four types of failures are anticipated: (1) adhesive failure at the coating/substrate interface, (2) cohesive failure within the coating, (3) cohesive failure within the glue, and (4) adhesive failure at the glue/coating interface. Figure 57 depicts the adhesion or cohesion bonding strengths and failure surface images of cold sprayed Cu coatings. An inspection of Figure 57 reveals that coatings using powders A, B, and C in adhesion test achieved average bond strengths of 5.9 ± 3.1 MPa, 21.2 ± 1.1 MPa, and 20.7 ± 2.3 MPa, respectively. For powder A, the failure was characterized by 15% adhesive and 85% cohesive within the coating, while powders B and C experienced only cohesive failures in their coatings. Linking these findings to the measured porosity levels (Table 13), it is clear that samples from powder A, with higher porosity in the coating, demonstrates significantly lower adhesive and cohesive bond strength. High porosity, especially near the coating/substrate interface, is likely to cause rapid crack propagation and early failure at the interface under tensile stress like that in tensile pull-off tests. Conversely, the presence of cohesive failures exclusively in the coatings of B and C with 1.7% and 0.6% porosity, respectively, highlights the strong adhesive bond at the interface with the substrates. During the cold spray process, the adhesion of particles to the substrate occurs through both metallurgical bonding and mechanical interlocking, which depend on the plastic deformation of the particles. The phenomenon of adiabatic shear instability, known to be critical for achieving high-quality cold spray depositions [40], is influenced by the condition of the feedstock powders. Specifically, feedstock powders with lower oxygen content and fewer oxides on their surface contribute to a decrease in the critical velocity needed for superior quality depositions. This highlights the need to take into account the morphology and surface area of the feedstock powders when evaluating their suitability for cold spray applications. Feedstock powders that are more spherical in nature tend to be more prone to adiabatic shear instability, leading to improved bonding between the particles themselves and between the particles and the substrate.

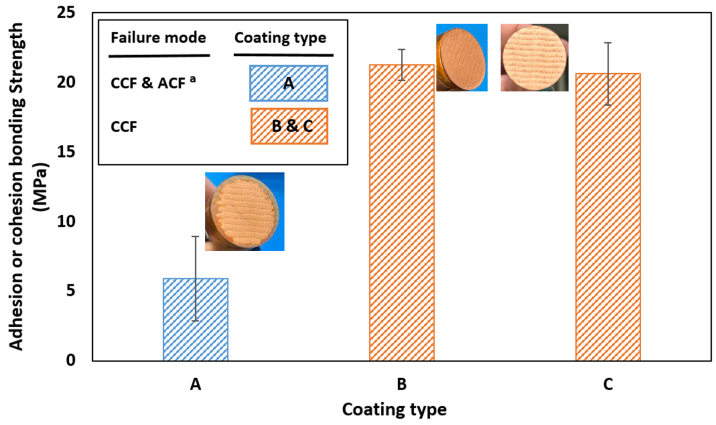


Figure 57: The adhesion or cohesion bonding strength and failure surface images of cold spray coatings evaluated through a tensile pull-off test, according to the ASTM C633 standards. [a] CCF-Cohesive Coating Failure, ACF-Adhesive Coating Failure.

5.4.7 Deposition behavior

Through microstructural and morphological analysis, it was found that powder A has irregular shaped (cauliflower like) morphology and a porous microstructure. Irregular shaped particles have a larger drag coefficient [152] which can achieve higher particle velocity during deposition. In addition, the porous microstructure with lower hardness is able to produce excellent compressibility and compaction behavior. Porosity in the particles, as the particles make an impact, absorbs the kinetic energy of particle and reduces the possibility of rebounding [67]. However, the experimental results show an opposite phenomenon, that is, the deposition performance of irregular shaped powder during low-pressure cold spray coating (LPCS) is the poorest. As a result, the oxidation behavior of feedstock powder should be considered. The irregular shaped particles have larger surface area compared with spherical powders, which result in more oxide layers during exposure to atmosphere [141]. However, this is not generalizable for all feedstock powder studies and depends on some factors. In one study, the quasi spherical and irregular shaped Tantalum powders were used to prepare cold spray coating, and the sphericity of the quasi spherical powder was more than irregular shaped one [116]. However, the results indicated that the coating deposited with irregular shaped powders was better with the low porosity, higher deposition efficiency, higher microhardness and strong adhesion bonding. Moreover, in another study, the cold spray coatings deposited from gas atomized and electrolytic Cu powders were

investigated [139]. Interestingly, the plastic deformation and final hardness of the latter was higher. The differences between our results and those studies may be attributed to the different diffusivity of oxygen in distinct metals, and different temperature and pressure of process gas, respectively. It has been demonstrated that the coefficient of oxygen surface diffusion for Cu (5.7×10^{-7} m^2/s) is almost 70% higher than Ta (3.5×10^{-7} m^2/s) [165]. Thus, oxidation is an inherent issue in application of Cu powders. Furthermore, the higher gas pressure (5Mpa) and temperature (600 °C) used in the second study was sufficient for the development of favorable properties in coating obtained from electrolytic Cu powder [139].

The observed results in this study can be ascribed to several underlying physical phenomena related to particle morphology, oxidation, and plastic deformation and grain refinement processes during the cold spray deposition of copper coatings. Notably, the irregular-shaped particles in powder A characterized by large surface areas, makes them prone to oxidation during exposure to atmospheric conditions. This indicates that overcoming the initial oxide layers on the irregular-shaped powder A particles requires higher levels of plastic deformation and restricts metallic bonding between the surfaces of primary copper particles and mechanical interlocking between the coating and the substrate. Conversely, coatings obtained from spherical copper powders such as B and C exhibit distinct characteristics influenced by their morphology and oxidation behavior. Spherical particles inherently possess fewer primary particle surfaces, reducing the likelihood of primary oxide layer formation. However, differences arise between powders B and C. Powder B, characterized by micro satellite particles displays specific features. Its smaller particle size results in a higher surface area-to-volume ratio, leading to an increased number of oxide layers within the particles. Furthermore, X-ray photoelectron spectroscopy (XPS) analyses confirm variations in the oxygen content near the surface of powders A, B, and C, with A and B displaying higher oxygen content. Therefore, in the case of powder A in our study, low temperature and more importantly low pressure (mentioned as the significant factor in DOE section) make it difficult to break the oxide layers and reach the condition of adiabatic shear instability. For powder B, also, it is predictable that better deposition properties could be obtained under higher temperature and pressure. As a result, it was feasible that to use less aggressive processing factors (i.e. LPCS coating), to reach high deposition quality for Cu powder type C with more spherical and satellite free morphology.

5.5 Conclusion

This research carried out an in-depth examination of four unique Cu feedstock powders, created via electrolysis and various gas atomization techniques, for their application in LPCS deposition onto a Cu substrate. It underscores the significant impact of feedstock powder attributes, along with gas pressure and temperature, on the properties and microstructural aspects of Cu coatings. These findings are crucial for optimizing LPCS parameters and establishing a link between the characteristics of Cu feedstock powder and the resultant properties. The principal conclusions drawn from this study include:

1. Statistical analysis revealed that the process gas pressure, in relation to its temperature, significantly influenced changes in coating weight and thickness. Optimal cold spray coatings were consistently achieved at an operating temperature of approximately 400°C and a pressure of around 1.99 MPa, close to the highest operational limits of the LPCS system, for all Cu powders tested.
2. Coatings deposited using gas atomized powder devoid of satellite particles, characterized by a more spherical morphology (Powder C), exhibited reduced porosity, higher hardness, increased flattening ratio, and high adhesion strength when compared to coatings deposited using gas atomized powder containing microsatellite particles (Powder B) and the electrolytic powder (Powder A).
3. The appealing characteristics of the coating are linked to the higher sphericity and absence of microsatellites in the Cu powder, which together diminish the particle surface area, thereby lowering the susceptibility to surface oxidation. This reduction in surface oxides leads to a decrease in the required critical velocity and allows for more extensive plastic deformation during deposition. Furthermore, the initial feedstock's larger grain size contributes to an increase in ductility and the plastic deformation capability of the feedstock. Therefore, attaining a high-quality deposition with this powder using LPCS technology is achievable.
4. The coating's microstructure is subject to uneven plastic deformation throughout, from the interface to the center and beyond, as well as within the individual powder particles. This process results in a heterogeneous grain size distribution and the formation of two distinct zones. The area adjacent to the interface is notably affected by the peening effect, leading to substantial grain refinement in this specific zone. Meanwhile, at the particle triple junction

boundaries, where intense deformation takes place, a large number of grain refinement develops. In contrast, closer to the center of the coating and within the core of the particles, the grains are larger. The powder C coating, in particular, shows a higher level of local plastic deformation and more pronounced grain refinement within its particles.

5. All substrates demonstrated grain refinement near the surface, primarily due to dynamic recrystallization induced by the peening effect of the powder during cold spray. Notably, the satellite-free gas atomized coating displayed an enhanced peening effect, leading to the formation of smaller grains near the substrate's surface.

Chapter 6

Evolution of Microstructure, Strength, and Ductility in 3D-Printed Low-Pressure Cold Spray Copper: Effects of Process Gas and Heat Treatment

(Published manuscript, International Thermal Spray Conference 85045, 153-158, 2025 and manuscript ready for submission to a Journal paper)

6.1 Abstract

The main objective of this study is to investigate the effects of N_2 and He process gases and heat treatment on the microstructure and mechanical properties of 3D-printed pure Cu through low-pressure cold spray system. Microstructural analysis is conducted using X-ray diffraction, optical microscopy, and electron backscatter diffraction. Mechanical properties are studied through hardness, and tensile tests. Deposit made using He display enhanced efficiency in deposition owing to the increased particle velocity attainable through its use. However, N_2 processed sample shows enhanced plastic deformation and a higher dislocation density, resulting in lower porosity compared to that made with He. This difference is influenced by the number of deposition passes and the peening effect, with N_2-processed sample requiring more passes to achieve the same thickness as He-processed sample. This microstructural characteristic leads to a microhardness of 112 HV for N_2 deposit, which is 1.3 times higher than that of He deposit. Both as-sprayed deposits exhibit brittle failure and limited ductility. Heat treatment is carried out at 500 °C and 700 °C for 4 hours to enhance the mechanical strength and ductility of the coatings. Microstructural observations reveal that recrystallization and grain growth occur at both temperatures, but they are more prominent at 700 °C. However, samples depositted with He exhibit a higher recrystallization temperature and display a finer distribution of grain sizes after annealing. Heat treatment at 500 °C partially heals non-bonded interfaces, while treatment at 700 °C effectively eliminates most non-bonded interfaces and enhances the prominence of spheroidized voids. Tensile tests show that after heat treatment at 500 °C, the N_2 and He samples achieve strengths of 180 MPa and 174 MPa, and ductility of 14% and 16%, respectively. Following heat treatment at 700 °C, the ultimate tensile strength increases to 213 MPa and 193 MPa, and elongations is improved to 28%

and 25%, respectively, for N_2 and He samples. This is a significant increase from the as-sprayed conditions, where tensile elongations were less than 0.2% and tensile strengths were only 70 MPa and 68 MPa for N_2 and He samples, respectively. However, despite these gains, the tensile strength and elongation of the samples still fall short of those observed in severe cold-rolled and annealed bulk Cu, reflecting the limitations of the low-pressure cold spray system and the heat treatment conditions used. Overall, the findings suggest that using N_2 at suitable deposition parameters as a process gas for cold spraying of Cu, along with annealing at optimal temperatures, can be a cost-effective alternative to using the more expensive He gas.

6.2 Introduction

Additive manufacturing (AM) processes are classified under a "bottom-up" manufacturing approach, where objects are constructed layer by layer [1,2]. This method primarily involves the layer-wise formation of intricate shapes from powders or wires, which are fused together by melting under the control of a high-power energy source such as laser, electron beam, or arc [3–5]. In metal AM, the rapid solidification of these melted materials leads to the creation of unique microstructures, which occur due to the quick cooling rates that deviate from equilibrium conditions. Technologies such as selective laser melting (SLM), directed energy deposition (DED), and electron beam melting (EBM) have successfully been used to manufacture complex components from alloys of titanium, iron, nickel, and metal matrix composites [166–168]. Yet, the suitability of metals for these fusion-based AM technologies depends on several critical properties: they must efficiently absorb laser energy, exhibit low thermal conductivity, and be free of elements with low boiling points. These requirements pose significant challenges for metals with lower melting points, like those based on aluminum, magnesium, or copper, highlighting the necessity for partial or non-melting AM processes.

Cold spray (CS) is a solid-state additive manufacturing technique primarily utilized to create specific metal-based mechanical structures or parts [7,27,34]. Unlike traditional high-temperature deposition methods, cold spray deposits are formed mainly through the substantial kinetic energy of high-speed feedstock particles rather than their thermal energy. In the CS process, these particles are accelerated to high velocities using a low-temperature supersonic compressed gas flow, typically nitrogen, helium or air [9,10,169]. Importantly, the relatively low temperature of the inert gas propellant stays below the melting point of the feedstock particles, and allows the particles to remain solid post-deposition. This

characteristic helps prevent common high-temperature deposition defects such as oxidation, residual thermal stress, or phase transformations. Consequently, due to its unique properties, cold spray technology has become an essential method for producing low-melting and oxidation-prone metal-based materials. Our focus is on copper and its alloys cold spray deposition.

Huang et al. [170] successfully created pure copper components that exhibited higher electrical conductivity and hardness than those made using SLM technique. Yang et al. [171] manufactured thick, dense copper bulks via cold spray, focusing on the impact behavior of the particles and the mechanical anisotropy of CS deposits. Chen et al. [87] showed that pure copper with exceptional strength and ductility could be achieved by managing grain refinement and dislocation density during CS fabrication. Bagherifard et al. [77] produced freestanding samples of CuCr1Zr alloy using a mix of microcrystalline (MC) and nanocrystalline (NC) powder particles, finding that cold spray deposition offers significant potential for creating bimodal materials with a heterogeneous phase structure. Jasthi et al. [15] illustrated that cold spray additive manufacturing could be utilized to deposit composites of Cu-Cr-Nb and Fe-Ni-Cr, providing an alternative method for producing components for rocket engine applications.

The microstructure and mechanical integrity of consolidated components are predominantly determined by the level of particle deformation; more extensive deformation typically enhances strength. The selection of the process gas is critical in this process, as it directly influences the degree of deformation and thus the overall mechanical performance of the deposit [172,173]. While helium is often preferred for its superior deposition outcomes in cold spray additive manufacturing (CSAM), it comes at the expense of a much higher cost. Research on process gases, crucial to the properties of cold sprayed materials, has focused on different aspects of deposition efficiency [174], particle velocity [169], and hardness [175]. Lama et al. [176] found that helium in aluminum alloy deposits resulted in microhardness of 149 HV, and yield and ultimate strengths of 383 MPa and 487 MPa, respectively, these are 1.1, 1.17, and 1.08 times higher than those achieved with nitrogen deposits. Similarly, Kim et al. [88] reported that the use of helium as a process gas resulted in yield strength of 415 MPa, which is higher than that obtained using nitrogen gas (340 MPa), during the compressive deformation of copper parts.

Currently, a significant challenge in CSAM is the low ductility of the deposits, which results from severe plastic deformation of powder particles and cold work hardening. To improve ductility, CSAM materials typically undergo post-processing treatments to facilitate recrystallization and consolidation [177]. For example, Yu et al. [178] found that Cu displayed high strength but poor ductility, with negligible elongation, which was significantly improved by 2 orders of magnitude (from ∼0.2% to ∼25% strain) trough low temperature annealing at 350 °C for 1 h. Meng et al. [179] reported that cold sprayed 304 stainless steel initially showed less than 1% elongation, which increased five times after heat treatment at 950 °C for 1 h. Similarly, for Inconel 718, elongation increased from a mere 0.5% in its as-sprayed state to 8–10 times that figure following annealing at temperatures between 990 °C and 1200 °C for 1 to 4 hours [180,181]. Yin et al. [182] observed approximately 2.5% elongation in as-sprayed cold-sprayed Cu, which increased to 7.6% after annealing at 500 °C for 4 hours. Additionally, innovative post-processing methods such as electric pulse processing (EPP) and friction stir processing (FSP) have been employed to enhance ductility of CSAM materials by 19% and 40% in CSAM Cu, respectively [183]. These results have established a foundation for further advances in enhancing ductility and strength within the cold spray community. Nonetheless, there remains a lack of comprehensive studies on how annealing behavior and the resulting ductility of CSAM materials are influenced by different levels of initial cold work hardening under the effect of various process gas species.

Due to its outstanding thermal and electrical conductivity, pure copper is one of the most extensively utilized materials in engineering [184]. These exceptional properties have led to its broad application across various industrial sectors. Consequently, significant research has been initiated into the CS fabrication and subsequent heat treatment of pure Cu components to meet diverse industrial requirements. Several researches have explored how post-spray heat treatment (PSHT) impacts the microstructural and mechanical anisotropies of Cu deposits. Yang et al. [34] demonstrated that the strong anisotropy in in-plane tensile strength can be effectively reduced with post-spray heat treatment. However, the presence of parallel multiple passes during cold spraying remains the primary obstacle to further improving the inherent in-plane tensile anisotropy. Yin et al. [31] found that mechanical anisotropy is significantly more pronounced in deposits produced with a bidirectional nozzle scanning strategy compared to those produced with a cross-hatching strategy, and that annealing had no substantial effect on mechanical anisotropy. Hutasoit et al. [35] suggested that although the

metallurgical bonding in sintered samples was significantly better than in as-deposited samples, the formation of large pores along grain boundaries acted as crack initiation sites, leading to poor mechanical properties regardless of the samples' build orientation. In addition, Yu et al. [178] examined the fracture mechanics of cold-sprayed copper before and after being subjected to low annealing temperatures. Their findings demonstrated that annealing could enhance the ductility in the areas surrounding pores, which serve as initiation points for cracks. However, a significant gap exists in a thorough assessment and comparison of the fundamental properties of cold sprayed Cu samples produced by low-pressure CS system parameters, especially those processed with various process gases such as N_2 and He, which induce different levels of work hardening, both prior to and following heat treatment. In response, this study has conducted a comprehensive analysis to evaluate the effects of each process gas on the velocity of Cu particles, the efficiency of CS deposition, and the microstructural alterations in 3D printing of Cu using a low pressure system. Additionally, examining post-heat treatments at various temperatures provides insights into the recrystallization processes of each sample, influenced by varying degrees of work hardening and dislocation density. This research also discusses the relationships between microstructure, hardness, and tensile properties.

6.3 Experimental Methods

6.3.1 Feedstock powder and CS manufacturing procedure

A bulk Cu material was 3D-printed using CSAM, with N_2 and He serving as the process gases. The initial Cu powder (5N Plus Inc., Quebec, Canada) shown in Figure 58a used in the manufacturing process had a purity of approximately 99.9%. The powder had an equiaxed grains microstructure with the average grain size of approximately 22.6 μm, as depicted by Figure 58b, with a particle size distribution ranging from 10−58 μm and an average particle size of 31 μm, as shown in Figure 58c and d. For morphological analysis, powders were put on the conductive carbon adhesive tapes and were studied via a scanning electron microscope (SEM, model: Zeiss Leo UltraPlus FESEM). Particles were spherical with some carrying smaller satellite particles. Powders were also vibratory polished for 6 hours using 50-nm colloidal silica to remove the deformed surface layer for electron backscatter diffraction (EBSD) characterization.

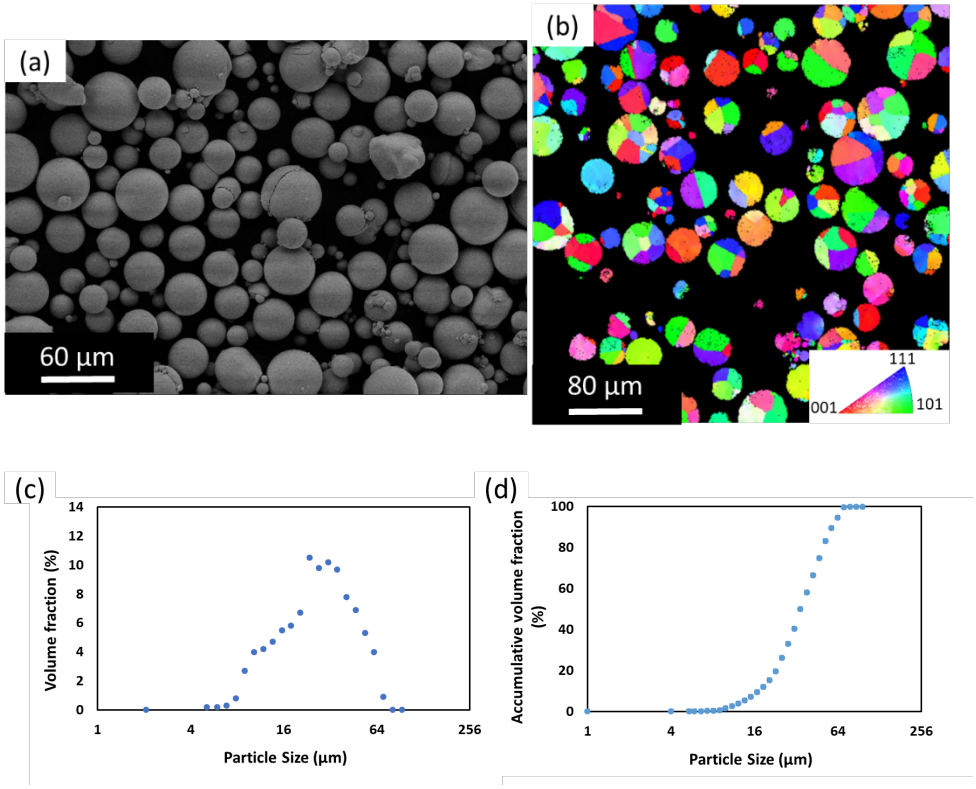


Figure 58: (a) Morphologies of copper powder observed by SEM, (b) EBSD grain orientation map for cross-sectional powder particles, (c) volume fraction (%) and (d) accumulative volume fraction (%) of pure Cu powder.

The parameters used for the cold spray are listed in Table 14, including nozzle pressure of 1.99 MPa, gun speed of 40 mm/s, and gas temperature of 400 °C, with the Cu powder being deposited onto an Al build plate from a distance of 30 mm. A commercial Supersonic Spray Technologies (SST) Series P Cold Spray System, produced by Centerline in Windsor, Canada, was employed to 3D-print the as-received Cu powders. In this process, the pure Cu powders were accelerated through a converging–diverging de Laval UltiLife TM nozzle to supersonic velocities in a low-pressure system. Table 15 outlines the specifications of the cold spray machine utilized in this study.

Table 14: Cold spray deposition parameters for N_2 and He processed samples

Sample type	standoff distance (mm)	nozzle speed (mm/s)	X-offset (mm)	No. of deposition passes	powder feed rate (g/min)	Gas Pressure (MPa)	Gas Temperature (°C)

N_2 processed	30	40	-0.5	6	20.8	1.99	400
He processed	30	40	-0.5	3	20.8	1.99	400

Table 15: Specification of SST cold spray nozzle

Nozzle type	Nozzle Length	Nozzle Orifice Diameter	Nozzle Exit Diameter
De Laval UltiLife™	120mm	2 mm	6.3 mm

Figure 59 presents images of the CSAM Cu; (a) depicts the use of N_2 gas and (b) the use of He gas. The dimensions of the cold sprayed Cu materials produced with both N_2 and He gases were 125 mm in length, 60 mm in width, and 3.5 mm in thickness. Additionally, as illustrated in Figure 59 , there was no spalling observed between the Al substrate and the deposited Cu, nor were there any cracks in the Cu material. Deposition efficiencies were assessed on Cu parts measuring 125 x 60 x 3.5 mm, that were 3D-printed on aluminum build plates. These build plates were initially cleaned in an acetone bath and subsequently weighed on a digital scale with a precision of 0.0001 g. They were weighed once more after the spraying process to determine the weight gain. Deposition efficiency was then calculated by dividing the weight gain by the product of the mass feed rate and the spray duration on the substrate. The cold-sprayed parts were subsequently removed from the substrate and machined through electrical discharge machining (EDM) with the precise dimensions of these specimens detailed in Figure 60a and tensile specimens as depicted in Figure 60b.

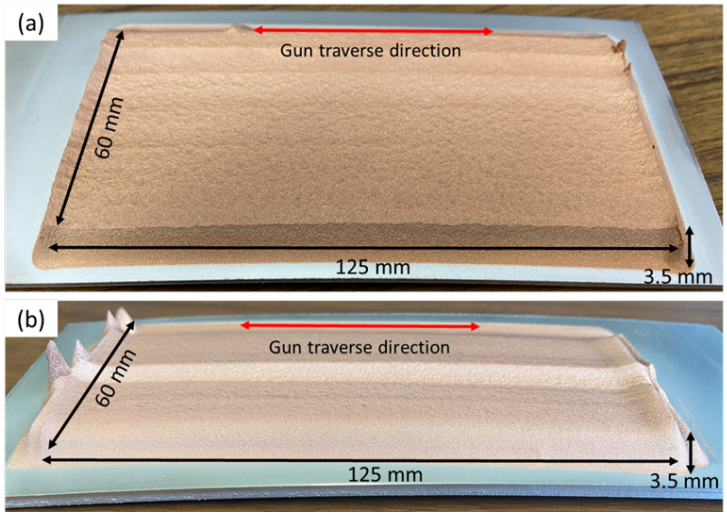


Figure 59: Macro images of cold sprayed Cu materials with different process gasses: (a) process gas N_2, (b) process gas He.

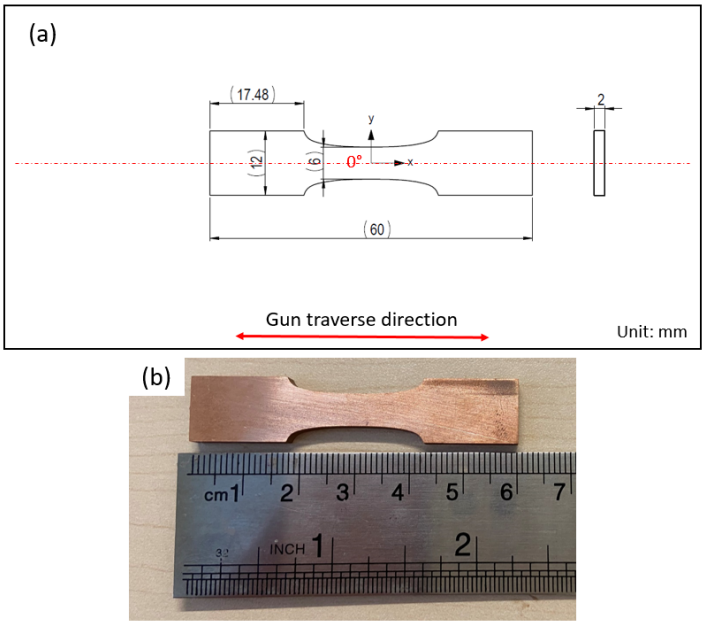


Figure 60: (a) dimensions of the tensile specimen; and (b) the extracted tensile specimen from the 3D-printed part.

6.3.2 Heat treatment

Heat treatments were conducted on the as-deposited samples to assess their impact on the evolution of microstructures and mechanical properties. The tensile samples were subjected to heat treatment in a vacuum tube furnace at temperatures of 500°C and 700°C, holding each temperature for 4 hours in an argon gas atmosphere, with a heating rate of 10°C per minute. Following the treatment, the samples were allowed to naturally cool to room temperature inside the furnace.

6.3.3 Microstructural characterization

Phase identifications and further analysis for the 3D-printed components were conducted using a Bruker D8-Discover X-ray diffraction (XRD) system, which is equipped with a VÅNTEC-500 area detector and utilizes Cu-Kα radiation (λ = 1.5406 Å) under operating conditions of 40 kV and 40 mA. X-ray measurements were conducted three times for each sample to obtain error bars for further analysis. To examine the microstructures before and after heat treatment, sections of the 3D-printed parts were cut perpendicular to the direction of the gun traverse, then hot mounted, polished, and etched. These sections were examined using a digital VHX-7000, Keyence microscope. Additionally, Electron backscatter diffraction (EBSD) analyses were performed by TESCAN VEGA3 SEM equipped with a BRUKER e^{-}Flash^{FS} detector. For EBSD investigations, metallography steps were completed by vibratory polishing in Buehler VibroMet2 machine for about 6 hours using 50-nm colloidal silica to remove the deformed surface layer. The EBSD characterization was conducted with an accelerating voltage of 25 kV and a step size of 500 nm.

6.3.4 Physical and mechanical properties

Porosity in the cold-sprayed coatings and 3D printed parts was evaluated in accordance with ASTM E2109, using SEM images captured at both lower (x2000) and higher (x8000) magnifications [104]. A total of 25 SEM images were analyzed across the cross-section of each coating, employing binary segmentation via ImageJ for quantification.

For all deposits, the Vickers microhardness was measured using a Manual Vickers Hardness Tester (Wilson) with a 200 g load and a dwell time of 15 seconds. An average value was determined from twenty measurements for each sample. Quasi-static tensile tests were conducted in accordance with ASTM E8/E8M-15a standards using an Instron 8874 servo-hydraulic machine, which has a load

capacity of ±25 kN. These tests were performed in displacement control mode at a rate of 0.05 mm per minute. Strain measurement was carried out using a GOM ARAMIS 3D digital image correlation (DIC) system, which features a resolution of 5 megapixels and a maximum capture rate of 15 frames per second. Three tensile specimens were tested from both as-sprayed and heat-treated 3D-printed samples. The fractured surfaces of the samples were examined using a scanning electron microscope (SEM, model: Zeiss Leo UltraPlus FESEM).

6.4 Results and discussion

6.4.1 Effect of process gas species on particle velocity and deposition efficiency

Particle velocity before impact is a critical factor in the cold spray process. For particles to adhere successfully to the substrate in cold spraying, they must be accelerated to a high enough velocity. Each sprayed material has a specific critical velocity required for effective deposition. Particles must exceed this critical velocity to form a coating on the substrate [40,150]. Figure 61 shows the velocities of Cu particles for different process gases, N_2 and He, based on particle size. The velocity of these particles is influenced by the size of the particles, the properties of the material, and the characteristics of the gas, as calculated using the following relation [31,149]:

$$v_p \approx \left(1 - \exp\left(-\frac{3C_d\rho_g L}{4\rho_p d_p v_g}\right)\right) \quad (7)$$

Here, V_p represents the particle velocity at the nozzle exit. V_g represents the average gas velocity at the nozzle exit, C_d is the drag coefficient, ρ_g indicates the process gas density, ρ_p indicates the density of the particle material (8960 kg/m^3), d_p is the diameter of the particle, L represents the length of the nozzle. Particle velocity calculations were made at a pressure of 1.99 MPa and temperature of 400 °C, which were determined as the optimal processing parameters for this powder in a prior study [146,185]. The drag coefficient varies depending on the particle's Mach number and size [31].

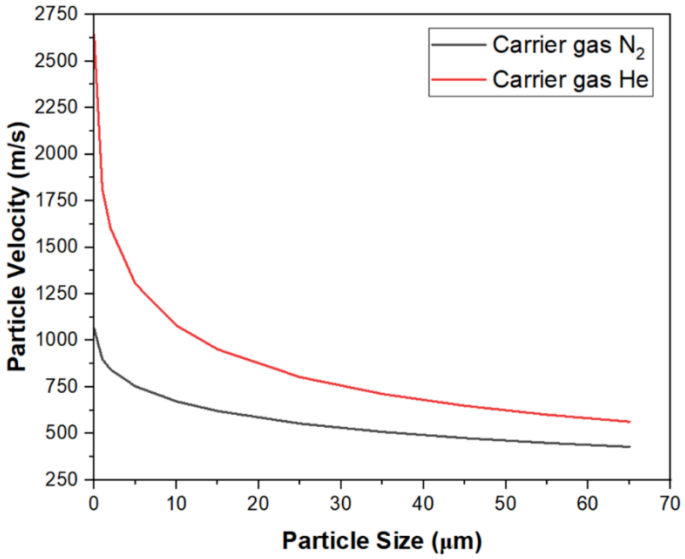


Figure 61: Particle velocities vs. particle size of pure Cu with different process gases of He and N_2 at optimum gas temperature and pressure of 400°C and 1.99 MPa, respectively.

Under the optimal processing conditions for this study, particle velocity was found to decrease as particle size increased, a trend consistent across both types of process gases as depicted in Figure 61. The graph shows that with helium as the process gas, particle velocity is significantly larger than with nitrogen across all particle sizes, with the difference being especially pronounced at smaller particle sizes. For instance, at particle sizes below 10 microns, velocities achieved with He gas can be more than double those with N_2 gas, leading to higher acceleration of particles when using He. Data from deposition efficiency calculations indicate that deposition efficiency is highly dependent on particle impact velocity, as discussed in [169,186]. The switch from nitrogen to helium as the driving gas significantly boosts deposition efficiency (DE_{N2}: 23% and DE_{He}: 45%), this is due to the higher gas velocity achieved with Helium, which has a lower molecular weight. The increase in velocity offsets the decrease in gas density, consequently raising the drag on the particles [186]. In practice, the deposition thickness of 3.5 mm is achieved with just three passes using He gas, whereas six passes are required to achieve the same thickness with N_2 gas.

6.4.2 Microstructures of CSAM Cu materials made by using different process gasses before and after heat treatment

Figure 62 presents the results of the X-ray diffraction analysis, showing that the CSAM Cu retained the α-Cu single phase, with no phase transformations occurring. This stability is attributed to the fact that, unlike conventional laser-based AM or thermal spray processes that rely on melting and solidifying materials, CSAM employs solid-state plastic deformation for material deposition, avoiding the need for high-temperature heat sources. Additionally, CSAM stands out among AM technologies as it does not melt the initial powder, thereby reducing the likelihood of degradation due to oxide or impurity formation. Furthermore, no phase transformations were detected following the heat treatment of the 3D printed parts.

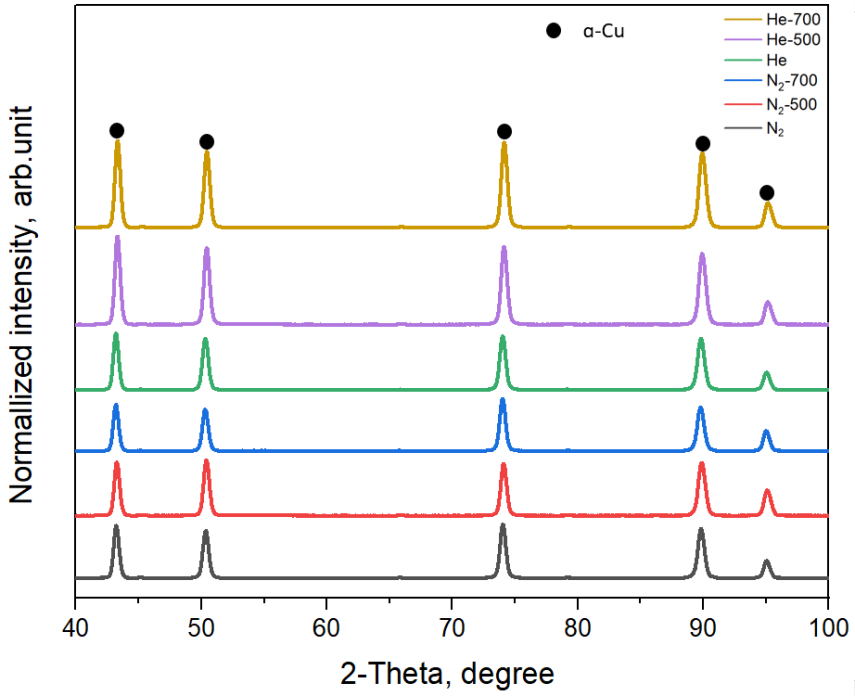


Figure 62: XRD spectra of the as-sprayed and heat treated Cu deposits produced using N_2 and He process gases, the XRD reference for pure copper is PDF card number 04-0836 from the ICDD PDF-4+ database.

Ideally, XRD peaks are broadened due to effects from crystallite size and intrinsic lattice strain [88,187]. From analyzing peak broadening, it is possible to ascertain values for intrinsic strain and average crystallite size. The Williamson–Hall method explains that diffraction peak profiles become

broader when sub grains are small and the crystal lattice is distorted by defects [188]. The overall broadening observed in an XRD peak is outlined in [189,190],

$$\boldsymbol{\beta_{\mathcal{T}} = \beta_{\mathcal{D}} + \beta_{\varepsilon}} \quad (8)$$

In this context, β_T represents the total broadening of the peak, β_D is the broadening attributed to crystallite size, and βε is the broadening resulting from strain. According to the Scherer equation:

$$\boldsymbol{\beta_{\mathcal{D}} = \frac{\mathcal{K}\lambda}{\mathcal{D}\cos\theta}} \quad (9)$$

In this equation, β_D represents the full width at half maximum (FWHM), which is the measure of peak broadening in radians. K=0.9 is the shape factor, λ= 0.15406 nm specifies the wavelength of the X-ray source, D stands for the crystallite size, and θ indicates the peak positions in radians. Additionally, the broadening of XRD peaks attributable to micro strain is described as follows:

$$\boldsymbol{\beta_{\varepsilon} = 4\varepsilon\tan\theta} \quad (10)$$

Here, βε represents the broadening of the peak caused by strain, ε denotes the strain itself, and θ is the position of the peak in radians. Therefore,

$$\boldsymbol{\beta_{\mathcal{T}} = \frac{\kappa\lambda}{\mathcal{D}\cos\theta} + 4\varepsilon\tan\theta} \quad (11)$$

Consequently, Equation 2, after rearrangement, can be written as follows:

$$\boldsymbol{\beta_{\mathcal{T}}\cos\theta = \frac{\kappa\lambda}{\mathcal{D}} + 4\varepsilon\sin\theta} \quad (12)$$

This equation represents the Uniform Deformation Model (UDM). A graph is created plotting 4SinΘ on the X-axis and βCosΘ on the Y-axis for various (hkl) planes of all 3D-printed Cu materials, both before and after heat treatment, as depicted in Figure 63a. From this graph, the intercept and slope provide measurements of crystallite size and lattice strain, respectively, and dislocation density is calculated using the formula $\rho = \frac{14.4\varepsilon^2}{b^2}$ [191,192], where b is the Burgers vector (0.3615 nm for Cu). It has been noted that the slope of the graph for each corresponding model is negative. Several studies have reported a negative slope in the Williamson–Hall plot [188,190], which suggests a shrinkage in lattice spacing. This relationship between lattice shrinkage and the negative slope is explained through the peak width in XRD peaks. As the Θ value increases, the intensity and width of the XRD peaks

diminish across different planes. According to the UDM equation, as the Θ value increases (2Θ value ranging from 40°-100°), both the CosΘ and β_T values decrease, while the SinΘ value increases, resulting in a linear plot with a negative slope. The results are displayed in Figure 63b. The higher levels of micro strain and dislocation density in the as-sprayed deposits result from the extremely high plastic strain rates caused by high-velocity impacts during CS, potentially reaching 10^9 s^{-1} [162,193]. It has been observed that the dislocation density in Cu material sprayed with N_2 process gas is over twice that of He, ρ_{N2}=1.04 x 10^{14} $1/m^2$ and ρ_{He}= 0.48 x 10^{14} $1/m^2$, likely due to more deposition passes and greater peening effects experienced by material printed by N_2 process gas. Also, the lower dislocation density observed in helium-based cold spray deposits, compared to those sprayed with nitrogen, results from the complex interplay between particle velocity and temperature. Helium, due to its low molecular weight and high specific heat ratio, produces higher gas and particle velocities but results in lower particle temperatures. This is because helium's high thermal conductivity and low density lead to more efficient cooling and less heat transfer to the particles during acceleration. As a result, particles deform intensely upon impact, but the associated adiabatic heating may promote dynamic recovery or localized recrystallization, reducing the net dislocation density. In contrast, nitrogen provides slightly higher particle temperatures and lower velocities, which facilitate more uniform plastic deformation with less dynamic recovery, leading to a higher accumulation of dislocations. Thus, the difference in dislocation density arises from the balance between dislocation generation and annihilation mechanisms, both influenced by the thermophysical properties of the process gas. In heat treated samples, microstrain and dislocation density are reduced compared to their as-sprayed counterparts due to recrystallization during heat treatment. Although recrystallization can occur in Cu particles during CS due to intense plastic deformation, this is generally limited to a small area near the particle interface [33, 34]. However, during annealing, recrystallization occurs over a much broader area, a finding supported by earlier studies [194,195] and discussed further below. The size of the crystallites or sub-grains in the sample microstructures remains consistent, approximately 14–15 nm, in both as-sprayed and heat-treated conditions.

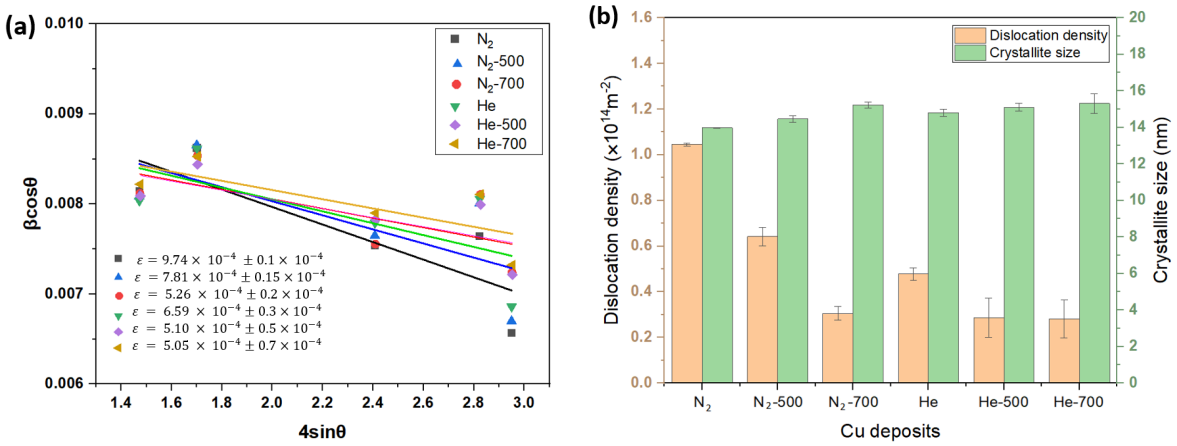


Figure 63: (a) Williamson-Hall plots for XRD diffraction patterns, (b) calculated dislocation density, and crystallite size for as sprayed and heat treated Cu deposits produced by N_2 and He process gases.

Figure 64a and b display the etched microstructures viewed under an optical microscope (OM) from the cross-sections of the as-sprayed samples produced using N_2 and He as process gases, respectively. The microstructures reveal flattened spray splats due to the plastic deformation of solid particles upon impact, although porosity is evident within the deposits. Some internal interfaces are well bonded, as marked by red arrows in Figure 64a and b. This strong bonding is attributed to shear instabilities facilitated by thermal softening, which occur due to the high impact velocities of Cu particles during CS [40]. The proportion of these well-bonded interfaces relative to the total interface areas aligns with the impact conditions predicted by the spraying parameters [31]. Owing to the use of a low-pressure system for CSAM in this study, there is a notable presence of poorly bonded interfaces. The deposited particles exhibit significant work hardening, with implications for the mechanical properties of the as-sprayed deposits to be discussed subsequently. Within the microstructure, characteristic features from the deformation are identifiable: 1) At the center of the splat (indicated by a green dashed line), grains show minimal deformation and refinement, maintaining sizes similar to the as-received powder (compare Figure 58b); 2) Grain refinement near the particle-particle interfaces results from dynamic recrystallization [161,162,196], as highlighted by the blue dotted line.

The strain to failure of as-sprayed deposits is relatively low, primarily due to the material being in a highly work-hardened state and the presence of some unbonded internal interfaces between the spray splats. Annealing can cause the microstructure to rearrange from its deformed state through diffusion-

driven processes, along with recrystallization and the spheroidization of planar inter-particle defects, which is akin to what occurs during sintering [197]. Consequently, ductility is anticipated to significantly improve following a post-spraying heat treatment. To explore the microstructural changes in the as-sprayed deposits, two different annealing temperatures are employed, each having distinct effects on diffusion and recrystallization processes.

Figure 64c and d display the microstructures that result from annealing deposits made with N_2 and He gases at 500 °C for four hours, respectively, while Figure 64e and f illustrate the microstructures annealing at 700 °C for the same duration. The etching process reveals distinct features at each temperature. At the lower annealing temperature of 500 °C, recrystallization begins early in the highly deformed areas, leading to the formation of new, small, strain-free grains and annealing twins. Nevertheless, some original particle-particle interfaces remain visible, with some non-bonded interfaces still present (indicated by yellow arrows in Figure 64c and d). It is important to note that the dislocation density in the microstructure deposited using N_2 gas is more than double that of the microstructure deposited with He gas. Consequently, the initial activation energy required and the subsequent progress of recrystallization after annealing are expected to be greater in the microstructures deposited by N_2 gas. When the annealing temperature is raised to 700 °C (Figure 64e and f), the original splat boundaries become indistinguishable. There is a more pronounced grain growth, and non-bonded interfaces begin to disappear. This suggests that annealing at 700 °C more effectively promotes recrystallization and grain growth, as well as reducing defects through surface diffusion along non-bonded interfaces.

The OM microstructural examination of cold-sprayed Cu deposits highlights that both porosity and non-bonded interfaces in the as sprayed state (as shown in Figure 64a and b) contribute significantly to potential fractures in the material. After undergoing annealing at 500 °C, it is observed that some non-bonded interfaces are found to be partially healed out due to diffusion, mimicking a sintering effect. This process also appears to transform the free volume defects in as-sprayed state into spheroidized voids, effectively reducing surface energy, indicated by green arrows in Figure 64c and d. Furthermore, this annealing temperature promotes a reduction in dislocation densities and encourages grain growth, leading to a more homogeneous microstructure. These improvements at the lower annealing temperature decrease defects and potentially enhance the mechanical properties of the deposit.

Increasing the annealing temperature to 700 °C, significantly above the recrystallization temperature (shown in Figure 64e and f), results in the elimination of most non-bonded interfaces while enhancing the prominence of spheroidized voids and grain growth. According to Huang et al. [197], during heat treatment, microvoids among deposited particles may merge to form larger, observable pores. In these annealed deposits, recrystallization twins are also evident, as indicated by purple arrows in Figure 64c-f.

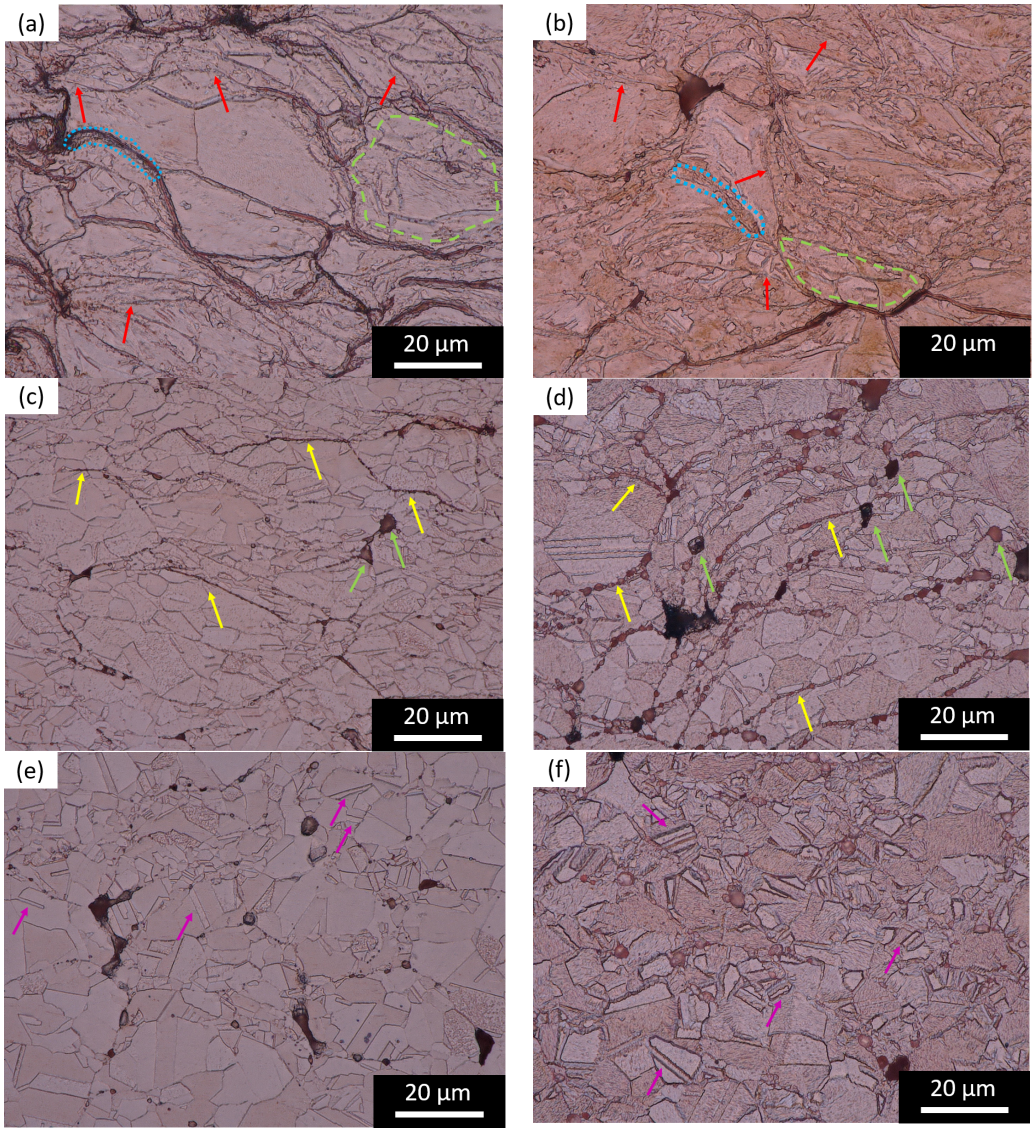
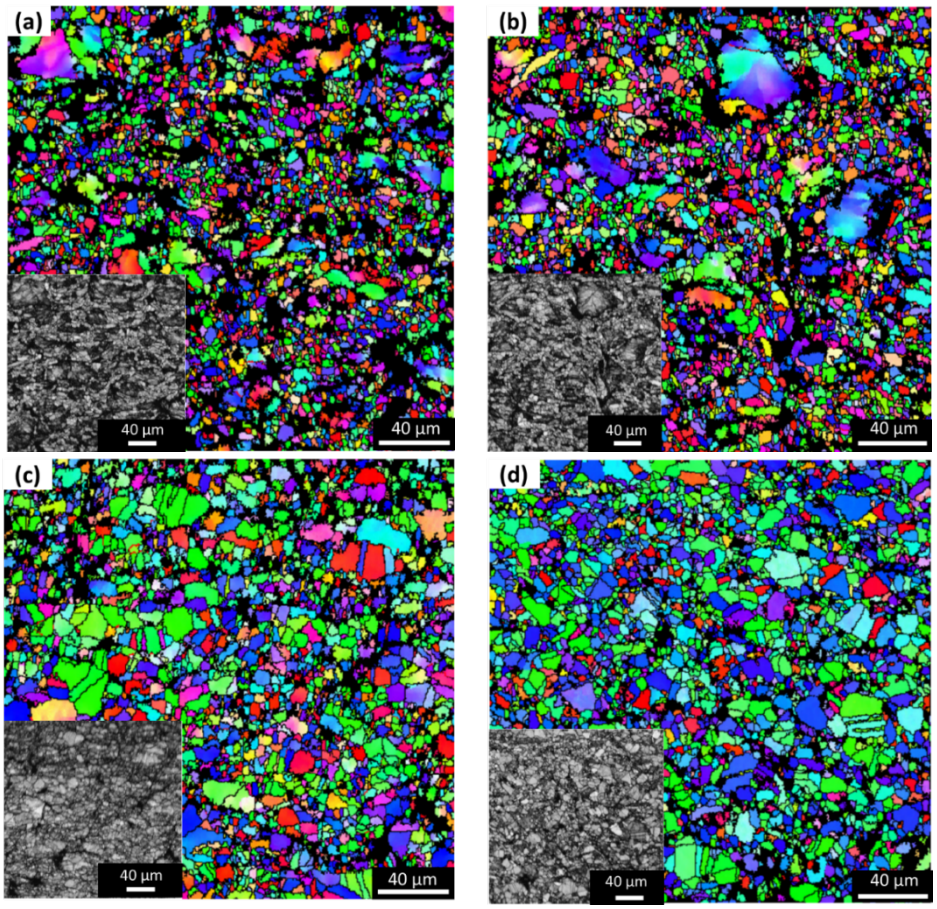


Figure 64: Optical micrographs of (a, b) as-sprayed, (c, d) 500 °C HT, (e, f) 700 °C HT. (a, c, e) show the cold spray deposits produced using N_2 process gas and (b, d, f) show the cold spray deposits produced using He process gas. The red arrows, green dashed and blue dotted lines in (a) and (b) shows well-bonded interfaces, grains with minimal deformation and recrystallized grains, respectively. The yellow and green arrows in (c) and (d) highlight the non-bonded particle–particle interface and spheroidized voids, respectively. Purple arrows in (e) and (f) indicate recrystallization twins.

The EBSD maps displaying the as-sprayed and heat-treated microstructures under various conditions are depicted in Figure 65. In the as-sprayed state, the microstructure created using N_2 gas exhibits significant flattening and plastic deformation, leading to more pronounced grain refinement (Figure 65a) compared to the microstructure obtained from He gas, where particles appear less flattened and show less grain refinement (Figure 65b). After heat treatment, differences between the two microstructures remain evident. Specifically, the grain size in the microstructure deposited by N_2 (Figure 65c and e) is noticeably larger than in the microstructure deposited by He (Figure 65d and f), likely due to the greater plastic deformation experienced by the N_2-deposited microstructure, which facilitates more recrystallization and subsequent grain growth. As the annealing temperature increases, grain growth is observed in both microstructures, particularly evident in Figure 65e and f. From the 'band contrast' images (Figure 65), it is noticeable that interfaces between deposited particles in both microstructures, deposited by N_2 and He, gradually fade due to diffusion from heat treatment. However, this process tends to occur more rapidly in the microstructure deposited by N_2, likely because of enhanced atomic diffusion, attributed to the closer particle contact resulting from a higher peening effect during deposition [197].

The statistical analysis of grain size distribution for both the as-sprayed and annealed states (Figure 66) highlights differences in the microstructures deposited by N_2 and He. In comparison to the as-sprayed state, the grain size distribution in the annealed states is noticeably larger. For instance, in the annealed microstructures produced from N_2 and He, the proportion of grains smaller than 6 μm is 50% and 64% at 500 °C, and 48% and 52% at 700 °C, respectively. This contrasts with 84% and 77% in the as-sprayed states of N_2 and He, respectively. Recrystallization, which involves dislocation rearrangement and/or grain rotation followed by grain growth during heat treatment, leads to an increase in grain size. Existing research [192,198] suggests that a high number of recrystallized grains is advantageous because they can effectively obstruct dislocations, thereby enhancing strain-hardening

capacity and improving both tensile strength and ductility. Notably, microstructures created using He exhibit a larger grain size distribution in the as-sprayed state and a smaller distribution after heat treatment compared to those created using N_2. This difference is attributed to the greater plastic deformation experienced by N_2, due to a higher number of deposition passes and the impact of peening, which results in finer grains in the as-sprayed state and accelerates recrystallization and subsequent grain growth in the annealed state due to a higher defect density [199].



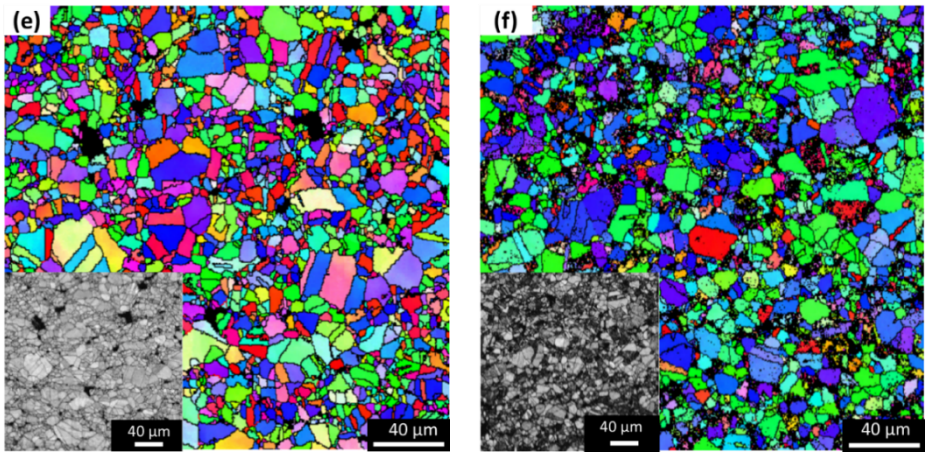
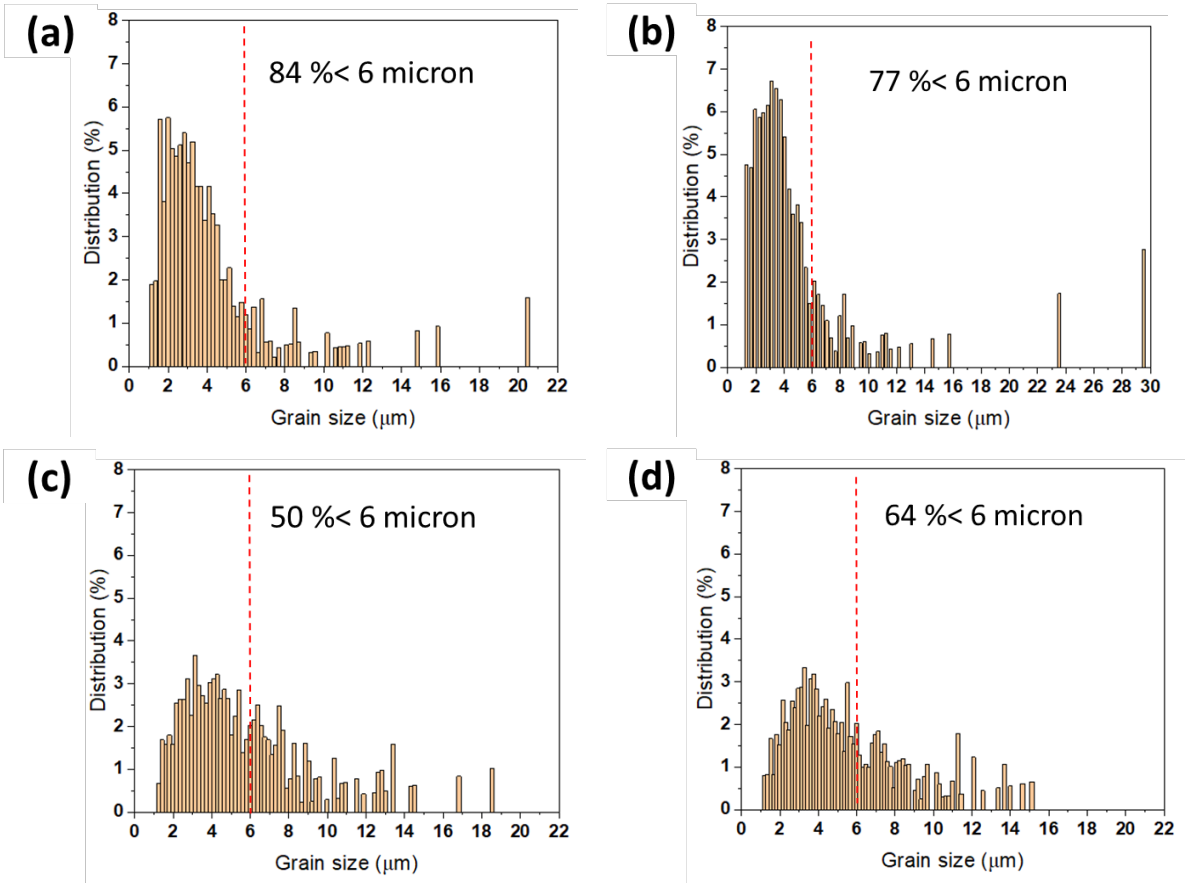


Figure 65: Inverse pole figure (IPF) and image quality (IQ) maps of (a, b) as-sprayed, (c, d) 500 °C HT, (e, f) 700 °C HT. (a, c, e) show the cold spray deposits produced using N_2 process gas and (b, d, f) show the cold spray deposits produced using He process gas.



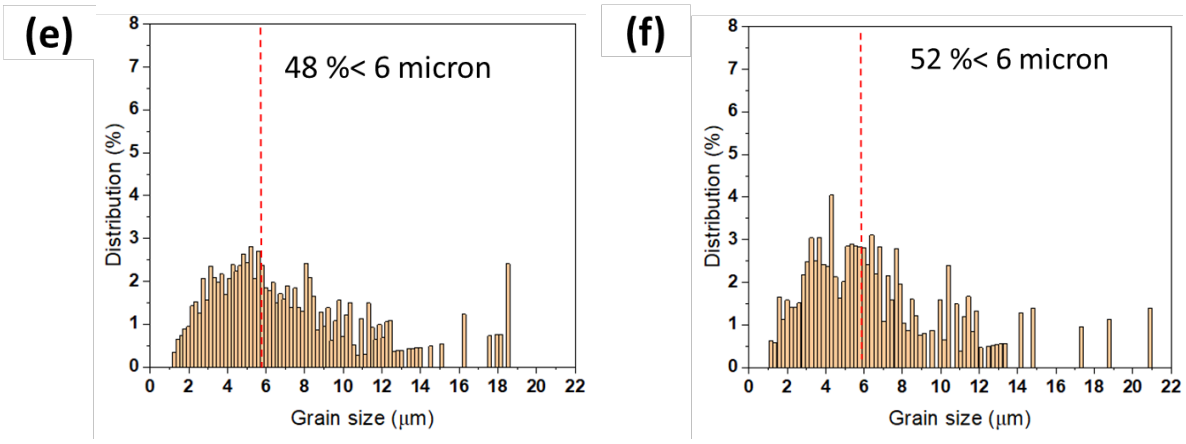


Figure 66: Grain size distribution of (a, b) as-sprayed, (c, d) 500 °C HT, (e, f) 700 °C HT. (a, c, e) show the cold spray deposits produced using N_2 process gas and (b, d, f) show the cold spray deposits produced using He process gas.

6.4.3 Microhardness

Figure 67 illustrates the microhardness of cold-sprayed deposits made using N_2 and He process gases both before and after annealing. Initially, the microhardness of the deposit produced with N_2 (112.19 ± 6.3 HV) is higher than that of the deposit produced with He (87.17 ± 13.12 HV). This difference is attributed to the greater plastic deformation experienced by the N_2 deposit. Such high strain/strain rate plastic deformation leads to increased dislocation density, grain refinement, and consequently, work hardening [171,197]. As indicated in Figure 63b, the dislocation density in the N_2 deposit exceeds that in the He deposit. It is important to note that the considerable standard deviation in the microhardness of both as-sprayed samples is linked to the varying levels of plastic deformation encountered by particles across the sample thickness, which results from the shot peening effect. Following heat treatment at 500 °C, static recrystallization and the reduction of dislocation buildup around inter-particle boundaries, as previously noted in studies [19,200,201], diminish the effects of work hardening. This reduction in work hardening decreases hardness to 93.34 ± 7.46 HV for the N_2 deposit and to 57.33 ± 4.5 HV for the He deposit. Following heat treatment at 700 °C, the work hardening effect is mitigated, and grain growth further reduces hardness to 84.86 ± 9.19 HV and 52.87 ± 3.43 HV for the N_2 and He deposits, respectively.

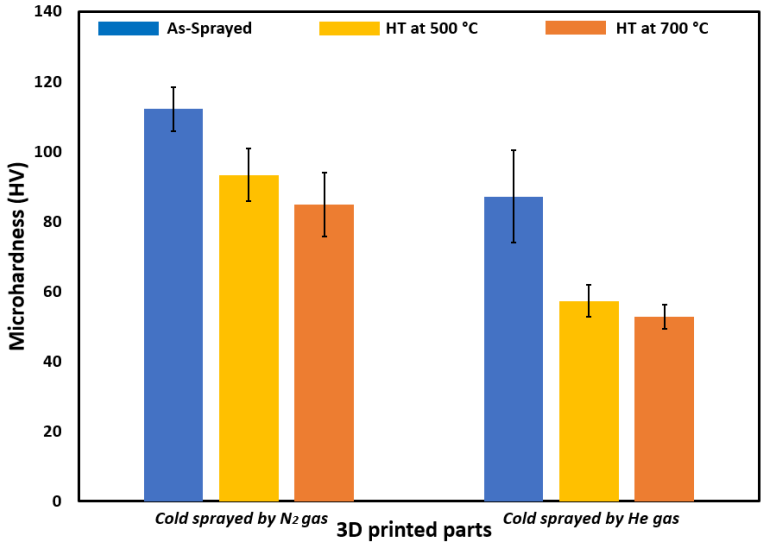


Figure 67: Comparison of microhardness of Cu cold spray deposits produced using N_2 and He process gases in the as-deposited and different heat-treated conditions.

6.4.4 Tensile properties

To assess the strength and fracture strain of both as-sprayed and annealed samples, tensile tests were conducted. The resulting engineering stress versus engineering strain curves until fracture are displayed in Figure 68. These curves indicate that the annealed samples exhibit uniform deformation, in contrast to the as-sprayed deposits, which fracture without displaying any plastic deformation. These results underline the profound impact of annealing on the mechanical properties of cold-sprayed deposits, corroborating findings in the literature [182,197,202]. Data from the tensile tests, including yield strength, ultimate tensile strength, and elongation at fracture, are averaged from three measurements and summarized in Figure 69.

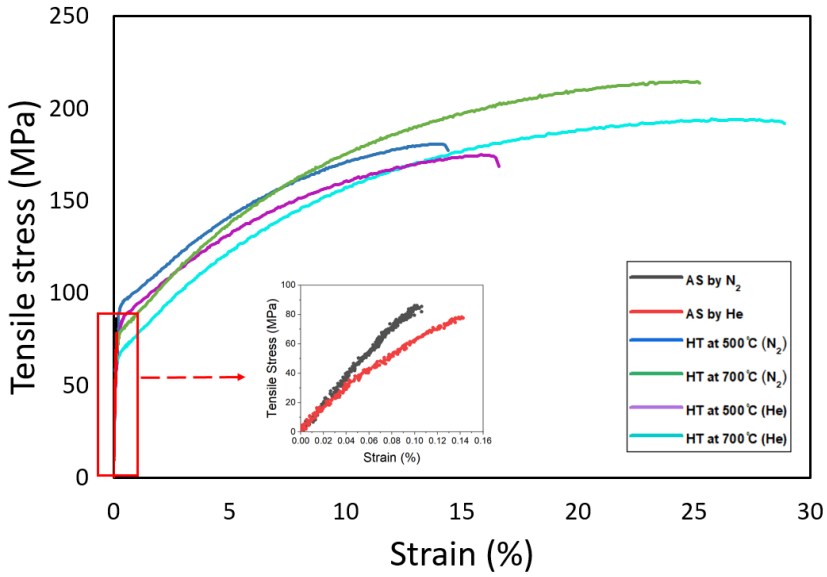


Figure 68: Stress-strain curves showing limited strength and elongation of as sprayed deposits, and higher strength and ductility of heat-treated deposits.

For both cold-sprayed samples produced using N_2 and He gases, the as-sprayed samples demonstrate tensile elongations of less than 0.2% and tensile strengths of approximately 70 MPa and 68 MPa, respectively, which are lower than those of bulk Cu [203]. After undergoing heat treatment at 500 °C, the cold-sprayed Cu materials exhibit enhanced mechanical properties with tensile strengths and ductility increasing to approximately 180 MPa and 174 MPa, and 14% and 16% for N_2 and He samples, respectively. By further increasing the heat treatment temperature to 700 °C, there is a notable improvement in mechanical properties. The tensile strength and strain to fracture for N_2 and He samples improved to approximately 213 MPa and 193 MPa, and 25% and 28%, respectively. However, the tensile strength and ductility of these samples still fall short of those for bulk Cu of 230 MPa and 50 % [86,203]. It appears that higher heat treatment temperatures can have a positive effect on enhancing the mechanical properties of cold-sprayed Cu materials.

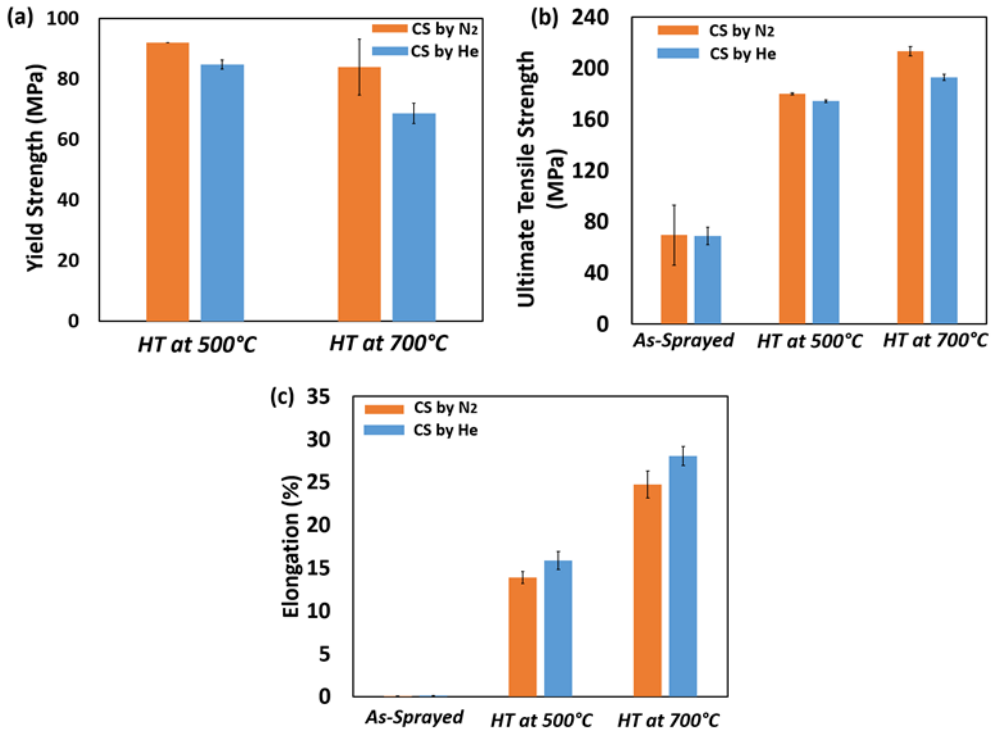


Figure 69: Comparison of tensile properties of Cu deposits produced using N_2 and He process gas in the as-deposited and different heat treated conditions showing: (a) yield strength; (b) ultimate tensile strength; and (c) elongation.

To explore the correlation between densification and mechanical properties, the porosity of both the as-sprayed and heat-treated samples was quantified, with results presented in Table 16. The varied mechanical behaviors of the cold-sprayed samples, along with their mechanical improvements post-heat treatment, are attributable to changes in their microstructures. The as-sprayed Cu samples exhibit a porous microstructure, as illustrated in Figure 64a and b, with porosities measured at 2.8 % and 3.8% for N_2 and He samples, respectively. Numerous defects visible within these microstructures lead to de-cohesive rupture due to early failure during the initial phase of elastic deformation in tensile testing, resulting in a tensile strength significantly lower than that of bulk material.

Table 16: Variation in porosity of pure Cu cold spray deposits in the as sprayed (AS) and heat-treated (HT) conditions produced using N_2 and He process gases

Material	Porosity (%)
N_2 –As sprayed	2.8
N_2 - HT at 500 °C	1.6
N_2 - HT at 700 °C	0.6
He – As sprayed	3.8
He - HT at 500 °C	2.6
He - HT at 700 °C	1.6

At a lower heat treatment temperature, some diffusion occurs between particles, which strengthens the interfaces and consequently enhances the overall strength and ductility of the material. However, at the temperature of 500 °C, only the tightly bonded interfaces will vanish, and porosities of 1.6% and 2.6% were recorded for N_2 and He samples, respectively. Despite this diffusion, the work hardening induced during the cold spray process may still persist in the material. The enhanced tensile strength and ductility observed in samples heat-treated at 700 °C confirm substantial diffusion at the particle interfaces, leading to their complete disappearance (Figure 64e and f) and porosities of 0.6% and 1.6%. Work hardening and the extensive plastic deformation produced during cold spraying are progressively eliminated through recrystallization and subsequent grain growth during heat treatment, as illustrated in Figure 65e and f, aligning with other studies indicating that the recrystallization temperature for Cu is above 400 °C [197,202]. Recrystallization in the plastically deformed samples results in the formation of fine grains, and further grain growth enlarges these grains. The grain size distribution shown in Figure 66 reveals that recrystallization and grain growth occur at both heat treatment temperatures of 500 °C and 700 °C. The evident grain growth observed in the heat-treated Cu materials suggests that these materials can undergo plastic deformation more readily at a lower yield strength. As a result, the yield strength of the Cu materials heat-treated by N_2 reduced from approximately 92 MPa at 500 °C to 83 MPa at 700 °C. Similarly, the yield strength of the Cu materials heat-treated by He dropped from around 84 MPa at 500 °C to 69 MPa at 700 °C.

As it has been noted, the printed Cu materials are not fully dense due to the presence of porosity. In this regard, at higher heat treatment temperatures, this process addresses the defects more effectively, mitigating the reductions in ultimate tensile strength and ductility that typically result from grain growth. Therefore, Cu materials heat-treated at 700 °C exhibit superior elongation and ultimate tensile strength compared to those treated at 500 °C. Additionally, the higher porosity in the helium-produced materials might inhibit the diffusion process between particle interfaces during heat treatment, thereby slightly increasing the recrystallization temperature.

It is important to highlight that even though recrystallization occurred in materials after heat treatment, the work hardening was not entirely eliminated from the materials and remains more pronounced in those produced by N_2 which can be attributed to the presence of persistent dislocation loops [204]. Consequently, samples produced by N_2 after heat treatment tend to exhibit higher tensile strength and reduced elongation compared to those heat-treated materials produced by He. Furthermore, the current heat treatment conditions are insufficient to rectify all defects in the samples. As a result, both the tensile strength and elongation of the samples are inferior to those of bulk Cu.

Figure 70a compares the ultimate tensile strengths (UTS) of as-sprayed and annealed samples from this study with those found in the literature. Among these comparisons, a single deposit processed with He gas at a pressure of 2.5 MPa displays a decline in strength with increasing annealing temperatures, mirroring the behavior of cold-rolled bulk material [203]. This similarity is likely due to significant work hardening achieved through cold spraying with He. The microhardness and observed deformation, indicating higher average dislocation density, in the as-sprayed sample using He gas surpasses that of bulk Cu cold-rolled to a 70% thickness reduction [203], aligning well with the observed strength measures. In contrast, other samples deposited using air, N_2, and lower-pressure He (0.8 MPa) exhibit lower initial strengths, which then improve with increasing annealing temperatures. Literature [182,183,197,202] suggests that under spray conditions with process gas temperatures above 600 °C and higher gas pressure (2.6-4 MPa), strengths comparable to annealed bulk Cu (about 270 MPa) are achieved at annealing temperatures between 300°C and 500°C. At these settings, surface diffusion during low-temperature annealing can effectively minimize non-bonded interfaces, reducing their likelihood to initiate cracks, thereby enhancing strength with rising annealing temperatures. However, for deposits sprayed at 800 °C, annealing above 350 °C leads to a reduction in strength, likely due to

grain growth, which further diminishes the material's strength [197,202]. Conversely, deposits sprayed with significantly lower gas temperatures [192,203,205] require higher annealing temperatures to achieve bulk-like properties, likely due to excessive quantities and larger sizes of poorly bonded interfaces.

Figure 70b compares the ultimate tensile strengths (UTS) of as-sprayed and annealed samples from this study with those found in the literature. Among these comparisons, a single deposit processed with He gas at a pressure of 2.5 MPa displays a decline in strength with increasing annealing temperatures, mirroring the behavior of cold-rolled bulk material [203]. This similarity is likely due to significant work hardening achieved through cold spraying with He. The microhardness and observed deformation, indicating higher average dislocation density, in the as-sprayed sample using He gas surpasses that of bulk Cu cold-rolled to a 70% thickness reduction [203], aligning well with the observed strength measures. In contrast, other samples deposited using air, N_2, and lower-pressure He (0.8 MPa) exhibit lower initial strengths, which then improve with increasing annealing temperatures. Literature [182,183,197,202] suggests that under spray conditions with process gas temperatures above 600 °C and higher gas pressure (2.6-4 MPa), strengths comparable to annealed bulk Cu (about 270 MPa) are achieved at annealing temperatures between 300°C and 500°C. At these settings, surface diffusion during low-temperature annealing can effectively minimize non-bonded interfaces, reducing their likelihood to initiate cracks, thereby enhancing strength with rising annealing temperatures. However, for deposits sprayed at 800 °C, annealing above 350 °C leads to a reduction in strength, likely due to grain growth, which further diminishes the material's strength [197,202]. Conversely, deposits sprayed with significantly lower gas temperatures [192,203,205] require higher annealing temperatures to achieve bulk-like properties, likely due to excessive quantities and larger sizes of poorly bonded interfaces.

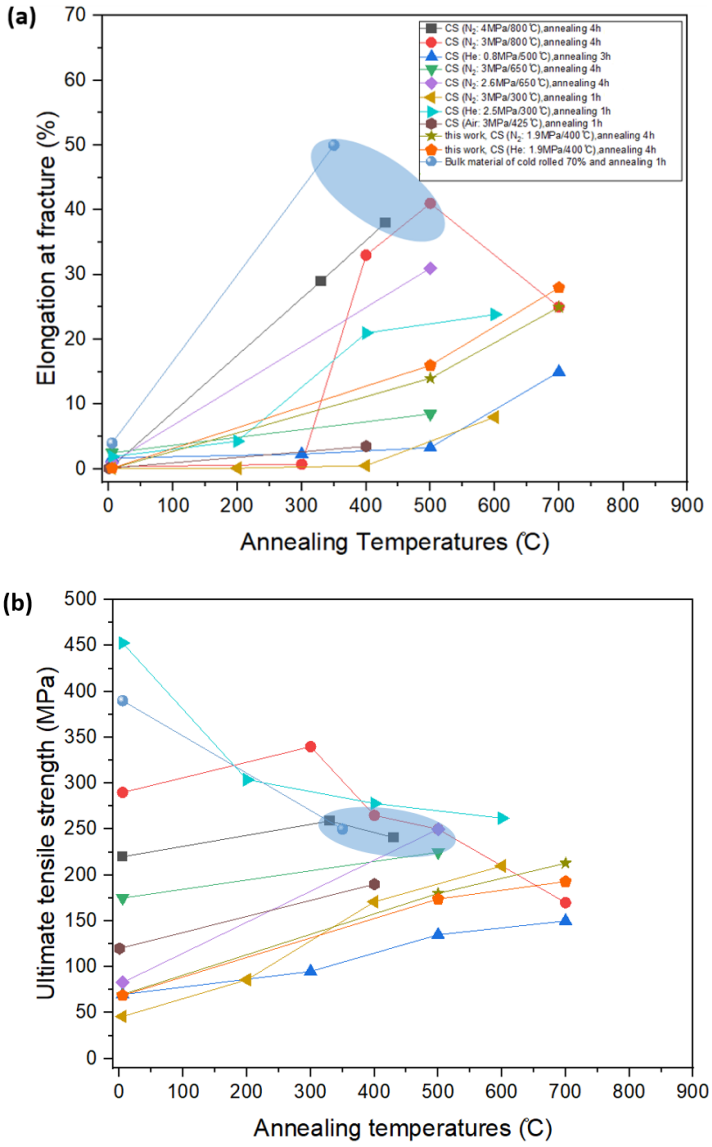


Figure 70: (a) Elongation to failure and (b) ultimate tensile strength of Cu deposits in the as-sprayed state and under various annealing conditions at different temperatures are presented for this study alongside other research findings in the literature. For comparison, the graph also includes data for severely cold-rolled and annealed bulk Cu [182,183,197,202,203].

Regarding potential applications, it is noteworthy that deposits sprayed with N_2 and He gases at sufficiently high temperatures (>600 °C) and/or pressures (2.6-4 MPa), followed by annealing within the 400 °C to 500 °C range, exhibit similar mechanical properties, including elongation to failure and

ultimate tensile strength, to highly deformed and annealed bulk Cu, as depicted in the colored sections of Figure 70. This finding suggests that using N_2 gas for cold spraying of Cu, coupled with annealing at temperatures between 400 and 500 °C, could serve as a cost-effective alternative to the more expensive He gas. Conversely, depositions conducted at the lower temperatures and pressures featured in this study fail to match the properties of bulk Cu, even when annealed at 700 °C. Additionally, it is unclear whether the improvements in interface bonding and micro void reduction after annealing at temperatures above 700 °C, can offset the negative impact of extensive grain growth on tensile strength.

6.4.5 Fracture surface analysis

For additional analysis, fractography of tensile samples produced with N_2 and He gases, both before and after annealing, are made and images are displayed in Figure 71. The fracture surfaces of the as-sprayed tensile samples (Figure 71a-d) for both N_2 and He gas-produced samples exhibit cleavage-like features. These features suggest interparticle failure and de-cohesion rupture, indicative of purely brittle fracture. Micro-cracks are visible along the interfaces of the deposited particles, and river-like patterns further confirm the typical nature of brittle fracture. After being heat-treated at 500 °C, the fracture surfaces (Figure 71e-h) show numerous dimples. Upon increasing the heat treatment temperature to 700 °C, the dimples on the fracture surfaces become more uniform (Figure 71i-l). In the annealed samples (Figure 71e-l), the fracture surfaces show a mix of cleavage-like and dimple-like features, pointing to both interparticle and intergranular failure. Intergranular fracture is often associated with high cohesion strength and ductility [182,203]. The fractographic images elucidate the improvements in ultimate tensile strength and elongation of the cold-sprayed copper deposits post-annealing. The low ductility of the as-produced deposits stems from incomplete bonding at the interfaces, which reduces the effective load area, concentrates stresses, and facilitates crack initiation and propagation, leading to easy fracturing and a smooth fracture surface morphology typical of brittle fractures. After heat treatment, the bond strength between particles is enhanced, as evidenced by the fractography in Figure 71e-l. The presence of dimples indicates improved plasticity, suggesting a plastic rupture through microvoid coalescence, which signifies stronger metallurgical bonding among deposited particles, although cracks may still indicate incomplete interface healing.

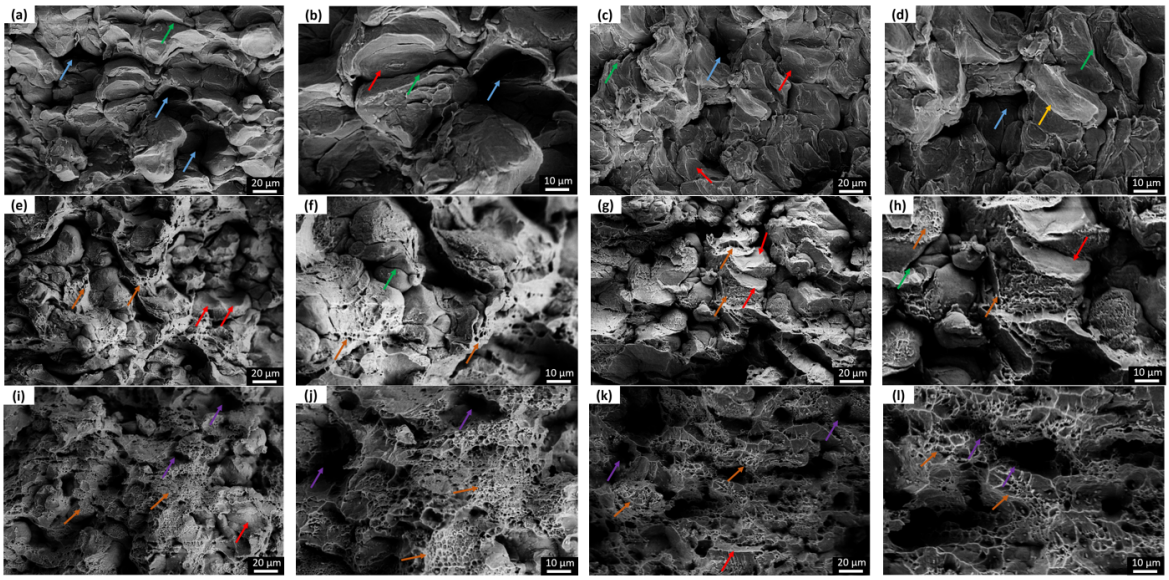


Figure 71: Fracture surface of different deposits: (a, b) as-sprayed by N_2, (c, d) as-sprayed by He, (e, f) 500 °C HT for N_2 samples, (g, h) 500 °C HT for He samples, (i, j) 700 °C HT for N_2 samples and (k, l) 700 °C HT for He samples. (b, d, f, h, j, l) are high magnification of (a, c, e, g, i, l), respectively. The fracture surfaces' distinctive traits are illustrated as follows: Blue arrows denote splat detachment, red arrows signify brittle inter-particle fractures, green arrows indicate micro-cracks along inter-splat boundaries, the yellow arrow points out a river-like pattern, brown arrows mark fine dimples, and purple arrows depict enlarged dimples.

6.5 Conclusion

Pure Cu deposits are generated through a low-pressure cold spray system, where the study focused on the effects of process gas and post-deposition heat treatment on the microstructural evolution and mechanical properties. The experimental findings lead to the following conclusions:

1. While He process gas could achieve higher particle velocities and subsequently enhanced deposition efficiency, cold spray deposits made with N_2 process gas exhibited lower porosity and enhanced plastic deformation compared to those made with He at the same thickness. This improvement with N_2 can be attributed to the greater number of deposition passes, and the

increased peening effect experienced by samples processed with N_2. Essentially, the plastic deformation of the particles was more pronounced due to peening than the higher velocities achieved using He process gas.

2. The work hardening that occurred during the cold spray process led to a higher dislocation density in the Cu material sprayed with N_2 process gas, more than doubling that observed for He. Consequently, a higher microhardness of 112 HV was recorded for the N_2-processed sample, which is 1.3 times higher than that of the He-processed sample.
3. Coatings processed with both N_2 and He exhibited brittle fractures in their as-sprayed states, showing negligible ductility. However, post-deposition heat treatments led to recrystallization and grain growth, significantly enhancing the ductility and tensile strength of both N_2 and He-treated deposits. EBSD analysis post-heat treatment revealed a finer grain size distribution in He-sprayed samples, attributed to a higher recrystallization temperature. Heat treatment at 500°C partially healed non-bonded interfaces, increasing ductility and tensile strength to 14% and 16%, and 180 MPa and 174 MPa for N_2 and He samples, respectively. Meanwhile, heat treatment at 700°C effectively removed most non-bonded interfaces, boosting the tensile strengths to 213 MPa and 193 MPa, and elongations to 25% and 28% for N_2 and He samples, respectively.

While the maximum tensile strength and elongation achieved in this study were lower than those of severe cold-rolled and annealed bulk Cu, due to incomplete defect healing, the findings contribute to a broader understanding of how spraying parameters such as temperature, pressure, process gas, and heat treatment conditions affect the mechanical properties of cold-sprayed deposits. These insights, when compared with other results from the literature, suggest that using N_2 gas for cold spraying of Cu at the higher pressures and temperatures applied in this study, along with annealing between 400 °C and 500 °C, could achieve performance similar to that of bulk copper without the necessity of using the more expensive He gas.

Chapter 7

Microstructural Evolution and Mechanical Behavior of Low-Pressure Cold-Sprayed 3D-Printed CuCrZr Alloy through Solution Annealing and Age Hardening

(Manuscript ready for submission)

7.1 Abstract

Heat treatment plays a crucial role in determining the properties of CuCrZr alloys. However, its specific effects on the microstructure and mechanical performance of cold spray additive manufactured (CSAM) CuCrZr remain insufficiently explored. In this study we successfully 3D-print a Cu-0.45Cr-0.05Zr alloy using a low-pressure CSAM and investigate the influence of various post-deposition heat treatments. The microstructure is examined using optical microscopy (OM), scanning electron microscopy (SEM), electron backscatter diffraction (EBSD), and X-ray diffraction (XRD), while the mechanical properties are evaluated through hardness and tensile testing. The as-sprayed CuCrZr alloy exhibited weakly bonded particle interfaces and porosity, which were significantly reduced by solution annealing (SA) and solution annealing + age hardening (SA+AH) through grain reorganization, interfacial healing, and solid-state diffusion bonding. Microstructural and texture analysis revealed that SA and SA+AH promoted near-fully recrystallization (~99% RX fraction) with random orientation, whereas direct age hardening (DAH) at 480°C resulted in partial recrystallization (~30% RX fraction). Hardness measurements showed that as-sprayed CuCrZr had a high initial hardness (163.2 HV) due to work hardening, which decreased following SA but increased with SA+AH (146.9 HV) and DAH (239.6 HV) due to precipitation strengthening. Tensile testing indicated that the CSAM as-sprayed sample had low strength (UTS: 89 MPa) and negligible ductility (0.15%). In contrast, SA+AH resulted in the highest tensile strength (UTS: 220 MPa), yield strength (YS: 184 MPa), and ductility (9%), whereas DAH exhibited lower strength (143 MPa) and poor elongation (0.2%) due to incomplete metallurgical bonding. A comparative analysis with SLM, LPBF, and WAAM demonstrated that DAH is most effective in strengthening of fusion-based methods through precipitation strengthening, whereas SA+AH is the optimal heat treatment for CSAM, enhancing densification and mechanical performance.

These results underscore the importance of tailored heat treatment strategies to optimize the microstructure and mechanical properties of cold-sprayed CuCrZr alloys.

7.2 Introduction

CuCrZr alloy is widely recognized for its outstanding mechanical properties, excellent electrical and thermal conductivities, and superior wear resistance [206–209]. These attributes make it a preferred material for applications such as high-speed railway contact wires, nuclear fusion reactors, switching contacts, and resistance welding electrodes [210–212]. However, traditional manufacturing methods like casting and forging face significant challenges in meeting the increasingly complex design and functional requirements of CuCrZr components. These methods often result in high material waste, as subtractive processes lead to excessive feedstock loss. Additionally, they struggle to produce complex geometries, requiring multiple machining steps to achieve intricate designs. Over time, CuCrZr components fabricated through these methods exhibit a decline in mechanical and tribological properties, affecting their long-term performance. Furthermore, the lengthy production cycles associated with traditional fabrication processes contribute to inefficiency and high costs. These limitations hinder the industrial adoption of CuCrZr alloy, prompting researchers to explore advanced manufacturing techniques that offer improved efficiency, better mechanical performance, and enhanced service life [213–215].

Additive manufacturing (AM) technology, known for its design flexibility, high material utilization, and production efficiency, is considered a promising alternative for manufacturing metal components Current. AM approaches primarily rely on fusion-based techniques to build near-net-shaped components[115,166,168]. However, these methods involve melting and solidification, which often lead to porosity, segregation, dilution in bimetallic joints, residual tensile stresses, and the formation of undesirable phases, ultimately compromising the mechanical properties of the fabricated parts. Since Cold Spray Additive Manufacturing (CSAM) is a solid-state deposition process, it eliminates most of the challenges associated with melting and liquid-to-solid phase transformations. As a member of the AM family, CSAM enables the deposition of a wide range of metal alloys and composite materials [7,8,112,146,185,216]. Unlike fusion-based AM, which depends on thermal energy, CSAM relies on kinetic energy to achieve bonding. In this process, inert gases such as helium or nitrogen are heated and used as process gases to accelerate metal powders to high velocities (500–1200 m/s) through a

converging-diverging nozzle. The powder particles are injected into the gas stream and propelled toward the substrate, where they undergo severe plastic deformation upon impact, resulting in localized mechanical interlocking and metallurgical bonding in the solid state. By eliminating fusion-related defects and enabling the efficient deposition of high-performance materials, CSAM presents a robust alternative to conventional fusion-based AM processes for manufacturing dense, defect-free metal components.

Since CuCrZr is a precipitation-hardened alloy, its mechanical properties can be enhanced by reinforcing the precipitated phases. Heat treatment is regarded as the most effective method for phase strengthening, as it improves precipitate distribution and overall material performance [217]. The three primary heat treatment methods applied to CuCrZr alloys, Solution Annealing (SA), Age Hardening (AH), and Direct Age Hardening (DAH), each serve distinct purposes in tailoring the alloy's strength, ductility, and thermal stability. Solution Annealing (SA) involves heating the alloy to ~950°C to dissolve Cr and Zr into the Cu matrix, creating a supersaturated solid solution. This process removes residual stresses, refines the microstructure, and improves ductility, with rapid cooling (typically water quenching) ensuring the elements remain dissolved for subsequent precipitation hardening. AH follows SA by reheating the alloy to a lower temperature, enabling Cr and Zr precipitation. DAH enhances the alloy's strength without requiring solution annealing while also restricting grain growth. Unlike SA+AH, DAH does not completely dissolve pre-existing precipitates, and in certain cases, precipitate coarsening may diminish its overall effectiveness [218,219].

Extensive research has been conducted to investigate the influence of heat treatment on the microstructure and mechanical properties of CuCrZr alloys fabricated via Laser Powder Bed Fusion (LPBF)/Selective Laser Melting (SLM) and Wire Arc Additive Manufacturing (WAAM) [217,220–228]. The effectiveness of heat treatment in CuCrZr alloys depends on fabrication method, temperature, treatment duration and cooling rate. Z. Kuai et al. [228] reported that increasing the solution annealing (SA) temperature led to greater dissolution of Cr and Zr into the matrix, significantly reducing precipitates within the grains while slightly increasing them along grain boundaries. At 950°C, nearly all precipitates within the grains were dissolved. Similarly, L. Li et al. [223] observed that SA treatment resulted in micron-sized Cr precipitates at grain boundaries and a limited number of nanoscale Cr precipitates within the grains. C. Zeng et al. [224] demonstrated that aging promotes phase segregation

and precipitation, reduces residual stresses, and coarsens the microstructure, with an aging temperature of 500°C yielding the highest hardness and yield strength. Furthermore, Q. Wang et al. [225] showed that direct aging (DAH) facilitated the precipitation of nanoscale Cr phases, significantly enhancing strength through precipitation strengthening. C. Wallis et al. [227] found that coarse Cr precipitates (100 nm – 1 μm) formed in SA and SA+AH-treated samples, whereas finer nanoscale Cr precipitates were observed in DAH samples, leading to improved hardness and strength. Z. Diao et al. [226] demonstrated that there is a slight variation in the impact of heat treatment on the overall performance of specimens produced by WAAM compared to those fabricated using other additive manufacturing techniques. In both as-built and DAH specimens, coarse Cr precipitates were present, whereas SA and SA+AH treatments effectively dissolved these precipitates, ensuring a more uniform Cr distribution in the Cu matrix. The SA+AH process yielded significant improvements in hardness and tensile strength due to the fine and uniformly distributed Cr precipitates. Additionally, N. Jeyaprakash et al.[217] examined the effects of cooling pathways following heat treatment at 600°C for 2 hours, concluding that furnace cooling resulted in higher texture intensity, superior hardness, and greater tensile strength compared to water or air cooling. Across multiple studies, precipitation strengthening emerged as the dominant strengthening mechanism in CuCrZr alloys, where the presence of fine, dispersed Cr precipitates effectively impedes dislocation motion, thereby enhancing strength and hardness.

Despite extensive research on fusion-based AM and subsequent heat treatment of CuCrZr alloys, studies on CSAM for this alloy remain limited. P. Coddet et al. [229] successfully deposited CuCrZr alloy using helium as the process gas, achieving low porosity and residual stress. After heat treatment at 455°C for 4 hours, the deposits reached a maximum ultimate tensile strength (UTS) of 610 MPa, surpassing the mechanical properties of plasma-sprayed and forged materials. The exceptionally high particle velocity and resulting tensile strength achieved in this cold spray process are attributed to several key factors. A long convergent–divergent De Laval nozzle with axial powder injection ensured efficient and uniform particle acceleration along the centerline. The helium process gas was preheated to approximately 600 °C, with the gun stabilized at ~550 °C, enhancing gas expansion and particle velocity. A nozzle pressure of 16.0 ± 1 bar and a chamber pressure of 500–550 mbar created a strong pressure gradient, critical for achieving supersonic flow. Helium provided superior particle acceleration compared to conventional gases like nitrogen. The system operated within a vacuum-tight chamber, purged and filled with helium to maintain oxygen levels below 100 ppm, preventing oxidation of the

powder. A closed-loop helium recirculation system preserved gas purity while minimizing loss. These combined conditions led to highly efficient deposition and significantly enhanced mechanical properties of the cold-sprayed material. Z. Jiang et al. [230] demonstrated that CuCrZr coatings deposited using nitrogen as the process gas at a temperature of 600 °C and a pressure of 3 MPa exhibit exceptional oxidation and wear resistance at high temperatures (400–600°C), attributed to work-hardening effects and the dense accumulation of oxide layers. K. Yang et al. [231] investigated the annealing effect during thermal testing over a temperature range from room temperature to 600 °C, showing significant improvements of cold sprayed depositions produced using nitrogen as the accelerating gas with pressure of 3 MPa and temperature of 600 ◦C in room-temperature thermal properties. These enhancements were driven by better interparticle metallurgical bonding, grain growth, solid solution precipitation, and reduced dislocation density. M. Yu et al. [232] studied the impact of annealing heat treatment on cold-sprayed CuCrZr deposits produced using compressed air as the propelling gas at a pressure of 3.5 MPa and a temperature of 500 °C, finding that annealing at 500°C for 2 hours resulted in moderate mechanical and thermal properties. This was attributed to an optimized particle interface and Cr and Zr precipitation, which contributed to strengthening.

Based on the reviewed literature, the impact of the three standard heat treatment procedures (SA, SA+AH, and DAH) on the microstructural evolution and mechanical properties of cold-sprayed CuCrZr alloys remains unexplored. Therefore, the primary objective of this study is to systematically examine the effects of conventional heat treatments on the microstructure, texture, and mechanical behavior of cold spray-deposited CuCrZr alloy. Cold spray deposits were fabricated using nitrogen (N_2) as the process gas by a low-pressure system, and the as-deposited microstructure, texture, and mechanical properties were characterized. To enhance mechanical performance, post-deposition heat treatment was applied, and its influence on microstructural evolution, and mechanical strengthening was analyzed. This study investigates how extensive plastic deformation during deposition and subsequent precipitate formation influence the balance between strength, ductility, and hardness in low-pressure cold-sprayed CuCrZr alloy. By integrating heat treatment strategies, this work aims to elucidate the interrelationship between microstructure and overall mechanical performance, providing valuable insights into the optimization of cold spray additive manufacturing for high-performance applications.

7.3 Experiment and characterization

7.3.1 Materials and equipment

The experiment utilized atomized CuCrZr alloy powder from EOS of North America Inc., with its chemical composition detailed in Table 17. The particle size distribution ranged from 15 µm to 45 µm. Scanning electron microscope (SEM) images at low and high magnifications, shown in Figure 72a and b, reveal small particles dispersed around larger powder particles. The powder's nearly spherical shape enhances its fluidity, ensuring uniform deposition during the cold spray (CS) process. Additionally, Figure 72c illustrates the equiaxed grain microstructure of the powder.

Table 17: Chemical composition of the CuCrZr alloy powder

Element	Cu	Cr	Zr	Fe	Si
Content (wt. %)	Balance	0.45	0.05	0.08	0.01

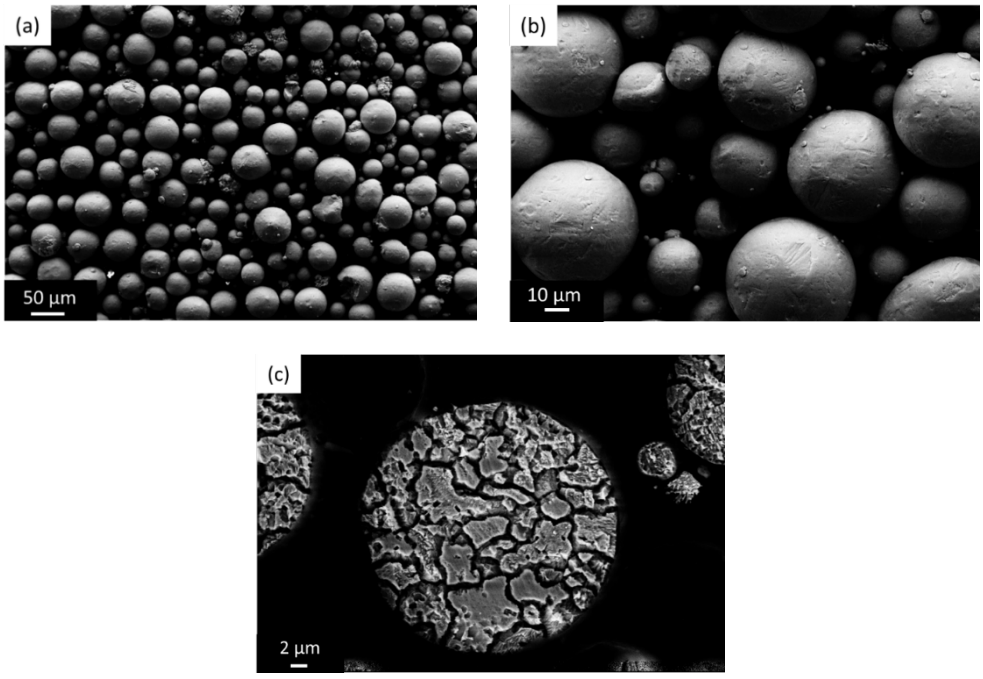


Figure 72: SEM morphology of CuCrZr powder in (a) low and (b) high magnification, and (c) cross section showing grain microstructure.

The samples were produced using the commercial Supersonic Spray Technologies (SST) Series P Cold Spray System, manufactured by Centerline in Windsor, Canada. In this process, CuCrZr powders were propelled to supersonic velocities through a converging–diverging de Laval UltiLife™ nozzle within a low-pressure system. The specifications of the cold spray machine used in this study are summarized Table 18.

Table 18: Specification of SST cold spray nozzle

Nozzle type	Nozzle Length	Nozzle Orifice Diameter	Nozzle Exit Diameter
De Laval UltiLife™	120mm	2 mm	6.3 mm

7.3.2 Experimental method and characterization

The cold spray parameters used in this study are summarized in Table 19, including a nozzle pressure of 1.99 MPa, a gun speed of 80 mm/s, and a gas temperature of 400 °C. The CuCrZr powder was deposited onto an aluminum build plate from a distance of 25 mm. Figure 73a displays an image of the cold spray additive manufactured (CSAM) CuCrZr. The deposited material, fabricated using nitrogen gas, measured 125 mm in length, 60 mm in width, and 3.5 mm in thickness. As shown in Figure 73a, no spalling was observed between the aluminum substrate and the deposited Cu layer, and no coarse cracks were present in the material. Following deposition, the cold-sprayed parts were detached from their substrates and shaped into tensile specimens using Electrical Discharge Machining (EDM). The specific dimensions of the specimens are provided in Figure 73b, with their final geometry depicted in c. All specimens were aligned parallel (0°) to the direction of the spray gun traversal.

Table 19: Cold spray deposition parameters

Sample	standoff distance (mm)	nozzle speed (mm/s)	X-offset (mm)	No. of deposition passes	Gas Pressure (MPa)	Gas Temperature (°C)	Process Gas
3D printed CuCrZr	25	80	-0.5	9	1.99	400	N_2

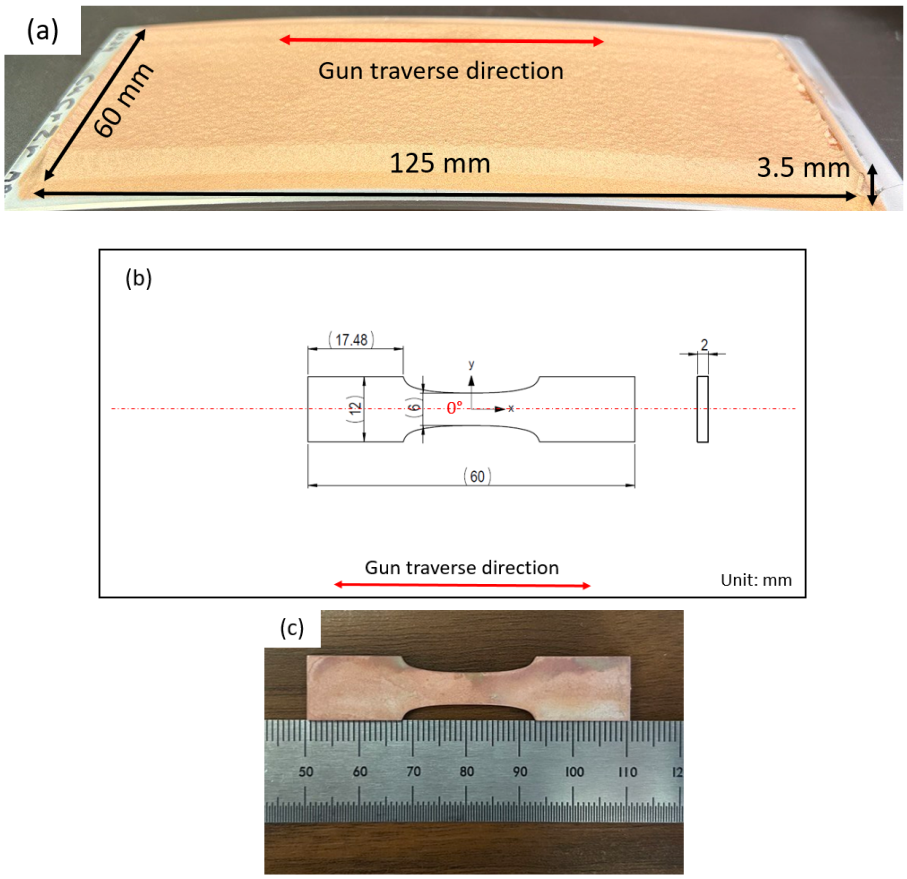


Figure 73: (a) Cold spray 3D printed CuCrZr, before machining samples, (b) the tensile specimen dimensions; and (c) the tensile specimen sectioned from the deposited material.

To enhance the mechanical properties of the cold-sprayed CuCrZr alloy, various heat treatment procedures were performed, as detailed in Table 20. Solution annealing (SA) was conducted in a tube furnace in a protective atmosphere, where the samples were heated to 950 °C for 30 minutes and then quenched in water. The solution-annealed samples subsequently underwent age hardening at 480 °C for 30 minutes. For direct age hardening (DAH), five different temperatures, 400 °C, 450 °C, 480 °C, 520 °C, and 560 °C, were applied. The samples were held at these temperatures for 30, 60, 120, and 170 minutes, respectively, before being air-cooled to room temperature. A schematic overview of the heat treatment process is provided in Figure 74a and b.

Table 20: Heat treatment types and process parameters of the experiment

Heat treatment	Temperature (°C)	Exposure time (min)	Cooling type
Solution Annealing (SA)	950	30	Water quenching
Solution Annealing + Age Hardening (SA+AH)	950 + 480	30 + 60	Water quenching + Air cooling
Direct Age Hardening (DAH)	400, 450, 480, 520, 560	30, 60, 120, 170	Air cooling

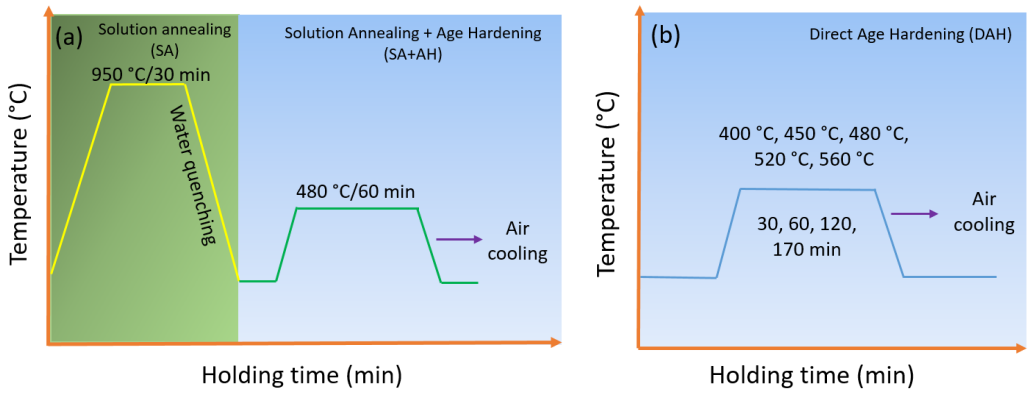


Figure 74: (a) and (b) Schematic of post heat treatment of cold sprayed printed CuCrZr (DAH: Direct Age Hardening, SA: Solution Annealing, SA+AH: Solution Annealing + Age Hardening).

The microstructure of the samples was examined using an optical microscope (Olympus BX41) after etching with a solution containing 2 mL HCl, 1 g $FeCl_3$, and 20 mL H_2O. A scanning electron microscope (SEM) equipped with an energy dispersive spectrometer (EDS) was used for microstructural and elemental distribution analysis of the cold-sprayed samples. To assess the porosity, ImageJ analysis-software was used. Porosity in the cold-sprayed coatings was evaluated in accordance with ASTM E2109, using SEM images captured at both lower (x2000) and higher (x8000) magnifications [104]. Additionally, to prepare for electron backscatter diffraction (EBSD) analysis, the samples were vibratory polished for six hours using 50-nm colloidal silica to remove the deformed surface layer. EBSD analysis was conducted using a Thermo Fisher Scientific Apreo 2 S LoVac SEM,

equipped with a Symmetry S3 EBSD detector and an Ultim Max 170 mm² EDS detector (both from Oxford Instruments Ltd.) and a standard scan used a step size of 100 nm. Data collection and analysis were performed using Aztec version 6.1 SP1 and ATEX© software. Phase identification of the powder and alloy samples was performed using a Bruker D8-Discover X-ray diffraction (XRD) system with a VÅNTEC-500 area detector and Cu-Kα radiation (λ = 1.5406 Å), operating at 40 kV and 40 mA.

Microhardness testing was carried out using a Vickers hardness tester with a 200 g load and a 15-second dwell time, with the final hardness value averaged over 20 measurements per sample. Tensile testing was performed at room temperature using an Instron 8874 servo-hydraulic machine with a load capacity of ±25 kN. The tensile specimens were tested in displacement control mode at a rate of 0.05 mm/min, and strain measurements were obtained using a GOM ARAMIS 3D digital image correlation (DIC) system with a 5-megapixel resolution and a maximum capture rate of 15 frames per second. Three tensile specimens were tested from both the as-sprayed and heat-treated 3D-printed samples. Subsequently, the fracture surfaces of the specimens were analyzed using SEM to examine their morphology.

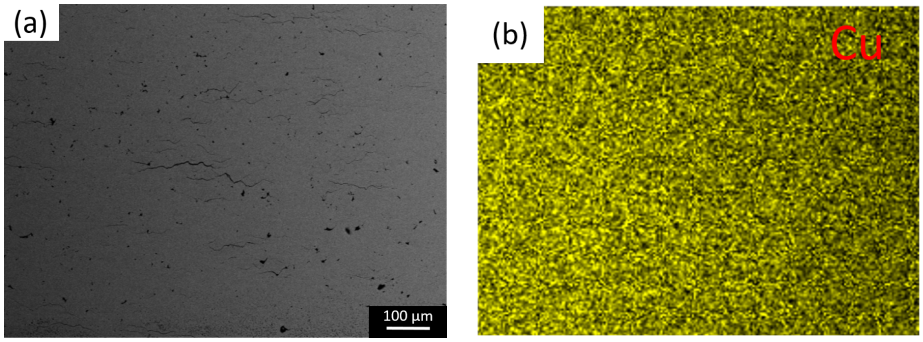
7.4 Results and discussion

7.4.1 Microstructure and texture of CSAM CuCrZr alloy in different states

Figure 75 presents SEM-EDS images of the as-sprayed (CS) specimen, illustrating a uniform distribution of Cr and Zr elements within the copper matrix. These elements were evenly deposited during the CS process without any noticeable segregation in large scale. To further support this, it is helpful to contrast the cold spray process with fusion-based additive manufacturing techniques such as Selective Laser Melting (SLM) and Laser Powder Bed Fusion (LPBF). In SLM/LPBF, the material undergoes complete melting followed by rapid solidification, often at cooling rates exceeding 10^5 - 10^6 K/s [221,233]. This results in highly non-equilibrium microstructures and can lead to microsegregation and elemental clustering. As a result, EDS maps of SLM/LPBF samples often reveal non-uniform distributions, with localized enrichment zones or bands of secondary phases, especially for elements with limited solubility in the matrix (like Cr and Zr in Cu).

Figure 76 displays optical microstructures of both as-sprayed and heat-treated CuCrZr deposits at lower and higher magnifications. As seen in Figure 76a and b, the CS sample consists of extensively

deformed CuCrZr splats. During deposition, the particles undergo significant plastic deformation, forming a dense coating. When they reach the substrate at a critical deposition velocity, adiabatic shear instability occurs, leading to intense strains and strain-rates causing severe plastic deformation. Consequently, a compact coating is established through a combination of grain boundary-like bonding, metallurgical bonding, and mechanical interlocking [26,216,231]. Additionally, smaller particles (<5 μm) are deposited less effectively due to their insufficient kinetic energy upon impact and the bow-shock effect [147,234]. The stacking of these splats results in visible pores at particle/particle interfaces, especially triple junction, primarily due to geometric constraints [235]. Moreover, inadequate metallurgical bonding leads to numerous weakly bonded particle interfaces. After solution annealing at 950 °C and solution annealing followed by age hardening at 480 °C, a notable reduction in mechanical interlocking and porosity is observed, accompanied by enhanced metallurgical bonding and the sphericalization of pores Figure 76c–5f). This transformation suggests that solution annealing promotes interfacial healing through solid-state diffusion bonding [179], significantly altering splat morphology into equiaxed grains. While annealing is known to reduce porosity in cold-sprayed coatings, it also facilitates the coalescence of initially small not well-bonded interfaces into spherical pores [236,237]. In addition, direct age hardening at 480 °C increases the compactness of the coating and reducing porosity (Figure 76g and h) while keeping the interior structure of powder particles. These results indicate that the decrease in porosity stems from the recovery of cold-deformed CuCrZr splats during direct age hardening.



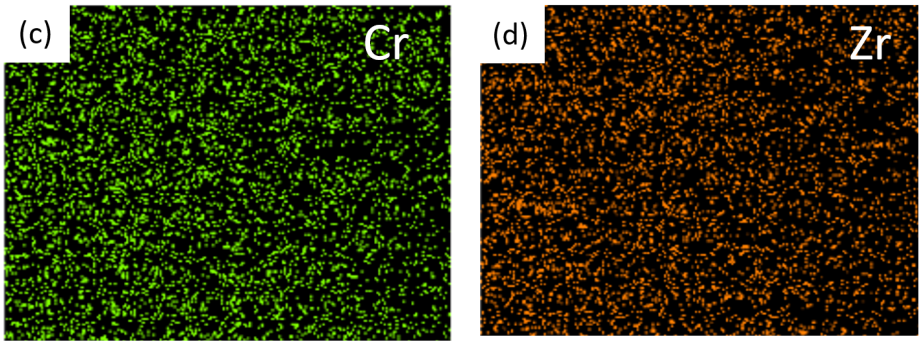
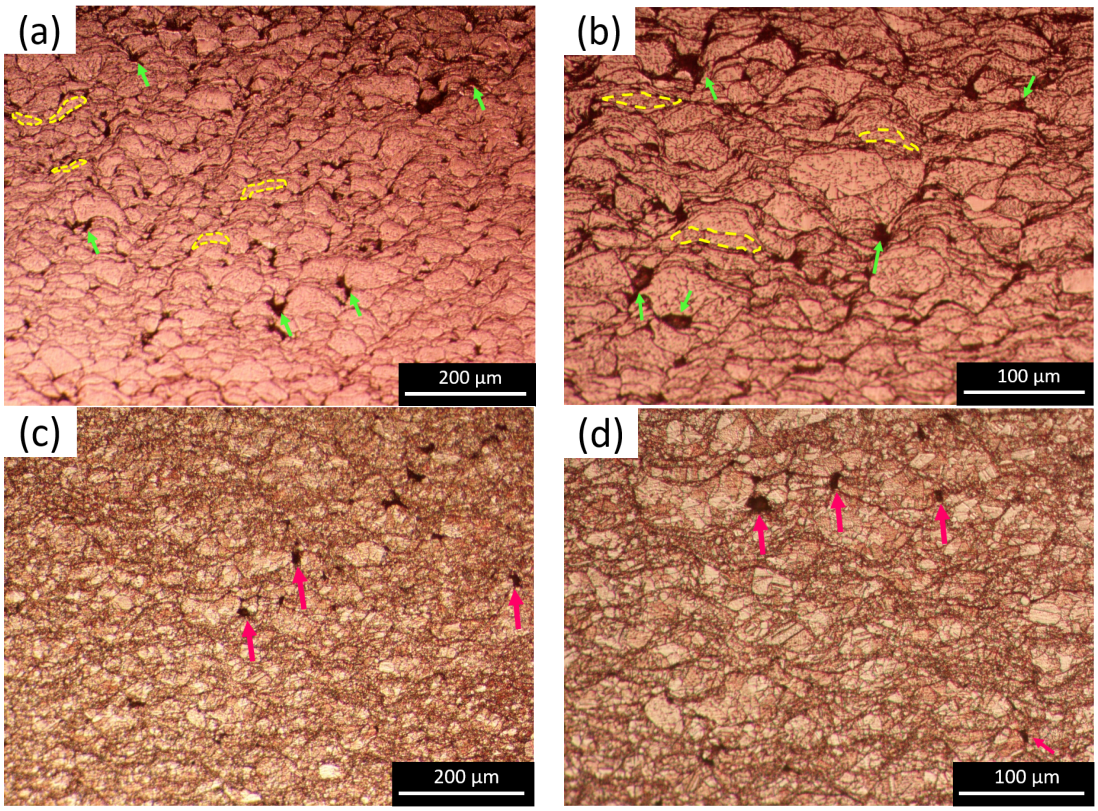


Figure 75: (a) SEM micrograph of as-printed CuCrZr, with corresponding EDS maps showing the elemental distribution maps of (b) Cu, (c) Cr and (d) Zr, showing uniform Cr and Zr distribution in copper matrix.



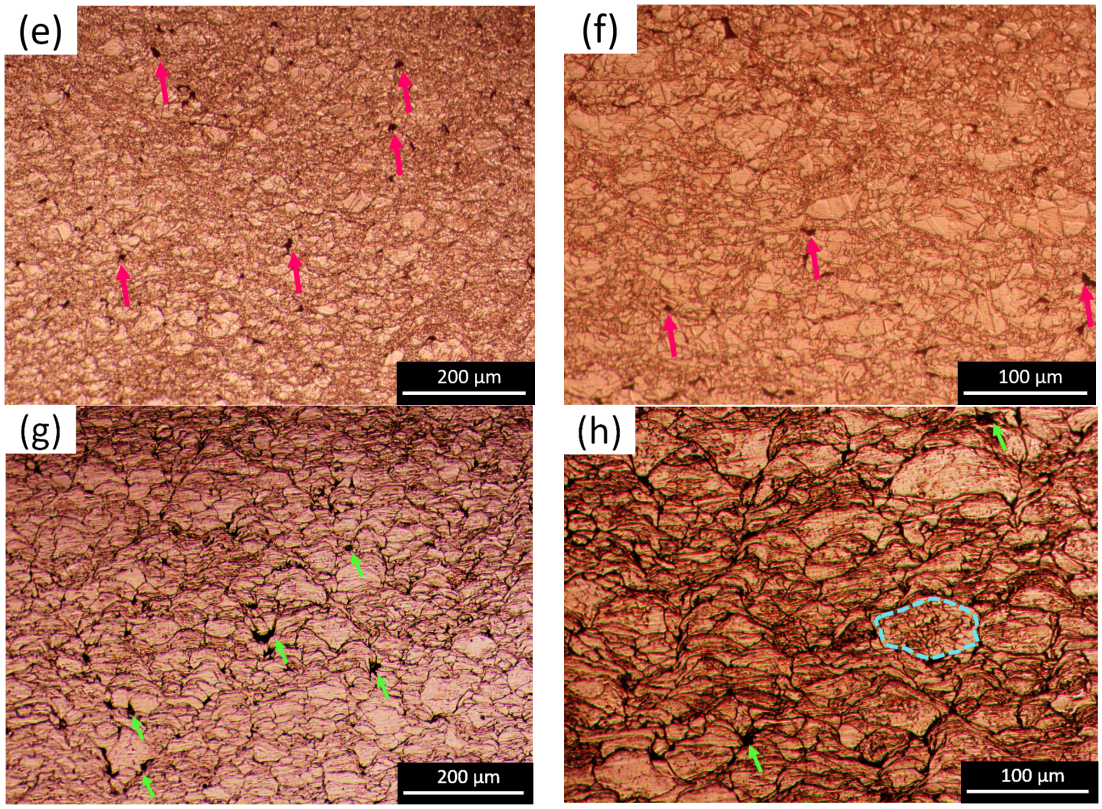


Figure 76: Microstructures of CuCrZr samples at low and high magnifications following the etching process in (a) and (b) as-sprayed (CS), (c) and (d) solution annealed (SA), (e) and (f) solution annealed +age hardened (SA+AH), and (g) and (h) direct age hardened state at 480 °C/1 h (DAH). Yellow ellipses indicate heavily deformed splats, while green arrows point to visible pores caused by the less effective deposition of smaller particles and poorly bonded interfaces. Pink arrows highlight sherardized voids, and blue ellipses reveal the internal grain structure within the powder splats.

To further analyze the CuCrZr deposits, SEM images of the coatings were captured, as shown in Figure 77. The CS specimen (Figure 77a) exhibits large pores (white arrows) and unbonded particle interfaces (red ellipses). In contrast, the SA and SA+AH specimens (Figure 77b and c) display a high-density microstructure, albeit with numerous micropores (yellow circles). Kumar et al. [20] suggested that this characteristic porosity reduction arises from the elimination of particle interface defects and the expulsion of pores and vacancies via grain reorganization and growth through thermal diffusion. However, the DAH specimen still exhibits similar defects to the CS sample, indicating that thermal diffusion at 480 °C for 1 hour was insufficient. This observation aligns with the measured average

porosity values obtained from higher magnified images [104]: 0.88% for the CS sample, decreasing to 0.58% (SA), 0.26% (SA+AH), and 0.78% (DAH).

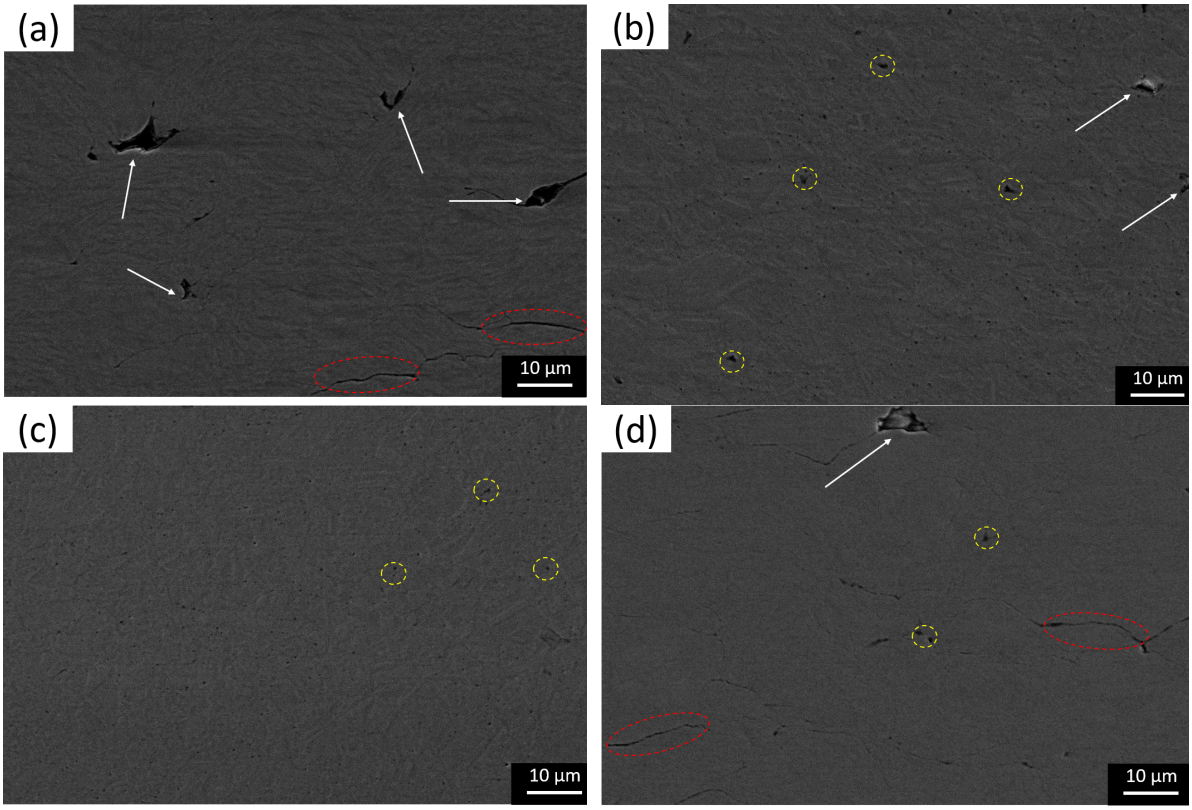


Figure 77: SEM images of CuCrZr alloy specimens. (a) CS, (b) SA, (c) SA+AH, (d) DAH. The white arrows, yellow circles and red ellipses highlight the porosity, micro-pores and non-bonded particle–particle interface, respectively.

Based on the optical and SEM microstructural observations the evolution of bonding quality, grain morphology, and deformation substructure in CuCrZr cold-sprayed coatings is strongly dependent on the post-deposition heat treatment conditions. Specifically, solution annealing and subsequent age hardening promote interfacial healing and recrystallization, transforming heavily deformed splats into equiaxed grains and enhancing metallurgical bonding, while direct age hardening at moderate temperatures may be insufficient to fully recover the cold-deformed microstructure. To test this hypothesis, EBSD will be employed to quantify grain size and morphology across different treatment conditions, identify recrystallized, recovered, and deformed grain fractions, assess misorientation distributions to infer stored strain energy, map grain boundary character (e.g., high-angle vs. low-angle

boundaries) to evaluate the degree of recovery and recrystallization and visualize texture evolution indicative of deformation or recrystallization pathways.

The Inverse Pole Figure (IPF) maps presented in Figure 78 reveal key microstructural features of the CuCrZr sample before and after heat treatment. As shown in Figure 78a, visible gaps and pores are present between adjacent powder particles, indicating incomplete bonding. The grain structure exhibits a non-uniform distribution, with an average grain size of approximately 0.55 μm. Notably, grains located at the inter-particle boundaries are significantly finer than those in the particle interiors. In fact, in cold-sprayed CuCrZr, the particles experience heterogeneous deformation. This grain refinement near particle interfaces is attributed to high plastic strains induced during deposition, which promote continuous dynamic recrystallization (CDRX), specifically, rotational dynamic recrystallization (RDRX) [162]. In contrast, toward the particle core, where the strain is comparatively lower, discontinuous dynamic recrystallization (DDRX) becomes the dominant mechanism [238]. The steep strain gradient across individual particles leads to a high density of geometrically necessary dislocations (GNDs), which serve as precursors for grain nucleation [239]. Along with nucleation, DDRX involves grain boundary migration, resulting in coarser grains within the particle interiors [240]. Additionally, the relatively low flow stress in the particle centers facilitates grain boundary movement and grain growth, whereas the higher flow stress at particle interfaces enhances strain-induced grain refinement. After solution annealing at 950 °C (Figure 78c), newly formed micron-scale equiaxed grains and annealing twins are observed in the microstructure, with an average grain size of 1.128 μm. When the deposit was subsequently age-hardened at 480 °C (Figure 78e), the average grain size increased slightly to 1.326 μm. However, in the sample that underwent direct age hardening at 480 °C (Figure 78g), the microstructure indicates that most of the splats still retained their structure, consisting of equiaxed grains within the particle interiors and ultrafine deformed grains at the particle interfaces with an average grain size of 0.543 μm similar to the as-sprayed state. When the deposit was directly heat-treated at 480 °C, it is expected that the heat diffusion promoted the growth of sub-micron grains via partial recrystallization. As the heat treatment temperature increased to 950 °C, ultrafine grains at the interfaces reorganized and grew extensively through static recrystallization, reducing the grain size disparity between the particle interiors and interfaces. This process resulted in a more homogeneous equiaxed microstructure. Additionally, further heat treatment after solution annealing contributed to continued grain growth and an increase in the average grain size [194,195].

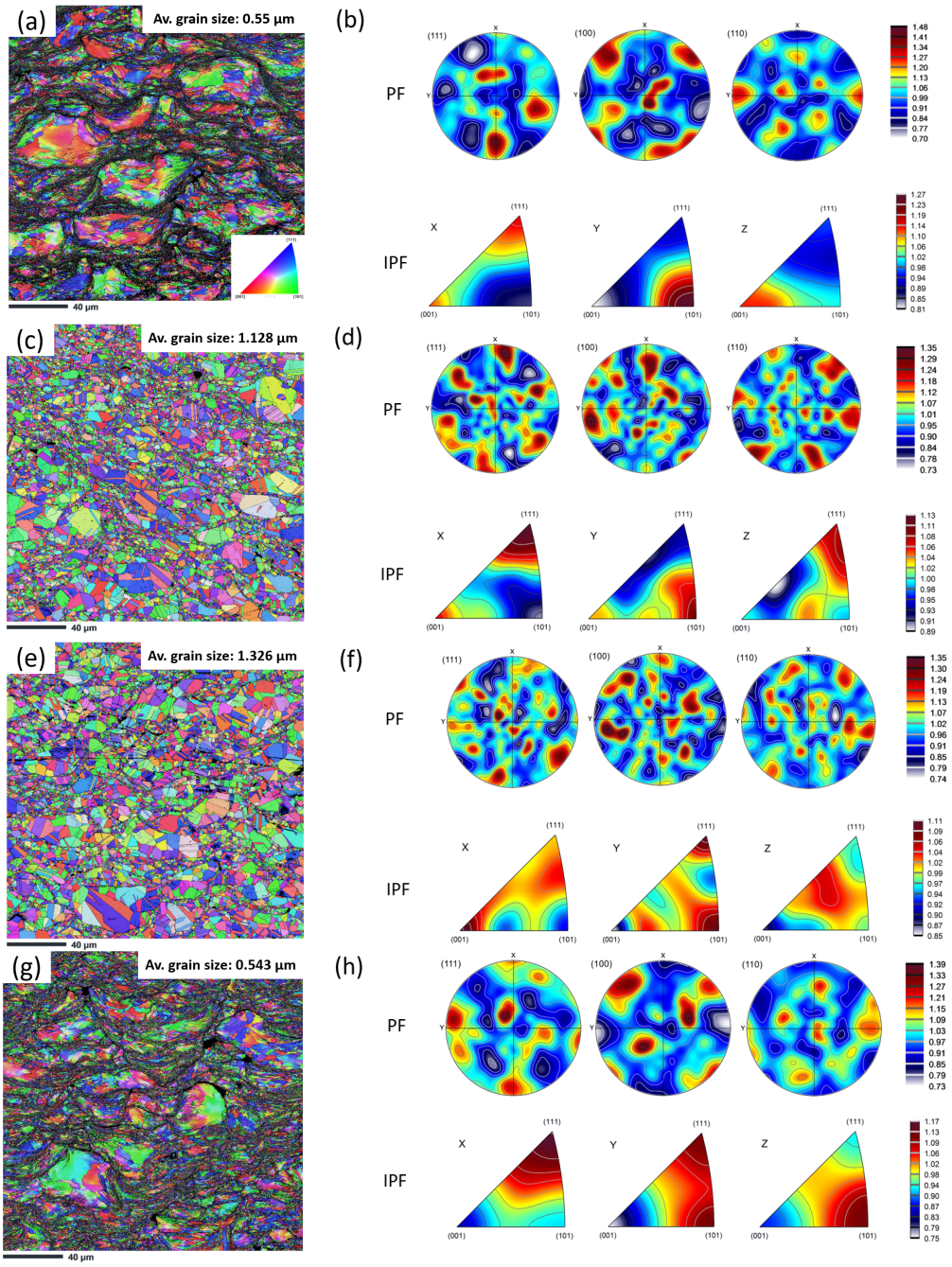


Figure 78: Cross-sectional EBSD images, PF maps, and IPF maps of (a) and (b) as-sprayed sample and different heat-treated samples: (c) and (d) SA sample; (e) and (f) SA+AH sample, and (g) and (h) DAH sample.

From the color-coded triangle map (Figure 78a, inset), grains oriented normal to the <001> direction are shown in pink, <111> in blue, and <101> in green, with intermediate grains between these planes represented by intermediate colors. Figure 78b, d, f and h illustrate the pole figure (PF) and inverse pole figure (IPF) maps obtained for as-sprayed and heat-treated CSAM CuCrZr samples offering some details on the micro-texture characteristics of the samples. The texture intensity in the pole figures can be quantified by the texture index (TI), calculated according to Equation 13 [241]:

$$\mathbf{TI} = \int_{euelerspace} [\boldsymbol{f(g)}]^{\mathbf{2}} \boldsymbol{dg} \tag{13}$$

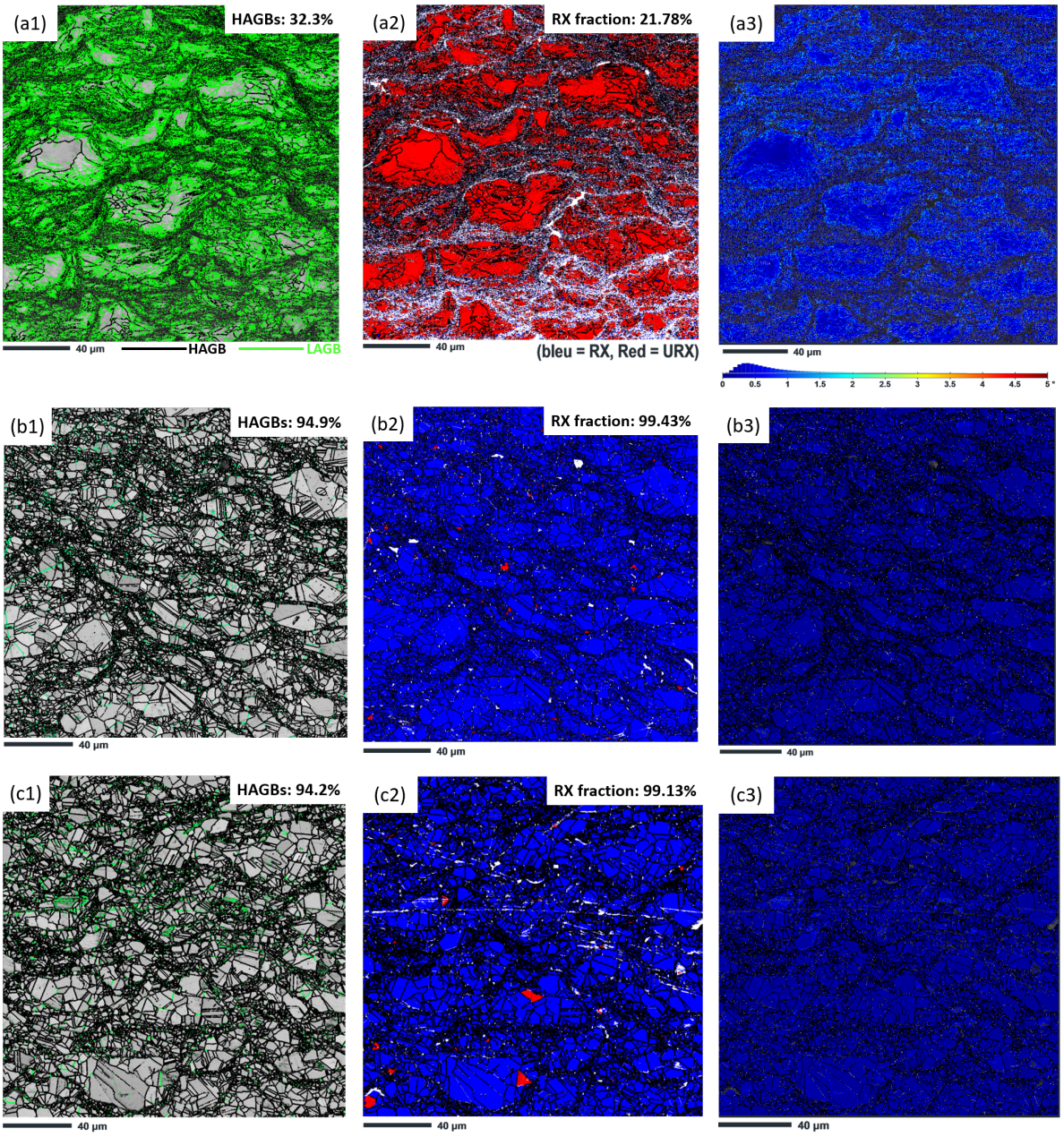
Where f(g) is the orientation distribution function (ODF) based on Euler space coordinates, *g*. Micro-texture intensity is measured in multiples of random distribution units, representing a random, non-textured structure, or indicating increasing levels of preferred crystallographic orientation, or stronger texture [233]. From the pole figures, maximum intensities were observed not only along a single plane but also rather along each of the <111>, <100>, and <110> planes. The pole figures indicate that although the grains become more equiaxed along the direction normal to the gun traverse, their crystallographic orientations exhibit little variation. The intensity values for the <111>, <100>, and <110> planes remain relatively consistent across different heat treatment conditions, suggesting that the grains undergo notable morphological transformations without substantial changes in orientation. This stability in texture intensity implies that the microstructural evolution of the CuCrZr alloy is primarily driven by dislocation activity and grain reshaping, rather than significant lattice reorientation. Additionally, the inverse pole figures indicate that grain textures did not exhibit dominance in any single direction; rather, each direction displayed dominance along different planes. This suggests that recrystallization occurred randomly in all samples, and no preferred orientation developed within their microstructures. Thus, it becomes clear that post-heat treatment did not lead to texture coarsening in CSAM CuCrZr samples. This behavior is notably different from additive manufacturing processes such as LPBF and SLM, where post-heat treatment typically results in a preferred orientation, enhancing the mechanical properties of the additively manufactured parts, in one orientation [217,222,228]. In LPBF and SLM processes, the repeated heating and cooling cycles can locally reheat or partially remelt previously solidified material, thereby promoting localized in situ recrystallization. However, this phenomenon does not occur in cold spray additive manufacturing. In fact, post-deposition heat treatment in LPBF and SLM typically results in the development or strengthening of a preferred

crystallographic orientation due to the inherent characteristics of the fusion-based process. During fabrication, rapid solidification under steep thermal gradients produces columnar grains aligned in the build direction, often exhibiting strong textures. When these parts are heat-treated, grain boundary migration tends to favor the growth of these pre-aligned grains. Additionally, the residual stress and stored energy in LPBF/SLM components are directionally biased due to the laser scanning strategy and melt pool geometry, further reinforcing grain growth along preferred orientations. Even newly recrystallized grains tend to adopt similar orientations, as orientation-dependent boundary mobility promotes alignment with neighboring grains. In contrast, CSAM produces deposits without melting, relying instead on severe plastic deformation for bonding. This results in an ultrafine, equiaxed, and randomly oriented grain structure with no inherent texture. Consequently, there is no driving force for preferential grain growth during post deposition. Recrystallization during post heat treatment in CSAM is static and governed primarily by the stored strain energy from particle impact, leading to random nucleation and grain growth without significant texture development. Furthermore, the absence of a strong pre-existing texture in as-sprayed samples means there is nothing to reinforce during heat treatment, resulting in a largely texture-free microstructure.

The grain boundary analyses for the as sprayed, SA, SA+AH, and DAH specimens are shown in Figure 79 a1, b1, c1 and d1, respectively. In these diagrams, low-angle grain boundaries (LAGBs), characterized by misorientation angles between 2° to 15°, and high-angle grain boundaries (HAGBs), with misorientation angles greater than 15°, are represented by green and black lines, respectively, superimposed on band contrast maps. This distinction is essential for understanding the deformation and recrystallization behavior of the material. Previous studies indicated that LAGBs, initially formed during deformation, typically transform into HAGBs as recrystallization advances [242]. Consistent with these findings, the as-sprayed sample exhibits a HAGB fraction of 32.3%, attributed to dynamic recrystallization, which leads to the formation of fine grains at particle interfaces. The SA and SA+AH specimens exhibit high HAGB fractions of 94.9% and 94.2%, respectively, confirming substantial recrystallization during heat treatment. In contrast, the DAH specimen exhibits a lower HAGB fraction of 41.8%, indicating that only partial recrystallization occurred during heat treatment, resulting in a slight increase in HAGB compared to the as-sprayed sample. The distribution of recrystallized grains can be visualized using EBSD recrystallized fraction (RF) maps, as illustrated in Figure 79 a2, b2, c2 and d2. RF maps represent the extent of recrystallization by analyzing the relationship between the

internal average misorientation angle within grains and the misorientation angles between grains. This analytical method is commonly employed to characterize both dynamic and static recrystallization processes [88]. In these maps, the red areas denote deformed structures, characterized by an internal grain misorientation angle greater than 2°, corresponding to low-angle grain boundary criteria and the blue areas indicate fully recrystallized regions, where grains consist almost entirely of a single crystal orientation. The as-sprayed microstructure contains a recrystallized area fraction of just 21.78%, following solution annealing and solution annealing plus age hardening, the fraction of recrystallized area exceeds 99% (Figure 79 b2 and c2), highlighting the significant impact of heat treatment on promoting recrystallization. In contrast, the directly age-hardened specimen exhibits a recrystallized area fraction of only 29.62% (Figure 79 d2). These values highlight the extent of substructure formation during cold working, the decrease in deformation due to post-heat treatment, and a trend toward a more thermodynamically stable grain structure; however, the DAH treatment has the least impact in this regard. Building on this observation, the Kernel Average Misorientation (KAM) maps presented in Figure 79a3–d3 provide insight into the local strain distribution across the microstructures. The KAM map of the as-sprayed sample (Figure 79a3) reveals widespread low-angle misorientations, with warmer colors concentrated around splat boundaries, indicating regions of elevated dislocation density and localized plastic strain. These areas of high KAM values reflect intense plastic deformation, resulting in substantial internal stresses and promoting dislocation formation. Such dislocations contribute to strain hardening and influence the material's mechanical properties, including strength and ductility. In contrast, the SA and SA+AH samples (Figure 79b3 and c3) display predominantly low KAM values (blue regions), corresponding to large recrystallized grains with reduced internal distortion. Meanwhile, the KAM map of the DAH sample (Figure 79d3) still shows elevated KAM values, indicative of a partially recrystallized microstructure where the crystal lattice remains significantly distorted. Such changes reflect the role of annealing in enabling grain boundary migration and the subsequent formation of new, strain-free grain structures. Together, the grain boundary analysis, recrystallized fraction maps, and KAM results provide a comprehensive understanding of the microstructural transformations induced by different post-deposition heat treatments. The findings confirm that solution annealing, with or without subsequent age hardening, leads to near-complete recrystallization, grain boundary reconfiguration, and a significant reduction in internal strain. In contrast, direct age hardening results in only partial recrystallization, with substantial retained deformation and dislocation structures. These

differences underscore the effectiveness of high-temperature heat treatments in facilitating grain boundary migration and microstructural recovery, ultimately contributing to a more stable and uniform grain structure in cold-sprayed CuCrZr deposits.



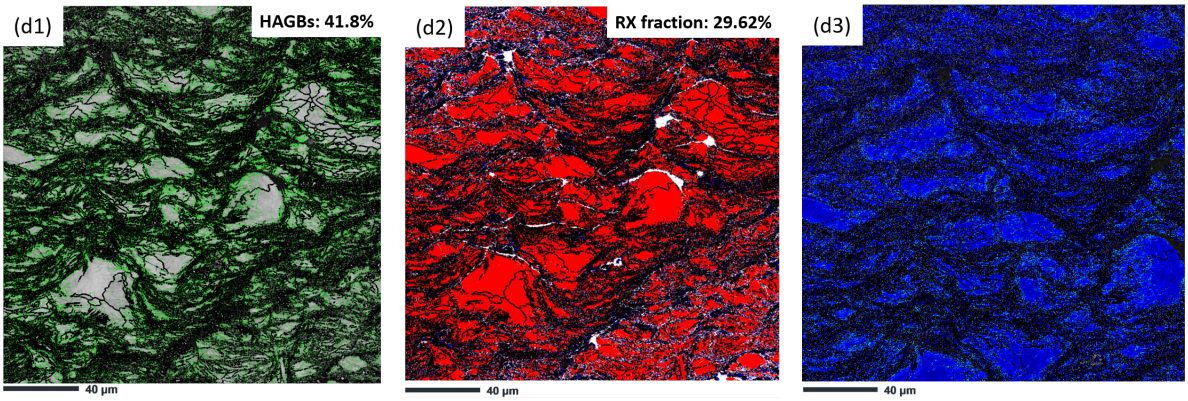


Figure 79: Grain boundary distribution map (superimposed on band contrast map), recrystallized fraction (RF) map and kernel average misorientation (KAM) map of samples before and after heat treatments: (a1)-(a3) as-sprayed sample, (b1)-(b3) SA sample, (c1)-(c3) SA+AH sample and (d1)-(d3) DAH sample.

7.4.2 XRD analysis

To build upon the microstructural insights provided by SEM and EBSD, X-ray diffraction (XRD) was employed to investigate phase composition, detect the precipitation of Cr- and Zr-rich secondary phases, and assess lattice distortion. Additionally, XRD enabled the quantitative evaluation of microstructural recovery and recrystallization by determining crystallite size and dislocation density through Williamson–Hall (W–H) analysis. Figure 80 presents the X-ray diffraction (XRD) patterns of CuCrZr samples in five different states: powder, as-sprayed, SA, SA+AH, and DAH. As seen in Figure 80a, the diffraction profiles are predominantly governed by peaks corresponding to the face-centered cubic (FCC) α-Cu phase, which is expected given the high copper content of the CuCrZr alloy. In addition to these dominant copper peaks, Figure 80b, a magnified view, reveals subtle reflections from secondary phases such as Cu_xZr_y intermetallics and Cr-rich precipitates. These minor phases are present across all sample conditions, from powder to heat-treated states. Supporting prior findings by Kang et al. [230], transmission electron microscopy (TEM) has identified Cr oxides as one form of the Cr-containing phases. Within the Cu–Zr system, the likely intermetallics include $Cu_{51}Zr_{14}$, $Cu_{10}Zr_7$, and Cu_8Zr_3 [221], although their nanoscale dimensions likely render them undetectable via conventional SEM.

The powder sample exhibits the sharpest and most intense peaks, confirming its low internal strain and large crystallite size resulting from minimal deformation during gas atomization. In contrast, the

cold-sprayed (CS) sample shows significant peak broadening, indicative of severe lattice distortion and elevated dislocation density induced by the high-strain impact of particles during deposition. As post-deposition heat treatment is applied, from CS to SA, SA+AH, and DAH, progressive peak narrowing is observed, suggesting a reduction in microstrain and an increase in grain size due to recovery and recrystallization processes. Closer analysis of the (111) FCC-Cu peak in Figure 80c reveals a shift toward lower 2θ angles from powder to cold sprayed and the heat-treated samples. According to Bragg's law, this shift suggests ongoing precipitation evolution of Cr and Zr elements, which leads to changes in the overall lattice parameter of the copper matrix [231]. To fully confirm the precise identity, distribution, and evolution of these second-phase particles, whether formed during gas atomization (in powder), cold spray impact, or heat treatment, advanced characterization techniques such as TEM will be necessary, and are planned as part of future work.

To complement the EBSD results and illustrate the extent of plastic deformation in the cold-sprayed state as well as recrystallization during subsequent heat treatments, dislocation density and crystallite size were estimated for each condition using the Williamson–Hall method [145,230], as depicted in Figure 81.

$$\boldsymbol{\beta_T \cos\theta = \frac{\kappa\lambda}{\mathcal{D}} + 4\varepsilon \sin\theta} \tag{14}$$

$$\boldsymbol{\rho = \frac{14.4\varepsilon^2}{b^2}} \tag{15}$$

In the Williamson–Hall analysis, β represents the full width at half maximum (FWHM) of the diffraction peak, λ is the X-ray wavelength used (0.1542 nm for Cu Kα radiation), D denotes the crystallite size, ε is the lattice strain, b is the Burgers vector for copper (0.3615 nm), and θ is the Bragg angle. The slope of the linear fit in the Williamson–Hall plot (Figure 81a) is used to calculate the lattice strain (ε), while the intercept is employed to estimate crystallite size (D). The calculated dislocation densities for the powder, cold-sprayed (CS), solution-annealed (SA), solution-annealed plus age-hardened (SA+AH), and directly age-hardened (DAH) samples are 3.01×10^{13} m^{-2}, 2.04×10^{15} m^{-2}, 2.20×10^{14} m^{-2}, 3.57×10^{14} m^{-2}, and 9.97×10^{14} m^{-2}, respectively. Corresponding crystallite sizes are 108.8 nm, 14.1 nm, 29.8 nm, 33.6 nm, and 19.6 nm, as illustrated in the bar chart of Figure 81b. Among all samples, the CS condition exhibits the highest dislocation density and the smallest crystallite size, reflecting the presence of highly deformed, ultrafine grains as a result of severe plastic deformation

during deposition. With post-deposition heat treatment, the W-H plots shift toward lower strain and larger crystallite sizes, aligning with the EBSD-observed formation of recrystallized, equiaxed grains and a reduction in lattice distortion.

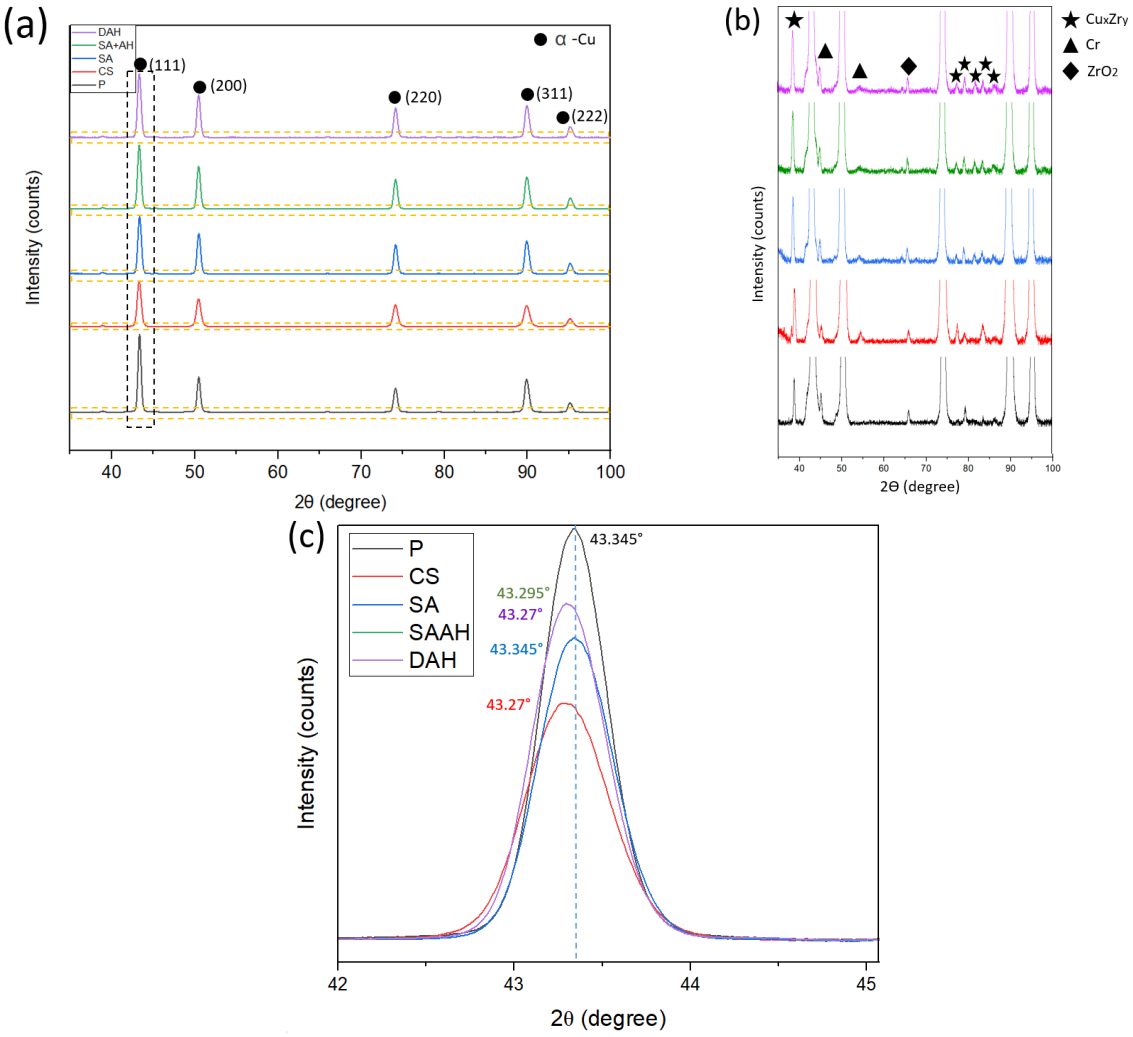


Figure 80: (a) XRD patterns of CuCrZr powder (P) and cold-sprayed (CS) samples subjected to different heat treatments, (b) a magnified view of the XRD peaks highlighted by yellow rectangles in (a) and (c) the enlarged spectra of 42–45◦ shown by black rectangle in (a).

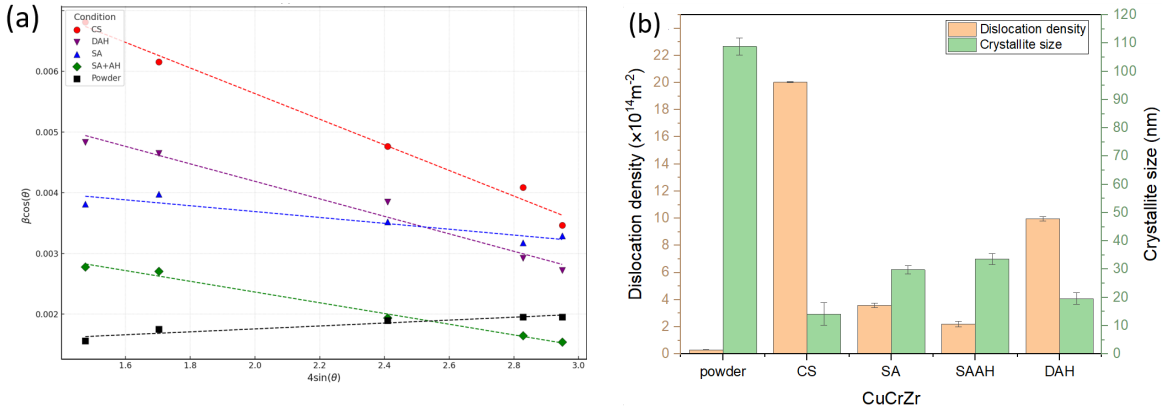


Figure 81: (a) Williamson-Hall plots for XRD diffraction patterns, (b) calculated dislocation density, and crystallite size for the powder, as sprayed and heat-treated CuCrZr deposits.

7.4.3 Microhardness

The average hardness of the CuCrZr samples in CS, SA, SA+AH and DAH states are determined and compared in Figure 82a, in which a change of properties before and after heat treatments can be recognized. As-sprayed CuCrZr part feature a Vickers hardness (HV) of 163.2 ± 12.9 which is explained by the work hardening effect induced by the extensively deformed CuCrZr particles. While SA sample have a hardness of 126.6 ± 6.7 HV, which suggests that the annealing heat treatment at the temperature of 950 ◦C causes to drop of the hardness when the work hardening of the coatings is largely released and subsequent recrystallization and grain growth (Figure 79) diminishing the dislocation density in CS part. Subsequent age hardening provokes an increase of the hardness to 146.9 ± 14.2 HV, although the microstructure shows a larger average grain size compared to the SA microstructure (Figure 78a and b). This could be compensated by the formation of fine dispersed precipitates consisting of Cr- and Zr- rich phases as described in literature because of age hardening [220,223,226]. Based on the assumption that direct age hardening (DAH), which has been performed at other additive manufactured parts, ameliorates the mechanical properties of CuCrZr parts [223,225], it has been shown that here there is a significant increase of hardness as well to 239.6 ± 10.3 HV compared to the SA +AH. This is attributed to recrystallization induced fine grains (Figure 78c) and lack of complete work hardening releasing. In addition, regarding the results in literature [223,226], a finer distribution of small Cr-particles within the Cu matrix is considered to be a major reason for the superior hardness of DAH CuCrZr samples.

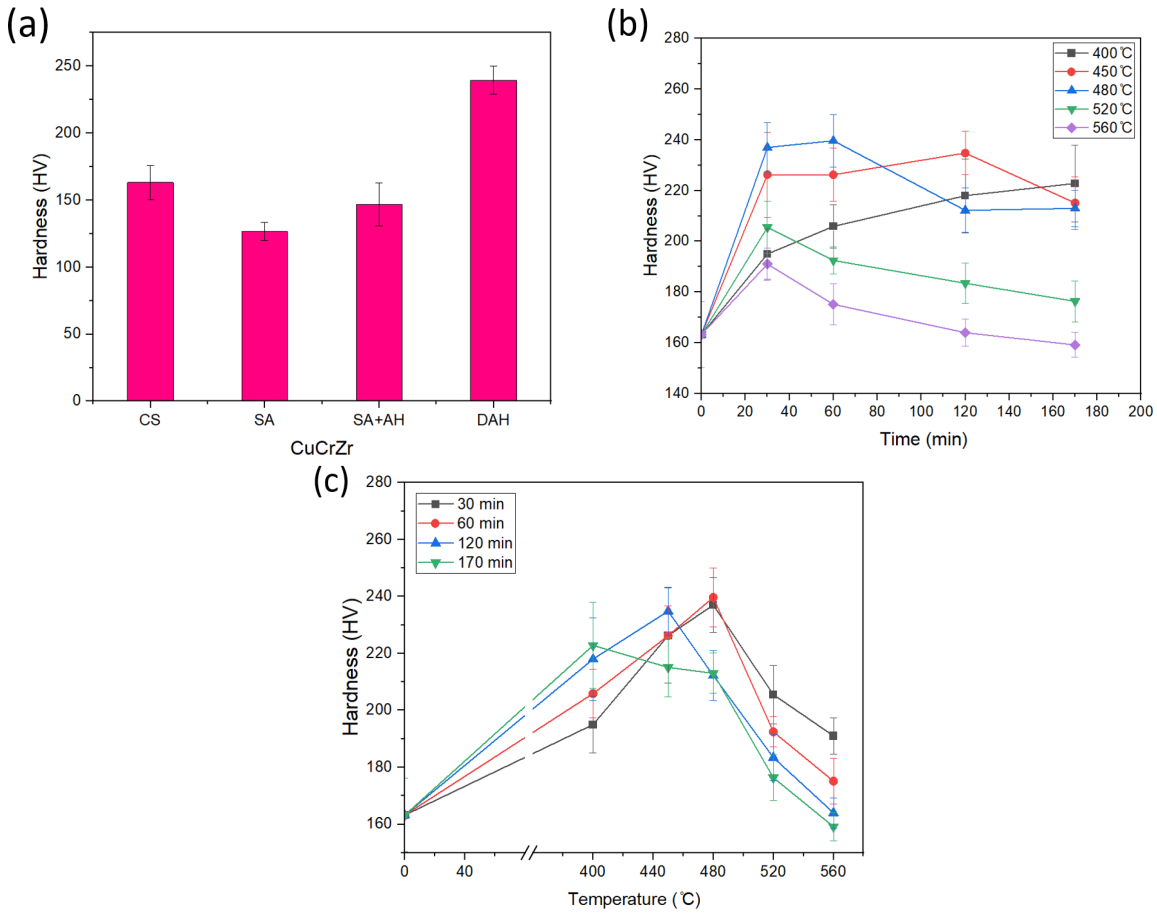


Figure 82: (a) Microhardness of CS CuCrZr specimens with and without heat treatment. (b) Variation in microhardness under different aging times. (c) Variation in microhardness under different aging temperatures.

To determine the optimal aging heat treatment for achieving maximum hardness, CuCrZr samples were age-hardened at 400–560 °C for 30–170 minutes. As shown in the DAH results (Figure 82b and c), hardness increased with exposure to elevated temperatures and longer durations. As expected, higher temperatures and extended exposure times initially led to an increase in hardness until a peak was reached, followed by a decline due to over aging [226]. In this stage, the precipitates have grown beyond a critical size, reaching the point where precipitation hardening is at its peak. At this size, the precipitates most effectively impede dislocation motion, maximizing the strengthening effect. As the aging temperature increases, the peak hardness is reached in shorter exposure times. This peak hardness was observed at 450 °C, 480 °C, 520 °C, and 560 °C after 120 min, 60 min, 30 min, and 30 min, respectively. The maximum hardness value of approximately 240 HV was recorded at 480 °C after 60

minutes of aging. Compared to aging duration, aging temperature had a more significant effect on microhardness. These findings provide an overview of the adjustable hardness range in CSAM CuCrZr alloy, allowing for tailored mechanical properties based on processing conditions.

7.4.4 Tensile properties

Figure 83 presents the tensile stress-strain curves of CuCrZr specimens subjected to different heat treatments at room temperature. The tensile properties exhibit significant variations, demonstrating that heat treatments have a direct impact on mechanical behavior. Among the specimens, SA+AH shows the highest ultimate tensile strength (UTS) along with the largest elongation, which is nearly equivalent to elongation of the SA specimen. In contrast, the as-deposited CS specimen has the lowest UTS and elongation.

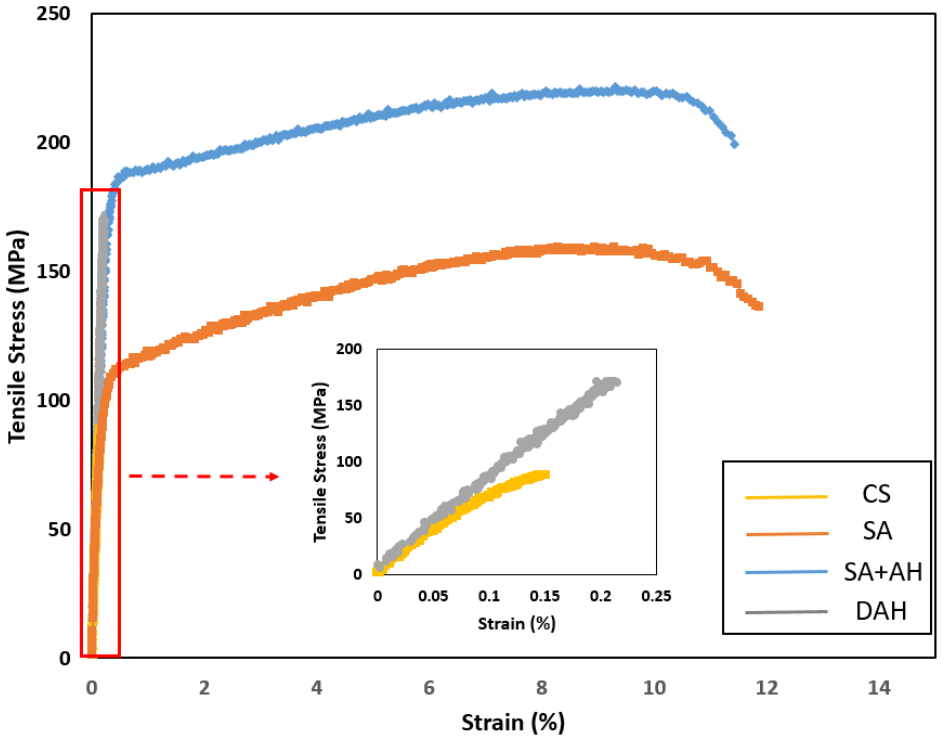


Figure 83: Comparison of stress–strain curves in different states of as sprayed, and after different heat-treatments.

To further assess the tensile properties of the heat-treated specimens, the tensile test results are summarized in Figure 84. The CS specimen exhibits a low UTS (89 ± 5 MPa) and negligible elongation

(0.15 ± 0.05%), primarily due to the presence of pores and unbonded areas along weak particle interfaces. After solution annealing (SA) at 950 °C, both UTS (154 ± 7 MPa) and yield strength (YS) (106 ± 5 MPa), as well as elongation (8.9 ± 0.5%), increase significantly. This improvement is attributed to the healing of particle interfaces, which are completely replaced by a recrystallized microstructure.

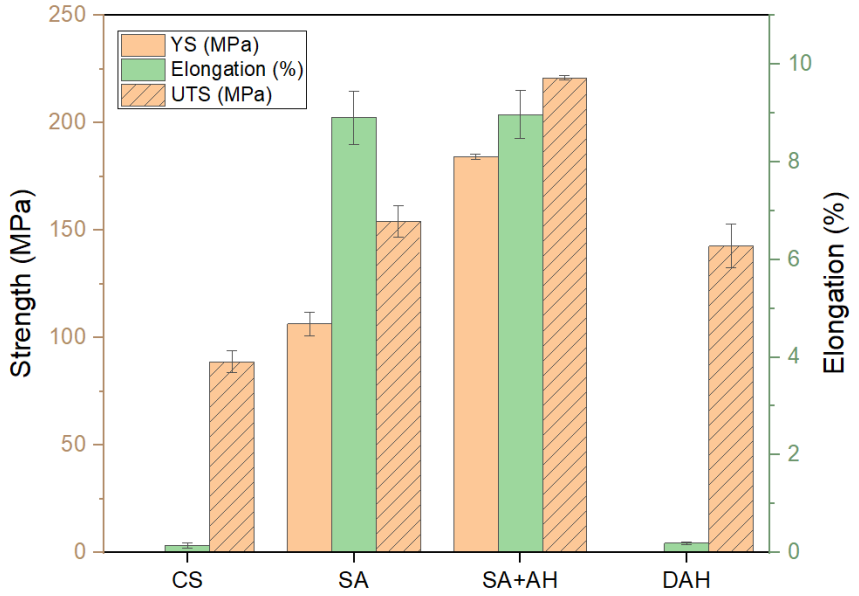


Figure 84: Comparison of tensile properties of CuCrZr deposits in the as-sprayed and different heat-treated conditions showing: (a) yield strength; (b) ultimate tensile strength; and (c) elongation.

Analyzing the tensile properties of heat-treated samples, it can be inferred that higher heat treatment temperatures with longer durations, regardless of their impact on the precipitation behavior of CuCrZr, a precipitation-hardened copper alloy, promote greater solid-state diffusion and stronger metallurgical bonding. Consequently, in low-pressure CSAM of CuCrZr alloy, the healing of particle interfaces plays a more dominant role in enhancing mechanical properties compared to precipitation hardening. This behavior contrasts with observations from heat-treated samples produced by other additive manufacturing processes, such as laser powder bed fusion (LPBF) and selective laser melting (SLM), where precipitation strengthening serves as the primary mechanism for improving mechanical properties in CuCrZr alloys [220,223,225].

Figure 85 presents the fracture surfaces of tensile samples subjected to different heat treatments. The CS and DAH specimens exhibit a characteristic cleavage fracture morphology, with no distinct preferential

propagation zones. This suggests that both samples underwent brittle failure with minimal plastic deformation, aligning with their observed negligible elongation values. In contrast, the SA and SA+AH specimens display numerous deep and shallow dimples, indicative of micro void coalescence. This microstructural feature confirms that these samples experienced plastic deformation, leading to a more ductile fracture mode. These observations are consistent with the higher ductility measured during tensile testing.

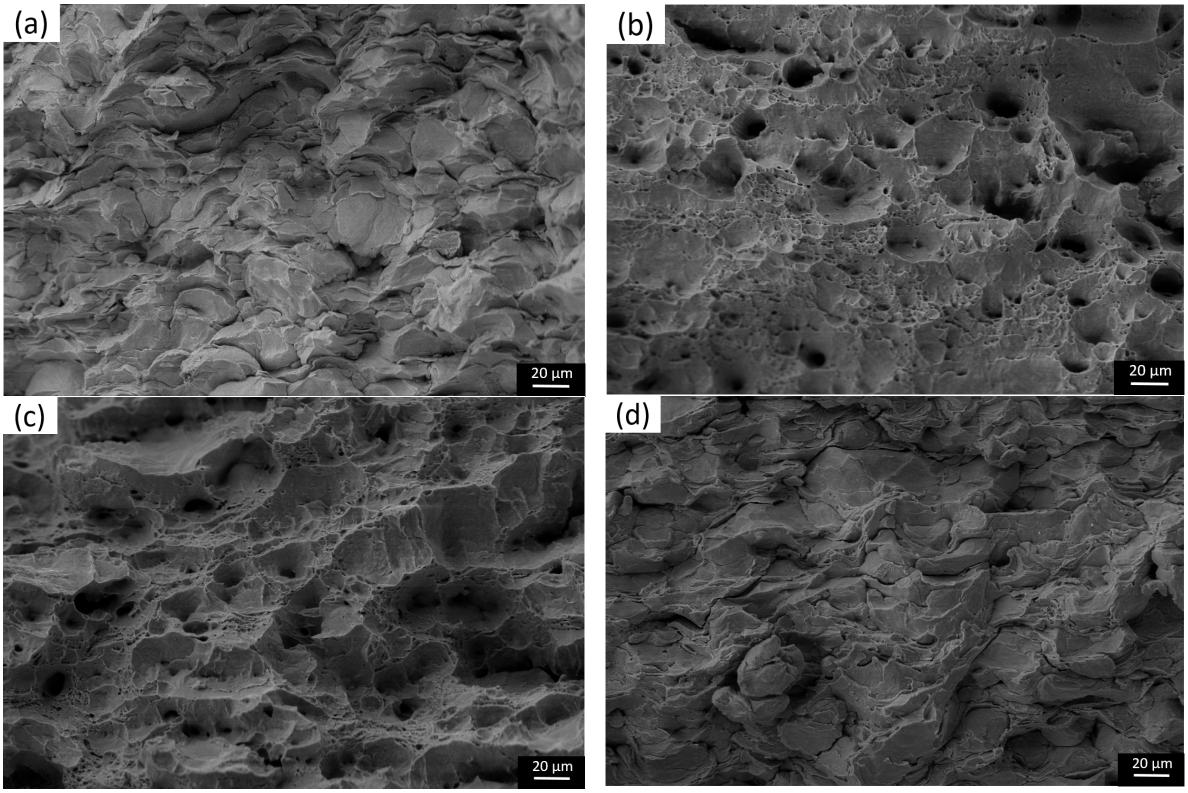


Figure 85: SEM images of the fracture surface of (a) CS, showing cleavage-like brittle fracture along splat boundaries, (b) SA, showing dimple-like morphology, indicating plastic deformation, (c) SA+AH, also showing plasticity and void formation and coalescence, (d) DAH specimens, showing failure along splat boundaries with no indication of plasticity.

To put these results in perspective, a comparison with available results on 3D-printing of CuCrZr was made. Figure 86 compares the properties obtained in this study with those of copper alloys containing Cr and Zr in similar concentrations, as reported in the literature. The specimens were fabricated using different additive manufacturing techniques, including selective laser melting (SLM)/

laser powder bed fusion (LPBF), and Wire Arc Additive Manufacturing (WAAM), all of which are based on melting and solidification, as well as CS additive manufacturing, which occurs in the solid-state. All the data presented were gathered from samples produced in two steps: fabrication and heat treatment. The results correspond to the heat treatment procedure that yielded the maximum tensile strength compared to other treatments. As shown in Figure 86a, all specimens produced via SLM and LPBF achieved their highest ultimate tensile strength (UTS) and yield strength (YS) after Direct Age Hardening (DAH). However, for WAAM, the highest UTS was obtained after Solution Annealing + Age Hardening (SA+AH). This difference can be attributed to the initial microstructural state of the samples after fabrication and the presence or absence of precipitates [226]. SLM and LPBF involve rapid solidification after melting, which results in a supersaturated solid solution without any initial precipitation in the as-built state. Consequently, DAH effectively promotes the formation of fine precipitates, significantly enhancing strength. In contrast, WAAM exhibits Cr precipitates in the as-built condition due to its slower solidification process [226]. As a result, DAH does not yield the highest tensile strength in WAAM, as it leads to precipitate coarsening, which weakens the material. Instead, solution annealing followed by age hardening (SA+AH) promotes the formation of finer and more uniformly distributed precipitates, resulting in maximum tensile strength. The CSAM sample from this study demonstrates a significantly lower maximum tensile strength compared to the other additive manufacturing methods primarily due to differences in bonding mechanisms and microstructural development. As a solid-state process, cold spray relies on plastic deformation and mechanical interlocking for bonding, without fully melting the particles. Consequently, cold spray lacks the extensive metallurgical fusion seen in SLM/LPBF, where complete melting and rapid solidification produce a highly dense and fully bonded microstructure with porosity below 0.01% [227], a value nearly 88 times lower than the 0.88% porosity measured in the as-sprayed sample of this study. In this regard, the residual porosity and weak interfaces act as stress concentrators and reduce both ductility and strength. This lower densification cannot be fully compensated by precipitation strengthening. In this context, a higher-temperature and longer-duration heat treatment (SA+AH) promotes greater solid-state diffusion, leading to the highest tensile strength in CS samples, outperforming SA and DAH. However, it is important to note that the maximum tensile strength of CS samples reported in the literature was obtained when heat treated in air (during 4 h) at 455 °C and then water quenched [229]. The observed discrepancy can be attributed to the use of a high-pressure cold spray system in those

samples, which enabled exceptionally high particle velocities and, consequently, superior tensile properties. This performance is the result of several synergistic system features. First, a long convergent–divergent De Laval nozzle with axial powder injection was employed, ensuring efficient and centralized acceleration of particles. The use of helium as the process gas, preheated to approximately 600 °C, and the stabilization of the gun temperature around 550 °C, significantly enhanced gas expansion and particle velocity. Operating at a nozzle pressure of 16.0 ± 1 bar and a chamber pressure between 500–550 mbar, the system established a strong pressure gradient critical for generating supersonic flow conditions. Helium, due to its lower molecular weight and higher thermal conductivity, offered superior acceleration capabilities compared to more conventional gases like nitrogen. The entire deposition process took place inside a vacuum-tight chamber, which was purged and filled with helium to keep oxygen levels below 100 ppm, effectively preventing powder oxidation. Additionally, a closed-loop helium circulation system maintained gas purity and minimized consumption. As a result, the process produced an ultra-dense microstructure with a porosity level below 0.1%, which remained largely unchanged after heat treatment. This porosity was nearly nine times lower than that of the as-sprayed sample in the present study. In this context, the remarkable density of the deposit in the as-sprayed condition played a crucial role in achieving its high initial tensile strength, which was further enhanced through precipitation strengthening during post-deposition heat treatment, ultimately exceeding the mechanical performance of both plasma-sprayed and forged copper alloys.

Additionally, as shown in Figure 86b, DAH due to the distribution of ultra fine precipitates significantly reduces elongation in SLM and LPBF samples. In contrast, SA+AH improves ductility in WAAM samples by reducing dislocation density and alleviating localized stresses during deformation [226]. However, both literature-reported cold-sprayed sample subjected to DAH [229] and those treated with SA+AH in this study have demonstrated improved ductility. This enhancement is attributed to increased metallurgical bonding and densification resulting from post-deposition heat treatment in CSAM. However, due to the inherent limitations of the DAH process, the improvement in elongation observed in the high-pressure cold-sprayed sample is less significant than the ductility enhancement achieved by SA+AH in the low-pressure cold-sprayed sample examined in this work.

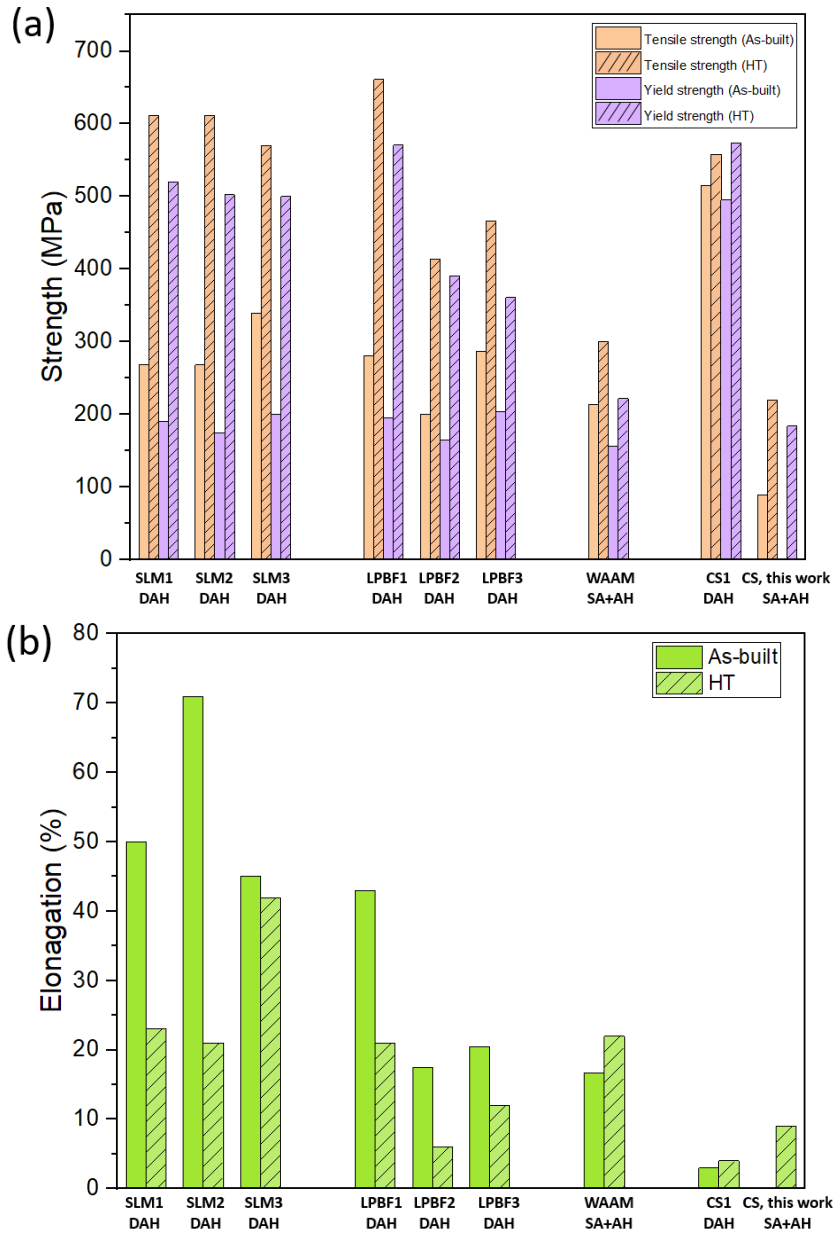


Figure 86: Comparison of the tensile properties of CuCrZr alloys in their as-built and heat-treated states, manufactured using SLM [220,225,228], LPBF [223,224,227], WAAM [226] and cold spray [229] additive manufacturing techniques, depicting: (a) ultimate tensile strength and yield strength and (b) percentage elongation.

It is worth noting the strengthening of CuCrZr alloys involves several mechanisms, including grain boundary, dislocation, solid solution, and precipitation strengthening [220,223]. In the as-sprayed state, the high dislocation density and refined grain structure are the primary contributors to strength. While it is likely that some nanoscale precipitates may form either during powder preparation or as a result of impact-induced effects during deposition, the exact nature and characteristics of these precipitates require further evaluation. Post-deposition heat treatments are expected to promote more defined precipitation, enhancing strength through particle-dislocation interactions. A complete understanding of precipitation strengthening will require future TEM analysis to clarify the size, distribution, and morphology of these phases across different processing conditions.

7.5 Conclusion

The CuCrZr alloy has been fabricated successfully by low-pressure CSAM and the effect of different heat treatment on microstructure, texture and mechanical properties were investigated. According to the observed results from various tests, the following conclusions are drawn:

1. The as-sprayed CuCrZr exhibits highly deformed splats and weakly bonded particle interfaces, leading to the formation of porosity and microcracks in the microstructure. Heat treatment significantly enhances the microstructure and densification of the deposition. SA and SA+AH promote grain reorganization, interfacial healing, and solid-state diffusion bonding, reducing porosity and strengthening particle interfaces. This transformation leads to the formation of equiaxed grains. Conversely, DAH at 480°C alone is less effective, as it does not fully dissolve existing defects, resulting in persistent porosity and weakly bonded regions. Among the studied heat treatment methods, SA+AH achieves the most dense and well-bonded microstructure.

2. SA promotes the formation of equiaxed grains and annealing twins, leading to a high degree of recrystallization. Subsequent AH slightly increases grain size, while DAH results in limited recrystallization, with most splats retaining their original structure and ultrafine deformed grains at particle interfaces. Grain boundary analysis confirms that SA and SA+AH specimens exhibit high HAGB fractions (~94%), indicating substantial recrystallization, whereas DAH specimens show a lower HAGB fraction (41.8%), suggesting only partial recrystallization. Post-heat treatment of CSAM CuCrZr samples resulted in random recrystallization without

developing a preferred grain orientation, as indicated by the distribution of texture intensities along multiple crystallographic planes.

3. As-sprayed CuCrZr exhibits a high hardness of 163.2 HV due to extensive work hardening, but this decreases to 126.6 HV after SA as recrystallization reduces dislocation density. Subsequent age hardening (SA+AH) increases hardness to 146.9 HV by promoting the precipitation of fine Cr- and Zr-rich phases. DAH achieves the highest hardness (239.6 HV), primarily due to the retained work hardening effects, formation of fine-grained recrystallized structures and a refined dispersion of precipitates, which effectively hinder dislocation motion. However, extended exposure to high temperatures leads to overaging, where precipitates coarsen beyond their optimal size, diminishing their strengthening effect. The peak hardness is achieved at 480°C after 60 minutes of aging.
4. The CS specimen exhibits the lowest strength (UTS: 89 MPa) and negligible elongation (0.15%) due to weak particle interfaces and pores. SA increases strength and ductility by recrystallizing the microstructure and healing particle interfaces. The SA+AH treatment achieves the highest UTS (220 MPa) and YS (184 MPa) due to precipitation strengthening and enhanced solid-state diffusion while maintaining good ductility (9%). In contrast, DAH results in lower strength and poor elongation due to insufficient metallurgical bonding and retained work hardening. Fracture analysis confirms that CS and DAH samples exhibit brittle failure, while SA and SA+AH samples demonstrate ductile behavior.
5. The mechanical performance of CuCrZr alloys depends on the additive manufacturing method and heat treatment applied. Fusion-based techniques like SLM and LPBF achieve the highest tensile strength through DAH, while WAAM benefits more from SA+AH to refine precipitate distribution. In CSAM samples, lower tensile strength is attributed to higher porosity and weak particle interfaces, with SA+AH proving the most effective by enhancing solid-state diffusion and densification. While DAH reduces elongation in SLM and LPBF, SA+AH improves ductility in WAAM and CSAM by mitigating dislocation density and strengthening metallurgical bonding. These findings highlight the need for process-specific heat treatments to optimize CuCrZr alloy properties.

Chapter 8
Engineering Dual Heterogeneous Laminated Microstructure to Unlock Strength and Ductility in Cold Sprayed Copper Alloys

(Manuscript ready for submission)

8.1 Abstract

The 3D printing capability of cold spray enables precise, layer-by-layer tailoring of powder compositions, sidestepping the formation of detrimental intermetallics, to strategically enhance both strength and ductility. In this work, we have leveraged this capability to fabricate dual-laminated Cu/CuCrZr structure with controlled interface spacing using a low-pressure cold spray system, followed by post-deposition heat treatment. The tailored heterogeneous microstructure, featuring alternating coarse- and fine-grained layers with distinct differences in composition and hardness, was systematically characterized for microstructural evolution, porosity, microhardness, and tensile performance. Tensile behavior revealed that reducing the interface spacing led to a simultaneous enhancement in both strength and ductility. In fact, the 14-layer laminate achieved an ultimate tensile strength of 244 MPa and a uniform elongation of 11%, representing substantial improvements of approximately 205% and 111% over monolithic Cu and 10% and 28% improvements over monolithic CuCrZr, respectively. Despite a slight reduction in yield strength, the laminate exhibited enhanced strain-hardening capacity and more uniform plastic deformation. Loading–Unloading–Reloading (LUR) experiments and geometrically necessary dislocation (GND) mapping confirmed that hetero-deformation-induced (HDI) strengthening, driven by strain partitioning and interface-induced back stress, was responsible for the improved mechanical response. These findings demonstrate that laminated heterostructures offer a promising strategy to enhance both strength and ductility in cold-sprayed materials. Further research is needed to optimize post heat treatment for enhancing ductility in soft domains and strength in hard domains.

8.2 Introduction

Cold Spray Additive Manufacturing (CSAM) is a solid-state deposition technology capable of producing freestanding components, thick surface coatings, and structural repairs [6,8,14,243,244]. It

has been applied to a wide range of metallic systems, including pure metals [245], conventional alloys [77], high-entropy alloys [246], amorphous metals [247], and metal matrix composites [248,249]. In CSAM, metal powders are accelerated by compressed gases, typically nitrogen, helium, or a mixture of both [174], and directed at a substrate at supersonic velocities. Upon impact, the particles undergo severe plastic deformation and bond to the substrate or previously deposited layers without melting. This sub-melting-point deposition distinguishes CSAM from fusion-based additive manufacturing techniques, offering advantages in thermal control and material preservation. Moreover, CSAM has demonstrated the ability to fabricate dense, high-strength structures with superior deposition rates and scalability compared to laser-based approaches [7,180,250–252]. However, a critical limitation remains: CSAM-deposited materials typically exhibit poor ductility in the as-sprayed state, largely due to severe plasticity, interfacial defects and weak particle bonding introduced during deposition [179,253].

To address the long-standing strength–ductility improvement in materials processed via thermomechanical treatments, powder metallurgy, and surface engineering techniques, numerous studies have focused on designing heterogeneous microstructures that enable simultaneous improvements in both strength and ductility. These include gradient structures [254–257], heterogeneous lamella structures [80], bimodal structures [258–261], harmonic structures [262–264], laminate architectures [101,265], dual-phase steels [84,266,267], nanodomained structures [268], and nanotwinned grains [269,270], among others [23]. A common trait among these materials is the significant variation in strength between domains, despite wide variability in domain size, geometry, and morphology, leading to pronounced microstructural heterogeneity. Wang et al. [259] developed a bimodal Cu structure using cryogenic rolling and secondary recrystallization, enhancing strain hardening resulting in a high tensile ductility with 65% elongation at fracture and 30% uniform elongation through geometrically necessary dislocation (GND) accumulation. Similarly, Ameyama et al. [71,262,271] introduced harmonic structures via mechanical milling and spark plasma sintering, forming ultrafine-grained shells around soft cores. The optimal properties in pure Cu were achieved in harmonic-structured samples containing around 40% ultrafine grain (UFG) fraction. Wu et al. [80] developed heterogeneous lamella structures in Ti through asymmetric rolling and partial recrystallization, generating significant back stress as confirmed by loading–unloading–reloading (LUR) tests. Following deformation of the heterogeneous lamellar Ti to a global true strain of 9.4%,

the recrystallized micrometer-sized grains exhibited an average true strain of 45%. Other notable advancements include gradient nano-grained surfaces fabricated by surface mechanical attrition treatment (SMGT) and surface mechanical grinding treatment (SMAT) [272–274], nanodomained Ni produced by pulse electrodeposition [268], and dynamically impacted Ag microcubes that form gradient structures with exceptional grain size contrast [275]. These examples collectively demonstrate that tailoring heterogeneity in grain size, interfacial character, and mechanical properties is a powerful strategy for overcoming the conventional strength–ductility trade-off.

Among various heterostructured designs, laminated architectures have proven particularly effective in balancing strength, ductility, and electrical conductivity. You et al. [99] developed a dual heterogeneous laminated (DHLed) Cu/CuCrZr composite via accumulative roll bonding (ARB) followed by annealing, achieving an impressive combination of high strength (563 MPa), elongation (~16.2%), and electrical conductivity. Ma et al. [101] studied Cu/bronze laminates fabricated by ARB and annealing, revealing that reducing interface spacing increased both strength and ductility through GND pile-up and enhanced back stress. Han et al. [100] employed powder metallurgy, rolling, and diffusion-based heat treatment to develop CuCrZr laminates with tunable hard/soft microstructural contrasts, resulting in UTS values between 366–412 MPa, elongation up to 26%, and high conductivity. Similarly, Wang et al. [97] evaluated CG/NS/CG laminates via LUR testing, identifying interface-induced back stress contributing up to 20% of the flow stress and supporting early-stage strain hardening. These findings reinforce that interface design and mechanical contrast in laminated metals can significantly enhance the synergistic response of strength and ductility. While the dual heterogeneous laminated structures achieve an impressive balance of strength, ductility, and conductivity, challenges related to scalability, thermal stability, microstructure complexity, and long-term durability remain unaddressed.

While extensive research has been conducted on hetero structures in conventionally processed materials, limited attention has been paid to their development in CSAM. Notably, Chen et al. [87] achieved an exceptional combination of strength (271 MPa UTS) and ductility (43.5% elongation to fracture) in CSAM-fabricated pure Cu. This was attributed to a heterogeneous microstructure composed of gradient nano-grained single splats and extensive twinning, formed during high-velocity impact, which together contributed to synergistic strengthening and ductility. In another pioneering study,

Bagherifard et al. [77] demonstrated the feasibility of creating freestanding bimodal CuCr1Zr structures by mechanically mixing as-atomized and ball-milled powders, forming micro- and nano-phase domains. Although the resulting structures exhibited high hardness and compressive residual stress, limited ductility remained a challenge. The study emphasized that mechanical performance was more influenced by volume fraction than phase morphology and suggested that post-deposition heat treatments could recover ductility by enhancing inter-splat bonding. These early efforts highlight the potential of CSAM for creating tailored heterogeneous microstructures, though further optimization of feedstock characteristics, processing parameters, and post-treatment strategies remains essential. Moreover, several innovative approaches have focused on enhancing the mechanical performance of CSAM samples through optimization of feedstock powder characteristics and processing parameter. For example, Singh et al. [86] showed that pure copper parts produced by CSAM using spherical powders and high-pressure cold spray using nitrogen can achieve nearly pore-free, highly conductive deposits with thermal conductivity close to bulk Cu. Without heat treatment, the deposits exhibited high strength (UTS 286 MPa) and 24% ductility, attributed to a bimodal microstructure comprising coarse grains embedded within a fine-grained network at particle boundaries. Fan et al. [91] proposed a novel strategy to enhance the mechanical performance of CSAM by using a wide particle size distribution and low processing parameters. This combination led to partial particle rebound during deposition, which in turn promoted in-process densification through severe plastic deformation and porosity reduction. As a result, the deposits attained tensile strengths similar to those obtained using high-temperature processing or expensive helium gas, although the improvement in ductility remained limited to under 3%.

Building on these advancements and aiming to further explore the potential of engineered heterogeneity in CSAM, we present the first successful fabrication of a dual-laminated heterogeneous microstructure using cold spray additive manufacturing. Pure Cu and CuCrZr powders with microcrystalline structures were deposited using nitrogen as the process gas to build a multilayered architecture composed of alternating coarse- and fine-grained layers. Flat freestanding tensile specimens were extracted from the builds for analysis. In this study, samples with varying layer counts and interface spacing were fabricated and subjected to post-deposition heat treatment. Detailed characterization was performed to evaluate porosity, microstructure, hardness, and mechanical properties. Furthermore, LUR tensile experiments were carried out to assess back stress evolution,

enabling deeper insight into the role of heterogeneity in enhancing the mechanical response of CSAM-fabricated materials. Given the precipitation and dispersion strengthening effects imparted by Cr and Zr in Cu alloys [207], and the challenges of traditional metallurgical methods [229], CSAM presents a promising alternative.

8.3 Experimental procedures

The experiment employed gas-atomized pure copper powder (99.9% purity) supplied by Metalpine GmbH (Austria), and a Cu–0.45 wt% Cr–0.05 wt% Zr alloy powder sourced from EOS North America Inc. The chemical composition of the alloy powder is presented in Table 21. SEM images of the pure Cu and CuCrZr alloy powders, shown in Figure 87a and b, respectively, reveal fine particles distributed around larger ones. The predominantly spherical morphology of the powders promotes good flowability, which is critical for achieving uniform deposition during the cold spray (CS) process. Furthermore, Figure 87c and d depict the equiaxed grain microstructures of the pure Cu and CuCrZr alloy powders, respectively. Cu shows larger equiaxed grains while CuCrZr exhibits finer grains. Both powders had a particle size distribution ranging from 15 μm to 45 μm as shown in Figure 87e.

The samples were fabricated using the commercial SST Series P Cold Spray System, manufactured by Centerline Ltd. in Windsor, Canada. In this low-pressure process, Cu and CuCrZr powders were accelerated to supersonic speeds through a converging–diverging de Laval-type UltiLife™ nozzle. The key specifications of the cold spray system employed in this study are outlined in Table 22.

Figure 88a and b show images of CSAM laminated samples consisting of 7 and 14 layers, respectively, fabricated from alternating layers of CuCrZr and pure Cu powders. The fabrication process involved sequential deposition of CuCrZr as the first layer, followed by Cu as the second, repeated to build up the desired number of layers. The 7-layer sample (7L), deposited using nitrogen gas, measured 125 mm in length, 60 mm in width, and 4.2 mm in thickness. The 14-layer sample (14L), also fabricated with nitrogen, measured 125 mm × 60 mm × 3.8 mm. As shown in Figure 88, no spalling occurred at the interface between the aluminum substrate and the deposited layers, and no cracks were observed within the material. Cold spray parameters used in this study are listed in Table 23. For the 7L sample, the process utilized a nozzle pressure of 1.99 MPa, a gas temperature of 400 °C, and a nozzle speed of 80 mm/s. For the 14L sample, the nozzle speed was increased to 120 mm/s. Cu and CuCrZr powders were sprayed from standoff distances of 20 mm and 25 mm, respectively, onto an aluminum substrate.

Table 21: Chemical composition of the CuCrZr alloy powder

Element	Cu	Cr	Zr	Fe	Si
Content (wt. %)	Balance	0.45 - 1.15	0.05 - 0.25	0.08	0.01

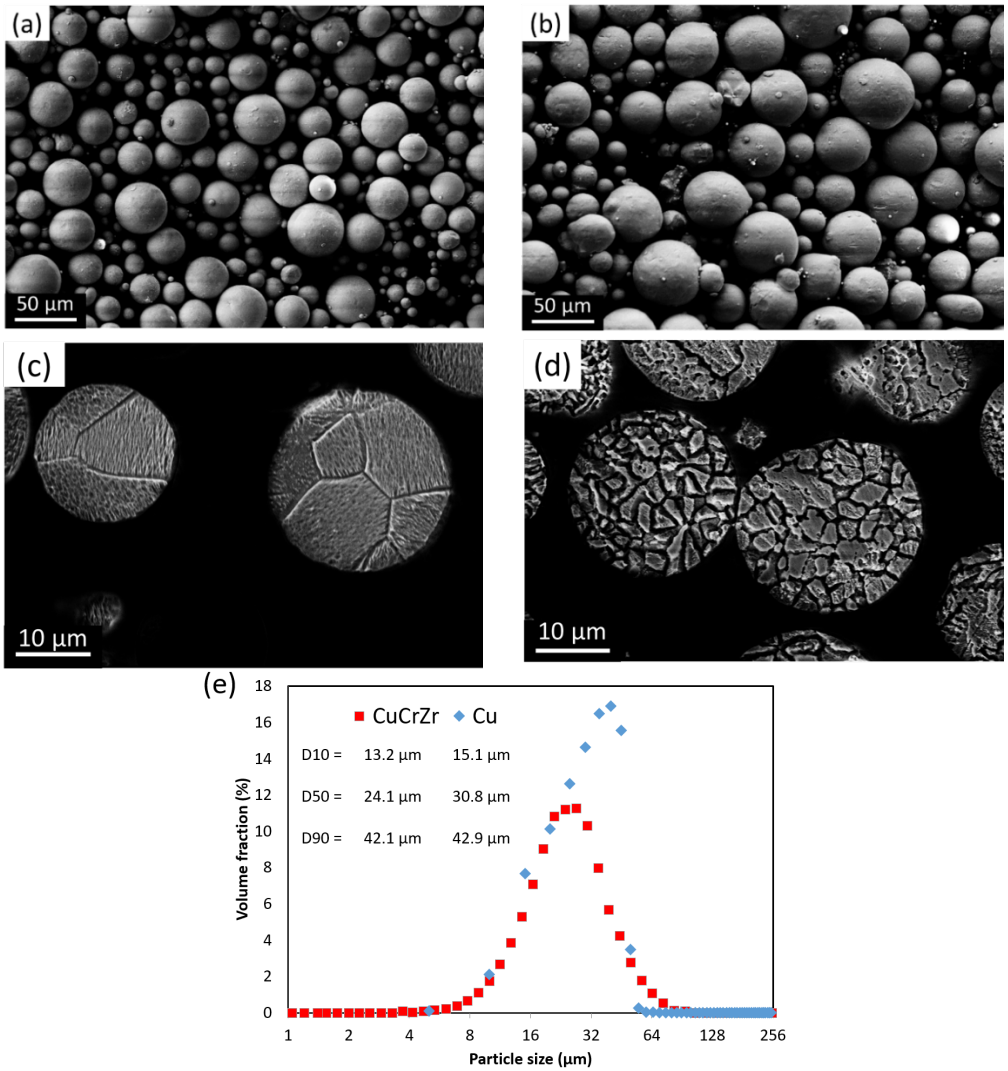


Figure 87: SEM micrographs of pure Cu (a, c) and CuCrZr (b, d) alloy powders: (a) and (b) display the morphology, while (c) and (d) show the equiaxed grain microstructure; and (e) Particle size distributions for pure Cu and CuCrZr.

Table 22: Specification of SST cold spray nozzle

Nozzle type	Nozzle Length	Nozzle Orifice Diameter	Nozzle Exit Diameter
De Laval UltiLife™	120mm	2 mm	6.3 mm

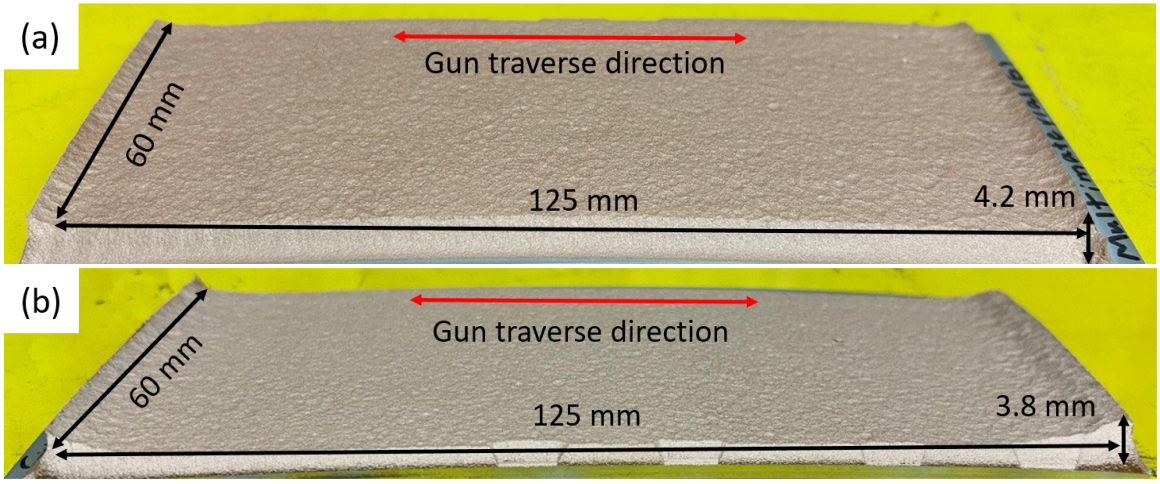


Figure 88: Macro images of laminated Cu/CuCrZr materials with different layer configurations: (a) 7-layer laminate and (b) 14-layer laminate.

Table 23: Cold spray deposition parameters [Chapter 6, Chapter 7]

Powder	standoff distance (mm)	X-offset (mm)	Gas Pressure (MPa)	Gas Temperature (°C)	Process Gas
Cu	20	-0.5	1.99	400	N_2
CuCrZr	25	-0.5	1.99	400	N_2

Following deposition, the cold-sprayed parts were detached from the substrate and machined into tensile specimens using electrical discharge machining (EDM). The detailed dimensions is provided in Figure 89a with the final specimen geometry illustrated in Figure 89b.

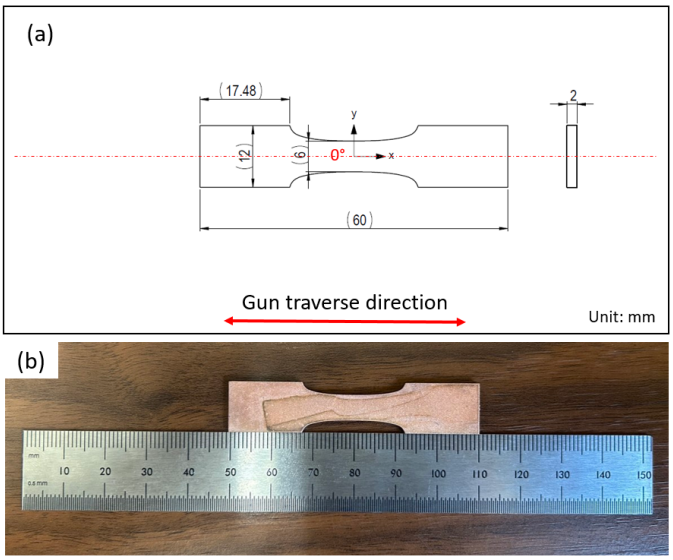


Figure 89: (a) Dimensions of the tensile specimen; and (b) the extracted tensile specimen from the 3D-printed part.

To improve the mechanical properties of the cold-sprayed laminated materials, a combined heat treatment consisting of solution annealing followed by age hardening was applied. Solution annealing (SA) was performed using a tube furnace (models GSL-1500X-50-UL and GSL-1600X-50-UL, manufactured by MTI Corporation) by heating the samples to 950 °C for 30 minutes, followed by water quenching. The solution-annealed specimens were then subjected to age hardening at 480 °C for 30 minutes. This heat treatment approach was chosen based on prior findings demonstrating its effectiveness in enhancing the mechanical properties of CSAM-fabricated pure CuCrZr [Chapter 7].

The microstructure of the samples was characterized using an optical microscope (Olympus BX41) and a scanning electron microscope (SEM) equipped with an energy dispersive spectrometer (EDS). For electron backscatter diffraction (EBSD) analysis, the specimens were vibratory polished for six hours with 50-nm colloidal silica to remove the mechanically deformed surface layer. EBSD analysis to assess microstructural evolution before and after heat treatment was conducted using an accelerating voltage of 25 kV, with a step size of 200 nm over an area of 550 × 550 μm². For detailed interface characterization, a finer step size of 50 nm and a scan area of 40 × 40 μm² were used.

Microhardness measurements were conducted using a Vickers hardness tester with a 200 gf load and a 15-second dwell time. The reported hardness values represent the average of 20 measurements per

sample. Tensile tests were carried out at room temperature using an Instron 8874 servo-hydraulic testing machine with a ±25 kN load capacity. Testing was performed under displacement control at a rate of 0.05 mm/min, and strain data were captured using a GOM ARAMIS 3D digital image correlation (DIC) system equipped with a 5-megapixel camera and a maximum frame rate of 15 fps. Each tensile test was repeated at least three times under identical conditions, and the average values were reported. To evaluate back stress during tensile deformation, loading–unloading–reloading (LUR) tests were performed. Specimens were unloaded at specific true strain levels using load-control mode, with an unloading rate of 200 N/min, until the applied load reached 20 N. The samples were then reloaded to the same load level and continued to the next unloading strain. The same specimen geometry was used as in the monotonic tensile tests. Fracture surfaces were analyzed using a scanning electron microscope (SEM, model: Zeiss Leo UltraPlus FESEM).

8.4 Results and discussion

8.4.1 Microstructure

Figure 90a and b present optical micrographs of the heterostructured samples, clearly revealing the well-defined laminated architecture with varying layer thicknesses and interface spacing. The brighter regions correspond to the Cu layers, while the darker areas represent the CuCrZr layers. Although the overall structure remains consistent, the layer thicknesses of Cu and CuCrZr vary throughout the build. It is well established that a low nozzle traverse speed or an increased number of scanning passes causes the coating profile to transition from a thin layer to a thicker, triangular-shaped form with reduced deposition efficiency. This transition is associated with a continuous increase in coating thickness and a gradual decrease in particle impact angle, which ultimately hinders further particle deposition [252]. Moreover, interruptions between passes to adjust printing parameters and then resume the process may compromise the precision of each deposited layer during 3D printing. As a result, these factors contribute to the observed variation in layer thickness across the build. In the 7L sample shown in Figure 90a, the Cu and CuCrZr layers are approximately 500 µm-570 µm and 700 µm-740 µm thick, respectively, while in the 14L sample (Figure 90b), they measure around 250 µm-400 µm and 300 µm-550 µm, respectively. As indicated by the yellow arrows in the laminated microstructure shown in Figure 90, the structure contains numerous pores, micro-voids, and unbonded particles. The interfaces

between layers are clearly visible, with no evident signs of delamination or separation, indicating good bonding between the pure Cu and CuCrZr alloy layers.

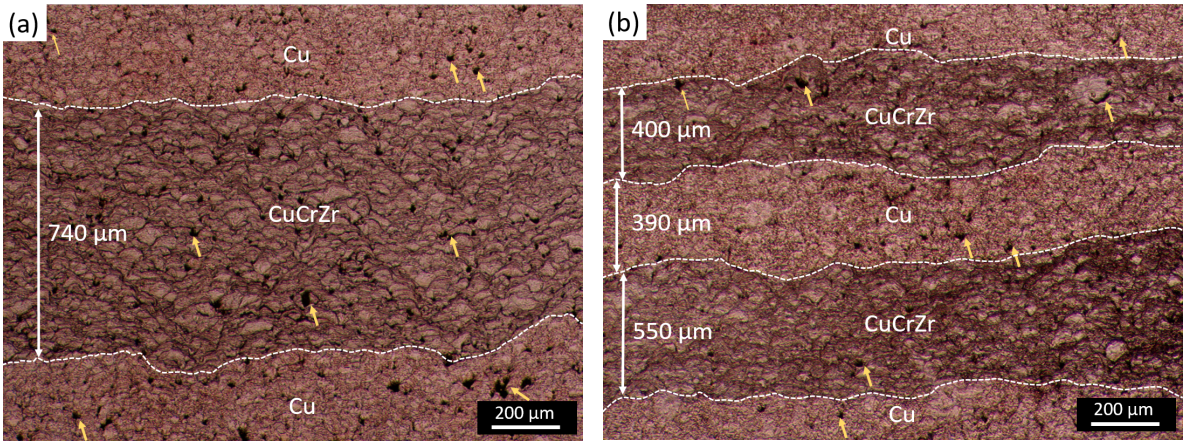


Figure 90: Optical micrographs of as-sprayed heterostructured laminated samples consisting of different Cu–CuCrZr layer counts: (a) 7 layers (7L) and (b) 14 layers (14L). Yellow arrows indicate the presence of porosity, micro-pores, and unbonded interfaces between the particles.

Since cold-sprayed additively manufactured parts in the as-sprayed condition typically do not exhibit optimal mechanical properties [179,253], the samples were subjected to a heat treatment process that previously yielded the best results for CuCrZr alloys. Figure 91a and b display the microstructure of laminated cold-sprayed samples that were solution annealed at 950 °C for 30 minutes, followed by water quenching and subsequent age hardening at 480 °C for one hour. The microstructure reveals a mixture of fine and coarse recrystallized grains, as well as distinct annealing twins indicated by blue arrows. Figure 91c and d further present the recrystallized microstructures of pure Cu and CuCrZr, respectively, at higher magnifications. The optical micrographs reveal a significantly higher porosity in the heat-treated cold-sprayed pure Cu sample compared to the CuCrZr counterpart. This disparity can be attributed to several fundamental differences in their microstructural evolution during post-processing. The higher work-hardening of CuCrZr facilitate more intense plastic deformation upon impact during cold spray, leading to better mechanical interlocking and metallurgical bonding, which improves particle bonding. Pure Cu, on the other hand, deforms more uniformly with less fragmentation, resulting in less effective mechanical bonding. This result in a denser, more cohesive microstructure in CuCrZr, while the pure Cu sample retains residual porosity even after solution annealing and age hardening. It is important to highlight that a previous comprehensive study by the

same authors determined the optimal post-deposition heat treatment for low-pressure cold-sprayed Cu produced under comparable conditions. In that study, samples were heat treated at 700 °C for 4 hours and subsequently allowed to cool naturally to room temperature within the furnace. This process resulted in an approximately dense microstructure with enhanced particle bonding. However, this optimal condition is significantly different from the heat treatment procedure selected for CS CuCrZr, which was applied to the Cu/CuCrZr laminated samples in the present study. Rapid cooling during water quenching can generate significant thermal shock, particularly when heat treatment is performed at elevated temperatures (950°C) [276,277]. The resulting thermal gradients may induce thermal stresses, leading to the formation of microcracks at weaker or partially bonded particle interfaces. In contrast, slower cooling rates promote more extensive atomic diffusion, allowing for the healing of imperfect boundaries and enhancing cohesive strength. However, rapid quenching interrupts this healing process prematurely, often leaving interfaces only partially bonded, potentially compromising the overall integrity of the microstructure.

Additionally, Figure 91c demonstrates that the Cu layer exhibits an equiaxed microstructure after heat treatment, with no visible splat structures remaining. In contrast, Figure 91d clearly reveals that the splat morphology is still preserved in the CuCrZr microstructure following heat treatment. In pure Cu, due to its high stacking fault energy (SFE) and higher atomic mobility, recrystallization occurs more readily. During solution annealing at 950 °C and subsequent age hardening, pure Cu undergoes recrystallization and extensive grain growth, resulting in the complete disappearance of the original splat boundaries and the formation of an equiaxed grain structure. In contrast, CuCrZr, being an alloy containing solute atoms of Cr and Zr, exhibits different behavior. These solute atoms contribute to Zener pinning, where fine Cr-Zr precipitates hinder grain boundary motion and retard grain growth [99,278]. As a result, even after heat treatment, full boundary migration is restricted in CuCrZr, leading to the preservation of the original splat morphology.

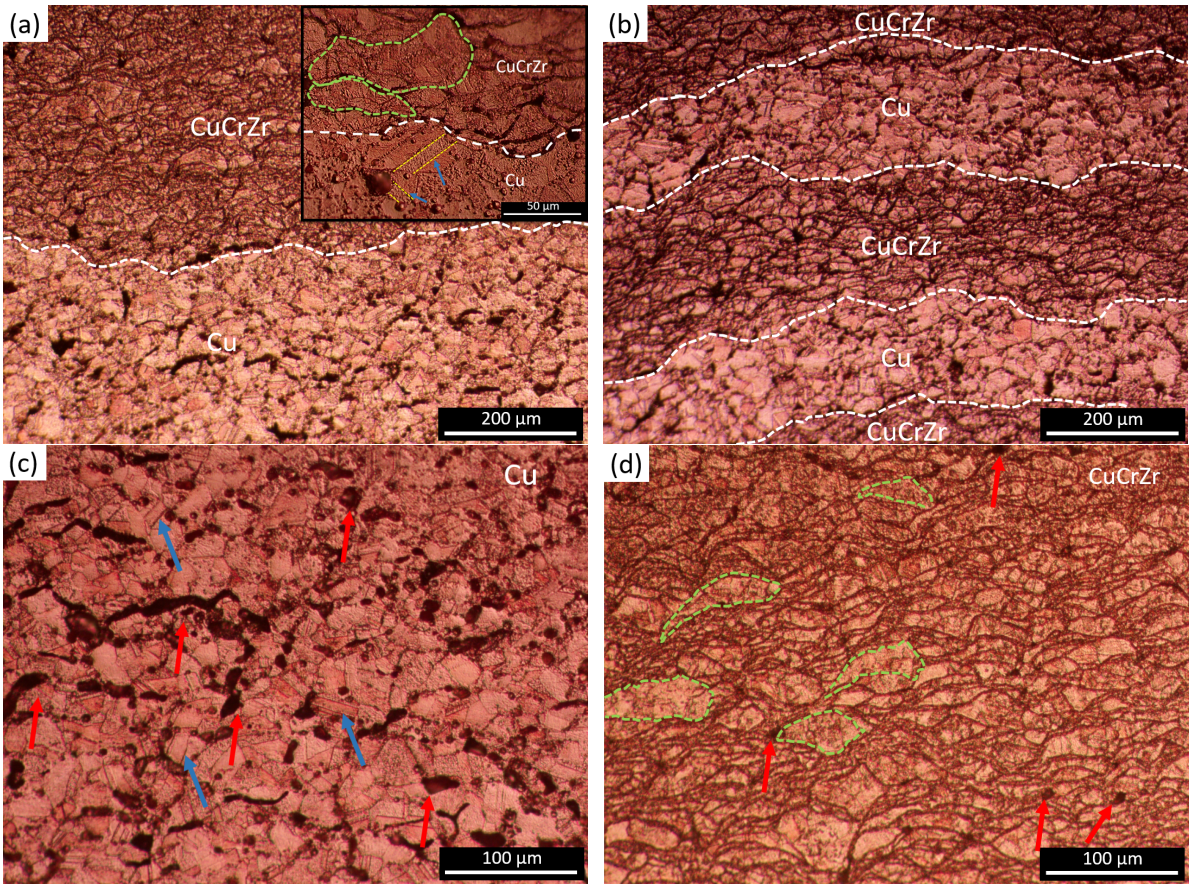


Figure 91: Optical micrographs of solution annealed+ age hardened heterostructured laminated Cu–CuCrZr samples with (a) 7L and (b) 14L. At this magnification, (a) displays portions of one Cu layer and one CuCrZr layer, while (b) reveals two Cu layers, one complete and two incomplete CuCrZr layers. The inset in (a) presents a higher magnification view of the interface between the Cu and CuCrZr layers. Images (c) and (d) show the microstructures of the heat-treated Cu and CuCrZr layers individually at higher magnifications. Blue arrows highlight annealing twins, red arrows indicate porosity and unbonded particle interfaces, and green ellipses highlight individual splats that have retained their morphology after heat treatment.

To gain deeper insight into the microstructural characteristics, deposition behavior, and recrystallization response of Cu and CuCrZr alloys within the laminated samples, EBSD analysis was conducted on both as-sprayed and heat-treated specimens. Figure 92a and b present the inverse pole figure (IPF) maps of the 7L and 14L samples in the as-sprayed condition. Cu and CuCrZr layers exhibit a non-uniform grain size distribution, with finer grains near particle boundaries and coarser grains in particle interiors as shown by yellow rectangles. This variation results from heterogeneous deformation

during cold spray deposition. High plastic strain at particle interfaces promotes continuous dynamic recrystallization (CDRX), while lower strain in particle cores favors discontinuous dynamic recrystallization (DDRX), leading to grain growth [162]. The strain gradient across particles generates geometrically necessary dislocations (GNDs), facilitating grain nucleation. Additionally, lower flow stress in particle centers supports grain boundary migration and growth, whereas higher flow stress at interfaces enhances grain refinement [239].

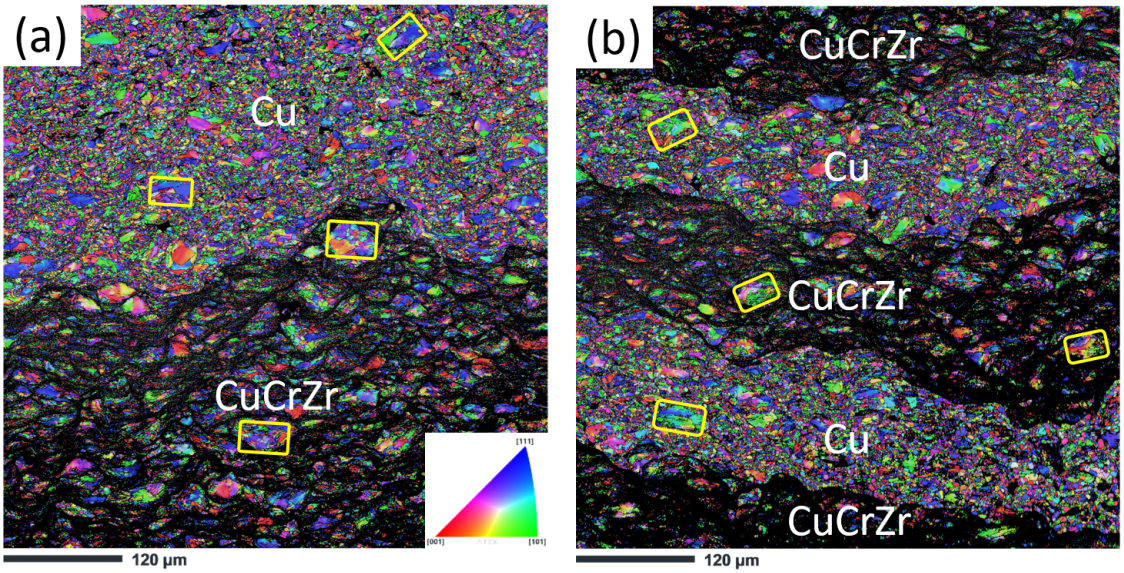


Figure 92: Inverse pole figure (IPF) maps of laminated Cu–CuCrZr samples with varying layer counts: (a) 7 layers (7L) and (b) 14 layers (14L), both in the as-sprayed condition. Yellow rectangles show larger grains in particle interiors.

The average grain sizes of the Cu and CuCrZr layers in the 7L and 14L samples, shown in Figure 92, were determined through image partitioning obtained from EBSD maps. In the 7L sample, the Cu and CuCrZr layers exhibited average grain sizes of 1.5 µm and 0.9 µm, respectively. Similarly, the average grain sizes in the 14L sample were measured at 1.2 µm for the Cu layer and 0.8 µm for the CuCrZr layer. In these maps, the CuCrZr layers exhibit heavily deformed, ultrafine grains that could not be reliably indexed, the reported average grain size is likely smaller because of unindexed grains, due to the high degree of strain, while the Cu layers reveal a broader grain size distribution with more distinguishable features. This contrast is attributed to the initially finer equiaxed grain structure of the CuCrZr powder (Figure 87d), as well as its higher work-hardening capability, which promote more

severe plastic deformation and grain fragmentation during the cold spray process. Due to the slight difference of grain size in 7L and 14L sample, it could be resulted that more peening effect in 14L sample has been lead to more grain refinement.

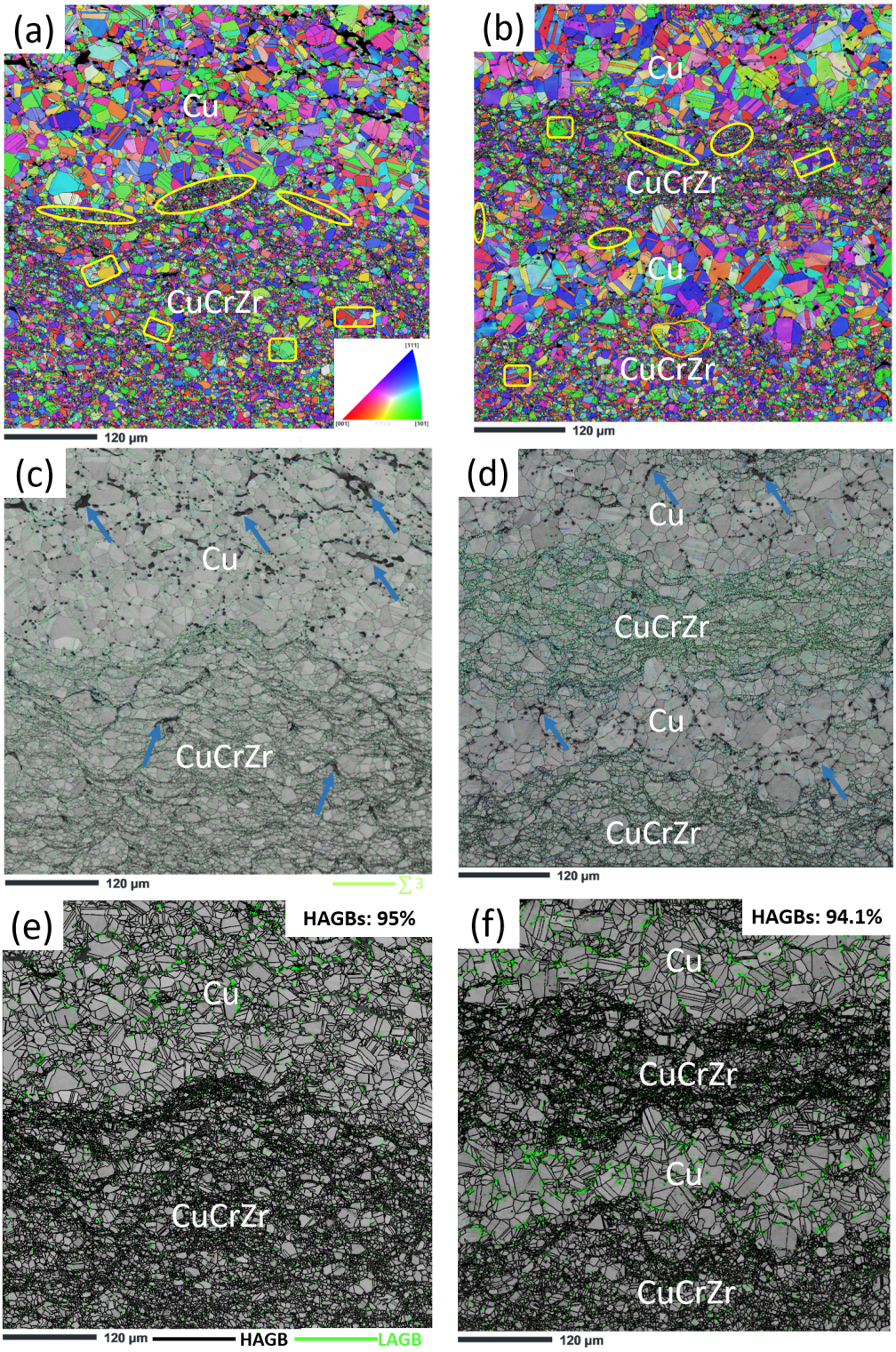
Figure 93 presents the EBSD analysis of heterostructured laminated samples produced with 7L and 14L after heat treatment. The inverse pole figure (IPF) maps (Figure 93a and b) show fully recrystallized dislocation free structure in the Cu and CuCrZr layers, while the CuCrZr layers retain finer grains with more fragmented boundaries, likely due to their initially smaller grain size, higher work hardening and stored strain energy which can highly activate recrystallization. The CuCrZr layers continue to show a non-uniform grain size distribution after recrystallization, due to the previously discussed heterogeneous plastic deformation. This deformation promotes the formation of more nucleation sites at splat boundaries especially in the build up direction (orange one splat marked in Figure 93b), resulting in finer grains near the interfaces and larger grains within the splat interiors, as indicated by the yellow rectangles in Figure 93a and b. The presence of a bimodal grain size distribution offers a beneficial combination [264,279], enabling simultaneous improvement in both strength and ductility of the CS CuCrZr.

The microstructural difference between the component layers of the 14L sample is more pronounced, with the average grain size difference between the Cu and CuCrZr layers reaching 2.65 μm, compared to 1.8 μm in the 7L sample. This suggests that the 14L sample exhibits a more heterogeneous microstructure. Additionally, the grain size near the CuCrZr/Cu layer interfaces is consistently smaller than in regions farther from the interfaces, as highlighted by the yellow ellipses in Figure 93a and b. This behavior can be attributed to the mechanical contrast between Cu and CuCrZr: Cu is softer and more ductile, whereas CuCrZr is harder and stronger due to solid solution strengthening and precipitation hardening. During the cold spray process, whether a Cu particle impacts a CuCrZr layer or a CuCrZr particle impacts a Cu layer, plastic deformation becomes highly localized at the interface. The softer Cu undergoes more plastic deformation while the harder CuCrZr resists deformation, resulting in a strain gradient across the interface. This mismatch leads to significant dislocation buildup and residual stresses, concentrating stored strain energy near the boundary. Upon subsequent heat treatment, the elevated stored energy at the interface promotes recrystallization, leading to the formation of finer grains in these regions. It is believed that these transitional interfaces, where the grain

size gradually increases away from the boundary, play a critical role in accommodating plastic incompatibility and sustaining larger strain gradients [100].

The band contrast images, with Σ3 boundaries indicated by green lines (Figure 93c and d), further illustrate the grain size variation between layers and reveal a higher concentration of porosity and microvoids within the Cu regions, marked by blue arrows, consistent with the optical microscopy observations in Figure 91. Σ3 boundaries, characterized by a 60° misorientation around the ⟨111⟩ axis in FCC metals, represent low-energy grain boundaries commonly linked to annealing twins. Their increased presence, particularly within the CuCrZr layers, reflects the enhanced recrystallization occurring in these regions [216]. Grain boundary maps (Figure 93e and f) indicate a high proportion of high-angle grain boundaries (HAGBs), reaching 95% in 7L and 94.1% in 14L, confirming effective recrystallization during heat treatment. However, a larger presence of low-angle boundaries (LAGBs, shown in green) is observed in the Cu layers. Recrystallized fraction (RX) maps (Figure 93g and h) further validate this, with RX values of 96.69% and 94.99% for 7L and 14L, respectively. Unrecrystallized grains (URX) remain more noticeable in the Cu regions. Kernel average misorientation (KAM) maps (Figure 93i and j) show generally low internal misorientation, indicating reduced dislocation density after heat treatment, though some localized strain accommodation is still evident in the Cu layers, likely due to incomplete recrystallization.

Overall, both microstructures display extensive recrystallization. The CuCrZr layers exhibit slightly higher recrystallization completeness and HAGB content due to the higher activation energy. Cr and Zr initially assist in facilitating grain boundary movement during the early stages of recovery. However, as the material undergoes aging, these elements contribute to the formation of fine precipitates that act as obstacles to grain boundary migration, thereby restricting further grain growth [99,100]. The essence of grain growth is the process of grain boundary migration, and the grain boundary migration rate determines the grain growth rate. The total amount of solute atoms and the precipitates play the critical role determining the grain boundary mobility. Consequently, CuCrZr maintains a finer grain structure post-treatment, in contrast to pure Cu, which undergoes grain coarsening due to the absence of such precipitate stabilization. In this regard, different grain size distribution, precipitation behavior and porosity level in Cu and CuCrZr layers result in a characteristic heterogeneous microstructure in both 7L and 14L samples.


(a)
Cu
CuCrZr
120 µm
(b)
Cu
CuCrZr
Cu
CuCrZr
120 µm
(c)
Cu
CuCrZr
120 µm
∑3
(d)
Cu
CuCrZr
Cu
CuCrZr
120 µm
(e)
HAGBs: 95%
Cu
CuCrZr
120 µm
HAGB
LAGB
(f)
HAGBs: 94.1%
Cu
CuCrZr
Cu
CuCrZr
120 µm

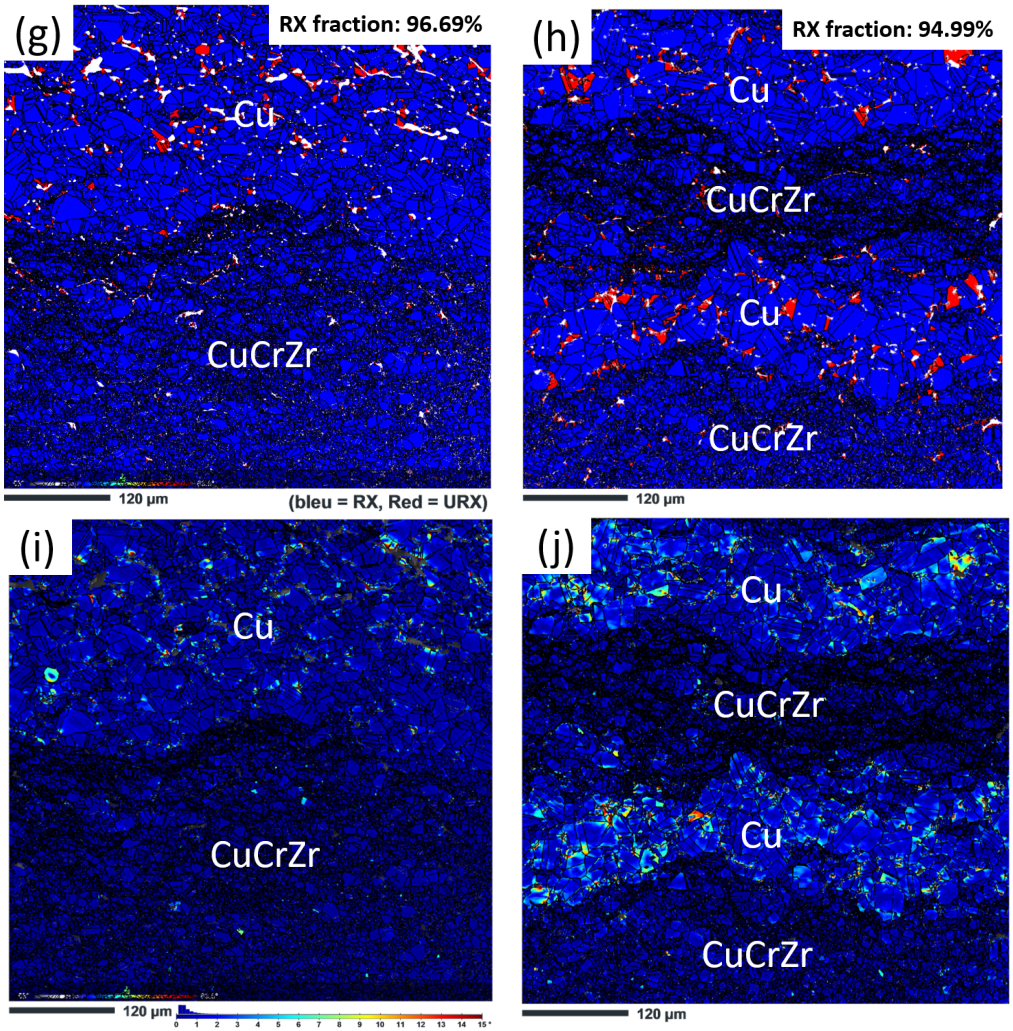


Figure 93: Inverse pole figure (IPF) maps, band contrast images, grain boundary distribution maps (overlaid on band contrast), recrystallized fraction (RF) maps, and kernel average misorientation (KAM) maps of heat-treated laminated samples: (a), (c), (e), (g), and (i) correspond to the 7-layer (7L) sample, while (b), (d), (f), (h), and (j) correspond to the 14-layer (14L) sample. IPF maps (a, b) show recrystallized structures in both Cu and CuCrZr, with CuCrZr exhibiting finer, more fragmented grains. Yellow rectangles highlight the coarser grains located within splat interiors, which, together with finer grains along splat boundaries, form a bimodal grain structure in the CuCrZr layer. An orange mark in (b) highlights a splat boundary along the build-up direction, and yellow ellipses indicate finer grains near Cu–CuCrZr interfaces. Band contrast images (c, d) show Σ3 twin boundaries (green lines), more prevalent in CuCrZr. Blue arrows indicate porosity more noticeable in Cu. Grain boundary maps (e, f) reveal a high fraction of HAGBs, while LAGBs (green lines) appear more in Cu. RF maps (g, h) confirm high recrystallization, and KAM maps (i, j) indicate low internal misorientation post-treatment, with some localized strain accommodation remaining in Cu.

8.4.2 Microhardness

As illustrated in Figure 94a, prior to heat treatment, the microhardness values of the Cu and CuCrZr layers are measured at 132 ± 5 HV and 170 ± 6 HV, respectively. Following solution annealing and age hardening (SA+AH), a noticeable reduction in hardness is observed, with Cu decreasing to 95 ± 3 HV and CuCrZr to 145 ± 4 HV. This decline is primarily attributed to stress relaxation and recrystallization and grain growth, diminishing the dislocation density in CS parts, which softens the microstructure. The more pronounced drop in the Cu layer results in a substantial hardness contrast between the Cu and CuCrZr layers, creating a microstructural heterogeneity characterized by alternating soft and hard layers. A slight change in the hardness difference between Cu and CuCrZr from 38HV before heat treatment to 50HV after heat treatment also worth noting. This may be the results of better thermal stability in CuCrZr due to the presence of hard precipitates that may act as barriers for dislocation movement.

Figure 94b presents the cross-sectional microhardness profile across the 7 layers of Cu/CuCrZr interfaces of 7L and 14L laminated materials. A distinct and abrupt transition in hardness is evident at the interfaces, shifting from the softer Cu to the harder CuCrZr alloy. Within each individual layer, however, the hardness distribution remains relatively uniform. The hardness transition between layers, as well as the hardness distribution within each layer (accounting for standard deviation), remains nearly consistent in the 14L sample. The Cu layers consistently exhibit lower hardness compared to their CuCrZr counterparts, with an average interlayer hardness difference of approximately 50 HV. This variation stems from differences in microstructural characteristics between the two materials. In the Cu layers, the relatively low hardness is attributed to limited alloying, resulting from insufficient bulk diffusion of alloying elements [99,100,280], a higher degree of grain coarsening during heat treatment and higher level of porosity, where grain size and elemental dilution increase from the CuCrZr/Cu interface toward the Cu layer. It is important to note that, based on Fick's law, the total amount of alloying elements diffusing from the CuCrZr layer into the adjacent pure Cu layer remains constant [100,281]. However, with increasing Cu layer thickness, the diffusion path lengthens, leading to a lower concentration of alloying elements per unit volume within the Cu layer. As a result, the number and size of precipitates within the Cu layer tend to decrease due to the reduced diffusion of alloying elements. Nevertheless, in the present study, the hardness difference of layers between the

samples with different Cu layer thicknesses remains less pronounced due to small variation and is limited to the standard deviations shown in the Figure 94b.

These sharp structural and mechanical contrasts across suggests a significant degree of mechanical incompatibility, which is likely to induce back-stress hardening, a mechanism that can enhance both strength and ductility during plastic deformation [80,81].

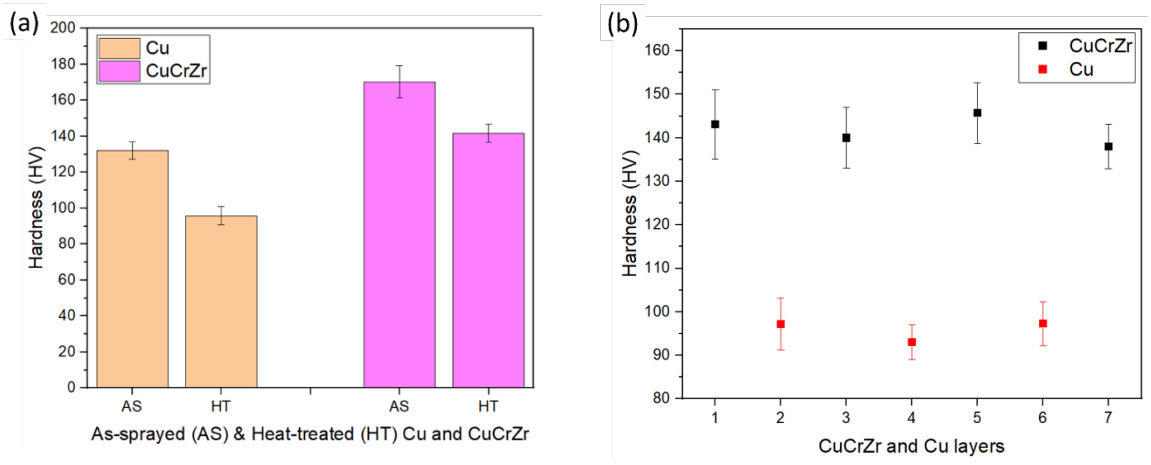


Figure 94: (a) Microhardness of Cu and CuCrZr layers before and after heat treatment, showing better thermal stability, likely due to Cr and Zr presence; (b) Micro-hardness in both the heat-treated Cu and CuCrZr layers for the first 7 layers in 7L and 14L samples. This sharp mechanical contrast between layers suggests a significant degree of mechanical incompatibility.

8.4.3 Tensile Behavior

Figure 95a displays the engineering stress–strain curves of heat-treated samples, including pure Cu, pure CuCrZr, and Cu–CuCrZr laminates with 7 (7L) and 14 (14L) layers, alongside predicted curves based on the rule of mixtures (ROM) for the laminated samples. The corresponding mechanical parameters, ultimate tensile strength (UTS), yield strength, and uniform elongation, extracted from these curves are summarized in Figure 96.

The stress–strain response of pure Cu is characterized by a brief strain hardening phase followed by early saturation of flow stress and premature failure, indicating poor ductility. In contrast, pure CuCrZr displays greater tensile strength and elongation. The limited deformability of pure Cu can be primarily attributed to its coarse grains and higher levels of porosity and microvoids observed in the

microstructure (Figure 91). Both UTS and uniform elongation increase in the laminated samples with increasing number of layers and interfaces. The 7L and 14L heterostructured laminates exhibit superior uniform elongation compared to both Cu and CuCrZr. Specifically, tensile strength increases from 80 MPa (pure Cu) and 221 MPa (CuCrZr) to 226 MPa and 244 MPa for the 7L and 14L laminates, respectively, representing an increase of approximately 182% and 205% over pure Cu, and 2.26% and 10.41% over pure CuCrZr. According to the ROM, the mechanical property f_{ROM} of the laminate can be expressed as [255]:

$$f_{ROM} = \sum_{i=1}^{2} V_i \ f_i \tag{16}$$

where V_i and f_i are the volume fraction and mechanical property of component i, respectively. Based on the average layer thicknesses of Cu and CuCrZr measured from multiple images across different regions of the 3D-printed samples, the volume fractions in the 7L sample are 36% Cu and 64% CuCrZr, while in the 14L sample they are 44% Cu and 56% CuCrZr. Accordingly, the tensile stress–strain curves predicted using these volume fractions indicate UTS of 170 MPa for the 7L sample and 159 MPa for the 14L sample. The discrepancy in flow stress between the experimentally measured and ROM-predicted curves reaches 56 MPa for the 7L sample and 85 MPa for the 14L sample, accounting for 24.7% and 34.8% of the total flow stress, respectively. The deviation of experimentally measured values from ROM highlights the contribution of hetero-deformation-induced (HDI) strengthening due to the interface effects, as discussed later, and suggested [78].

In terms of ductility, the uniform elongation increases from 5.2% (pure Cu) and 8.64% (CuCrZr) to 10.3% and 11% for the 7L and 14L laminates, respectively, representing improvements of approximately 98% and 111.5% over pure Cu, and 19% and 28% over CuCrZr. The experimentally measured ductility values for the 7L and 14L samples exceed the ROM-based predictions by 3% and 3.9%, respectively.

These findings demonstrate that the introduction of a layered microstructure with alternating soft and hard domains enhances both strain tolerance and uniform deformation capability. This improvement is further amplified by increasing the number of interfaces, each contributing to the formation of an interface-affected zone due to the accumulation of geometrically necessary dislocations (GNDs) [101]. As a result, a higher interface density leads to greater GND accumulation within a given volume, thereby improving both tensile strength and ductility.

Ironically, while UTS improves in the laminates, their yield strength slightly declines. For instance, the yield strength decreases from 186 MPa (CuCrZr) to 167 MPa in 7L and 184 MPa in 14L. This suggests that the designed laminated architecture and associated interface spacing are more effective at enhancing strain-hardening behavior than yield strength. It is worth noting that strength–ductility synergies have been reported in earlier Cu/CuCrZr laminated composites studies using other manufacturing routs than cold spray [97–100,280], however, the strength and ductility gains reported in those studies, reaching up to 350% and 90%, respectively, were generally more substantial than the results obtained in this work, notably due to the additional work hardening caused by post manufacturing treatments like rolling. This discrepancy may also stem from the post-deposition heat treatment used in this study, which may not have sufficiently developed the intended soft and hard domains, and their corresponding interfaces. Specifically, the Cu layers, expected to serve as soft domains, did not exhibit greater ductility than the CuCrZr layers, which were intended as hard domains. This stems from the fact that the heat treatment under consideration was based on the optimized process for CuCrZr [Chapter 7], which differs from the optimized treatment developed for pure Cu [Chapter 6]. This limited mechanical contrast reduces the strain incompatibility required to effectively activate HDI strengthening.

To further elucidate ductility optimization, the strain hardening rate (Θ) was analyzed as a function of true strain, as shown in Figure 95b. All materials exhibit an initial rapid drop in strain hardening rate, but the laminated samples (7L and 14L) maintain a more gradual decline, reflecting superior work-hardening capability throughout deformation. The 14L laminate consistently sustains a slightly higher hardening rate than both 7L and CuCrZr across the entire strain range, which correlates well with its higher uniform elongation. In contrast, pure Cu demonstrates a sharp drop in hardening rate followed by a notably irregular and fluctuating hardening response. This unstable behavior is indicative of early dislocation saturation and limited capacity for further strain hardening consistent with its low strength and poor plastic deformability.

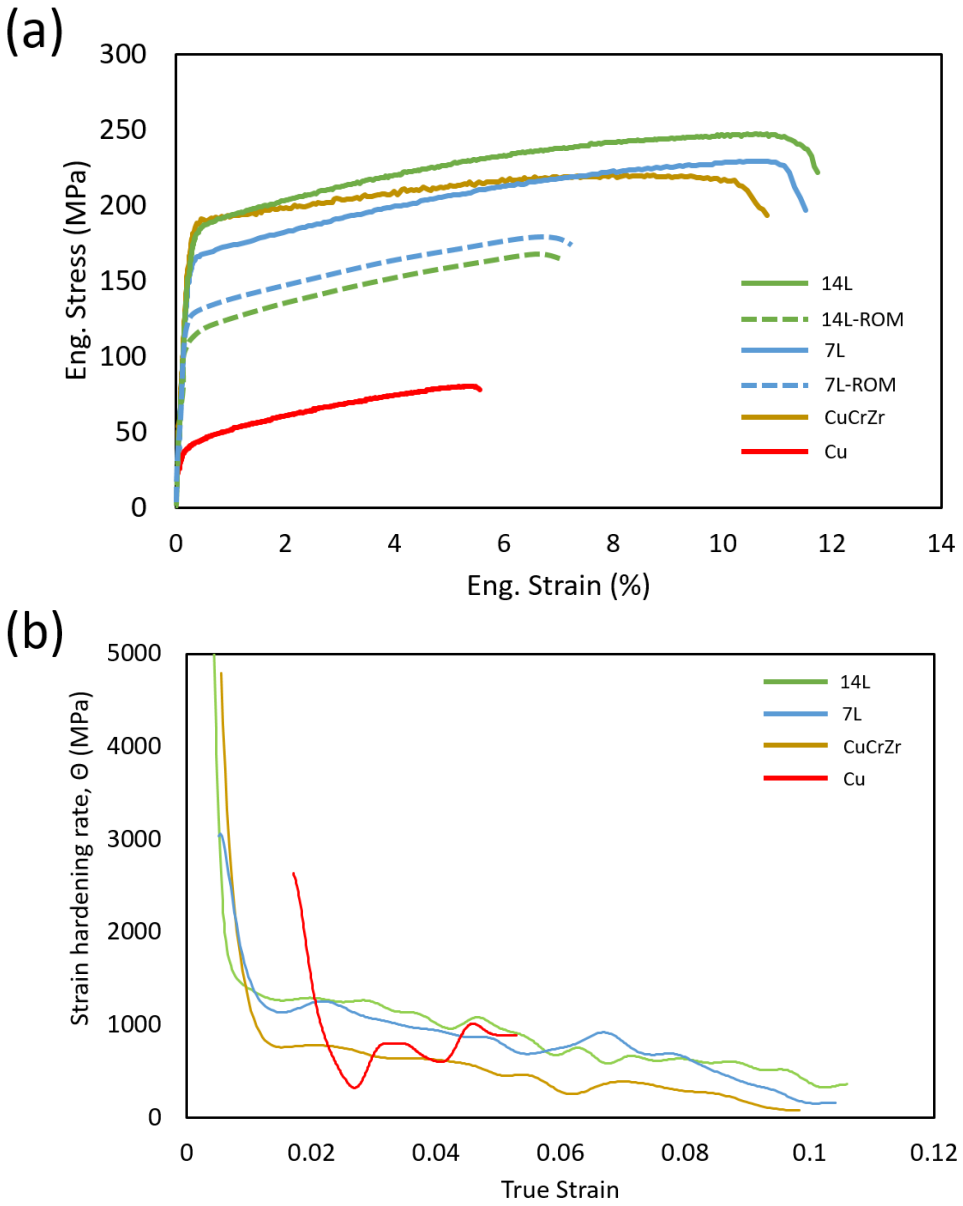


Figure 95: (a) Engineering stress–strain curves of heat-treated Cu–CuCrZr laminated alloys with 7 layers (7L) and 14 layers (14L), alongside pure CuCrZr and pure Cu for comparison. Also shown are the predicted curves based on ROM for 7L and 14L, a; (b) corresponding strain hardening rate versus true strain curves, derived from the experimental data in (a), for pure Cu, pure CuCrZr, 7L, and 14L samples.

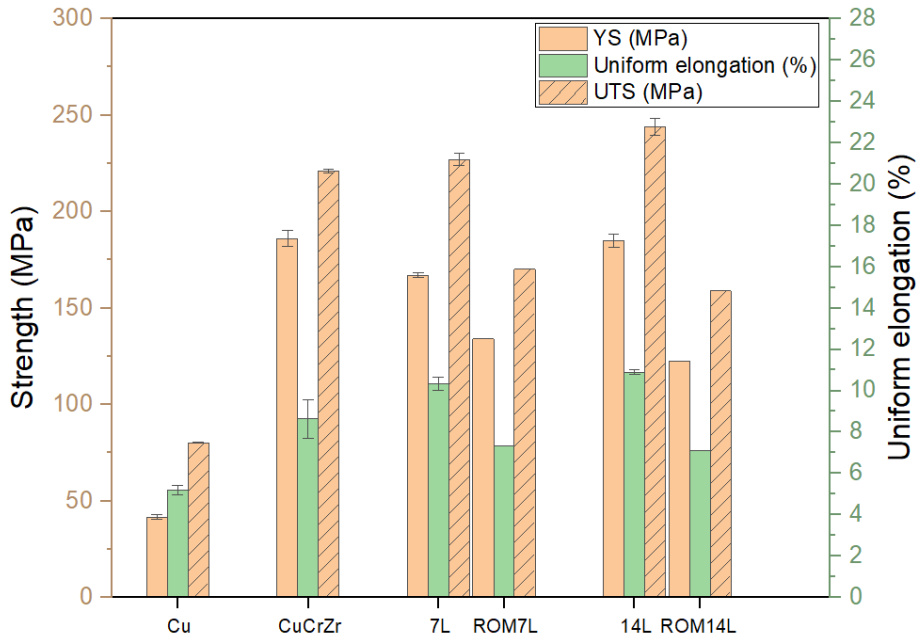
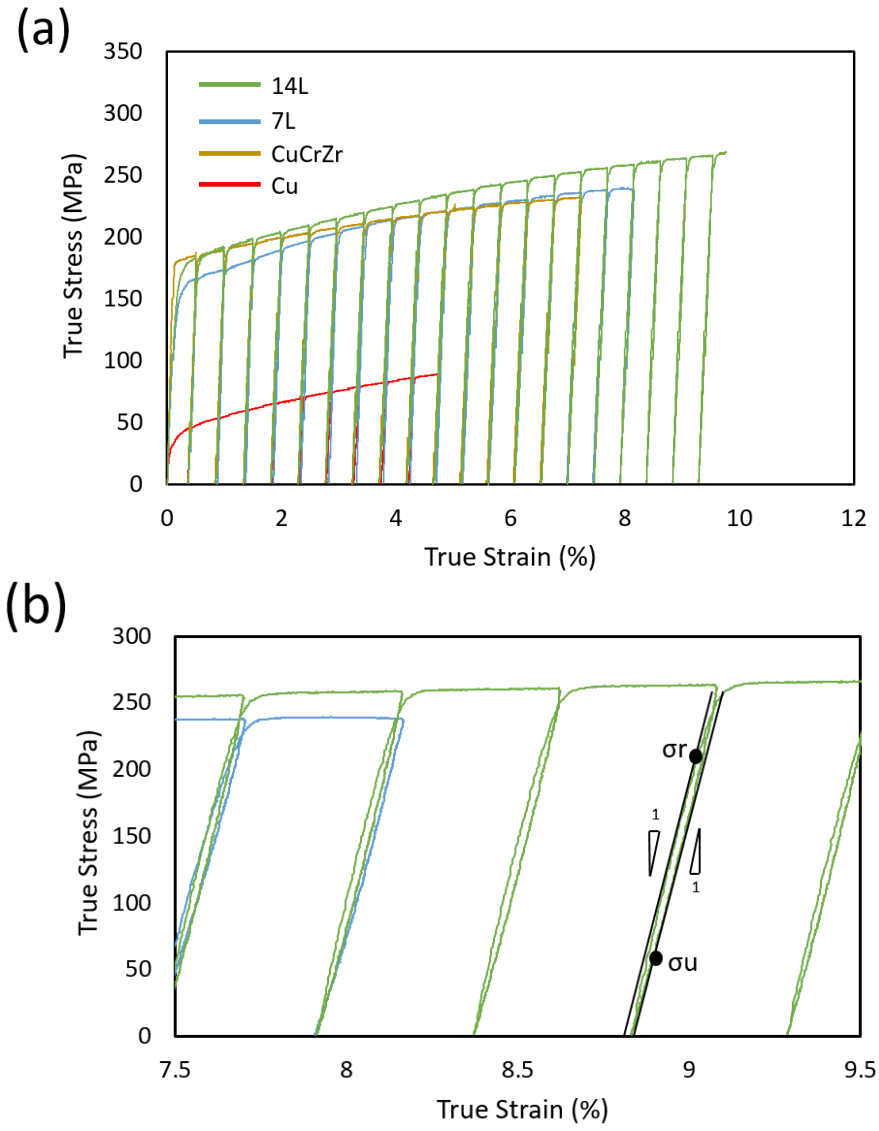


Figure 96: Comparison of experimentally measured tensile properties of yield strength, ultimate tensile strength, and uniform elongation (%) for heat-treated pure Cu, pure CuCrZr, and laminated 7L and 14L samples. Also included are the corresponding values for pure Cu after optimum heat treatment from previous work, as well as predictions based on the rule of mixtures (ROM) for the 7L and 14L laminates.

8.4.4 Discussion on the improvement of strength-ductility

To investigate the underlying mechanisms driving the remarkable synergy of strength and ductility in the developed heterostructured laminated Cu–CuCrZr composites (7L and 14L), we deployed high-resolution Loading–Unloading–Reloading (LUR) experiments alongside geometrically necessary dislocation (GND), shedding light on the complex dislocation dynamics governing these architecture materials. Figure 97a and b present the true stress–strain responses obtained from LUR tests on pure Cu, pure CuCrZr, and the two laminated 7L and 14L samples. The laminated structures exhibit broad and pronounced hysteresis loops, indicating a strong Bauschinger effect [282,283]. The Bauschinger effect refers to the reduction in yield strength when a material is unloaded after prior plastic deformation, due to internal back-stresses. Figure 97c and d illustrate a notable anelastic recovery strain (ε_{ae}) during unloading in the laminates, likely resulting from rapid plastic yielding initiated during reverse loading. This behavior suggests the presence of hetero-deformation-induced (HDI) stress (back-stress), which becomes more prominent as the number of interfaces increases. Figure 97e shows the variation of HDI

stress with true strain, derived from the hysteresis loops in Figure 97b using a method previously reported in [81]. While HDI stress increases with strain across all samples, the laminated 14L structure consistently exhibits higher HDI stress values than 7L. At a true strain of 9.54%, the HDI stress in the 14L sample reaches 154 MPa, accounting for approximately 60% of the total flow stress (σ_b/σ_0, where σ_b is the back stress and σ_0 is the flow stress).



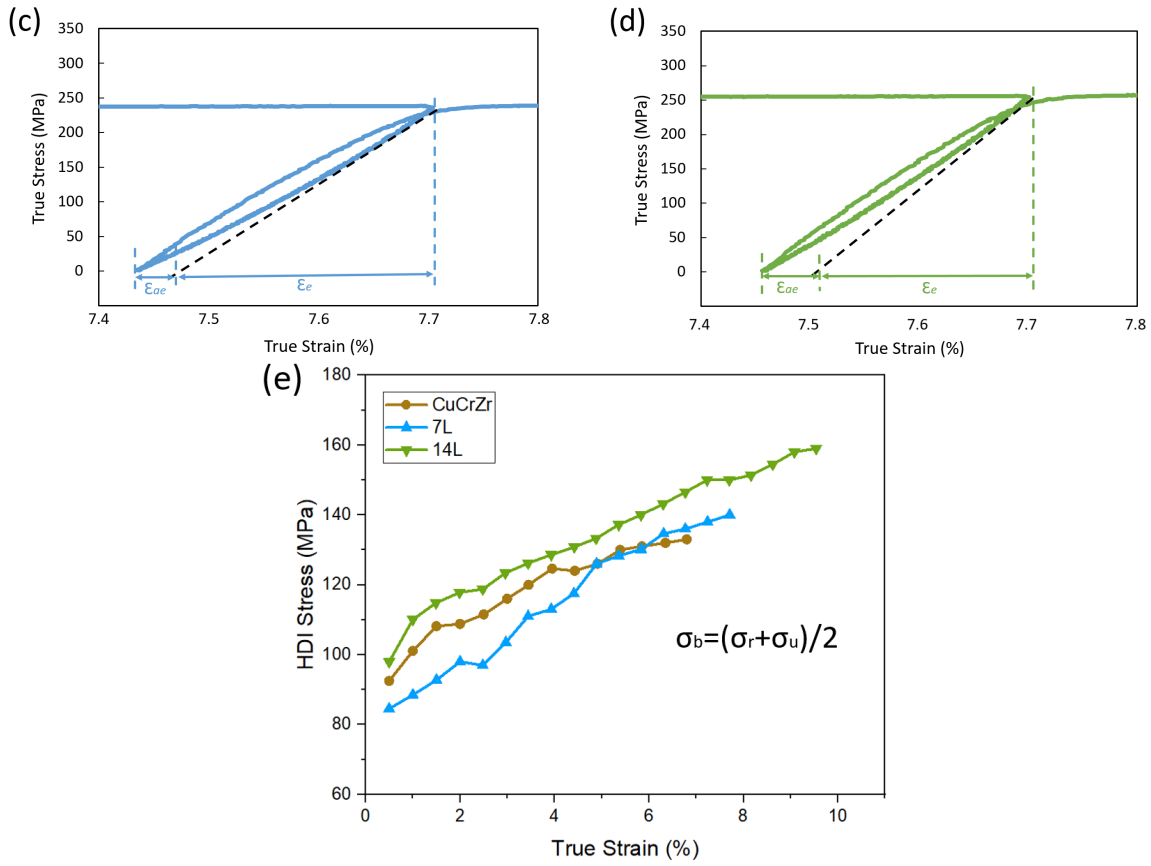


Figure 97: (a) LUR curves obtained from samples of pure Cu, pure CuCrZr, 7L, 14L, (b) Enlarged LUR curves showing the hysteresis loops, (c) and (d) The individual hysteresis loops observed in the 7L and 14L laminates indicate early yielding and considerable anelastic recovery strain (ε_{ae}) during unloading. Here, ε_e represents the elastic portion of the recovery strain, and (e) Calculated HDI stress of different samples.

This elevated HDI stress in the 14L laminate can be attributed to the enhanced strain partitioning between the coarse grain Cu and the stronger CuCrZr domains due to the reduced interface spacing. Such partitioning results in more severe hetero-deformation and, consequently, a stronger back stress response. The generation of this back stress is closely linked to the accumulation of GNDs near the interfaces, which occurs due to mechanical incompatibility between adjacent layers. Figure 98a and c present band contrast maps illustrating the interfaces between fine-grained CuCrZr layers and coarse-grained Cu regions in the 7L and 14L laminated samples, deformed to true strains of 7.5% and 9%, respectively. The corresponding GND density maps in Figure 98b and d reveal the spatial distribution of dislocations across both fine and coarse grain domains. A clear gradient in GND density is observed

near the CuCrZr/Cu interfaces, highlighting the strain incompatibility inherent to the heterogeneous microstructure. This gradient arises from the requirement to accommodate continuous but non-uniform strain across layers, with GNDs forming to compensate for the resulting strain mismatch [284]. Consequently, higher GND concentrations are localized near the interface, gradually diminishing with increasing distance into the Cu layers, indicating the localized nature of the interface-affected zone. The accumulation of GNDs at the hetero interface reflects the mechanical incompatibility between the Cu and the stronger CuCrZr layers. This results in long-range internal stress fields which contribute to hetero-deformation-induced (HDI) hardening, a key mechanism responsible for the enhanced work-hardening behavior observed in the tensile curves of both 7L and 14L laminates. It is also important to note that the high back stress observed in monolithic fine-grained CuCrZr samples primarily originates from the inhomogeneous dislocation distribution, caused by solute atom pinning and the barrier effect of a high grain boundary density [238,285,286].

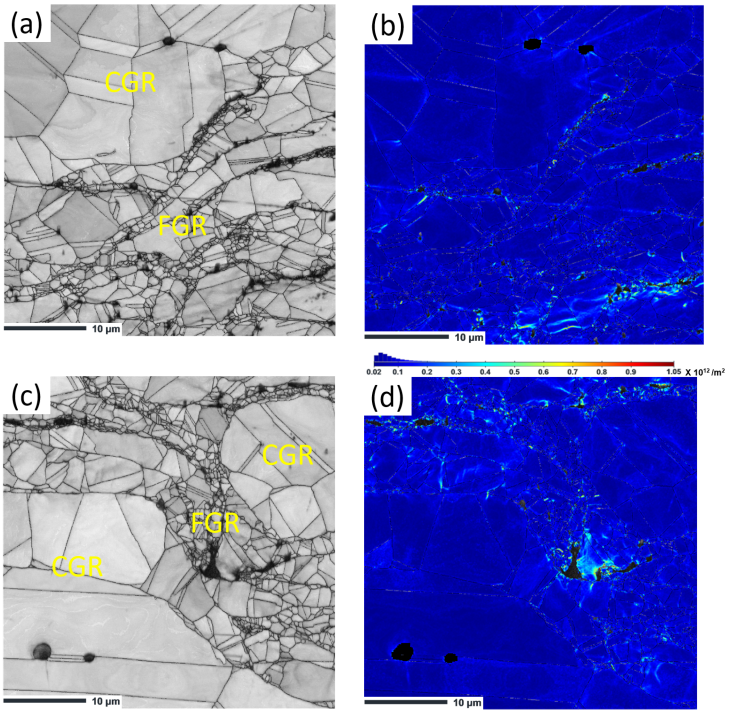


Figure 98: (a) and (c) Band contrast maps depicting the interfaces between fine-grained CuCrZr and coarse-grained Cu regions in the laminated 7L and 14L sample subjected to a true strain of 7.5% and 9%, respectively. (b) and (d) Corresponding GND (geometrically necessary dislocation) density maps of the same regions, illustrating the dislocation distribution within both fine and coarse grain domains.

Figure 99 provides a schematic representation designed to illustrate the underlying mechanisms for the observed HDI strengthening. The degree of HDI stress correlates with the contrast in mechanical properties and microstructure between the layers. Greater differences in strength and grain structure lead to more pronounced plastic strain incompatibility, intensifying GND formation and HDI hardening [101,287]. In fact, piled-up GNDs serve dual roles: they act as strong barriers to dislocation motion through short-range interactions and generate long-range internal stresses that accelerate the accumulation of statistically stored dislocations, contributing to additional strain hardening. In summary, the simultaneous improvement in strength and ductility in the Cu–CuCrZr laminated structures (both 7L and 14L) can be attributed to their heterogeneous architecture. The fine-grained CuCrZr layers, strengthened by nanoscale precipitates, contribute to high intrinsic strength via Hall–Petch and precipitation hardening mechanisms. The significant difference in strength between Cu and CuCrZr domains promotes strain partitioning during deformation, leading to the generation of GNDs at the interfaces. These GNDs not only obstruct dislocation motion but also promote long-range HDI stress, resulting in enhanced work-hardening capacity and the retention of tensile ductility. As the number of interfaces increases, so does the density of these GND pile-ups, amplifying the HDI stress and contributing to both strain hardening and strength enhancement [78,101]. Moreover, a high back stress level can activate additional, harder slip systems in both coarse-grained (CG) and fine-grained (FG) regions [80,238], facilitating the nucleation and interaction of dislocations. This promotes entanglement and accumulation of dislocations during later stages of deformation, resulting in a higher strain-hardening rate under large strains. In this study, the heat-treated Cu did not achieve higher ductility compared to CuCrZr and therefore could not serve as the best soft domain. As a result, an ideal or extreme heterogeneous structure could not be fully generated. In this context, CuCrZr, exhibiting both higher ductility and strength than Cu, functions simultaneously as both the soft and hard domain. At later stages of deformation, the CuCrZr regions undergo significantly higher strain than the Cu regions, leading to a greater accumulation of GNDs at the domain boundaries within the CuCrZr layers.

Figure 100 presents the representative fracture surface of the 14L laminated Cu–CuCrZr sample. The interfaces between layers are clearly distinguishable, yet show no signs of delamination or separation, confirming strong metallurgical bonding between the pure Cu and CuCrZr alloy layers. Ductile dimples are evident in the fine-grained (FGR) CuCrZr regions, located adjacent to brittle fracture features extending from the coarse-grained (CGR) Cu layers toward the interface. This mixed fracture mode

supports the presence of strong lateral constraint between the CG and FG regions during high plastic strain deformation.

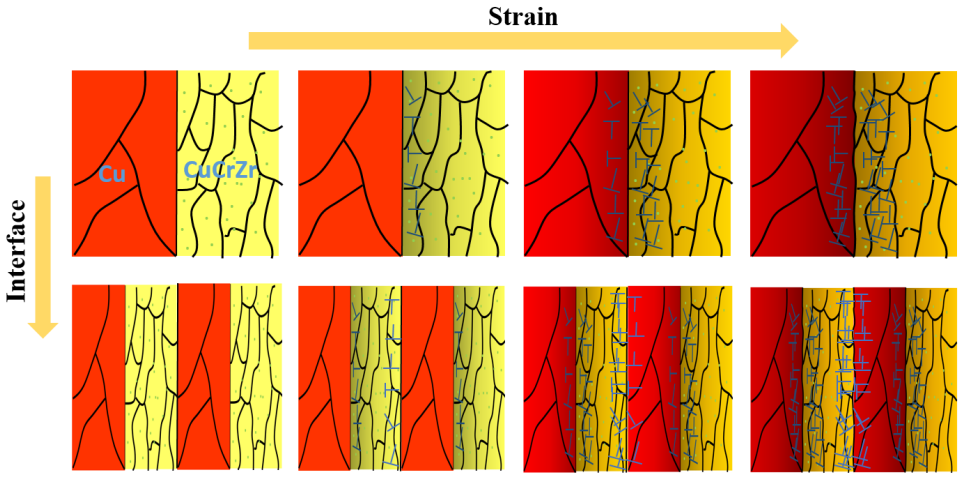


Figure 99: Schematic representation of deformation behavior in laminated Cu/CuCrZr structures with increasing strain and interface density. The buildup of GNDs near interfaces arises from mechanical incompatibility between neighboring layers. As interface density increases, so does the accumulation of GNDs, leading to the development of long-range internal stress fields that contribute to HDI hardening.

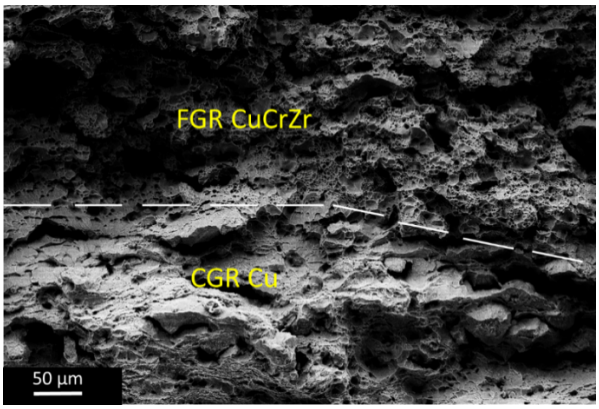


Figure 100: Representative fracture surface at the interface between coarse-grained Cu and fine-grained CuCrZr in the 14L laminate. The interface location is indicated by white dotted arrows. Dimple features are visible in the fine-grained CuCrZr region, adjacent to brittle fracture zones observed in the coarse-grained Cu layer.

8.5 Conclusion

Freestanding laminated structures composed of alternating coarse- and fine-grained layers of Cu and CuCrZr were successfully fabricated using cold spray technology and post-deposition heat treatment. Following conclusions can be drawn from the results, analysis and discussions presented:

1. The microstructural analysis reveals that heat treatment led to substantial recrystallization in both Cu and CuCrZr regions, though the CuCrZr layers retained finer grains and lower porosity due to enhanced plastic deformation during deposition. In contrast, the pure Cu layers exhibited coarser grains, residual porosity, and incomplete recrystallization, attributed to the absence of strengthening precipitates and lower deformation-induced strain. The clear difference in grain morphology, porosity, and recrystallization behavior between Cu and CuCrZr resulted in a characteristic heterogeneous microstructure, with gradual grain transitions near the interfaces.
2. The microhardness analysis demonstrates that post-heat treatment softens both Cu and CuCrZr layers due to recrystallization, with a more significant reduction in the Cu layers, resulting in pronounced hardness contrast across the laminate. This sharp transition in hardness at the Cu/CuCrZr interfaces, combined with uniform hardness within each layer, establishes a mechanically heterogeneous structure.
3. The mechanical evaluation reveals that laminated Cu–CuCrZr structures with 7 and 14 layers exhibit improvements in strength and ductility compared to monolithic Cu and CuCrZr, with performance further enhanced by increasing the number of interfaces. The 14-layer laminate, in particular, achieved an ultimate tensile strength of 244 MPa and a uniform elongation of 11%, representing approximately 10% and 28% improvements, respectively, over the stronger CuCrZr alloy. While a slight reduction in yield strength is observed, the laminated architecture, particularly the 14-layer sample, demonstrates higher strain hardening capacity and more uniform plastic deformation. Overall, introducing a high-density laminated structure offers an effective pathway to improve the strength–ductility in cold-sprayed Cu-based materials.
4. The enhanced strength–ductility observed in the laminated Cu–CuCrZr composites is closely linked to hetero-deformation-induced (HDI) strengthening mechanisms, confirmed through LUR tests and GND analysis. The 14-layer laminate, with its higher interface density, exhibited broader hysteresis loops and higher back stress levels during LUR testing, indicating stronger

HDI effects. GND mapping revealed dislocation accumulation near Cu/CuCrZr interfaces, driven by strain partitioning and mechanical incompatibility between layers. These effects promote sustained strain hardening, enhanced dislocation interactions, and improved plastic strain accommodation. These mechanisms explain the improvements in mechanical performance, validating the effectiveness of the laminated architecture for achieving simultaneous strength and ductility.

While cold spray deposition demonstrates strong potential for fabricating laminated materials with heterogeneous architectures, the modest improvement in ductility highlights the need for further process optimization. In particular, post-heat treatment strategies should aim to enhance ductility in the soft domains, as well as, strength in the hard domains by promoting inter-particle metallurgical bonding and minimizing residual porosity. Continued research will focus on designing heterogeneous microstructures with alternative topologies, such as lamellar configurations, to increase the density of domain interfaces, critical sites for dislocation pile-up and back-stress generation. Additionally, increasing the strength contrast between domains can improve strain partitioning, elevate strain gradients, and intensify HDI-induced work hardening. To achieve this, co-deposition of nanocrystalline and microcrystalline powders combined with optimized heat treatments is being considered as a promising approach to amplify mechanical heterogeneity and achieve superior strength–ductility synergy.

Chapter 9
Summary, Conclusions, and Future Work/Outlook

9.1 Summary

This thesis investigates the potential of CSAM, a solid-state powder-based technique, for producing high-performance copper components and engineered heterogeneous structures. Unlike traditional thermal spray methods, CSAM enables particle bonding through high-velocity impact without melting, thus preserving the microstructure and avoiding oxidation or phase changes. Despite its growing industrial relevance, critical gaps remain in understanding the relationship between feedstock powder properties and final material performance, as well as in enhancing the limited ductility of as-sprayed components. This research addresses both challenges by systematically analyzing copper feedstock powders and exploring advanced architectural designs to improve the mechanical performance of CS-deposited materials.

This study focuses on four main objectives. First, it involves the characterization of copper powders produced through gas atomization, electrolysis, and mechanical grinding, along with an evaluation of their deposition behavior in cold spray processes. Second, it aims to optimize the mechanical performance of 3D-printed pure Cu by investigating the influence of different process gases, helium and nitrogen, as well as post-deposition heat treatments. Third, it investigates the CSAM of the CuCrZr alloy, a precipitation-hardened material, along with three standard post-deposition heat treatment methods to identify the most effective treatment. Finally, the study seeks to develop a laminated heterogeneous Cu/CuCrZr structure, designed to achieve a synergistic improvement in both strength and ductility. Advanced microscopy, spectroscopy, and mechanical testing techniques were used to establish the influence of powder characteristics on deposition quality, porosity, grain refinement, and interfacial bonding. Optimal spray parameters were identified through statistical modeling, enabling the production of coatings with high density and strong adhesion.

Building on these findings, the most promising powder was used to fabricate 3D-printed components under varied gas and heat treatment conditions. Results demonstrated that nitrogen, when combined with an optimized thermal treatment, can serve as a cost-effective alternative to helium while maintaining excellent mechanical properties. Finally, the thesis introduces a novel approach for designing laminated heterostructures composed of alternating layers of coarse-grained Cu and fine-

grained CuCrZr. These architected materials were shown to enhance both strength and ductility through hetero-deformation-induced (HDI) strengthening mechanisms. The contributions of this work offer a deeper understanding of CS powder-material interactions and present a practical pathway for producing next-generation metallic components with tailored properties by cold spray 3D printing.

9.2 Conclusions

This thesis leads to the following key conclusions:

1. Gas atomized Cu powders with equiaxed grain structures demonstrated the most favorable cold sprayability. Among the evaluated powders, spherical gas-atomized feedstock with dense, equiaxed grains offered an optimal combination of high flowability and sufficient deformability. These powders achieved better deposition quality than electrolytic, dendritic-structured and ground powders due to reduced surface interactions and enhanced impact behavior.
2. Powder characteristics such as morphology, microstructure, and nano-hardness strongly influence deposition outcomes. Porous electrolytic powders showed high deformability but suffered from poor flow. Gas-atomized powders with dendritic microstructures had higher hardness but lower plasticity. The ground powder consisted of irregularly shaped particles with an ultrafine-grained microstructure, resulting in limited flowability, maximum nano-hardness and reduced deformability. Thus, an optimal cold spray performance requires balancing powder hardness and microstructural compactness.
3. Process gas parameters significantly affect coating properties in low-pressure cold spray. Higher gas pressures (~1.99 MPa) and elevated temperatures (~400 °C) led to improved coating mass and thickness across all feedstocks. Coating performance is highly sensitive to the interplay between temperature and pressure, emphasizing the need for parameter tuning based on feedstock properties.
4. Satellite-free gas-atomized powders produced the densest coatings with enhanced mechanical properties. These powders reduced surface oxide formation, leading to lower critical velocity requirements and more extensive plastic deformation upon impact. The result was a dense microstructure with reduced porosity, refined grains near the interface, and higher bonding strength.

5. Cold spray results in heterogeneous microstructures with deformation gradients. Grain refinement was most pronounced near the substrate and particle-particle interfaces due to severe plastic deformation. Larger grains persisted near particle cores, highlighting non-uniform dynamic recrystallization across the coating cross-section.
6. Nitrogen can replace helium as a process gas while maintaining or enhancing coating performance. Although He provides higher particle velocities, N_2-sprayed samples exhibited better plastic deformation due to higher cumulative peening. This resulted in higher dislocation density and microhardness in Cu coatings, making N_2 a cost-effective and technically viable alternative.
7. Post-deposition heat treatment is essential to recover ductility and improve interfacial bonding in cold-sprayed pure Cu. As-sprayed Cu deposits showed brittleness and negligible elongation. However, annealing at 500–700 °C enhanced tensile strength and ductility by promoting recrystallization and healing unbonded interfaces. For example, heat treatment at 700 °C improved elongation to 25% and UTS to 213 MPa for N_2-sprayed samples.
8. For CuCrZr alloy, the SA+AH heat treatment route yielded the most desirable microstructure and mechanical performance. This method promoted full recrystallization, interfacial healing, and fine precipitate formation, leading to dense, equiaxed grains and improved bonding. The resulting coatings reached 220 MPa UTS, 184 MPa YS, and 9% elongation, significantly outperforming DAH-treated or untreated samples.
9. Direct age hardening (DAH) was less effective in CuCrZr due to insufficient recrystallization and persistent defects. While DAH led to high hardness through precipitation and retained work hardening, it failed to sufficiently eliminate porosity and weak interfaces, resulting in brittle fracture and limited ductility.
10. Laminated Cu/CuCrZr heterostructures fabricated via sequential cold spray exhibited improved strength–ductility. Alternating layers of coarse-grained Cu and fine-grained CuCrZr formed mechanically distinct domains. The 14-layer laminate achieved 244 MPa UTS and 11% elongation, approximately 10% and 28% improvements over monolithic CuCrZr, highlighting the effectiveness of structural design in tuning mechanical response.
11. Heat treatment of laminates preserved microstructural contrast while enhancing bonding. Post-heat treatment led to full recrystallization in CuCrZr regions, partial recrystallization, and grain

growth in Cu layers. This resulted in hardness contrast across interfaces, promoting hetero-mechanical behavior while maintaining distinct microstructural domains.

12. Hardness mismatch between Cu and CuCrZr layers contributed to strain partitioning and increased strain hardening. Post-heat-treatment hardness values were significantly different (e.g., ~147 HV for CuCrZr vs. ~95 HV for Cu), leading to controlled strain localization, gradual load transfer, and improved overall plastic deformation capability.
13. Mechanical performance of laminates improves with increased interface density. Increasing the number of Cu/CuCrZr layers (e.g., from 7 to 14) enhanced both UTS and uniform elongation. This was attributed to more frequent interruptions of dislocation motion and greater opportunities for strain redistribution across soft/hard domains.
14. HDI (hetero-deformation-induced) strengthening was the dominant mechanism in layered structures. LUR testing revealed stronger back stress and larger hysteresis loops in the 14-layer laminate. GND mapping showed dislocation accumulation near interfaces, confirming the role of mechanical incompatibility in enhancing strength and delaying failure.
15. CSAM combined with powder selection, process optimization, and architectural design, enables high-performance copper-based components. The thesis demonstrates a materials–process–structure integration framework that addresses both microstructural control and mechanical enhancement. This opens a viable pathway for producing ductile, strong, and architected functional components using solid-state additive manufacturing.

9.3 Thesis contributions

The main contributions of this research are as follows:

- Established the relationship between powder manufacturing methods and cold sprayability through powder morphology, microstructure, and flow behavior analysis. (Paper 1, published manuscript, International Thermal Spray Conference 84536, 560-566, 2023)
- Demonstrated the correlation between feedstock powder characteristics and the resulting microstructure and mechanical performance of cold-sprayed Cu coatings. (Paper 2, Published manuscript, Journal of Thermal Spray Technology 33 (2), 629-651, 2024)
- Optimized low-pressure CS and post-deposition heat treatment conditions for pure Cu, enabling improved strength and ductility and validated the use of nitrogen as a cost-effective

process gas alternative to helium, achieving competitive deposition quality and mechanical performance. (Paper 3, Published manuscript, International Thermal Spray Conference 85045, 153-158, 2025 and manuscript ready for submission to a journal paper)

- Established optimized post-deposition heat treatment parameters for low-pressure cold sprayed CuCrZr alloy, achieving a significant improvement in both tensile strength and ductility. (Paper 4, Manuscript ready for submission)
- Developed and characterized novel 3D-printed Cu/CuCrZr laminated heterostructures with enhanced strength–ductility, identified and confirmed hetero-deformation-induced (HDI) strengthening as the dominant mechanism in architected laminated structures. (Paper 5, Manuscript ready for submission)

9.4 Recommendations and future work

Building upon the current study, the following section outlines suggested directions for future research.

1. This study's investigations into cold sprayability, coating quality, optimal process parameters, the effects of process gases, 3D printing, and post-spray heat treatments were all conducted using a low-pressure cold spray (LPCS) system. Given the significant influence of temperature and pressure on particle bonding mechanisms, deposition behavior, and resulting mechanical properties, future research is recommended to replicate these analyses using a high-pressure cold spray (HPCS) system. This would enable a more comprehensive understanding of feedstock performance across different cold spray regimes and broaden the applicability of the findings.

2. In this study, the flowability of feedstock powders was assessed using the shear cell method, which provided valuable insights into cohesion, flow function, and internal friction, key parameters reflecting the rheological behavior of powders. However, alternative techniques such as the Hall or Carney flowmeter methods may offer more accurate measurements of flow rate and apparent density, both of which are critical factors influencing cold sprayability. Future work is recommended to incorporate these methods for a more comprehensive evaluation of powder flow characteristics.

3. As noted, CuCrZr is a precipitation-hardened alloy whose mechanical properties are highly dependent on its precipitation behavior and the size, distribution, and evolution of precipitates in the as-received powder, as-sprayed state, and under various heat treatment conditions. To gain a deeper understanding of these effects, it is recommended that future research employ high-resolution transmission electron microscopy (TEM) to examine the microstructure of both the feedstock powder and CS samples before and after heat treatment. This would enable detailed characterization of precipitate types, sizes, and their locations at grain boundaries and within grain interiors. Correlating these microstructural features with mechanical performance would enhance understanding of strengthening mechanisms and allow for meaningful comparisons with other additive manufacturing processes.

4. The post-deposition heat treatment applied to the laminated heterostructures in this study was selected based on the optimal parameters for enhancing the mechanical properties of the CuCrZr alloy. However, this treatment may not be ideal for promoting interfacial bonding and ductility enhancement in the pure Cu domains. Therefore, it is recommended that future research conduct a comprehensive investigation into alternative post-deposition heat treatment strategies specifically tailored for laminated CS structures. The goal would be to simultaneously maximize tensile strength in the CuCrZr (hard domains) and ductility in the Cu (soft domains), thereby emphasizing the mechanical contrast and strain partitioning between the two regions. Such optimization would further advance the strength–ductility synergy, a key advantage of heterogeneous material systems.

5. Given that back-stress strengthening arises from dislocation pile-up at domain boundaries, future research should focus on designing heterogeneous structures with a high density of domain interfaces to enhance this effect and optimize mechanical performance. A promising topology to explore is a lamellar architecture, where soft domains are periodically embedded within a continuous hard matrix. Such a configuration offers a near-ideal heterogeneous structure: the rigid constraint imposed by the hard matrix elevates the effective strength of the soft domains during deformation, while the pronounced strain partitioning between domains

promotes significant back-stress accumulation and exceptional strain hardening. This combination leads to a desirable balance of high strength and ductility, making it an optimal design for advanced structural applications.

6. Utilizing nano-sized grains is a promising approach to induce microstructural heterogeneity and achieve enhanced mechanical performance. It is recommended that future studies investigate the co-deposition of nanograins alongside micrograins of the same chemical composition to develop a hierarchical structure. This configuration can help delocalize strain concentrations typically found in nanograined regions by redistributing them through the more ductile micrograins, promoting a more uniform and stable plastic flow. Such a grain-size gradient is expected to significantly improve the strength–ductility balance by combining the high strength of nanograins with the strain accommodation capability of micrograins.

7. To enable heterogeneity in CS microstructures, it is recommended to explore alternative powder manufacturing and post-processing techniques aimed at producing nano-grained feedstock materials. Among these, powder granulation is suggested as an effective method for generating micron-sized particles suitable for CS deposition while preserving a nano-grained internal structure. Additionally, ball milling offers a promising route to refine grain size and produce powders with a harmonic or gradient microstructure, facilitating enhanced strain distribution and improved mechanical properties in the final coatin

References

[1] D. Herzog, V. Seyda, E. Wycisk, C. Emmelmann, Additive manufacturing of metals, Acta Mater. 117 (2016) 371–392. https://doi.org/10.1016/j.actamat.2016.07.019.

[2] S.H. Huang, P. Liu, A. Mokasdar, L. Hou, Additive manufacturing and its societal impact: A literature review, Int. J. Adv. Manuf. Technol. 67 (2013) 1191–1203. https://doi.org/10.1007/s00170-012-4558-5.

[3] Y. Liu, J. Zhang, Q. Tan, Y. Yin, S. Liu, M. Li, M. Li, Q. Liu, Y. Zhou, T. Wu, F. Wang, M.X. Zhang, Additive manufacturing of high strength copper alloy with heterogeneous grain structure through laser powder bed fusion, Acta Mater. 220 (2021) 117311. https://doi.org/10.1016/j.actamat.2021.117311.

[4] Z.C. Cordero, H.M. Meyer, P. Nandwana, R.R. Dehoff, Powder bed charging during electron-beam additive manufacturing, Acta Mater. 124 (2017) 437–445. https://doi.org/10.1016/j.actamat.2016.11.012.

[5] K.S. Derekar, A review of wire arc additive manufacturing and advances in wire arc additive manufacturing of aluminium, Mater. Sci. Technol. (United Kingdom) 34 (2018) 895–916. https://doi.org/10.1080/02670836.2018.1455012.

[6] W. Li, K. Yang, S. Yin, X. Yang, Y. Xu, R. Lupoi, Solid-state additive manufacturing and repairing by cold spraying: A review, J. Mater. Sci. Technol. 34 (2018) 440–457. https://doi.org/10.1016/j.jmst.2017.09.015.

[7] S. Pathak, G.C. Saha, Cold Spray in the Realm of Additive Manufacturing, 2020. http://link.springer.com/10.1007/978-3-030-42756-6.

[8] S. Yin, P. Cavaliere, B. Aldwell, R. Jenkins, H. Liao, W. Li, R. Lupoi, Cold spray additive manufacturing and repair: Fundamentals and applications, Addit. Manuf. 21 (2018) 628–650. https://doi.org/10.1016/j.addma.2018.04.017.

[9] H. Assadi, H. Kreye, F. Gärtner, T. Klassen, Cold spraying – A materials perspective, Acta Mater. 116 (2016) 382–407. https://doi.org/10.1016/j.actamat.2016.06.034.

[10] V. Kenneth, C. Jr, Practical Cold Spray, 2021. https://doi.org/10.1007/978-3-030-70056-0.

[11] S. Amin, H. Panchal, A. Professor, A Review on Thermal Spray Coating Processes, Int. J. Curr. Trends Eng. Res. Sci. J. Impact Factor 2 (2016) 556–563. http://www.ijcter.com.

[12] F. Gärtner, T. Schmidt, T. Stoltenhoff, H. Kreye, Recent developments and potential applications of cold spraying, Adv. Eng. Mater. 8 (2006) 611–618. https://doi.org/10.1002/adem.200600048.

[13] C.M. Sample, V.K. Champagne, A.T. Nardi, D.A. Lados, Factors governing static properties and fatigue, fatigue crack growth, and fracture mechanisms in cold spray alloys and coatings/repairs: A review, Addit. Manuf. 36 (2020) 101371. https://doi.org/10.1016/j.addma.2020.101371.

[14] W. Li, C. Cao, S. Yin, Solid-state cold spraying of Ti and its alloys: A literature review, Prog. Mater. Sci. 110 (2020) 100633. https://doi.org/10.1016/j.pmatsci.2019.100633.

[15] B.K. Jasthi, T.S. Kuca, M.D. Ellingsen, D.L. Ellis, V.A.S. Kandadai, T.R. Curtis, Microstructure and mechanical properties of cold spray additive manufactured Cu-Cr-Nb and Fe-Ni-Cr alloys, Addit. Manuf. 61 (2023) 103354. https://doi.org/10.1016/j.addma.2022.103354.

[16] M.R. Hirmand, J. Tang, H. Jahed, A Particle-Based Numerical Model for Impact-Induced Bonding in Cold Spray, J. Therm. Spray Technol. 33 (2024) 1886–1913. https://doi.org/10.1007/s11666-024-01803-6.

[17] D.C. Saha, S.J. Boegel, S. Tanvir, C.L. Nogueira, M.G. Aucoin, W.A. Anderson, H. Jahed, Antiviral and Antibacterial Cold Spray Coating Application on Rubber Substrate, Disruption in Disease Transmission Chain, J. Therm. Spray Technol. 32 (2023) 818–830. https://doi.org/10.1007/s11666-023-01553-x.

[18] B. Marzbanrad, E. Toyserkani, H. Jahed, Fatigue crack initiation in cold spray coated AZ31B-H24 with AA7075 powder, Int. J. Fatigue 163 (2022) 107084. https://doi.org/10.1016/j.ijfatigue.2022.107084.

[19] M.R. Rokni, C.A. Widener, V.K. Champagne, G.A. Crawford, S.R. Nutt, The effects of heat treatment on 7075 Al cold spray deposits, Surf. Coatings Technol. 310 (2017) 278–285. https://doi.org/10.1016/j.surfcoat.2016.10.064.

[20] S. Kumar, V. Vidyasagar, A. Jyothirmayi, S. V. Joshi, Effect of Heat Treatment on Mechanical Properties and Corrosion Performance of Cold-Sprayed Tantalum Coatings, J.

Therm. Spray Technol. 25 (2016) 745–756. https://doi.org/10.1007/s11666-016-0388-6.

[21] M.R. Rokni, C.A. Widener, O.C. Ozdemir, G.A. Crawford, Microstructure and mechanical properties of cold sprayed 6061 Al in As-sprayed and heat treated condition, Surf. Coatings Technol. 309 (2017) 641–650. https://doi.org/10.1016/j.surfcoat.2016.12.035.

[22] J. Li, Q. Zhang, R. Huang, X. Li, H. Gao, Towards understanding the structure–property relationships of heterogeneous-structured materials, Scr. Mater. 186 (2020) 304–311. https://doi.org/10.1016/j.scriptamat.2020.05.013.

[23] E. Ma, T. Zhu, Towards strength–ductility synergy through the design of heterogeneous nanostructures in metals, Mater. Today 20 (2017) 323–331. https://doi.org/10.1016/j.mattod.2017.02.003.

[24] T.H. Van Steenkiste, J.R. Smith, R.E. Teets, J.J. Moleski, D.W. Gorkiewicz, R.P. Tison, D.R. Marantz, K.A. Kowalsky, W.L. Riggs, P.H. Zajchowski, B. Pilsner, R.C. McCune, K.J. Barnett, Kinetic spray coatings, Surf. Coatings Technol. 111 (1999) 62–71. https://doi.org/10.1016/S0257-8972(98)00709-9.

[25] T. Stoltenhoff, H. Kreye, H.J. Richter, An analysis of the cold spray process and its coatings, J. Therm. Spray Technol. 11 (2002) 542–550. https://doi.org/10.1361/105996302770348682.

[26] A. Moridi, S.M. Hassani-Gangaraj, M. Guagliano, M. Dao, Cold spray coating: Review of material systems and future perspectives, Surf. Eng. 30 (2014) 369–395. https://doi.org/10.1179/1743294414Y.0000000270.

[27] M.C. Spray, Modern Cold Spray, 2015. https://doi.org/10.1007/978-3-319-16772-5.

[28] E. Irissou, J.G. Legoux, A.N. Ryabinin, B. Jodoin, C. Moreau, Review on cold spray process and technology: Part I - Intellectual property, J. Therm. Spray Technol. 17 (2008) 495–516. https://doi.org/10.1007/s11666-008-9203-3.

[29] C.J. Li, H.T. Wang, Q. Zhang, G.J. Yang, W.Y. Li, H.L. Liao, Influence of spray materials and their surface oxidation on the critical velocity in cold spraying, J. Therm. Spray Technol. 19 (2010) 95–101. https://doi.org/10.1007/s11666-009-9427-x.

[30] Q. Tang, D. Veysset, H. Assadi, Y. Ichikawa, M. Hassani, Strength gradient in impact-induced

metallic bonding, Nat. Commun. 15 (2024) 9630. https://doi.org/10.1038/s41467-024-53990-z.

[31] H. Assadi, T. Schmidt, H. Richter, J.O. Kliemann, K. Binder, F. Gärtner, T. Klassen, H. Kreye, On parameter selection in cold spraying, J. Therm. Spray Technol. 20 (2011) 1161–1176. https://doi.org/10.1007/s11666-011-9662-9.

[32] S. Yin, X.F. Wang, W.Y. Li, H.E. Jie, Effect of substrate hardness on the deformation behavior of subsequently incident particles in cold spraying, Appl. Surf. Sci. 257 (2011) 7560–7565. https://doi.org/10.1016/j.apsusc.2011.03.126.

[33] S. Grigoriev, A. Okunkova, A. Sova, P. Bertrand, I. Smurov, Cold spraying: From process fundamentals towards advanced applications, Surf. Coatings Technol. 268 (2015) 77–84. https://doi.org/10.1016/j.surfcoat.2014.09.060.

[34] D. Guo, M. Kazasidis, A. Hawkins, N. Fan, Z. Leclerc, D. MacDonald, A. Nastic, R. Nikbakht, R. Ortiz-Fernandez, S. Rahmati, M. Razavipour, P. Richer, S. Yin, R. Lupoi, B. Jodoin, Cold Spray: Over 30 Years of Development Toward a Hot Future, J. Therm. Spray Technol. (2022). https://doi.org/10.1007/s11666-022-01366-4.

[35] S.B. Dayani, S.K. Shaha, R. Ghelichi, J.F. Wang, H. Jahed, The impact of AA7075 cold spray coating on the fatigue life of AZ31B cast alloy, Surf. Coatings Technol. 337 (2018) 150–158. https://doi.org/10.1016/j.surfcoat.2018.01.008.

[36] Y. Xiong, M.X. Zhang, The effect of cold sprayed coatings on the mechanical properties of AZ91D magnesium alloys, Surf. Coatings Technol. 253 (2014) 89–95. https://doi.org/10.1016/j.surfcoat.2014.05.018.

[37] W. Wong, P. Vo, E. Irissou, A.N. Ryabinin, J.G. Legoux, S. Yue, Effect of particle morphology and size distribution on cold-sprayed pure titanium coatings, J. Therm. Spray Technol. 22 (2013) 1140–1153. https://doi.org/10.1007/s11666-013-9951-6.

[38] R.C.V. McGee, Y. She, A. Nardi, D. Goberman, Z. Dardas, Enhancement of Ti-6Al-4V powder surface properties for cold spray deposition using fluidized Gas-Nitriding technique, Mater. Lett. 290 (2021) 129429. https://doi.org/10.1016/j.matlet.2021.129429.

[39] B. Young, J. Heelan, S. Langan, M. Siopis, C. Walde, A. Birt, Novel characterization techniques for additive manufacturing powder feedstock, Metals (Basel). 11 (2021) 1–19. https://doi.org/10.3390/met11050720.

[40] H. Assadi, F. Gärtner, T. Stoltenhoff, H. Kreye, Bonding mechanism in cold gas spraying, Acta Mater. 51 (2003) 4379–4394. https://doi.org/10.1016/S1359-6454(03)00274-X.

[41] T. Schmidt, H. Assadi, F. Gärtner, H. Richter, T. Stoltenhoff, H. Kreye, T. Klassen, From particle acceleration to impact and bonding in cold spraying, J. Therm. Spray Technol. 18 (2009) 794–808. https://doi.org/10.1007/s11666-009-9357-7.

[42] H. Aydin, M. Alomair, W. Wong, P. Vo, S. Yue, Cold Sprayability of Mixed Commercial Purity Ti Plus Ti6Al4V Metal Powders, J. Therm. Spray Technol. 26 (2017) 360–370. https://doi.org/10.1007/s11666-017-0528-7.

[43] E. Irissou, J.G. Legoux, B. Arsenault, C. Moreau, Investigation of Al-Al 2O 3 cold spray coating formation and properties, J. Therm. Spray Technol. 16 (2007) 661–668. https://doi.org/10.1007/s11666-007-9086-8.

[44] A. Sova, A. Papyrin, I. Smurov, Influence of ceramic powder size on process of cermet coating formation by cold spray, J. Therm. Spray Technol. 18 (2009) 633–641. https://doi.org/10.1007/s11666-009-9359-5.

[45] E. Irissou, D. Poirier, P. Vo, C. V. Cojocaru, M. Aghasibeig, S. Yue, How to Unleash the Remarkable Potential of Cold Spray: A Perspective, J. Therm. Spray Technol. (2022). https://doi.org/10.1007/s11666-022-01363-7.

[46] P.H. Gao, Y.G. Li, C.J. Li, G.J. Yang, C.X. Li, Influence of powder porous structure on the deposition behavior of cold-sprayed WC-12Co coatings, J. Therm. Spray Technol. 17 (2008) 742–749. https://doi.org/10.1007/s11666-008-9258-1.

[47] M.R. Rokni, A.T. Nardi, V.K. Champagne, S.R. Nutt, Effects of Preprocessing on Multi-Direction Properties of Aluminum Alloy Cold-Spray Deposits, J. Therm. Spray Technol. 27 (2018) 818–826. https://doi.org/10.1007/s11666-018-0723-1.

[48] A. Sabard, H.L. de Villiers Lovelock, T. Hussain, Microstructural Evolution in Solution Heat

Treatment of Gas-Atomized Al Alloy (7075) Powder for Cold Spray, J. Therm. Spray Technol. 27 (2018) 145–158. https://doi.org/10.1007/s11666-017-0662-2.

[49] R. Li, M. Qin, H. Huang, C. Liu, Z. Chen, M. Huang, L. Zhang, X. Qu, Fabrication of fine-grained spherical tungsten powder by radio frequency (RF) inductively coupled plasma spheroidization combined with jet milling, Adv. Powder Technol. 28 (2017) 3158–3163. https://doi.org/10.1016/j.apt.2017.09.019.

[50] M. Superalloy, L. Tan, G. He, F. Liu, Y. Li, L. Jiang, Effects of Temperature and Pressure of Hot Isostatic Pressing on the Grain Structure of Powder, (n.d.). https://doi.org/10.3390/ma11020328.

[51] C. Schade, G.K.N. Hoeganaes, J.J. Dunkley, Atomization *, 7 (2015). https://doi.org/10.31399/asm.hb.v07.a0006084.

[52] A. Ünal, Effect of processing variables on particle size in gas atomization of rapidly solidified aluminium powders, Mater. Sci. Technol. (United Kingdom) 3 (1987) 1029–1039. https://doi.org/10.1179/mst.1987.3.12.1029.

[53] A.S. Baskoro, S. Supriadi, Review on Plasma Atomizer Technology for Metal Powder, 05004 (2019) 1–9.

[54] E. Peissker, Production and handling of electrolytic powders, Met. Powder Rep. 46 (1991) 20–25. https://doi.org/10.1016/0026-0657(91)90545-C.

[55] M. Boz, M. Hasheminiasari, The effect of process parameters on copper powder particle size and shape produced by electrolysis method, Steel Compos. Struct. 15 (2013) 151–162. https://doi.org/10.12989/scs.2013.15.2.151.

[56] A. Nouri, A. Sola, Powder morphology in thermal spraying, J. Adv. Manuf. Process. 1 (2019) 1–19. https://doi.org/10.1002/amp2.10020.

[57] H.S. Dhami, P.R. Panda, K. Viswanathan, Production of powders for metal additive manufacturing applications using surface grinding, Manuf. Lett. 32 (2022) 54–58. https://doi.org/10.1016/j.mfglet.2022.02.004.

[58] F. Habashi, Metal powders by hydrometallurgical route - A review, InterCeram Int. Ceram.

Rev. 59 (2010) 287–297.

[59] A.R. Burkin, Production of some metal powders by hydrometallurgical processes, Powder Metall. 12 (1969) 243–250. https://doi.org/10.1179/pom.1969.12.23.012.

[60] A. Agrawal, V. Kumar, B.D. Pandey, K.K. Sahu, A comprehensive review on the hydro metallurgical process for the production of nickel and copper powders by hydrogen reduction, Mater. Res. Bull. 41 (2006) 879–892. https://doi.org/10.1016/j.materresbull.2005.09.028.

[61] J. Zegzulka, D. Gelnar, L. Jezerska, R. Prokes, J. Rozbroj, Characterization and flowability methods for metal powders, Sci. Rep. 10 (2020) 1–19. https://doi.org/10.1038/s41598-020-77974-3.

[62] A. Cooke, J. Slotwinski, Properties of metal powders for additive manufacturing: A review of the state of the art of metal powder property testing, Addit. Manuf. Mater. Stand. Test. Appl. (2015) 21–48.

[63] M.F. Morks, S.H. Zahiri, J. Lang, X.B. Chen, S. Gulizia, I.S. Cole, The influence of powder morphology on the microstructure and mechanical properties of as-sprayed and heat-treated cold-sprayed CP Ti, Int. J. Adv. Manuf. Technol. 118 (2022) 3869–3881. https://doi.org/10.1007/s00170-021-08222-9.

[64] Y. Wang, S. Koynov, B.J. Glasser, F.J. Muzzio, A method to analyze shear cell data of powders measured under different initial consolidation stresses, Powder Technol. 294 (2016) 105–112. https://doi.org/10.1016/j.powtec.2016.02.027.

[65] 1 Shear cell methods, 2 (2003) 3–6.

[66] D.C. Zapisotski, M. Wallhed, Characterizing flowability of metal powders, (2019).

[67] V.N.V. Munagala, V. Akinyi, P. Vo, R.R. Chromik, Influence of Powder Morphology and Microstructure on the Cold Spray and Mechanical Properties of Ti6Al4V Coatings, J. Therm. Spray Technol. 27 (2018) 827–842. https://doi.org/10.1007/s11666-018-0729-8.

[68] Y. Kudo, M. Yasuda, S. Matsusaka, Effect of particle size distribution on flowability of granulated lactose, Adv. Powder Technol. 31 (2020) 121–127. https://doi.org/10.1016/j.apt.2019.10.004.

[69] V.K. Champagne, The cold spray materials deposition process: Fundamentals and applications, 2007. https://doi.org/10.1533/9781845693787.

[70] V. Champagne, D. Helfritch, The unique abilities of cold spray deposition, Int. Mater. Rev. 61 (2016) 437–455. https://doi.org/10.1080/09506608.2016.1194948.

[71] T. Sekiguchi, K. Ono, H. Fujiwara, K. Ameyama, New microstructure design for commercially pure titanium with outstanding mechanical properties by mechanical milling and hot roll sintering, Mater. Trans. 51 (2010) 39–45. https://doi.org/10.2320/matertrans.MB200913.

[72] N. Kang, P. Coddet, H. Liao, C. Coddet, Cold gas dynamic spraying of a novel micro-alloyed copper: Microstructure, mechanical properties, J. Alloys Compd. 686 (2016) 399–406. https://doi.org/10.1016/j.jallcom.2016.06.037.

[73] C.J. Akisin, F. Venturi, M. Bai, C.J. Bennett, T. Hussain, Microstructure, mechanical and wear resistance properties of low-pressure cold-sprayed Al-7 Mg/Al2O3 and Al-10 Mg/Al2O3 composite coatings, Emergent Mater. 4 (2021) 1569–1581. https://doi.org/10.1007/s42247-021-00293-4.

[74] X. Chu, H. Che, C. Teng, P. Vo, S. Yue, A multiple particle arrangement model to understand cold spray characteristics of bimodal size 316L/Fe powder mixtures, Surf. Coatings Technol. 381 (2020) 125137. https://doi.org/10.1016/j.surfcoat.2019.125137.

[75] J.M. Lamarre, F. Bernier, Permanent Magnets Produced by Cold Spray Additive Manufacturing for Electric Engines, J. Therm. Spray Technol. 28 (2019) 1709–1717. https://doi.org/10.1007/s11666-019-00917-6.

[76] K. Ito, Y. Ichikawa, Microstructure control of cold-sprayed pure iron coatings formed using mechanically milled powder, Surf. Coatings Technol. 357 (2019) 129–139. https://doi.org/10.1016/j.surfcoat.2018.10.016.

[77] S. Bagherifard, A. Heydari Astaraee, M. Locati, A. Nawaz, S. Monti, J. Kondás, R. Singh, M. Guagliano, Design and analysis of additive manufacturedbimodal structures obtained by cold spray deposition, Addit. Manuf. 33 (2020) 101131. https://doi.org/10.1016/j.addma.2020.101131.

[78] X. Wu, Y. Zhu, Heterogeneous materials: a new class of materials with unprecedented mechanical properties, Mater. Res. Lett. 5 (2017) 527–532. https://doi.org/10.1080/21663831.2017.1343208.

[79] X.L. Wu, P. Jiang, L. Chen, J.F. Zhang, F.P. Yuan, Y.T. Zhu, Synergetic strengthening by gradient structure, Mater. Res. Lett. 2 (2014) 185–191. https://doi.org/10.1080/21663831.2014.935821.

[80] X. Wu, M. Yang, F. Yuan, G. Wu, Y. Wei, X. Huang, Y. Zhu, Heterogeneous lamella structure unites ultrafine-grain strength with coarse-grain ductility, Proc. Natl. Acad. Sci. U. S. A. 112 (2015) 14501–14505. https://doi.org/10.1073/pnas.1517193112.

[81] M. Yang, Y. Pan, F. Yuan, Y. Zhu, X. Wu, Back stress strengthening and strain hardening in gradient structure, Mater. Res. Lett. 4 (2016) 145–151. https://doi.org/10.1080/21663831.2016.1153004.

[82] D. Witkin, Z. Lee, R. Rodriguez, S. Nutt, E. Lavernia, Al-Mg alloy engineered with bimodal grain size for high strength and increased ductility, Scr. Mater. 49 (2003) 297–302. https://doi.org/10.1016/S1359-6462(03)00283-5.

[83] P. Chekhonin, J. Scharnweber, M. Scharnweber, C.G. Oertel, T. Hausöl, H.W. Höppel, J. Jaschinski, T. Marr, W. Skrotzki, Mechanical properties of aluminium laminates produced by accumulative roll bonding, Cryst. Res. Technol. 48 (2013) 532–537. https://doi.org/10.1002/crat.201300121.

[84] K. Park, M. Nishiyama, N. Nakada, T. Tsuchiyama, S. Takaki, Effect of the martensite distribution on the strain hardening and ductile fracture behaviors in dual-phase steel, Mater. Sci. Eng. A 604 (2014) 135–141. https://doi.org/10.1016/j.msea.2014.02.058.

[85] O.F. Crystals, B.Y. Non-deforming, Particles and, Arbeit (1970) 2–4.

[86] R. Singh, J. Kondás, C. Bauer, J. Cizek, J. Medricky, S. Csaki, J. Čupera, R. Procházka, D. Melzer, P. Konopík, Bulk-like ductility of cold spray additively manufactured copper in the as-sprayed state, Addit. Manuf. Lett. 3 (2022) 100052. https://doi.org/10.1016/j.addlet.2022.100052.

[87] C. Chen, Y. Xie, S. Yin, W. Li, X. Luo, X. Xie, R. Zhao, C. Deng, J. Wang, H. Liao, M. Liu, Z. Ren, Ductile and high strength Cu fabricated by solid-state cold spray additive manufacturing, J. Mater. Sci. Technol. 134 (2023) 234–243. https://doi.org/10.1016/j.jmst.2022.07.003.

[88] Y.K. Kim, K.A. Lee, Effect of carrier gas species on the microstructure and compressive deformation behaviors of ultra-strong pure copper manufactured by cold spray additive manufacturing, J. Mater. Sci. Technol. 97 (2022) 264–271. https://doi.org/10.1016/j.jmst.2021.04.062.

[89] J. Zhu, Y. Zhang, M. Xu, S. Zhao, X. Hui, Y. Wu, Y. Wu, H. Zheng, S. Zhu, Y. Shen, Z. Wang, Development of low-cost high entropy alloys composite coating with gradient structures on Mg alloys manufactured by supersonic solid-state cold spray, J. Alloys Compd. 1021 (2025) 179699. https://doi.org/10.1016/j.jallcom.2025.179699.

[90] Evaluation of Cold Spray Processing as a Novel Approach of Fabricating Bulk N anocrystalline AI Alloys by Andres Rodela IN PARTIAL FULFILLMENT OF THE Doctor of Philosophy, (2015).

[91] N. Fan, J. Cizek, C. Huang, X. Xie, Z. Chlup, R. Jenkins, R. Lupoi, S. Yin, A new strategy for strengthening additively manufactured cold spray deposits through in-process densification, Addit. Manuf. 36 (2020) 101626. https://doi.org/10.1016/j.addma.2020.101626.

[92] C.X. Huang, Y.F. Wang, X.L. Ma, S. Yin, H.W. Höppel, M. Göken, X.L. Wu, H.J. Gao, Y.T. Zhu, Interface affected zone for optimal strength and ductility in heterogeneous laminate, Mater. Today 21 (2018) 713–719. https://doi.org/10.1016/j.mattod.2018.03.006.

[93] X. Liu, F. Yuan, Y. Zhu, X. Wu, Extraordinary Bauschinger effect in gradient structured copper, Scr. Mater. 150 (2018) 57–60. https://doi.org/10.1016/j.scriptamat.2018.03.007.

[94] X. Wu, M. Yang, F. Yuan, G. Wu, Y. Wei, X. Huang, Y. Zhu, Heterostructured Lamella Structure Unites Ultrafine-Grain Strength with Coarse-Grain Ductility, Heterostruct. Mater. 112 (2021) 73–88. https://doi.org/10.1201/9781003153078-7.

[95] X.L. Liu, Q.Q. Xue, W. Wang, L.L. Zhou, P. Jiang, H.S. Ma, F.P. Yuan, Y.G. Wei, X.L. Wu, Hetero-Deformation Induced (HDI) Strengthening and Strain Hardening in Dual-Phase Steel,

Heterostruct. Mater. 7 (2021) 797–819. https://doi.org/10.1201/9781003153078-48.

[96] X.L. Ma, C.X. Huang, W.Z. Xu, H. Zhou, X.L. Wu, Y.T. Zhu, Strain hardening and ductility in a coarse-grain/nanostructure laminate material, Scr. Mater. 103 (2015) 57–60. https://doi.org/10.1016/j.scriptamat.2015.03.006.

[97] Y. Wang, M. Yang, X. Ma, M. Wang, K. Yin, A. Huang, C. Huang, Improved back stress and synergetic strain hardening in coarse-grain/nanostructure laminates, Mater. Sci. Eng. A 727 (2018) 113–118. https://doi.org/10.1016/j.msea.2018.04.107.

[98] Z. Lai, Y. Mai, H. Song, J. Mai, X. Jie, Heterogeneous microstructure enables a synergy of strength, ductility and electrical conductivity in copper alloys, J. Alloys Compd. 902 (2022) 163646. https://doi.org/10.1016/j.jallcom.2022.163646.

[99] C. You, L. Zeng, R. Gao, X. Zhang, H. Wang, A dual heterogeneous laminated microstructure design for improving the mechanical properties and electrical conductivity of copper alloys, Mater. Charact. 187 (2022) 111878. https://doi.org/10.1016/j.matchar.2022.111878.

[100] F. Han, Y. Jiang, F. Cao, L. Han, J. Zhu, W. Wang, S. Liang, Enhanced strength, ductility and electrical conductivity of CuCrZr alloys by tailoring a heterogeneous layered microstructure, Mater. Sci. Eng. A 863 (2023) 144502. https://doi.org/10.1016/j.msea.2022.144502.

[101] X. Ma, C. Huang, J. Moering, M. Ruppert, H.W. Höppel, M. Göken, J. Narayan, Y. Zhu, Mechanical properties of copper/bronze laminates: Role of interfaces, Acta Mater. 116 (2016) 43–52. https://doi.org/10.1016/j.actamat.2016.06.023.

[102] W.C. Oliver, G.M. Pharr, Measurement of hardness and elastic modulus by instrumented indentation: Advances in understanding and refinements to methodology, J. Mater. Res. 19 (2004) 3–20. https://doi.org/10.1557/jmr.2004.19.1.3.

[103] C.H. Ng, S. Yin, R. Lupoi, J. Nicholls, Correlation between flattening ratio and wear performance of cold sprayed metal matrix composite coatings, Mater. Lett. 283 (2021) 128773. https://doi.org/10.1016/j.matlet.2020.128773.

[104] M. Michalak, L. Łatka, P. Szymczyk, P. Sokołowski, Computational image analysis of Suspension Plasma Sprayed YSZ coatings, ITM Web Conf. 15 (2017) 06004.

https://doi.org/10.1051/itmconf/20171506004.

[105] ASTM E112, Standard Test Methods for Determining Average Grain Size E112-13, Astm E112-10 96 (2010) 1–27. https://doi.org/10.1520/E0112-10.Copyright.

[106] ASTM, Standard Test Method for Microindentation Hardness of MaterialsKnoop and Vickers Hardness of Materials 1, Annu. B. ASTM Stand. i (2010) 1–42.

[107] S.T. Method, Standard Test Method for Adhesion or Cohesion Strength of Thermal Spray Coatings 1, Current 03 (2001) 1–7. https://doi.org/10.1520/C0633-13R17.1.

[108] S.B. Behravesh, S. Lambert, H. Jahed, A Constitutive Model for Asymmetric Cyclic Hysteresis of Wrought Magnesium Alloys under Variable Amplitude Loading, Metals (Basel). 14 (2024). https://doi.org/10.3390/met14020221.

[109] M. Yang, Y. Pan, F. Yuan, Y. Zhu, X. Wu, Back stress strengthening and strain hardening in gradient structure, Mater. Res. Lett. 4 (2016) 145–151. https://doi.org/10.1080/21663831.2016.1153004.

[110] F. Gärtner, T. Stoltenhoff, T. Schmidt, H. Kreye, The cold spray process and its potential for industrial applications, J. Therm. Spray Technol. 15 (2006) 223–232. https://doi.org/10.1361/105996306X108110.

[111] P. Poza, M.Á. Garrido-Maneiro, Cold-sprayed coatings: Microstructure, mechanical properties, and wear behaviour, Prog. Mater. Sci. 123 (2022) 100839. https://doi.org/10.1016/j.pmatsci.2021.100839.

[112] S. Pathak, G.C. Saha, Development of sustainable cold spray coatings and 3D additive manufacturing components for repair/manufacturing applications: A critical review, Coatings 7 (2017). https://doi.org/10.3390/coatings7080122.

[113] D. Poirier, Y. Thomas, B. Guerreiro, M. Martin, M. Aghasibeig, E. Irissou, Improvement of Tool Steel Powder Cold Sprayability Via Softening and Agglomeration Heat Treatments, J. Therm. Spray Technol. 31 (2022) 145–158. https://doi.org/10.1007/s11666-022-01320-4.

[114] Y. Tan, J. Zhang, X. Li, Y. Xu, C.Y. Wu, Comprehensive evaluation of powder flowability for additive manufacturing using principal component analysis, Powder Technol. 393 (2021) 154–

164. https://doi.org/10.1016/j.powtec.2021.07.069.

[115] S.E. Brika, M. Letenneur, C.A. Dion, V. Brailovski, Influence of particle morphology and size distribution on the powder flowability and laser powder bed fusion manufacturability of Ti-6Al-4V alloy, Addit. Manuf. 31 (2020) 100929. https://doi.org/10.1016/j.addma.2019.100929.

[116] J. Tang, Z. Zhao, N. Li, X. Qiu, Y. Shen, X. Cui, H. Du, J. Wang, T. Xiong, Influence of feedstock powder on microstructure and mechanical properties of Ta cold spray depositions, Surf. Coatings Technol. 377 (2019) 124903. https://doi.org/10.1016/j.surfcoat.2019.124903.

[117] K. Tsaknopoulos, C. Walde, V. Champagne, D. Cote, Gas-Atomized Al 6061 Powder: Phase Identification and Evolution During Thermal Treatment, Jom 71 (2019) 435–443. https://doi.org/10.1007/s11837-018-3175-7.

[118] T. Liu, W.A. Story, L.N. Brewer, Effect of Heat Treatment on the Al-Cu Feedstock Powders for Cold Spray Deposition, Metall. Mater. Trans. A Phys. Metall. Mater. Sci. 50 (2019) 3373–3387. https://doi.org/10.1007/s11661-019-05230-z.

[119] G. Orhan, G. Hapçi, Effect of electrolysis parameters on the morphologies of copper powder obtained in a rotating cylinder electrode cell, Powder Technol. 201 (2010) 57–63. https://doi.org/10.1016/j.powtec.2010.03.003.

[120] D.R. Gabe, G.D. Wilcox, J. Gonzalez-Garcia, F.C. Walsh, The rotating cylinder electrode: Its continued development and application, J. Appl. Electrochem. 28 (1998) 759–780. https://doi.org/10.1023/A:1003464415930.

[121] N.D. Nikolić, L.J. Pavlović, M.G. Pavlović, K.I. Popov, Morphologies of electrochemically formed copper powder particles and their dependence on the quantity of evolved hydrogen, Powder Technol. 185 (2008) 195–201. https://doi.org/10.1016/j.powtec.2007.10.014.

[122] N.D. Nikolić, K.I. Popov, L.J. Pavlović, M.G. Pavlović, Morphologies of copper deposits obtained by the electrodeposition at high overpotentials, Surf. Coatings Technol. 201 (2006) 560–566. https://doi.org/10.1016/j.surfcoat.2005.12.004.

[123] V.S. Bhattiprolu, K.W. Johnson, O.C. Ozdemir, G.A. Crawford, Influence of feedstock powder and cold spray processing parameters on microstructure and mechanical properties of

Ti-6Al-4V cold spray depositions, Surf. Coatings Technol. 335 (2018) 1–12. https://doi.org/10.1016/j.surfcoat.2017.12.014.

[124] M. Reza Rokni, S.R. Nutt, C.A. Widener, G.A. Crawford, V.K. Champagne, Structure-properties relations in high-pressure cold-sprayed deposits, 2017. https://doi.org/10.1007/978-3-319-67183-3_5.

[125] H. Jones, Microstructure of rapidly solidified materials, Mater. Sci. Eng. 65 (1984) 145–156. https://doi.org/10.1016/0025-5416(84)90208-8.

[126] F. Wang, B. Xiong, yongan Zhang, H. Liu, X. He, Microstructural development of spray-deposited Al-Zn-Mg-Cu alloy during subsequent processing, J. Alloys Compd. 477 (2009) 616–621. https://doi.org/10.1016/j.jallcom.2008.10.115.

[127] K.F. Kobayashi, P.H. Shingu, The solidification process of highly undercooled bulk Cu-O melts, J. Mater. Sci. 23 (1988) 2157–2166. https://doi.org/10.1007/BF01115783.

[128] E.J. Lavernia, T.S. Srivatsan, The rapid solidification processing of materials: Science, principles, technology, advances, and applications, J. Mater. Sci. 45 (2010) 287–325. https://doi.org/10.1007/s10853-009-3995-5.

[129] L. Zheng, T.L. Lee, N. Liu, Z. Li, G. Zhang, J. Mi, P.S. Grant, Numerical and physical simulation of rapid microstructural evolution of gas atomised Ni superalloy powders, (n.d.) 1–32.

[130] J. Bruce See, G.H. Johnston, Interactions between nitrogen jets and liquid lead and tin streams, Powder Technol. 21 (1978) 119–133. https://doi.org/10.1016/0032-5910(78)80115-6.

[131] G.G. Giwangkara, A. Mohamed, H.M. Nor, N. Hafizah A., R. Mudiyono, Analysis of Internal Friction Angle and Cohesion Value for Road Base Materials in a Specified Gradation, J. Adv. Civ. Environ. Eng. 3 (2020) 58. https://doi.org/10.30659/jacee.3.2.58-65.

[132] S.Y. Chang, T.K. Chang, Grain size effect on nanomechanical properties and deformation behavior of copper under nanoindentation test, J. Appl. Phys. 101 (2007). https://doi.org/10.1063/1.2432873.

[133] R.F. Váz, A. Silvello, P.D. Cavalière, S. Dosta, I.G. Cano, L. Capodieci, A. Rizzo, D.

Valerini, Fretting Wear and Scratch Resistance of Cold-Sprayed Pure Cu and Ti, Metallogr. Microstruct. Anal. 10 (2021) 496–513. https://doi.org/10.1007/s13632-021-00758-2.

[134] H. Hajipour, A. Abdollah-zadeh, H. Assadi, E. Taheri-Nassaj, H. Jahed, Effect of Feedstock Powder Morphology on Cold-Sprayed Titanium Dioxide Coatings, J. Therm. Spray Technol. 27 (2018) 1542–1550. https://doi.org/10.1007/s11666-018-0782-3.

[135] H. Koivuluoto, A. Coleman, K. Murray, M. Kearns, P. Vuoristo, High pressure cold sprayed (HPCS) and low pressure cold sprayed (LPCS) coatings prepared from OFHC Cu feedstock: Overview from powder characteristics to coating properties, J. Therm. Spray Technol. 21 (2012) 1065–1075. https://doi.org/10.1007/s11666-012-9790-x.

[136] T. Hussain, D.G. McCartney, P.H. Shipway, D. Zhang, Bonding mechanisms in cold spraying: The contributions of metallurgical and mechanical components, J. Therm. Spray Technol. 18 (2009) 364–379. https://doi.org/10.1007/s11666-009-9298-1.

[137] M. Walker, Microstructure and bonding mechanisms in cold spray coatings, Mater. Sci. Technol. (United Kingdom) 34 (2018) 2057–2077. https://doi.org/10.1080/02670836.2018.1475444.

[138] J.T. Liang, S.F. Chang, C.H. Wu, S.H. Chen, C.W. Tsai, K.C. Cheng, K. Hsu, Influence of Feedstock in the Formation Mechanism of Cold-Sprayed Copper Coatings, Coatings 13 (2023). https://doi.org/10.3390/coatings13061065.

[139] F.J. Wei, B.Y. Chou, K.Z. Fung, S.Y. Tsai, Thermomechanical properties of cold-sprayed copper coatings from differently fabricated powders, Surf. Coatings Technol. 434 (2022) 128128. https://doi.org/10.1016/j.surfcoat.2022.128128.

[140] D. Poirier, J.G. Legoux, P. Vo, B. Blais, J.D. Giallonardo, P.G. Keech, Powder Development and Qualification for High-Performance Cold Spray Copper Coatings on Steel Substrates, J. Therm. Spray Technol. 28 (2019) 444–459. https://doi.org/10.1007/s11666-019-00833-9.

[141] H. Koivuluoto, P. Vuoristo, Effect of powder type and composition on structure and mechanical properties of Cu + Al 2O 3 coatings prepared by using low-pressure cold spray process, J. Therm. Spray Technol. 19 (2010) 1081–1092. https://doi.org/10.1007/s11666-010-9491-2.

[142] Y.J. Li, X.T. Luo, H. Rashid, C.J. Li, A new approach to prepare fully dense Cu with high conductivities and anti-corrosion performance by cold spray, J. Alloys Compd. 740 (2018) 406–413. https://doi.org/10.1016/j.jallcom.2017.11.053.

[143] T. Stoltenhoff, C. Borchers, F. Gärtner, H. Kreye, Microstructures and key properties of cold-sprayed and thermally sprayed copper coatings, Surf. Coatings Technol. 200 (2006) 4947–4960. https://doi.org/10.1016/j.surfcoat.2005.05.011.

[144] P. Sudharshan Phani, D. Srinivasa Rao, S. V. Joshi, G. Sundararajan, Effect of process parameters and heat treatments on properties of cold sprayed copper coatings, J. Therm. Spray Technol. 16 (2007) 425–434. https://doi.org/10.1007/s11666-007-9048-1.

[145] T. Kairet, M. Degrez, F. Campana, J.P. Janssen, Influence of the powder size distribution on the microstructure of cold-sprayed copper coatings studied by x-ray diffraction, J. Therm. Spray Technol. 16 (2007) 610–618. https://doi.org/10.1007/s11666-007-9116-6.

[146] N. Eftekhari, D. Saha, H. Jahed, A comparative study on the powder manufacturing effect on flowability and deformability of pure Cu powders for cold spray application, (2023).

[147] J. Pattison, S. Celotto, A. Khan, W. O'Neill, Standoff distance and bow shock phenomena in the Cold Spray process, Surf. Coatings Technol. 202 (2008) 1443–1454. https://doi.org/10.1016/j.surfcoat.2007.06.065.

[148] O.C. Ozdemir, C.A. Widener, D. Helfritch, F. Delfanian, Estimating the Effect of Helium and Nitrogen Mixing on Deposition Efficiency in Cold Spray, J. Therm. Spray Technol. 25 (2016) 660–671. https://doi.org/10.1007/s11666-016-0394-8.

[149] B. Marzbanrad, E. Toyserkani, H. Jahed, Characterization of single- and multilayer cold-spray coating of Zn on AZ31B, Surf. Coatings Technol. 416 (2021) 127155. https://doi.org/10.1016/j.surfcoat.2021.127155.

[150] T. Schmidt, F. Gärtner, H. Assadi, H. Kreye, Development of a generalized parameter window for cold spray deposition, Acta Mater. 54 (2006) 729–742. https://doi.org/10.1016/j.actamat.2005.10.005.

[151] X.T. Luo, Y.J. Li, C.J. Li, A comparison of cold spray deposition behavior between gas

atomized and dendritic porous electrolytic Ni powders under the same spray conditions, Mater. Lett. 163 (2016) 58–60. https://doi.org/10.1016/j.matlet.2015.10.048.

[152] Y.J. Li, X.T. Luo, C.J. Li, Dependency of deposition behavior, microstructure and properties of cold sprayed Cu on morphology and porosity of the powder, Surf. Coatings Technol. 328 (2017) 304–312. https://doi.org/10.1016/j.surfcoat.2017.08.070.

[153] W.Y. Li, C.J. Li, H. Liao, Significant influence of particle surface oxidation on deposition efficiency, interface microstructure and adhesive strength of cold-sprayed copper coatings, Appl. Surf. Sci. 256 (2010) 4953–4958. https://doi.org/10.1016/j.apsusc.2010.03.008.

[154] M. Razavipour, S. Rahmati, A. Zúñiga, D. Criado, B. Jodoin, Bonding Mechanisms in Cold Spray: Influence of Surface Oxidation During Powder Storage, J. Therm. Spray Technol. 30 (2021) 304–323. https://doi.org/10.1007/s11666-020-01123-5.

[155] S. Yin, P. He, H. Liao, X. Wang, Deposition features of Ti coating using irregular powders in cold spray, J. Therm. Spray Technol. 23 (2014) 984–990. https://doi.org/10.1007/s11666-014-0116-z.

[156] X.T. Luo, C.X. Li, F.L. Shang, G.J. Yang, Y.Y. Wang, C.J. Li, High velocity impact induced microstructure evolution during deposition of cold spray coatings: A review, Surf. Coatings Technol. 254 (2014) 11–20. https://doi.org/10.1016/j.surfcoat.2014.06.006.

[157] G. Sarriegui, J.M. Martín, N. Burgos, M. Ipatov, A.P. Zhukov, J. Gonzalez, Effect of particle size on grain growth of Nd-Fe-B powders produced by gas atomization, Mater. Charact. 187 (2022) 111824. https://doi.org/10.1016/j.matchar.2022.111824.

[158] M. Grujicic, C.L. Zhao, W.S. DeRosset, D. Helfritch, Adiabatic shear instability based mechanism for particles/substrate bonding in the cold-gas dynamic-spray process, Mater. Des. 25 (2004) 681–688. https://doi.org/10.1016/j.matdes.2004.03.008.

[159] N.H. Tariq, L. Gyansah, J.Q. Wang, X. Qiu, B. Feng, M.T. Siddique, T.Y. Xiong, Cold spray additive manufacturing: A viable strategy to fabricate thick B4C/Al composite coatings for neutron shielding applications, Surf. Coatings Technol. 339 (2018) 224–236. https://doi.org/10.1016/j.surfcoat.2018.02.007.

[160] J.H. Cho, Y.M. Jin, D.Y. Park, H.J. Kim, I.H. Oh, K.A. Lee, Manufacture and properties of cold spray deposited large thickness Cu coating material for sputtering target, Met. Mater. Int. 17 (2011) 157–166. https://doi.org/10.1007/s12540-011-0222-0.

[161] Y. Zou, W. Qin, E. Irissou, J.G. Legoux, S. Yue, J.A. Szpunar, Dynamic recrystallization in the particle/particle interfacial region of cold-sprayed nickel coating: Electron backscatter diffraction characterization, Scr. Mater. 61 (2009) 899–902. https://doi.org/10.1016/j.scriptamat.2009.07.020.

[162] Z. Liu, H. Wang, M.J.R. Haché, X. Chu, E. Irissou, Y. Zou, Prediction of heterogeneous microstructural evolution in cold sprayed copper coatings using local Zener-Hollomon parameter and strain, Acta Mater. 193 (2020) 191–201. https://doi.org/10.1016/j.actamat.2020.04.041.

[163] A. Mishra, B.K. Kad, F. Gregori, M.A. Meyers, Microstructural evolution in copper subjected to severe plastic deformation: Experiments and analysis, Acta Mater. 55 (2007) 13–28. https://doi.org/10.1016/j.actamat.2006.07.008.

[164] V.K. Champagne, D.J. Helfritch, M.D. Trexler, B.M. Gabriel, The effect of cold spray impact velocity on deposit hardness, Model. Simul. Mater. Sci. Eng. 18 (2010). https://doi.org/10.1088/0965-0393/18/6/065011.

[165] R. Kirchheim, Metals as sinks and barriers for interstitial diffusion with examples for oxygen diffusion in copper, niobium and tantalum, Acta Metall. 27 (1979) 869–878. https://doi.org/10.1016/0001-6160(79)90122-6.

[166] H.D. Nguyen, A. Pramanik, A.K. Basak, Y. Dong, C. Prakash, S. Debnath, S. Shankar, I.S. Jawahir, S. Dixit, D. Buddhi, A critical review on additive manufacturing of Ti-6Al-4V alloy: Microstructure and mechanical properties, J. Mater. Res. Technol. 18 (2022) 4641–4661. https://doi.org/10.1016/j.jmrt.2022.04.055.

[167] C. Wang, X.P. Tan, Z. Du, S. Chandra, Z. Sun, C.W.J. Lim, S.B. Tor, C.S. Lim, C.H. Wong, Additive manufacturing of NiTi shape memory alloys using pre-mixed powders, J. Mater. Process. Technol. 271 (2019) 152–161. https://doi.org/10.1016/j.jmatprotec.2019.03.025.

[168] Y. Karabulut, R. Ünal, Additive manufacturing of ceramic particle-reinforced aluminum-

based metal matrix composites: a review, J. Mater. Sci. 57 (2022) 19212–19242. https://doi.org/10.1007/s10853-022-07850-0.

[169] X. Suo, S. Yin, M.P. Planche, T. Liu, H. Liao, Strong effect of carrier gas species on particle velocity during cold spray processes, Surf. Coatings Technol. 268 (2015) 90–93. https://doi.org/10.1016/j.surfcoat.2014.04.039.

[170] J. Huang, X. Yan, C. Chang, Y. Xie, W. Ma, R. Huang, R. Zhao, S. Li, M. Liu, H. Liao, Pure copper components fabricated by cold spray (CS) and selective laser melting (SLM) technology, Surf. Coatings Technol. 395 (2020) 125936. https://doi.org/10.1016/j.surfcoat.2020.125936.

[171] K. Yang, W. Li, X. Yang, Y. Xu, Anisotropic response of cold sprayed copper deposits, Surf. Coatings Technol. 335 (2018) 219–227. https://doi.org/10.1016/j.surfcoat.2017.12.043.

[172] M.R. Rokni, C.A. Widener, G.A. Crawford, Microstructural evolution of 7075 Al gas atomized powder and high-pressure cold sprayed deposition, Surf. Coatings Technol. 251 (2014) 254–263. https://doi.org/10.1016/j.surfcoat.2014.04.035.

[173] D. Goldbaum, J.M. Shockley, R.R. Chromik, A. Rezaeian, S. Yue, J.G. Legoux, E. Irissou, The effect of deposition conditions on adhesion strength of Ti and Ti6Al4V cold spray splats, J. Therm. Spray Technol. 21 (2012) 288–303. https://doi.org/10.1007/s11666-011-9720-3.

[174] W. Wong, E. Irissou, A.N. Ryabinin, J.G. Legoux, S. Yue, Influence of helium and nitrogen gases on the properties of cold gas dynamic sprayed pure titanium coatings, J. Therm. Spray Technol. 20 (2011) 213–226. https://doi.org/10.1007/s11666-010-9568-y.

[175] M.J. Lee, H.J. Kim, I.H. Oh, K.A. Lee, Effects of carrier gases on the microstructures and properties of Ti coating layers manufactured through the cold spraying, Adv. Mater. Res. 690 693 (2013) 2116–2119. https://doi.org/10.4028/www.scientific.net/AMR.690-693.2116.

[176] A. Lama, R. Sarvesha, D. John, T. Paul, A. Sukumaran, A. Agarwal, Role of nitrogen and helium gases on microstructure and anisotropic mechanical properties of cold-sprayed scalmalloy deposits, J. Mater. Res. Technol. 30 (2024) 1341–1353. https://doi.org/10.1016/j.jmrt.2024.03.201.

[177] M. Ashokkumar, D. Thirumalaikumarasamy, T. Sonar, M. Ivanov, S. Deepak, P. Rajangam, R. Barathiraja, Effect of post-processing treatments on mechanical performance of cold spray coating - an overview, J. Mech. Behav. Mater. 32 (2023). https://doi.org/10.1515/jmbm-2022-0271.

[178] B. Yu, J. Tam, W. Li, H.J. Cho, J.G. Legoux, D. Poirier, J.D. Giallonardo, U. Erb, Microstructural and bulk properties evolution of cold-sprayed copper coatings after low temperature annealing, Materialia 7 (2019). https://doi.org/10.1016/j.mtla.2019.100356.

[179] X.M. Meng, J.B. Zhang, W. Han, J. Zhao, Y.L. Liang, Influence of annealing treatment on the microstructure and mechanical performance of cold sprayed 304 stainless steel coating, Appl. Surf. Sci. 258 (2011) 700–704. https://doi.org/10.1016/j.apsusc.2011.07.107.

[180] S. Bagherifard, G. Roscioli, M.V. Zuccoli, M. Hadi, G. D'Elia, A.G. Demir, B. Previtali, J. Kondás, M. Guagliano, Cold Spray Deposition of Freestanding Inconel Samples and Comparative Analysis with Selective Laser Melting, J. Therm. Spray Technol. 26 (2017) 1517–1526. https://doi.org/10.1007/s11666-017-0572-3.

[181] W. Ma, Y. Xie, C. Chen, H. Fukanuma, J. Wang, Z. Ren, R. Huang, Microstructural and mechanical properties of high-performance Inconel 718 alloy by cold spraying, J. Alloys Compd. 792 (2019) 456–467. https://doi.org/10.1016/j.jallcom.2019.04.045.

[182] S. Yin, R. Jenkins, X. Yan, R. Lupoi, Microstructure and mechanical anisotropy of additively manufactured cold spray copper deposits, Mater. Sci. Eng. A 734 (2018) 67–76. https://doi.org/10.1016/j.msea.2018.07.096.

[183] W. Li, D. Wu, K. Hu, Y. Xu, X. Yang, Y. Zhang, A comparative study on the employment of heat treatment, electric pulse processing and friction stir processing to enhance mechanical properties of cold-spray-additive-manufactured copper, Surf. Coatings Technol. 409 (2021). https://doi.org/10.1016/j.surfcoat.2021.126887.

[184] A. Cañadilla, A. Romero, G.P. Rodríguez, M. Caminero, Ó.J. Dura, Mechanical, Electrical, and Thermal Characterization of Pure Copper Parts Manufactured via Material Extrusion Additive Manufacturing, Materials (Basel). 15 (2022). https://doi.org/10.3390/ma15134644.

[185] N. Eftekhari, H. Jahed, Comparative Analysis of Microstructural and Mechanical Attributes in

Low-Pressure Cold-Spray Coatings: Impact of Varied Cu Feedstock Powders, J. Therm. Spray Technol. (2024). https://doi.org/10.1007/s11666-024-01762-y.

[186] D.L. Gilmore, R.C. Dykhuizen, R.A. Neiser, T.J. Roemer, M.F. Smith, Particle velocity and deposition efficiency in the cold spray process, J. Therm. Spray Technol. 8 (1999) 576–582. https://doi.org/10.1361/105996399770350278.

[187] D.C. Saha, J.V.S.N. Sripada, G.C. Saha, H. Jahed, Microstructure and Interfacial Bonding Evolution of Cold Spray Deposited Graphene-Reinforced Composite Feedstock on AZ80 Magnesium Substrate, J. Therm. Spray Technol. 32 (2023) 984–1001. https://doi.org/10.1007/s11666-022-01524-8.

[188] P.C. Dey, R. Das, Impact of Silver Doping on the Crystalline Size and Intrinsic Strain of MPA-Capped CdTe Nanocrystals: A Study by Williamson–Hall Method and Size–Strain Plot Method, J. Mater. Eng. Perform. 30 (2021) 652–660. https://doi.org/10.1007/s11665-020-05358-9.

[189] P. Bindu, S. Thomas, Estimation of lattice strain in ZnO nanoparticles: X-ray peak profile analysis, J. Theor. Appl. Phys. 8 (2014) 123–134. https://doi.org/10.1007/s40094-014-0141-9.

[190] Current Science Association Determination of intrinsic strain in poly (vinylpyrrolidone) - capped silver nano-hexapod using X-ray diffraction technique Author (s): Ratan Das and Sumit Sarkar Published by : Current Science Association Stable URL : https, 109 (2021) 775–778.

[191] G.K. Williamson, W.H. Hall, X-ray line broadening from filed aluminium and wolfram, Acta Metall. 1 (1953) 22–31. https://doi.org/10.1016/0001-6160(53)90006-6.

[192] K. Yang, W. Li, X. Yang, Y. Xu, A. Vairis, Effect of heat treatment on the inherent anisotropy of cold sprayed copper deposits, Surf. Coatings Technol. 350 (2018) 519–530. https://doi.org/10.1016/j.surfcoat.2018.07.046.

[193] P.C. King, S.H. Zahiri, M. Jahedi, Microstructural refinement within a cold-sprayed copper particle, Metall. Mater. Trans. A Phys. Metall. Mater. Sci. 40 (2009) 2115–2123. https://doi.org/10.1007/s11661-009-9882-5.

[194] N. Eftekhari, A. Zarei-Hanzaki, A. Shamsolhodaei, A.-L. Helbert, T. Baudin, Microstructural evolution and texture analysis in a thermomechanically processed low SFE super-austenitic steel (alloy-28), Adv. Eng. Mater. 20 (2018). https://doi.org/10.1002/adem.201700928.

[195] N. Eftekhari, W. Muhammad, F. Haftlang, A. Zarei-Hanzaki, É. Martin, Microstructural evolution and corrosion behavior of Sanicro 28 during thermomechanical processing, Mater. Today Commun. 24 (2020) 101228. https://doi.org/10.1016/j.mtcomm.2020.101228.

[196] H. Esmaeilpour, A. Zarei-Hanzaki, N. Eftekhari, H.R. Abedi, M.R. Ghandehari Ferdowsi, Strain induced transformation, dynamic recrystallization and texture evolution during hot compression of an extruded Mg-Gd-Y-Zn-Zr alloy, Mater. Sci. Eng. A 778 (2020). https://doi.org/10.1016/j.msea.2020.139021.

[197] R. Huang, M. Sone, W. Ma, H. Fukanuma, The effects of heat treatment on the mechanical properties of cold-sprayed coatings, Surf. Coatings Technol. 261 (2015) 278–288. https://doi.org/10.1016/j.surfcoat.2014.11.017.

[198] W. Li, Y. Feng, M.P. Planche, H. Liao, G. Montavon, Microstructural evolution and mechanical properties enhancement of a cold-sprayed Cu[sbnd]Zn alloy coating with friction stir processing, Mater. Charact. 125 (2017) 76–82. https://doi.org/10.1016/j.matchar.2017.01.027.

[199] Z. Yanushkevich, A. Belyakov, R. Kaibyshev, C. Haase, D.A. Molodov, Effect of cold rolling on recrystallization and tensile behavior of a high-Mn steel, Mater. Charact. 112 (2016) 180–187. https://doi.org/10.1016/j.matchar.2015.12.021.

[200] M.R. Rokni, C.A. Widener, V.K. Champagne, G.A. Crawford, Microstructure and mechanical properties of cold sprayed 7075 deposition during non-isothermal annealing, Surf. Coatings Technol. 276 (2015) 305–315. https://doi.org/10.1016/j.surfcoat.2015.07.016.

[201] M.R. Rokni, C.A. Widener, V.R. Champagne, Microstructural stability of ultrafine grained cold sprayed 6061 aluminum alloy, Appl. Surf. Sci. 290 (2014) 482–489. https://doi.org/10.1016/j.apsusc.2013.11.127.

[202] C. Huang, M. Arseenko, L. Zhao, Y. Xie, A. Elsenberg, W. Li, F. Gärtner, A. Simar, T. Klassen, Property prediction and crack growth behavior in cold sprayed Cu deposits, Mater.

Des. 206 (2021) 109826. https://doi.org/10.1016/j.matdes.2021.109826.

[203] F. Gärtner, T. Stoltenhoff, J. Voyer, H. Kreye, S. Riekehr, M. Koçak, Mechanical properties of cold-sprayed and thermally sprayed copper coatings, Surf. Coatings Technol. 200 (2006) 6770–6782. https://doi.org/10.1016/j.surfcoat.2005.10.007.

[204] C. Borchers, F. Gärtner, T. Stoltenhoff, H. Kreye, Formation of persistent dislocation loops by ultra-high strain-rate deformation during cold spraying, Acta Mater. 53 (2005) 2991–3000. https://doi.org/10.1016/j.actamat.2005.02.048.

[205] N. Hutasoit, R.A.R. Rashid, S. Palanisamy, A. Duguid, Correction to: Effect of build orientation and post-build heat treatment on the mechanical properties of cold spray additively manufactured copper parts (The International Journal of Advanced Manufacturing Technology, (2020), 110, 9-10, (2341-2357), 10.10, Int. J. Adv. Manuf. Technol. 110 (2020) 2359. https://doi.org/10.1007/s00170-020-06051-w.

[206] A.H. Huang, Y.F. Wang, M.S. Wang, L.Y. Song, Y.S. Li, L. Gao, C.X. Huang, Y.T. Zhu, Optimizing the strength, ductility and electrical conductivity of a Cu-Cr-Zr alloy by rotary swaging and aging treatment, Mater. Sci. Eng. A 746 (2019) 211–216. https://doi.org/10.1016/j.msea.2019.01.002.

[207] H. Fuxiang, M. Jusheng, N. Honglong, G. Zhiting, Analysis of phases in a Cu–Cr–Zr alloy, Scr. Mater. 48 (2003) 97–102. http://www.sciencedirect.com/science/article/pii/S1359646202003536.

[208] A. Chatterjee, R. Mitra, A.K. Chakraborty, C. Rotti, K.K. Ray, Thermal fatigue damage of Cu-Cr-Zr alloys, J. Nucl. Mater. 443 (2013) 8–16. https://doi.org/10.1016/j.jnucmat.2013.06.046.

[209] J. Chen, J. Wang, X. Xiao, H. Wang, H. Chen, B. Yang, Contribution of Zr to strength and grain refinement in Cu[sbnd]Cr[sbnd]Zr alloy, Mater. Sci. Eng. A 756 (2019) 464–473. https://doi.org/10.1016/j.msea.2019.04.053.

[210] J. Li, L. Chang, S. Li, X. Zhu, Z. An, Microstructure and properties of as-cast Cu-Cr-Zr alloys with lanthanum addition, J. Rare Earths 36 (2018) 424–429. https://doi.org/10.1016/j.jre.2017.11.006.

[211] S. Huang, W. Huang, W. Xie, H. Chen, H. Wang, B. Yang, Microstructure and strengthening mechanisms of CuCrZr alloy by two-step thermomechanical treatment, J. Mater. Sci. Mater. Electron. 31 (2020) 17798–17809. https://doi.org/10.1007/s10854-020-04333-3.

[212] K.V. León, M.A. Muñoz-Morris, D.G. Morris, Optimisation of strength and ductility of Cu-Cr-Zr by combining severe plastic deformation and precipitation, Mater. Sci. Eng. A 536 (2012) 181–189. https://doi.org/10.1016/j.msea.2011.12.098.

[213] N. Ordás, L. Portolés, M. Azpeleta, A. Gómez, J.R. Blasco, M. Martinez, J. Ureña, I. Iturriza, Development of CuCrZr via Electron Beam Powder Bed Fusion (EB-PBF), J. Nucl. Mater. 548 (2021). https://doi.org/10.1016/j.jnucmat.2021.152841.

[214] J. Zhou, P. Diao, Z. Qi, F. Wang, S. Wu, X. Chu, Y. Long, B. Lu, Y. Xie, Microstructure, mechanical properties, and tribological properties of laser assisted cold sprayed CuCrZr coatings: Influences of laser power and laser position, J. Alloys Compd. 968 (2023) 172151. https://doi.org/10.1016/j.jallcom.2023.172151.

[215] J.X. Fang, S.Y. Dong, S.B. Li, Y.J. Wang, B.S. Xu, J. Li, B. Liu, Y.L. Jiang, Direct laser deposition as repair technology for a low transformation temperature alloy: Microstructure, residual stress, and properties, Mater. Sci. Eng. A 748 (2019) 119–127. https://doi.org/10.1016/j.msea.2019.01.072.

[216] Y. Zou, Cold Spray Additive Manufacturing: Microstructure Evolution and Bonding Features, Accounts Mater. Res. 2 (2021) 1071–1081. https://doi.org/10.1021/accountsmr.1c00138.

[217] N. Jeyaprakash, I.A. Alnaser, Y. Cheng, Tribology International Effect of heat treatment on microstructure and mechanical characteristics of laser powder bed fusion (LPBF) produced CuCrZr alloy, Tribol. Int. 197 (2024) 109826. https://doi.org/10.1016/j.triboint.2024.109826.

[218] K. Zhang, E. Gaganidze, M. Gorley, Development of the material CuCrZr, (n.d.).

[219] A.D. Ivanov, A.K. Nikolaev, G.M. Kalinin, M.E. Rodin, Effect of heat treatments on the properties of CuCrZr alloys, J. Nucl. Mater. 307–311 (2002) 673–676. https://doi.org/10.1016/S0022-3115(02)01110-8.

[220] Q. Wang, J. Song, W. Wang, Y. Zhang, K. Wang, Z. Du, The Influence of Heat Treatment on

Microstructure and Properties of Selective Laser Melting CuCrZr Alloy, Adv. Eng. Mater. 26 (2024) 1–13. https://doi.org/10.1002/adem.202301680.

[221] Y. Bai, C. Zhao, Y. Zhang, J. Chen, H. Wang, Additively manufactured CuCrZr alloy: Microstructure, mechanical properties and machinability, Mater. Sci. Eng. A 819 (2021) 141528. https://doi.org/10.1016/j.msea.2021.141528.

[222] X. Tang, X. Chen, F. Sun, P. Liu, H. Zhou, S. Fu, The current state of CuCrZr and CuCrNb alloys manufactured by additive manufacturing: A review, Mater. Des. 224 (2022) 111419. https://doi.org/10.1016/j.matdes.2022.111419.

[223] L. Li, Q. Wang, K. Wang, W. Wang, Y. Zhang, X. Zhang, Precipitation behavior of supersaturated solid-solubility CuCrZr alloy by additive manufacturing, Mater. Sci. Eng. A 901 (2024) 146557. https://doi.org/10.1016/j.msea.2024.146557.

[224] C. Zeng, H. Wen, B.C. Bernard, H. Ding, J.R. Raush, P.R. Gradl, M. Khonsari, S. Guo, Tensile Properties of Additively Manufactured C-18150 Copper Alloys, Met. Mater. Int. 28 (2022) 168–180. https://doi.org/10.1007/s12540-021-01052-0.

[225] Q. Wang, Y. Zhang, K. Wang, S. Liu, X. Zhang, H. Shao, Effect of process parameters and heat treatment on the microstructure and properties of CuCrZr alloy by selective laser melting, Mater. Sci. Eng. A 857 (2022) 144054. https://doi.org/10.1016/j.msea.2022.144054.

[226] Z. Diao, F. Yang, R. wang, Y. Zhang, L. Chen, T. Xiong, W. Yang, M. Rong, Effect of heat treatment on the microstructure and properties of CuCrZr alloy manufactured by wire arc additive manufacturing, J. Alloys Compd. 967 (2023) 171786. https://doi.org/10.1016/j.jallcom.2023.171786.

[227] C. Wallis, B. Buchmayr, Effect of heat treatments on microstructure and properties of CuCrZr produced by laser-powder bed fusion, Mater. Sci. Eng. A 744 (2019) 215–223. https://doi.org/10.1016/j.msea.2018.12.017.

[228] Z. Kuai, Z. Li, B. Liu, Y. Chen, S. Lu, P. Bai, Effect of heat treatment on CuCrZr alloy fabricated by selective laser melting: microstructure evolution, mechanical properties and fracture mechanism, J. Mater. Res. Technol. 23 (2023) 2658–2671. https://doi.org/10.1016/j.jmrt.2023.01.124.

[229] P. Coddet, C. Verdy, C. Coddet, F. Lecouturier, F. Debray, Comparison of the properties of cold-sprayed Cu-0.5Cr-0.05Zr alloys after various heat treatments versus forged and vacuum plasma-sprayed alloys, J. Therm. Spray Technol. 23 (2014) 486–491. https://doi.org/10.1007/s11666-013-0028-3.

[230] Z. Jiang, K. Yang, Y. Xin, S. Zhang, W. Li, S. Wang, Microstructure, high-temperature oxidation and tribological performance of cold-sprayed CuCrZr coating, Surf. Coatings Technol. 469 (2023) 129810. https://doi.org/10.1016/j.surfcoat.2023.129810.

[231] K. Yang, Z. Jiang, S. Zhang, W. Li, Quantitative analysis of microstructural evolution in cold-sprayed CuCrZr: Understanding heat transfer mechanisms from room temperature to 600°C, Addit. Manuf. 92 (2024) 104405. https://doi.org/10.1016/j.addma.2024.104405.

[232] M. Yu, Y. Zhang, P. Lv, H. Chen, Relationship between particle interface structure and performance of cold sprayed CuCrZr deposit, Appl. Surf. Sci. 683 (2025) 161794. https://doi.org/10.1016/j.apsusc.2024.161794.

[233] N. Azizi, H. Asgari, M. Hasanabadi, A. Odeshi, E. Toyserkani, On the microstructure and dynamic mechanical behavior of Cu–Cr–Zr alloy manufactured by high-power laser powder bed fusion, Mater. Des. 253 (2025) 113826. https://doi.org/10.1016/j.matdes.2025.113826.

[234] A.P. Alkhimov, V.F. Kosarev, S. V. Klinkov, The features of cold spray nozzle design, J. Therm. Spray Technol. 10 (2001) 375–381. https://doi.org/10.1361/105996301770349466.

[235] S. Weiller, F. Delloro, A numerical study of pore formation mechanisms in aluminium cold spray coatings, Addit. Manuf. 60 (2022) 103193. https://doi.org/10.1016/j.addma.2022.103193.

[236] B. Yu, J. Tam, W. Li, H.J. Cho, J.G. Legoux, D. Poirier, J.D. Giallonardo, U. Erb, Microstructural and bulk properties evolution of cold-sprayed copper coatings after low temperature annealing, Materialia 7 (2019). https://doi.org/10.1016/j.mtla.2019.100356.

[237] J. Tam, B. Yu, W. Li, D. Poirier, J.G. Legoux, J.D. Giallonardo, J. Howe, U. Erb, The effect of annealing on trapped copper oxides in particle-particle interfaces of cold-sprayed Cu coatings, Scr. Mater. 208 (2022) 114333. https://doi.org/10.1016/j.scriptamat.2021.114333.

[238] M.F. Ashby, The deformation of plastically non-homogeneous materials, Philos. Mag. 21 (1970) 399–424. https://doi.org/10.1080/14786437008238426.

[239] A. Heidarzadeh, T. Saeid, V. Klemm, A. Chabok, Y. Pei, Effect of stacking fault energy on the restoration mechanisms and mechanical properties of friction stir welded copper alloys, Mater. Des. 162 (2019) 185–197. https://doi.org/10.1016/j.matdes.2018.11.050.

[240] A. Belyakov, T. Sakai, H. Miura, K. Tsuzaki, Grain refinement in copper under large strain deformation, Philos. Mag. A Phys. Condens. Matter, Struct. Defects Mech. Prop. 81 (2001) 2629–2643. https://doi.org/10.1080/01418610108216659.

[241] Y. Zhou, X. Zeng, Z. Yang, H. Wu, Effect of crystallographic textures on thermal anisotropy of selective laser melted Cu-2.4Ni-0.7Si alloy, J. Alloys Compd. 743 (2018) 258–261. https://doi.org/10.1016/j.jallcom.2018.01.335.

[242] K. Huang, R.E. Logé, A review of dynamic recrystallization phenomena in metallic materials, Mater. Des. 111 (2016) 548–574. https://doi.org/10.1016/j.matdes.2016.09.012.

[243] X. Wang, F. Feng, M.A. Klecka, M.D. Mordasky, J.K. Garofano, T. El-Wardany, A. Nardi, V.K. Champagne, Characterization and modeling of the bonding process in cold spray additive manufacturing, Addit. Manuf. 8 (2015) 149–162. https://doi.org/10.1016/j.addma.2015.03.006.

[244] R.N. Raoelison, Y. Xie, T. Sapanathan, M.P. Planche, R. Kromer, S. Costil, C. Langlade, Cold gas dynamic spray technology: A comprehensive review of processing conditions for various technological developments till to date, Addit. Manuf. 19 (2018) 134–159. https://doi.org/10.1016/j.addma.2017.07.001.

[245] T. Suhonen, T. Varis, S. Dosta, M. Torrell, J.M. Guilemany, Residual stress development in cold sprayed Al, Cu and Ti coatings, Acta Mater. 61 (2013) 6329–6337. https://doi.org/10.1016/j.actamat.2013.06.033.

[246] R. Nikbakht, M. Saadati, T.S. Kim, M. Jahazi, H.S. Kim, B. Jodoin, Cold spray deposition characteristic and bonding of CrMnCoFeNi high entropy alloy, Surf. Coatings Technol. 425 (2021) 127748. https://doi.org/10.1016/j.surfcoat.2021.127748.

[247] J. Henao, A. Concustell, I. G.Cano, S. Dosta, N. Cinca, J.M. Guilemany, T. Suhonen, Novel Al-based metallic glass coatings by Cold Gas Spray, Mater. Des. 94 (2016) 253–261. https://doi.org/10.1016/j.matdes.2016.01.040.

[248] S. Yin, J. Cizek, C. Chen, R. Jenkins, G. O'Donnell, R. Lupoi, Metallurgical bonding between metal matrix and core-shelled reinforcements in cold sprayed composite coating, Scr. Mater. 177 (2020) 49–53. https://doi.org/10.1016/j.scriptamat.2019.09.023.

[249] S. Yin, Y. Xie, J. Cizek, E.J. Ekoi, T. Hussain, D.P. Dowling, R. Lupoi, Advanced diamond-reinforced metal matrix composites via cold spray: Properties and deposition mechanism, Compos. Part B Eng. 113 (2017) 44–54. https://doi.org/10.1016/j.compositesb.2017.01.009.

[250] S. Bagherifard, S. Monti, M.V. Zuccoli, M. Riccio, J. Kondás, M. Guagliano, Cold spray deposition for additive manufacturing of freeform structural components compared to selective laser melting, Mater. Sci. Eng. A 721 (2018) 339–350. https://doi.org/10.1016/j.msea.2018.02.094.

[251] A. Sova, S. Grigoriev, A. Okunkova, I. Smurov, Potential of cold gas dynamic spray as additive manufacturing technology, Int. J. Adv. Manuf. Technol. 69 (2013) 2269–2278. https://doi.org/10.1007/s00170-013-5166-8.

[252] H. Wu, X. Xie, M. Liu, C. Verdy, Y. Zhang, H. Liao, S. Deng, Stable layer-building strategy to enhance cold-spray-based additive manufacturing, Addit. Manuf. 35 (2020) 101356. https://doi.org/10.1016/j.addma.2020.101356.

[253] K. Yang, W. Li, X. Guo, X. Yang, Y. Xu, Characterizations and anisotropy of cold-spraying additive-manufactured copper bulk, J. Mater. Sci. Technol. 34 (2018) 1570–1579. https://doi.org/10.1016/j.jmst.2018.01.002.

[254] X. Wu, P. Jiang, L. Chen, F. Yuan, Y.T. Zhu, Extraordinary strain hardening by gradient structure, Proc. Natl. Acad. Sci. U. S. A. 111 (2014) 7197–7201. https://doi.org/10.1073/pnas.1324069111.

[255] X.L. Wu, P. Jiang, L. Chen, J.F. Zhang, F.P. Yuan, Y.T. Zhu, Synergetic strengthening by gradient structure, Mater. Res. Lett. 2 (2014) 185–191. https://doi.org/10.1080/21663831.2014.935821.

[256] A. Chen, J. Liu, H. Wang, J. Lu, Y.M. Wang, Gradient twinned 304 stainless steels for high strength and high ductility, Mater. Sci. Eng. A 667 (2016) 179–188. https://doi.org/10.1016/j.msea.2016.04.070.

[257] Y. Wei, Y. Li, L. Zhu, Y. Liu, X. Lei, G. Wang, Y. Wu, Z. Mi, J. Liu, H. Wang, H. Gao, Evading the strength-ductility trade-off dilemma in steel through gradient hierarchical nanotwins, Nat. Commun. 5 (2014). https://doi.org/10.1038/ncomms4580.

[258] Y. Zhao, T. Topping, J.F. Bingert, J.J. Thornton, A.M. Dangelewicz, Y. Li, W. Liu, Y. Zhu, Y. Zhou, E.J. Lavernia, High tensile ductility and strength in bulk nanostructured nickel, Adv. Mater. 20 (2008) 3028–3033. https://doi.org/10.1002/adma.200800214.

[259] W. Yinmin, C. Mingwei, Z. Fenghua, M. En, High tensile ductility in a nanostructured metal, Nature 419 (2002) 912. http://dx.doi.org/10.1038/nature01133.

[260] B.Q. Han, J.Y. Huang, Y.T. Zhu, E.J. Lavernia, Strain rate dependence of properties of cryomilled bimodal 5083 Al alloys, Acta Mater. 54 (2006) 3015–3024. https://doi.org/10.1016/j.actamat.2006.02.045.

[261] B.Q. Han, Z. Lee, D. Witkin, S. Nutt, E.J. Lavernia, Deformation behavior of bimodal nanostructured 5083 Al alloys, Metall. Mater. Trans. A Phys. Metall. Mater. Sci. 36 (2005) 957–965. https://doi.org/10.1007/s11661-005-0289-7.

[262] C. Sawangrat, S. Kato, D. Orlov, K. Ameyama, Harmonic-structured copper: Performance and proof of fabrication concept based on severe plastic deformation of powders, J. Mater. Sci. 49 (2014) 6579–6585. https://doi.org/10.1007/s10853-014-8258-4.

[263] S.K. Vajpai, M. Ota, T. Watanabe, R. Maeda, T. Sekiguchi, T. Kusaka, K. Ameyama, The Development of High Performance Ti-6Al-4V Alloy via a Unique Microstructural Design with Bimodal Grain Size Distribution, Metall. Mater. Trans. A Phys. Metall. Mater. Sci. 46 (2015) 903–914. https://doi.org/10.1007/s11661-014-2649-7.

[264] Z. Zhang, S.K. Vajpai, D. Orlov, K. Ameyama, Improvement of mechanical properties in SUS304L steel through the control of bimodal microstructure characteristics, Mater. Sci. Eng. A 598 (2014) 106–113. https://doi.org/10.1016/j.msea.2014.01.023.

[265] I.J. Beyerlein, J.R. Mayeur, S. Zheng, N.A. Mara, J. Wang, A. Misra, Emergence of stable interfaces under extreme plastic deformation, Proc. Natl. Acad. Sci. U. S. A. 111 (2014) 4386–4390. https://doi.org/10.1073/pnas.1319436111.

[266] M. Calcagnotto, Y. Adachi, D. Ponge, D. Raabe, Deformation and fracture mechanisms in fine- and ultrafine-grained fer- rite/martensite dual-phase steels and the effect of aging, Acta Mater. 59 (2011) 658–670. https://doi.org/10.1016/j.actamat.2010.10.002.

[267] Z. Li, K.G. Pradeep, Y. Deng, D. Raabe, C.C. Tasan, Metastable high-entropy dual-phase alloys overcome the strength-ductility trade-off, Nature 534 (2016) 227–230. https://doi.org/10.1038/nature17981.

[268] X. Wu, F. Yuan, M. Yang, P. Jiang, C. Zhang, L. Chen, Y. Wei, E. Ma, Nanodomained nickel unite nanocrystal strength with coarse-grain ductility, Sci. Rep. 5 (2015) 1–10. https://doi.org/10.1038/srep11728.

[269] K. Lu, F.K. Yan, H.T. Wang, N.R. Tao, Strengthening austenitic steels by using nanotwinned austenitic grains, Scr. Mater. 66 (2012) 878–883. https://doi.org/10.1016/j.scriptamat.2011.12.044.

[270] Y.S. Li, N.R. Tao, K. Lu, Microstructural evolution and nanostructure formation in copper during dynamic plastic deformation at cryogenic temperatures, Acta Mater. 56 (2008) 230–241. https://doi.org/10.1016/j.actamat.2007.09.020.

[271] D. Orlov, H. Fujiwara, K. Ameyama, Obtaining copper with harmonic structure for the optimal balance of structure-performance relationship, Mater. Trans. 54 (2013) 1549–1553. https://doi.org/10.2320/matertrans.MH201320.

[272] K. Lu, J. Lu, Surface nanocrystallization (SNC) of metallic materials-presentation of the concept behind a new approach, J. Mater. Sci. Technol. 15 (1999) 193–197.

[273] K. Lu, J. Lu, Nanostructured surface layer on metallic materials induced by surface mechanical attrition treatment, Mater. Sci. Eng. A 375–377 (2004) 38–45. https://doi.org/10.1016/j.msea.2003.10.261.

[274] W.L. Li, N.R. Tao, K. Lu, Fabrication of a gradient nano-micro-structured surface layer on

bulk copper by means of a surface mechanical grinding treatment, Scr. Mater. 59 (2008) 546–549. https://doi.org/10.1016/j.scriptamat.2008.05.003.

[275] R. Thevamaran, O. Lawal, S. Yazdi, S.J. Jeon, J.H. Lee, E.L. Thomas, Dynamic creation and evolution of gradient nanostructure in single-crystal metallic microcubes, Science (80-.). 354 (2016) 312–316. https://doi.org/10.1126/science.aag1768.

[276] Y. Wang, S. Liang, P. Xiao, J. Zou, Experimental and simulation analysis of thermal shock with rapid heating followed by water quenching for CuW70 alloys, Xiyou Jinshu Cailiao Yu Gongcheng/Rare Met. Mater. Eng. 41 (2012) 393–396. https://doi.org/10.1016/s1875-5372(12)60034-4.

[277] D.H. Lassila, T. Shen, B.Y. Cao, M.A. Meyers, Effect of low-temperature shock compression on the microstructure and strength of copper, Metall. Mater. Trans. A Phys. Metall. Mater. Sci. 35 A (2004) 2729–2739. https://doi.org/10.1007/s11661-004-0219-0.

[278] Z.Y. Zhang, L.X. Sun, N.R. Tao, Raising thermal stability of nanograins in a CuCrZr alloy by precipitates on grain boundaries, J. Alloys Compd. 867 (2021) 159016. https://doi.org/10.1016/j.jallcom.2021.159016.

[279] Z. Lee, V. Radmilovic, B. Ahn, E.J. Lavernia, S.R. Nutt, Tensile deformation and fracture mechanism of bulk bimodal ultrafine-grained Al-Mg alloy, Metall. Mater. Trans. A Phys. Metall. Mater. Sci. 41 (2010) 795–801. https://doi.org/10.1007/s11661-009-0007-y.

[280] F. Han, Y. Jiang, F. Cao, L. Cai, S. Liang, A hard/soft layered micro-structured CuCrZr alloy with strength, ductility and electrical conductivity synergy, Mater. Charact. 199 (2023) 112836. https://doi.org/10.1016/j.matchar.2023.112836.

[281] C.Y. Sun, L. Li, M.W. Fu, Q.J. Zhou, Element diffusion model of bimetallic hot deformation in metallurgical bonding process, Mater. Des. 94 (2016) 433–443. https://doi.org/10.1016/j.matdes.2016.01.058.

[282] H. Kato, R. Moat, T. Mori, K. Sasaki, P. Withers, Back stress work hardening confirmed by bauschinger effect in a TRIP steel using bending tests, ISIJ Int. 54 (2014) 1715–1718. https://doi.org/10.2355/isijinternational.54.1715.

[283] X. Feaugas, On the origin of the tensile flow stress in the stainless steel AISI 316L at 300 K: Back stress and effective stress, Acta Mater. 47 (1999) 3617–3632. https://doi.org/10.1016/S1359-6454(99)00222-0.

[284] H. Gao, Y. Huang, Geometrically necessary dislocation and size-dependent plasticity, Scr. Mater. 48 (2003) 113–118. https://doi.org/10.1016/S1359-6462(02)00329-9.

[285] M.E. Kassner, P. Geantil, L.E. Levine, Long range internal stresses in single-phase crystalline materials, Int. J. Plast. 45 (2013) 44–60. https://doi.org/10.1016/j.ijplas.2012.10.003.

[286] H. Haddou, M. Risbet, G. Marichal, X. Feaugas, The effects of grain size on the cyclic deformation behaviour of polycrystalline nickel, Mater. Sci. Eng. A 379 (2004) 102–111. https://doi.org/10.1016/j.msea.2003.12.069.

[287] J. Li, S. Wang, Q. Mao, Z. Huang, Y. Li, Soft/hard copper/bronze laminates with superior mechanical properties, Mater. Sci. Eng. A 756 (2019) 213–218. https://doi.org/10.1016/j.msea.2019.04.069.